ASPECTS OF GROUP 14 ELEMENT - TRANSITION METAL CLUSTER CHEMISTRY

A thesis submitted to
the University of Waikato
for the degree of
Doctor of Philosophy

by

GLEN CLIFTON BARRIS

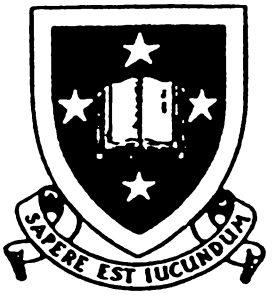

University of Waikato

1990

To
Jan Maree Whittaker

ABSTRACT

The synthesis of $Sn[Fe_2(CO)_8]_2$ from the $SnCl_4/[Fe(CO)_4]^{2-}$ and $SnCl_4/[Fe_2(CO)_8]^{2-}$ systems has been investigated. The reaction of $SnCl_4$ with the product mixture obtained by Na/amalgam reduction of $Fe(CO)_5$ provided the optimum yield (64% based on Sn).

$E[Co_2(CO)_7]_2$ (E = Si, Ge), $(CO)_4CoECo_3(CO)_9$ (E = Si, Ge) and $E[Fe_2(CO)_8]_2$ (E = Si, Ge, Sn) have been reacted with various transition metal carbonyl anions. The $Si[Co_2(CO)_7]_2/[Co(CO)_4]^-$ synthesis of $[SiCo_9(CO)_{21}]^{2-}$, has also yielded $[CCo_8(CO)_{18}]^{2-}$ (characterised by infrared spectroscopy and FABS mass spectroscopy) and $[Cl_2SiCo_7(CO)_{21}]^-$ (characterised by X-ray crystallography as the $[Et_4N]^+$ salt). A $[CCo_{10}(CO)_{24}]^{n-}$ species has also been detected by FABS mass spectroscopy. $(CO)_4CoGeCo_3(CO)_9$ with $[Mn(CO)_5]^-$ provided $(CO)_5MnGeCo_3(CO)_9$ in improved yields (72%). The reaction of the Si analogue gave $(CO)_5MnSiCo_3(CO)_9$, characterised by infrared spectroscopy and FABS mass spectroscopy. $[Co_6(CO)_{15}]^=$ acted as a source of $[Co(CO)_4]^-$ and $Co_4(CO)_{12}$ in reactions with $(CO)_4CoECo_3(CO)_9$ (E = Si,Ge). $[SiCo_9(CO)_{21}]^{2-}$ and $Co_4(CO)_{12}$ were isolated as the major products from the Si reaction, and $[GeCo_5(CO)_{16}]^-$ from the Ge reaction. $[GeCo_5(CO)_{16}]^-$ was also isolated as the major product from the reaction of $Ge[Co_2(CO)_7]_2$ with $[CpNi(CO)]_2$. In reactions of $Si[Co_2(CO)_7]_2$ with $[Fe_2(CO)_8]^{2-}$ and $[Fe(CO)_3NO]^-$, no Si-containing clusters were detected amongst the products. The first reaction yielded $[FeCo_3(CO)_{12}]^-$ (characterised by infrared spectroscopy and preliminary X-ray diffraction), $Co_4(CO)_{12}$ and $Fe(CO)_5$; and the latter reaction, $[FeCo_3(CO)_{12}]^-$, $Co_4(CO)_{12}$ and the nitrido cluster, $[NCo_6(CO)_{15}]^-$ (characterised by infrared spectroscopy and X-ray crystallography). Combining $E[Fe_2(CO)_8]_2$ with $[Co(CO)_4]^-$, $[Fe_2(CO)_8]^{2-}$ or $[Mn(CO)_5]^-$ also failed to produce clusters containing E atoms. No reaction was detected with $[Co(CO)_4]^-$; the second reaction yielded $[HFe_3(CO)_{11}]^-$ and $[Fe_4(CO)_{13}]^{2-}$; and the third, $Mn_2(CO)_{10}$ and the carbido cluster $[CFe_6(CO)_{16}]^{2-}$ (characterised by infrared spectroscopy and FABS mass spectroscopy).

Some reactions of $[SiCo_9(CO)_{21}]^{2-}$ and $[GeCo_5(CO)_{16}]^-$ have been investigated. With $[Ph_3PAu]^+$, $[SiCo_9(CO)_{21}]^{2-}$ yielded a species formulated as $[SiCo_9(CO)_{22}]^{3-}$ (from infrared and FABS mass spectroscopy data). A $[CCo_{10}(CO)_{24}]^-$ species was also detected by FABS mass

spectroscopy. NO^+ appeared to add on to $[SiCo_9(CO)_{21}]^{2-}$ but the exact nature of this product is not known. Reactions with Cp_2Co, $[BuNCAu]^+$ and H^+ have also yielded products which have not been fully characterised. Treatment of $[SiCo_9(CO)_{21}]^{2-}$ with $[(MeCN)_4Cu]^+$ led to disintegration of the cluster. $[GeCo_5(CO)_{16}]^-$ did not react with $[Ph_3PAu]^+$ or $[CpNi(CO)]_2$, but with $CpFe(CO)_2I$ yielded $Co_4(CO)_{12}$, $CpFeCo(CO)_6$ and $[GeCo_7(CO)_{20}]^-$ (characterised by infrared spectroscopy and FABS mass spectroscopy).

The electrochemistry of clusters containing trigonal pyrimidal and *spiro* μ_4-EM_4 groups has been investigated using cyclic voltammetry. $L_nMECo_3(CO)_9$ (E = Si, Ge; and ML_n = $Co(CO)_4$, $Mn(CO)_5$) compounds undergo an electrochemically reversible one electron reduction process, conforming with what has been reported for $YCCo_3(CO)_9$ compounds. $[Ge_2Co_7(CO)_{21}]^-$ and $[Ge_2Co_5Fe_2(CO)_{22}]^-$ contain two EM_3 redox centres which appear to behave independently. Reduction of *spiro*- $E[Fe_2(CO)_8]_2$ clusters occurs via two routes leading to $[(CO)_4FeEFe_3(CO)_{10}]^-$ (more important for Si and Ge) or $[(CO)_8Fe_2]E[Fe(CO)_4]_2^{2-}$ (more important for Sn and Pb). The cobaltocene reduction of $Si[Fe_2(CO)_8]_2$ yielded $[(CO)_4FeSiFe_3(CO)_{10}]^-$, characterised using infrared spectroscopy.

The vibrational spectra of $E[Fe_2(CO)_8]_2$ (E = Si, Ge, Sn), $E[Co_2(CO)_7]_2$ (E = Si, Ge) and $(CO)_4CoECo_3(CO)_9$ (E = Si, Ge) have been recorded and assigned where possible. For the $E[Co_2(CO)_7]_2$ systems a 'double-Bor' model, based on Bor's analysis of $(\mu$-$E)_2M_2(CO)_6$ compounds, provides a consistent assignment for the carbonyl vibrations.

ACKNOWLEDGEMENTS

I would like to thank all the staff and students of the chemistry department for their cooperation and support during the course of this work. In particular I wish to thank the following people:

My supervisors Assoc. Prof. Brian Nicholson and Prof. Ken Mackay for their invaluable advice and encouragement.

Prof. Brian Robinson and Assoc. Prof. Jim Simpson of the University of Otago for making me welcome in Dunedin and for showing me the mysteries of cyclic voltammetry.

Dr Tony Cartner and Brett Loper for assistance with Raman spectroscopy.

S. Stokes and John Little for electron probe analyses.

Prof. M.I. Bruce and co-workers for obtaining FABS mass spectra at the University of Adelaide

Prof. W.T. Robinson for collecting X-ray diffraction intensity data at the University of Canterbury

Finally, I would especially like to thank Jan Whittaker, not only for typing and proof-reading much of this thesis, but also for putting up with a zombie and an ever-threatening tide of notes, papers, journals and theses for the last few months.

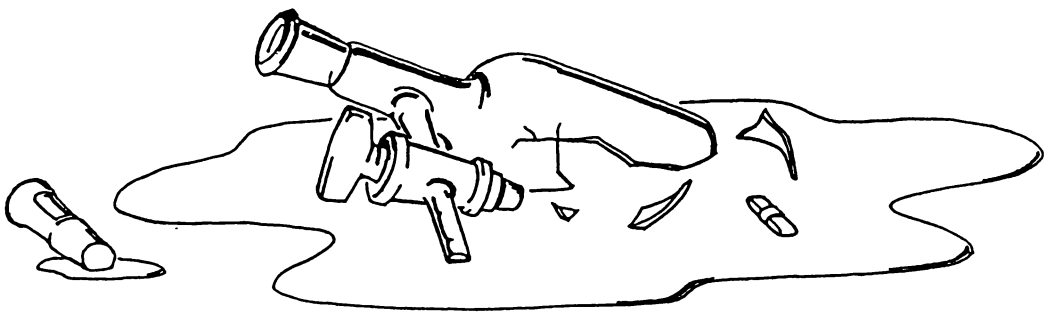

TABLE OF CONTENTS

Chapter 6 Spectroscopic Studies

LIST OF FIGURES

APPENDICES

LIST OF TABLES

ABBREVIATIONS

The following abbreviations are used in this thesis:

E	Main Group Atom
M	Transition Metal Atom
L	Ligand
R	Substituent - usually alkyl or aryl
Y	Substituent - nonspecific
X	Halogen
Me	Methyl
Et	Ethyl
Bu	Butyl
Cp	Cyclopentadienyl
Ph	Phenyl
PPN	Bis-triphenylphosphine Imine
THF	Tetra-hydro-furan
TBAP	Tetra-butyl-Ammonium Perchlorate
CE	Control Electrode
RE	Reference Electrode
WE	Working Electrode
CVMO	Cluster Valence Molecular Orbital
HOMO	Highest Occupied Molecular Orbital
LUMO	Lowest Unoccupied Molecular Orbital
IR	Infrared-active
R	Raman-active
i.a.	inactive
vs	very strong
s	strong
m	medium
w	weak
vw	very weak
br	broad
sh	shoulder
pol or p	polarised
min	minute
h	hour

Chapter One

CHAPTER 1 INTRODUCTION TO TRANSITION METAL CLUSTERS CONTAINING GROUP 14 ATOMS

1.1 GENERAL

The field of main group-transition metal cluster chemistry has evolved rapidly in recent years. Whereas early literature was concerned mainly with the synthesis and characterisation of novel clusters, today increasing emphasis is being placed on understanding structural trends [1,2,3,4], the reactivity of clusters [5], their spectroscopic [6] and bonding properties [7,8], and their potential uses (*eg.* as catalysts). The presence of partially or fully encapsulated main group atoms has been found to impart stability to transition metal clusters; give unusual geometries such as square antiprisms (*eg.* $[CCo_8(CO)_{18}]^{2-}$ [9]) and open butterflies (*eg.* $[CFe_4(CO)_{12}]^{2-}$ [10]); and allow the formation of high nuclearity clusters by providing an internal source of electrons. In this respect, encapsulated atoms can be regarded as internal ligands.

Relevant to the work related in this thesis are clusters containing group 14 atoms with coordination numbers greater than three, bonded *solely* to transition metal atoms. The group 14 atoms in these clusters can be described as 'bare' atoms, the description used by Herrmann in his review [11]. The majority of the literature in this field is devoted to clusters containing carbido atoms, and several good reviews describing this class of compound are available [12,10]. In comparison, silicon, germanium, tin and lead clusters are under-represented. This reflects the increased size of the lower group 14 atoms, the availability of carbon, which is often derived by disproportionation of CO ligands, and also the lack of attention that has been given to compounds incorporating the larger group 14 atoms. Group 14-transition metal clusters are found to be most prevalent amongst the metals of the iron and cobalt groups. To the left of the transition metal series, a paucity of electrons makes clusterification unfavourable, and to the right of the series, the abundance of electrons diminishes the demand for electrons from internal sources.

List of transition metal clusters containing 'bare' group 14 atoms are given in tables 1.2, 1.3, 1.5 and 1.6. For the lower group 14 elements (Si to Pb), this list contains all known clusters which have

been well characterised. The list of carbido clusters may not be as comprehensive, but it is representative of the different structures which are found, and gives an indication of the relative abundance of carbido clusters.

The array of methods which have been used to synthesise group 14-transition metal clusters is bewildering. The task of reviewing these methods is formidable and has not been attempted here. Any preparative routes of direct interest to this work have been discussed where appropriate (in particular see sections 3.1 and 4.1). A number of review articles, describing the preparations and reactivities of these clusters, are available [11,18,5,13] and readers are referred to these for further information.

1.2 ELECTRON COUNTING

Electron counting schemes are frequently used to rationalise the structures adopted by transition metal clusters. In particular, the electron counting schemes proposed by Wade and by Lauher are referred to in this piece of work, and warrant a brief mention.

The basic premise that transition metal atoms require eighteen electrons to fill their valence orbitals, and that this is achieved by forming conventional M-L and M-M bonds (the "eighteen electron rule"), offers little understanding of the structures and bonding within transition metal clusters. It also begins to fail for larger clusters where multi-centre cluster bonding is important.

The semi-empirical approach offered by Wade [14] is more widely applicable and provides a means of rationalising the observed structures. It can also be used to predict stable geometries for new clusters. Wade's rules originate from boron hydride chemistry, and assume a basic $M(CO)_3$ building block (*cf.* the BH unit). Six atomic orbitals on each metal atom are allocated to metal-ligand bonding within the $M(CO)_3$ group, and the remaining three atomic orbitals are involved in cluster bonding. The orbitals available for ligand bonding are the first to be filled by valence electron pairs, and those electron pairs which remain are then assigned to cluster bonding (n + 1 skeletal electron pairs). Therefore, for a given cluster, the number of skeletal electron pairs (n + 1) is given by the formula:

$n + 1 = (NVE - 12N)/2$ NVE = number of valence electrons
N = number of skeletal atoms

If N = n then a closo structure, consisting of a regular polyhedron with n vertices, is adopted. If N < n then corners of the regular n-vertex polyhedron become vacant, giving nido (N = n - 1) or arachno (N = n - 2) structures. If N > n then the extra metal atoms occupy bridging or capping positions. Mingos *et al.* [15] have shown that the introduction of an edge-bridging or face-capping metal carbonyl fragment increases the cluster total valence electron count by increments of 12 or 14 respectively. This however does not effect the number of skeletal electrons and hence the geometry of the basic metal polyhedron is unchanged. With larger clusters, the applicability of Wades rules declines. This is because the number of alternative structures increases, and the difference in energy between them becomes small.

An alternative electron counting scheme, proposed by Lauher [16], is able to account for the electronic situation of most known clusters. He proposed that a metal cluster of a given geometry will have a certain number of cluster valence molecular orbitals (CVMO's), corresponding to half the number of cluster valence electrons, where:

$CVMO = 6N + x$ x = number of extra bonding orbitals available, varying between 3 and 12

For a given N, geometries in which the metal atoms are more efficiently packed, tend to have lower x values. Generally, as the number of CVMO's/N decreases towards 6, the structure approaches that of the bulk metal. Lauher's counting scheme is illustrated for a variety of structures in table 1.1.

Note that for each of these electron counting schemes, care must be taken with clusters containing early- and late-row transition metal elements for which valence electron counts other than eighteen become stable (anomalies associated with gold-containing clusters are discussed in section 4.1.1)

Table 1.1: Electron counting for various structures (taken from reference [16])

geometry	N	$9 \times N$	HLA	CVMO	CVE	CVMO/N	example
monomer	1	9	0	9	18	9.0	$Ni(CO)_4$
dimer	2	18	1	17	34	8.5	$Fe_2(CO)_9$
trimer	3	27	3	24	48	8.0	$Os_3(CO)_{12}$
tetrahedron	4	36	6	30	60	7.5	$Rh_4(CO)_{12}$
butterfly	4	36	5	31	62	7.75	$Re_4(CO)_{16}^{2-}$
square plane	4	36	4	32	64	8.0	$Pt_4(O_2CCH_3)_8$
trigonal bipyramid	5	45	9	36	72	7.2	$Os_5(CO)_{16}$
square pyramid	5	45	8	37	74	7.4	$Fe_5(CO)_{15}C$
bicapped tetrahedron	6	54	12	42	84	7.0	$Os_6(CO)_{18}$
octahedron	6	54	11	43	86	7.17	$Ru_6(CO)_{17}C$
capped square pyramid	6	54	11	43	86	7.17	$Os_6(CO)_{18}H_2$
edge shared bitetrahedron	6	54	11	43	86	7.17	
pentagonal pyramid	6	54	10	44	88	7.33	
trigonal prism	6	54	9	45	90	7.5	$Rh_6(CO)_{15}C^{3-}$
capped octahedron	7	63	14	49	98	7.0	$Rh_7(CO)_{16}^{3-}$
pentagonal pyramid	7	63	14	49	98	7.0	
capped trigonal prism	7	63	12	51	102	7.29	
bicapped octahedron	8	72	17	55	110	6.88	
triangular dodecahedron	8	72	16	56	112	7.0	
square antiprism	8	72	15	57	114	7.13	$Co_8(CO)_{18}C^{2-}$
bicapped trigonal prism	8	72	15	57	114	7.13	
cube	8	72	12	60	120	7.5	$Ni_8(PC_6H_5)_6(CO)_8$
tricapped octahedron	9	81	18	63	126	7.0	
tricapped trigonal prism	9	81	17	64	128	7.11	
capped square antiprism	9	81	16	65	130	7.22	
capped cube	9	81	15	66	132	7.33	
tetrahedron	10	90	20	70	140	7.0	
bicapped cube	10	90	19	71	142	7.1	
bicapped square antiprism	10	90	19	71	142	7.1	
truncated trigonal bipyramid	12	108	28	80	160	6.67	
icosahedron	12	108	23	85	170	7.08	
cube octahedron	12	108	23	85	170	7.08	
truncated hexagonal bipyramid	12	108	23	85	170	7.08	
icosahedron	13	117	32	85	170	6.54	
cube octahedron	13	117	32	85	170	6.54	
truncated hexagonal bipyramid	13	117	32	85	170	6.54	$Rh_{13}(CO)_{24}H_3^{2-}$
face centered cube	14	126	36	90	180	6.43	
rhombic dodecahedron	14	126	30	96	192	6.86	
rhombic dodecahedron	15	135	39	96	192	6.40	

[a] N is the number of atoms; $9 \times N$ is the number of atomic orbitals; HLAO is the number of high lying antibonding orbitals; CVMO is the number of cluster valence molecular orbitals; CVE is the number of cluster valence electrons.

1.3 GROUP 14-TRANSITION METAL CLUSTERS

1.3.1 CLUSTERS IN WHICH E IS COORDINATED TO FOUR M ATOMS

All five group 14 atoms are known to exhibit four-fold coordination in transition metal clusters. Six different coordination geometries have been reported, containing zero to five M-M bonds. Each of these six μ_4-EM_4 structures has a distinct electron count, the number of valence electrons decreasing with increasing degree of closure:

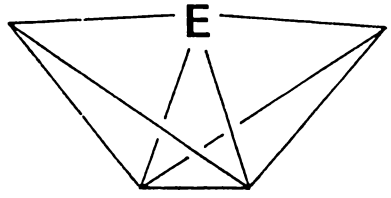

A OPEN BUTTERFLY
NVE = 62

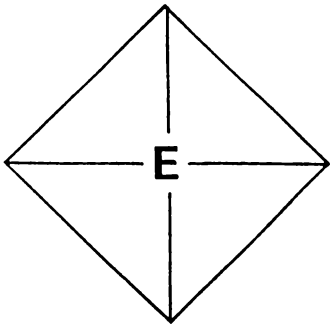

B DISTORTED SQUARE
NVE = 64

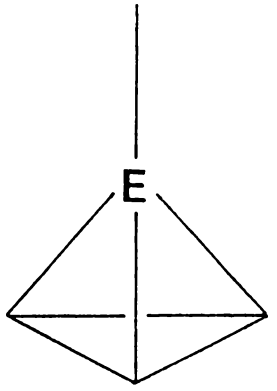

C TRIGONAL PRISMATIC
NVE = 66

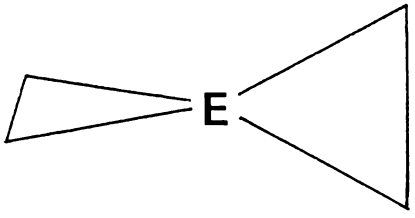

D SPIRO
NVE = 68

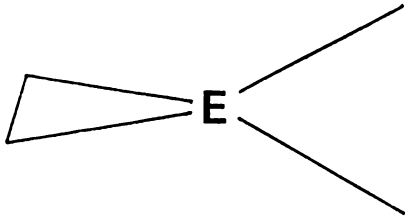

E OPEN-ENDED SPIRO
NVE = 70

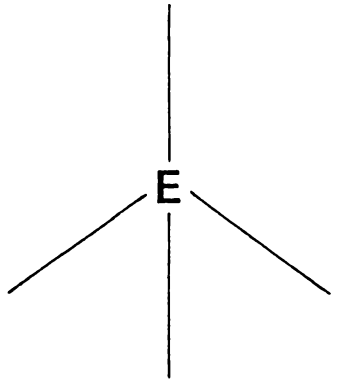

F ALL-TERMINAL
NVE = 72

Clusters containing 'bare' four-coordinate group 14 atoms are listed in table 1.2.

It is very noticeable that the smaller group 14 elements favour configurations which maximise M-M bonding, while larger E atoms prefer more open structures. This appears to be related primarily to the covalent radii of the main group atoms [17].

Only a handful of μ_4-carbido clusters are known, and these are a relatively recent addition to the carbido cluster family. A series of μ_4-CFe_4 clusters have been reported, in which the CFe_4 core exhibits an 'open butterfly' or *cis-arachno*-octahedral geometry (A), with 62 valence electrons as predicted by Wades Rules. $CFe_4(CO)_{13}$ (figure 1.1a and b) was indeed prepared via oxidative decapping of the

Table 1.2: Clusters containing group 14 atoms coordinated to four transition metal atoms

CLUSTER	REF.	CLUSTER	REF.
A BUTTERFLY			
* $CFe_4(CO)_{13}$	[10]	$[CFe_3Cr(CO)_{13}]^{2-}$	[19]
* $[CFe_4(CO)_{12}]^{2-}$	[10]	$[CFe_3W(CO)_{13}]^{2-}$	[19]
* $[CFe_4(H)(CO)_{12}]^{-}$	[10]	$[CFe_3Mn(CO)_{13}]^{-}$	[19]
* $CFe_4(CO)_{10}(PMe_3)_3$	[18]	* $CW_4(OPr^i)_{12}(CNMe)$	[20]
* $[CFe_3Rh(CO)_{12}]^{-}$	[18]		
B DISTORTED SQUARE			
* $[CRe_4(CO)_{15}I]^{-}$	[21]	* $CRu_2Pt_2(H)(CO)_2(PPr^i_3)_2Cp_2$	[22]
C TRIGONAL PYRAMIDAL			
* $(CO)_4CoSiCo_3(CO)_9$	[23]	$Cp(CO)_2FeGeCo_2Mo(CO)_8Cp$	[30]
$Cp(CO)_2FeSiCo_3(CO)_9$	[24]	* $[(CO)_4FeGeFe_3(CO)_9]^{2-}$	[31]
* $(CO)_9Fe_3[SiFe(CO)_2Cp]_2$	[25]	* $[(CO)_4FeGeFe_2Co(CO)_{10}]^{-}$	[25]
* $(CO)_4CoGeCo_3(CO)_9$	[26]	* $[GeCo_7(CO)_{20}]^{-}$	[32]
$Cp(CO)_3CrGeCo_3(CO)_9$	[27]	* $[Ge_2Co_7(CO)_{21}]^{-}$	[32]
$Cp(CO)_3MoGeCo_3(CO)_9$	[27]	* $[Ge_2Co_5Fe_2(CO)_{22}]^{-}$	[33]
$Cp(CO)_3WGeCo_3(CO)_9$	[27]	* $(CO)_9Fe_3[GeFe(CO)_2Cp]_2$	[34]
$(CO)_5MnGeCo_3(CO)_9$	[28]	* $(CO)_9Fe_3[GeCo(CO)_4]_2$	[25]
* $Cp(CO)_2FeGeCo_3(CO)_9$	[29]	* $(CO)_9Fe_3[GeRe(CO)_5]_2$	[35]
$Cp(CO)NiGeCo_3(CO)_9$	[29]	* $(CO)_9Fe_3[SnFe(CO)_2Cp]_2$	[36]
$Cp(CO)_3MoGeCo_2Mo(CO)_8Cp$	[30]	* $(CO)_9Fe_3[SnRe(CO)_5]_2$	[37]
* $Cp(CO)_3WGeCo_2Mo(CO)_8Cp$	[30]		
D SPIRO			
* $Si[Fe_2(CO)_8]_2$	[38]	$Ge[Co_2(CO)_6(GeMe2)]_2$	[44]
* $Si[Co_2(CO)_7]_2$	[39]	* $(EtGe)_2Co_4(CO)_{10}[GeCo_2(CO)_7]$	[44]
* $Ge[Fe_2(CO)_8]_2$	[40]	$(CO)_6Co_2[GeCo_2(CO)_7]_2$	[43]
* $(CO)_8Fe_2GeFeMn(CO)_6(CpMe)$	[41]	$(CO)_6Co_2[GeCo_2(CO)_6(GeMe_2)]_2$	[43]
* $Ge[Co_2(CO)_7]_2$	[42]	* $Ge_3Co_8(CO)_{26}$	[45]
$(CO)_7Co_2GeCo_2(CO)_6(GeMeH)$	[43]	* $(CO)_7Fe_2[GeFe_2(CO)_8]_2$	[46]
$(CO)_7Co_2GeCo_2(CO)_6(GeEtH)$	[44]	* $(CO)_7Fe_2[GeCo_2(CO)_7]_2$	[47]
$(CO)_7Co_2GeCo_2(CO)_6(GePhH)$	[44]	* $(CO)_7Fe_2[GeCo_2(CO)_6(GeMe_2)]_2$	[25]
$(CO)_7Co_2GeCo_2(CO)_6(GeMeCl)$	[44]	* $(CO)_{10}Fe_3[GeFe_2(CO)_8]_2$	[46]
* $(CO)_7Co_2GeCo_2(CO)_6(GeMe_2)$	[44]	* $Sn[Fe_2(CO)_8]_2$	[48]
$Ge[Co_2(CO)_6(GeMeH)]_2$	[44]	* $(CO)_{11}Fe_3SnFe_2(CO)_8$	[25]
$Ge[Co_2(CO)_6(GeEtH)]_2$	[44]	* $(CO)_7Fe_2[SnFe_2(CO)_8]_2$	[46]
$Ge[Co_2(CO)_6(GePhH)]_2$	[44]	* $(CO)_{10}Fe_3[SnFe_2(CO)_8]_2$	[46]
$Ge[Co_2(CO)_6(GeMeCl)]_2$	[44]	* $Pb[Fe_2(CO)_8]_2$	[31]
E OPEN-ENDED SPIRO			
$[(CO)_8Fe_2]Sn[Fe(CO)_4]_2^{2-}$	[31]	$Ge_2Co_4Fe_2(CO)_{22}$	[47]
* $[(CO)_8Fe_2]Pb[Fe(CO)_4]_2^{2-}$	[49]	* $Pb_2Fe_6(CO)_{24}$	[50]
F ALL-TERMINAL			
$Si[Mn(CO)_5]_4$	[51]	$Sn[Co(CO)_4]_4$	[53]
$Si[Re(CO)_5]_4$	[51]	* $Me_4Sn_3Fe_4(CO)_{16}$	[54]
$Ge[Co(CO)_4]_4$	[52]	$Pb[Co(CO)_4]_4$	[55]

* Clusters which have been characterised crystallographically

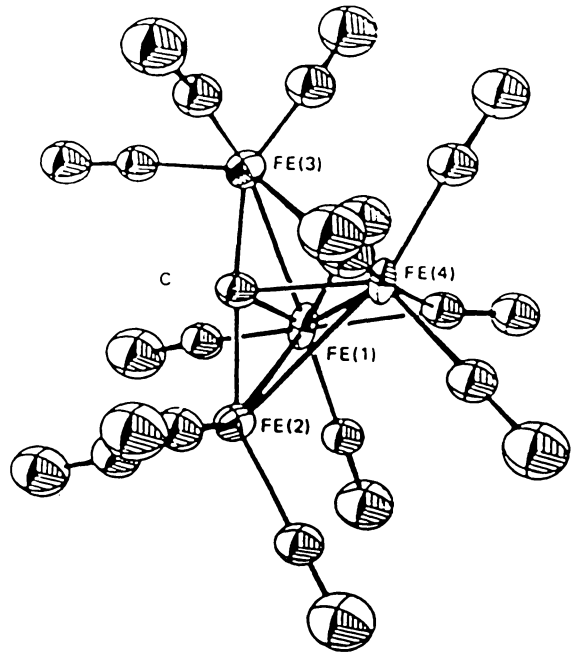

a) $CFe_4(CO)_{13}$

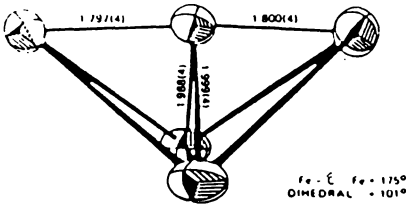

b) Skeletal core of $CFe_4(CO)_{13}$

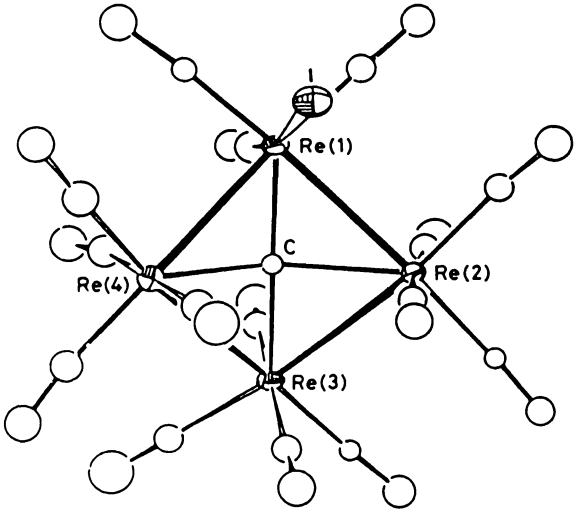

c) $[CRe_4(CO)_{15}I]^-$

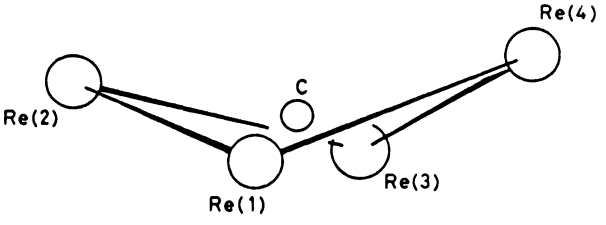

d) Skeletal core of $[CRe_4(CO)_{15}I]^-$

Figure 1.1: Some clusters containing 'bare' four-coordinate carbido atoms

$[CFe_6(CO)_{16}]^{2-}$ octahedral carbido cluster. Mixed metal species have been formed by treating $[(CO)_9Fe_3(CCO)]^{2-}$ with electrophilic transition metal complexes (*eg.* $[CpNi(CO)]_2$ and $Rh(CO)_2(py)Cl$). In each case, the hetero-atom occupies a 'hinge' position.

In $CFe_4(CO)_{13}$, the 'butterfly' angle between the two triangular wings of the butterfly (101°) is less than the angle subtended by neighbouring faces in a regular octahedron (109°). This correlates with a lengthening of the C-$Fe_{'hinge'}$ bonds (1.94 Å) with respect to the C-$Fe_{'wingtip'}$ bonds (1.80 Å). The latter C-$Fe_{'wingtip'}$ bonds remain approximately the same length as the C-Fe bonds in the parent $[CFe_6(CO)_{16}]^{2-}$ cluster. The carbido atom also protrudes slightly from the cluster giving an $Fe_{'wingtip'}$-C-$Fe_{'wingtip'}$ bond angle of 175°. The exposure of the carbido atom in these clusters is thought to be responsible for their reactivity, which is discussed in reference [10]. Huckel molecular orbital calculations have been used to rationalise this reactivity [8].

An alternative CM_4 structure (B) has been reported for $[CRe_4(CO)_{15}I]^-$ [21]. This consists of a μ_4-carbido atom at the centre of a distorted square of 4 Re atoms, as shown in figure 1.1c. This structure can be regarded as a distorted *trans-arachno*-octahedron and contains the expected 64 valence electrons. This species was also formed by oxidative fragmentation of a larger cluster, the monocapped octahedral $[CRe_7(CO)_{21}]^{3-}$ anion. Figure 1.1d shows the buckling of the Re_4 ring. The folding angle (42°) is comparable with that found in cyclobutane (35°), and is likewise attributed to inter-ligand repulsion. A perfectly planar structure would require the ligands on adjacent metal atoms to adopt an eclipsing configuration. The recently reported $CRu_2Pt_2H(CO)_2(PPr_3)_2Cp_2$ cluster has structure a similar to that of $[CRe_4(CO)_{15}I]^-$, but with greater distortion.

Configurations A and B are not known for the larger group 14 elements. The most closed configuration observed for 'bare' four-coordinate Si, Ge and Sn atoms, consists of a closed EM_3 trigonal pyramid, bonded through the E to a fourth metal atom. This structure was first reported for $(CO)_9Co_3SiCo(CO)_4$ (figure 1.2a), synthesised by Schmid and Etzrodt in the reaction of SiI_4 with $NaCo(CO)_4$ [23]. Clusters containing $YCCo_3(CO)_9$ trigonal pyramids have been known for some time [56], but as yet, there are no examples where the carbon is bonded to a fourth transition metal atom. The Ge analogue,

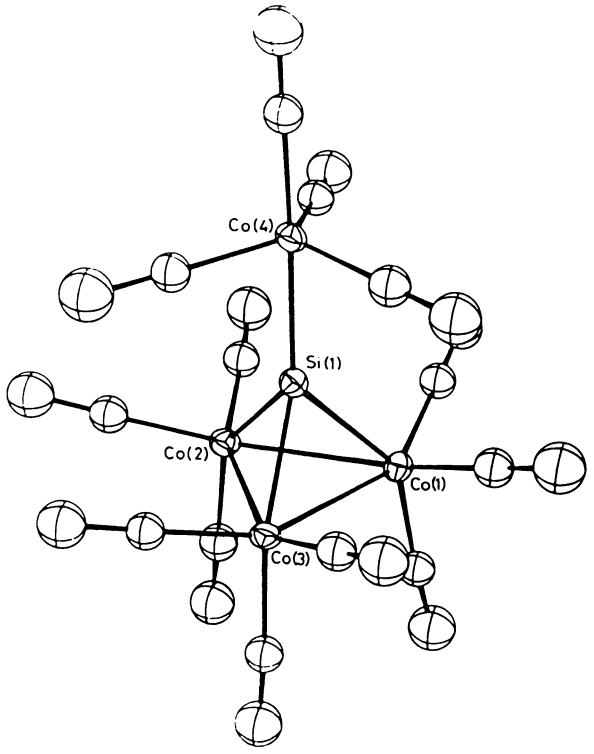

a) $(CO)_4CoSiCo_3(CO)_9$

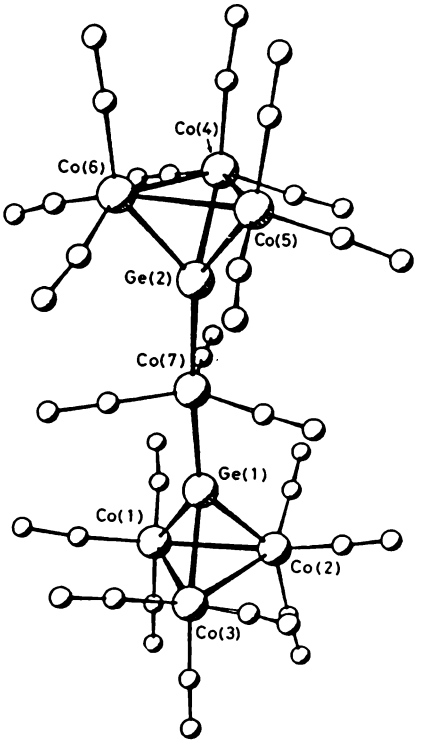

b) $[Ge_2Co_7(CO)_{21}]^-$

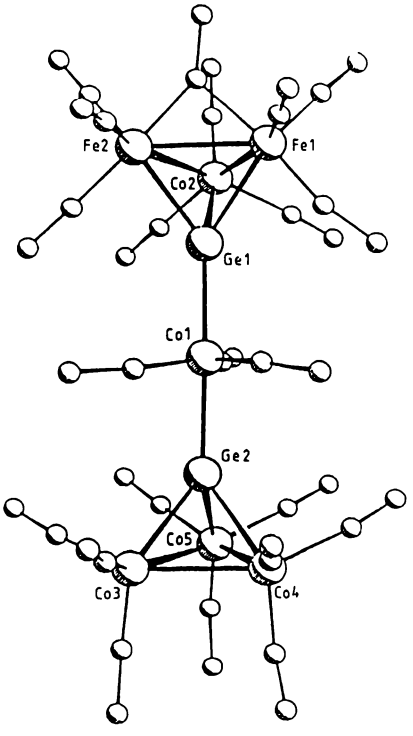

c) $[Ge_2Co_5Fe_2(CO)_{22}]^-$

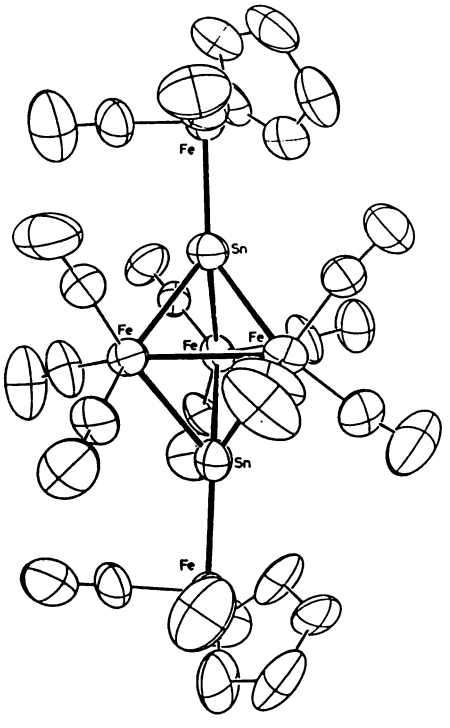

d) $(CO)_9Fe_3[SnFe(CO)_2Cp]_2$

Figure 1.2: Some clusters containing EM_3 trigonal pyramids

$(CO)_4CoGeCo_3(CO)_9$, was reported a short time later. A number of mixed metal clusters have been synthesised by substitution of the terminal metal atom and/or one of the EM_3 metals [57,58,59,60].

The EM_3 tetrahedron which comprises part of this structure is found in many main group-transition metal clusters, and appears to be particularly stable. Chain structures, where MEM_3 units are linked via the terminal metal atom (*eg.* $[Ge_2Co_7(CO)_{21}]^-$ [32,151] and $[Ge_2Co_5Fe_2(CO)_{22}]^-$ [33] in figures 1.2b and 1.2c), or share a common M_3 triangle (*eg.* $(CO)_9Fe_3[EFe(CO)_2Cp]_2$ (E = Si, Ge, Sn [25,34,36]), $(CO)_9Fe_3[ERe(CO)_5]_2$ (E = Ge, Sn [35,37]), and $(CO)_9Fe_3[GeCo(CO)_4]_2$ [25]), are also known. The syntheses and structures of $[Ge_2Co_7(CO)_{21}]^-$ and $[Ge_2Co_5Fe_2(CO)_{22}]^-$ are discussed in Chapter 3. $(CO)_9Fe_3[SnFe(CO)_2Cp]_2$ (figure 1.2d) and $(CO)_9Fe_3[SnRe(CO)_5]_2$ are the only relevant examples of clusters containing SnM_3 trigonal pyramids. Perhaps the long Fe-Fe bonds (2.792 Å for $(CO)_9Fe_3[Sn(CO)_2Cp]_2$ *cf.* ave 2.673 Å for the unbridged bonds in $Fe_3(CO)_{12}$) allowed by this bicapped structure lessen the angular strain required for a large Sn atom to bond to a M_3 triangle.

The *spiro* μ_4-EM_4 structure, D, was first reported for $Ge[Co_2(CO)_7]_2$ (figure 1.3a). This cluster was initially prepared by Gerlach by reacting GeH_4 with $Co_2(CO)_8$ [53,42]. The skeletal core of $Ge[Co_2(CO)_7]_2$ consists of two mutually perpendicular $GeCo_2$ triangles (dihedral angle = 97°) with a common Ge apex. The individual $Co_2(CO)_7$ units closely resemble the bridged isomer of $Co_2(CO)_8$, with a bridging Ge atom replacing a μ-CO group. The Co-Co bond length (ave 2.56 Å) in $Ge[Co_2(CO)_7]_2$ is slightly longer than that in $Co_2(CO)_8$ (2.52 Å), presumably to accommodate the larger Ge atom. Both $GeCo_2$ triangles in $Ge[Co_2(CO)_7]_2$ are asymmetric with one Ge-Co bond (ave 2.38 Å) being significantly longer than the other (ave 2.34 Å). The carbonyl groups bridging the Co-Co bonds show a similar asymmetry, being displaced towards the Co atom with the longer Ge-Co bond. For $Ge[Co_2(CO)_7]_2$, the crystal lattice contains two distinct molecules per unit cell, both showing the same degree of asymmetry. This appears to rule out crystal packing forces as a source of asymmetry, assuming the two molecules experience different crystal force fields.

$Ge[Co_2(CO)_7]_2$ has also been prepared by reacting GeI_4 with $NaCo(CO)_4$ [42] and a related cluster, $[(CO)_7Co_2]Ge[Co_2(CO)_6(\mu\text{-}HgCo(CO)_4)]$ [93,61], was isolated as a byproduct (the bridging Hg atom

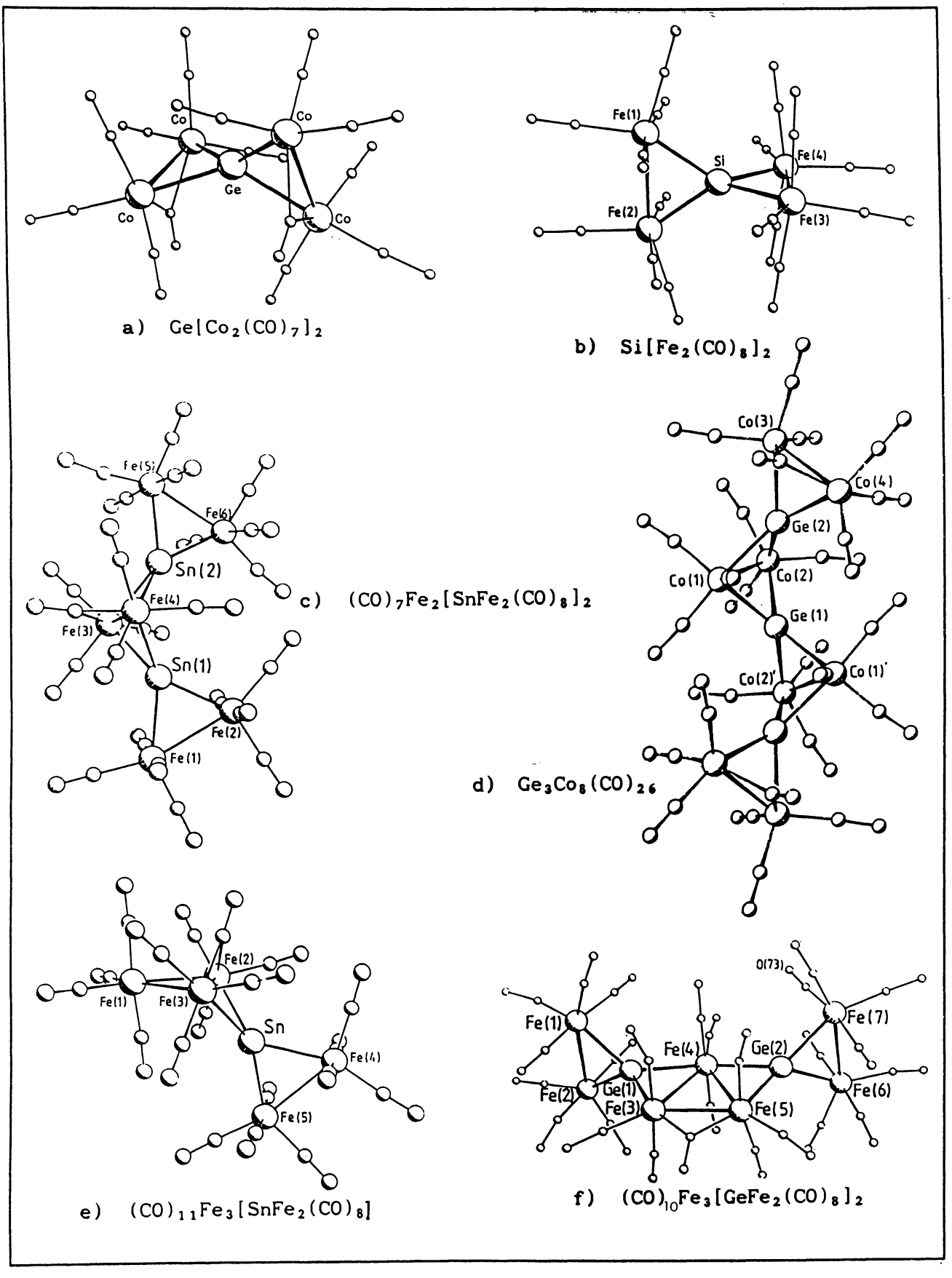

Figure 1.3: Some clusters containing *spiro* μ_4-EM_4 groups

being derived from the amalgam used to prepare the $NaCo(CO)_4$). The Si analogue of $Ge[Co_2(CO)_7]_2$ has also been reported [63,64]. All of these *spiro* clusters show asymmetry in the ECo_2 triangles.

This asymmetry is perhaps best understood by considering the bonding within these compounds. Based on a discussion of the bonding within $(\mu\text{-}Me_2Ge)_3Fe_2(CO)_6$ [62], a significant component of the bonding in the $GeCo_2$ triangles of $Ge[Co_2(CO)_7]_2$ probably involves an interaction between one p orbital on Ge and the d_{XZ} orbitals on each Co:

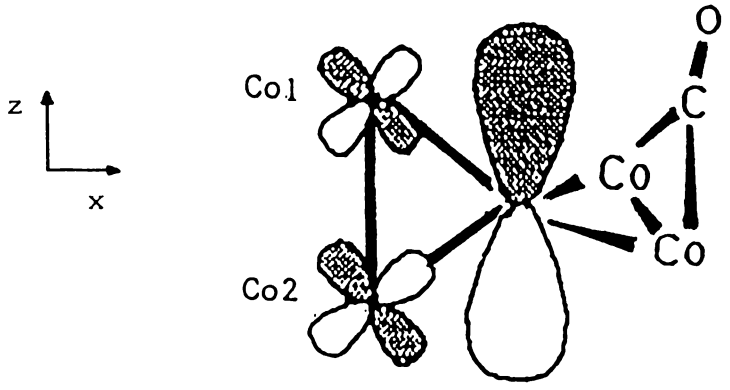

Clearly the opposite bridging carbonyl group is close enough and in the correct orientation for a filled p_π or p_π^* orbital to interact with the Ge p orbital. This would, in turn, reduce the $Ge\text{-}Co_1$ interaction, lengthening this bond relative to the $Ge\text{-}Co_2$ bond.

The $E[Fe_2(CO)_8]_2$ (E = Si, Ge, Sn, Pb) [38,40,48,31] (figure 1.3b) and $[(CO)_8Fe_2]Ge[FeMn(CO)_6(CpMe)]$ [41], which contain no bridging carbonyls, also show a small but significant amount of asymmetry. For $Ge[Fe_2(CO)_8]_2$, the authors [40] attributed the difference in Ge-Fe bond lengths to ring strain, caused by the relative Pauling's covalent radii of iron (1.24 Å) and germanium (1.22 Å).

A series of larger clusters have been reported which have structures based on $E[Co_2(CO)_7]_2$ and $E[Fe_2(CO)_8]_2$. $(CO)_6Co_2[GeCo_2(CO)_7]_2$ [47] and $Ge_3Co_8(CO)_{26}$ [65] (figure 1.3d) which consist of $GeCo_2$ triangles linked through common M-M bonds or Ge apices, have been formed by reacting $Co_2(CO)_8$ with Ge_2H_6 and Ge_3H_8 respectively. In reactions with $RR'GeH_2$, the bridging carbonyls on $Ge[Co_2(CO)_7]_2$ and the longer chain homologues are easily displaced to give a series of RR'Ge-substituted species. The reactions of SnH_4 and GeH_4 with $Fe_2(CO)_9$, as well as giving $E[Fe_2(CO)_8]_2$, have also yielded $(CO)_{11}Fe_3[SnFe_2(CO)_6]$ (figure 1.3e), $(CO)_{10}Fe_3[EFe_2(CO)_8]_2$ (figure 1.3f) and $(CO)_7Fe_2[EFe_2(CO)_8]_2$ (figure 1.3c). The structures of

$(CO)_{11}Fe_3[SnFe_2(CO)_8]$ and $(CO)_{10}Fe_3[EFe_2(CO)_8]_2$ are both based on a triangle of Fe atoms which is bridged by $EFe_2(CO)_8$ groups. The structure of $(CO)_7Fe_2[EFe_2(CO)_8]_2$ is similar to that observed for the concatenated cobalt clusters, but requires a bridging carbonyl to provide an 18 electron count at each of the central Fe atoms.

The asymmetry observed for the *spiro*-EM_4 clusters is exaggerated in the extended-chain homologues, particularly at the centres of these chains. This is consistent with increasing steric interactions. The degrees of asymmetry in the EM_2 triangles, the dihedral angles and the 'butterfly' angles (about doubly-bridged Fe-Fe bonds) vary from cluster to cluster, and this suggests that the metal core of these compounds is quite flexible.

Configuration E is found in $[(CO)_8Fe_2]Sn[Fe(CO)_4]_2^{2-}$ and $[(CO)_8Fe_2]Pb[Fe(CO)_4]_2^{2-}$. The lead compound has been characterised crystallographically, and is shown in **figure 1.4a**. These compounds are related to the $E[Fe_2(CO)_8]_2$ clusters by cleavage of one of the Fe-Fe bonds, and interconversion between these two structures occurs with two-electron oxidation and reduction (Chapter 5). The interesting feature of $[(CO)_8Fe_2]E[Fe(CO)_4]_2^{2-}$ is the fact that the Fe-Fe bond is bridged by two carbonyls, whereas no bridging carbonyls have been detected for $E[Fe_2(CO)_8]_2$ (**figure 1.4b**) in solid or solution. In this case the carbonyl-bridged configuration may allow more efficient dissipation of the negative charge. $Pb_2Fe_6(CO)_{24}$ **[50]** and $Ge_2Co_4Fe_2(CO)_{22}$ **[47]** form chain structures where two E-units are linked via both terminal metal atoms. Note that $Pb_2Fe_6(CO)_{24}$ (**figure 1.4c**) does not contain bridging carbonyls.

$Si[Mn(CO)_5]_4$ and $Si[Re(CO)_5]_4$ **[51]**, characterised by infrared and mass spectroscopy, reportedly contain four terminal metal atoms tetrahedrally bonded to the Si atom (configuration F), however the small size of the Si atom suggests these compounds would be very sterically crowded. $Ge[Co(CO)_4]_4$ has also been characterised spectroscopically, but at room temperature, undergoes rapid decarbonylation to give $Ge[Co_2(CO)_7]_2$. It is only for large Sn and Pb atoms that this most open structure is favourable. $Sn[Co(CO)_4]_4$ **[53]** and $Pb[Co(CO)_4]_4$ **[55]** are known, and the central tin atom in $Me_4Sn_3Fe_4(CO)_{16}$ **[54]** (**figure 1.4d**) also has this configuration.

The syntheses and structures of $EM_4(CO)_x$ (M = Co, Fe) clusters are discussed further in Chapter Three.

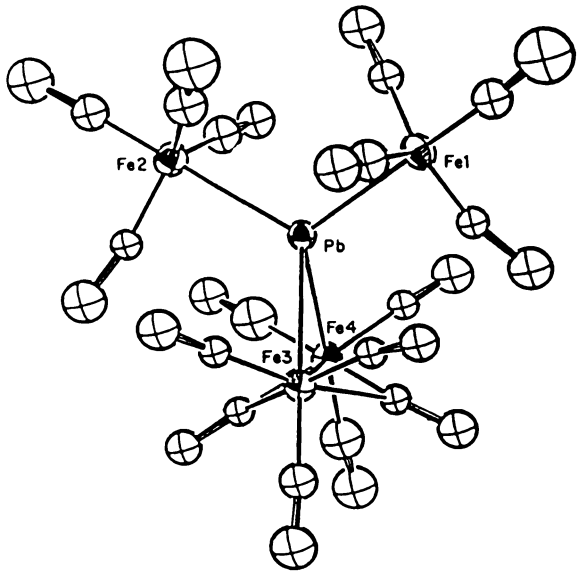

a) $[(CO)_8Fe_2]Pb[Fe(CO)_4]_2^{2-}$

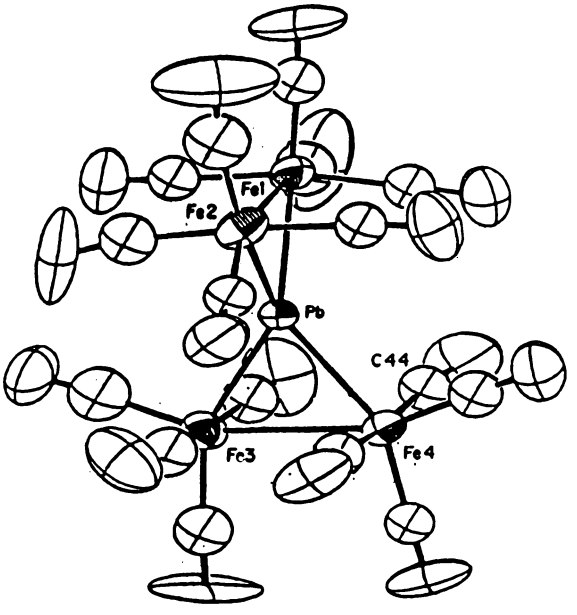

b) $Pb[Fe_2(CO)_8]_2$

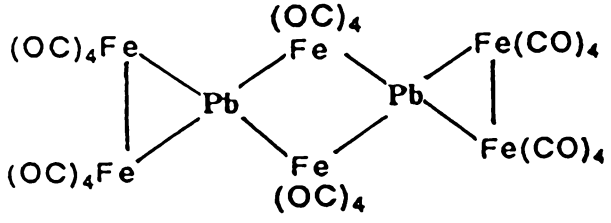

c) $Pb_2Fe_6(CO)_{24}$

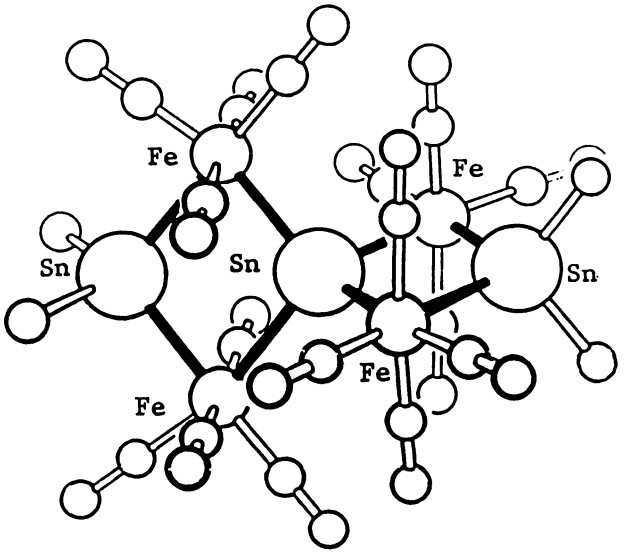

d) $Me_4Sn_3Fe_4(CO)_{16}$

Figure 1.4: Some transition metal clusters containing 'bare' Sn and Pb atoms

1.3.2 CLUSTERS IN WHICH E IS COORDINATED TO FIVE M ATOMS

Four different local bonding configurations are observed for 'bare' group 14 atoms coordinated to 5 transition metals:

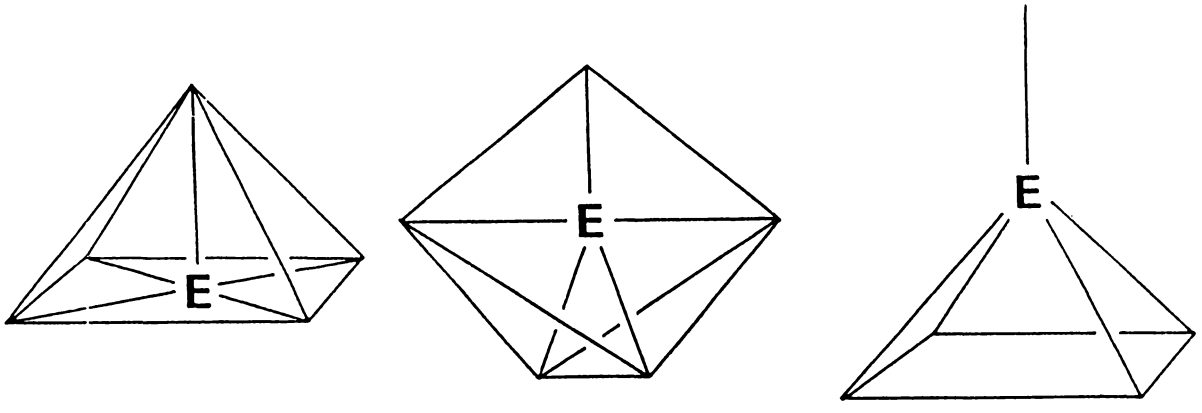

G SQUARE PRISMATIC *H BRIDGED BUTTERFLY* *I CAPPED SQUARE*

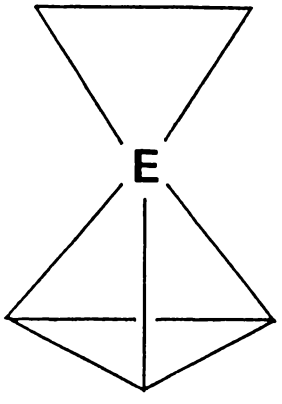

J M_2EM_3

Clusters containing 'bare' five-coordinate group 14 atoms are listed in table 1.3

Five-coordinate encapsulated carbido atoms are known for Fe, Ru and Os, and adopt one of two possible structures. The first of these clusters to be reported was $CFe_5(CO)_{15}$ [66]. This was originally isolated in low yields from the reaction of $Fe_3(CO)_{12}$ with methylphenylacetylene. An X-ray structural analysis, performed in 1962, revealed a square pyramidal core of Fe atoms, with a μ_5-carbido atom located slightly below the centre of the square base of the pyramid (configuration G, figure 1.5a). This structure contains 74 valence electrons, as expected for a *nido*-octahedron.

Table 1.3: Clusters containing group 14 atoms coordinated to five transition metal atoms

CLUSTER	REF.	CLUSTER	REF.
G SQUARE PYRAMID			
* $CFe_5(CO)_{15}$	[66]	$CRu_5(CO)_{14}(PMe_3)$	[73]
$[CFe_5(CO)_{14}H]^-$	[10]	$CRu_5(CO)_{14}(PPh_3)$	[73]
* $[CFe_5(CO)_{14}]^{2-}$	[66]	$[CRu_5(CO)_{13}(NO)]^-$	[74]
$[CFe_5(CO)_{12}Br_2]^{2-}$	[10]	* $CRu_5(CO)_{13}(NO)(AuPPh_3)$	[74]
$CFe_5(CO)_{14}(PPh_3)$	[67]	$CRu_5(CO)_{13}(PMe_3)_2$	[73]
$CFe_5(CO)_{14}(PMe_2Ph)$	[67]	* $CRu_5(CO)_{13}(PPh_3)_2$	[73]
$CFe_5(CO)_{13}(PMe_2Ph)_2$	[67]	* $CRu_5(CO)_{13}(PPh_3)H$	[75]
$CFe_5(CO)_{13}(P(OPh)_3)_2$	[67]	$CRu_5(CO)_{13}(Ph_2P(CH_2)PPh_2)$	[73]
$CFe_5(CO)_{14}(P(OC_3H_7)_3)$	[67]	$CRu_5(CO)_{13}(Ph_2P(CH_2)_2PPh_2)$	[73]
$CFe_5(CO)_{13}(P(OC_3H_7)_3)_2$	[67]	* $CRu_5(CO)_{13}(Ph_2P(CH_2)_4PPh_2)$	[76]
* $[CFe_5(CO)_{13}(SO_2)]^{2-}$	[68]	$CRu_5(CO)_{13}(Ph_2P(CH_2)_2Si(OEt)_3)$	[75]
* $[CFe_4Co(CO)_{14}]^-$	[69]	* $CRu_5(CO)_{12}H_2(Ph_2P(CH_2)_2PPh_2)$	[73]
* $[CFe_4Rh(CO)_{14}]^-$	[70]	* $CRu_5(CO)_{12}H(PPh_3)(SEt)$	[77]
$[CFe_4Cr(CO)_{16}]^-$	[70]	* $CRu_5(CO)_{11}(PPh_2)(PMePh_2)H_3$	[78]
$[CFe_4Mo(CO)_{16}]^-$	[70]	* $COs_5(CO)_{15}$	[79]
$CFe_3Rh_2(CO)_{14}$	[19]	* $[COs_5(CO)_{14}]^{2-}$	[72]
* $CRu_5(CO)_{15}$	[71]	* $COs_5(CO)_{14}(AuPPh_3)_2$	[72]
$[CRu_5(CO)_{14}]^{2-}$	[72]	* $COs_5(CO)_{15}(MeCCMe)$	[80]
H BRIDGED BUTTERFLY			
* $[CFe_5(CO)_{12}Br_2]^{2-}$	[81]	* $CRu_5(CO)_{13}Cp(AuPPh_3)$	[84]
* $CFe_4AuH(CO)_{12}(PPh_3)$	[82]	$CRu_4(CO)_{12}(AuPEt_3)_2$	[85]
* $CRu_5(CO)_{15}(MeCN)$	[73]	$CRu_4(CO)_{12}(AuPPh_3)_2$	[85]
$[CRu_5(CO)_{15}I]^-$	[71]	$CRu_4(CO)_{12}(AuPMe_2Ph)_2$	[85]
$[CRu_5(CO)_{15}F]^-$	[73]	* $CRu_4(CO)_{12}(AuPEt_3)I$	[85]
$[CRu_5(CO)_{15}Cl]^-$	[73]	$CRu_4(CO)_{12}(AuPPh_3)I$	[85]
$[CRu_5(CO)_{15}Br]^-$	[73]	$CRu_4(CO)_{12}(AuPEt_3)H$	[85]
$CRu_5H(CO)_{15}F$	[73]	$CRu_4(CO)_{12}(AuPPh_3)H$	[85]
$CRu_5H(CO)_{15}Cl$	[71]	* $CRu_6(CO)_{15}(SEt)_3$	[10]
$CRu_5H(CO)_{15}Br$	[71]	* $COs_5(CO)_{16}$	[21]
$CRu_5H(CO)_{15}I$	[73]	* $COs_5(CO)_{15}[Ph_2P(CH_2)_2PPh_2]$	[86]
$CRu_5(CO)_{15}I_2$	[73]	* $[COs_5(CO)_{15}I]^-$	[79]
* $CRu_5(CO)_{15}(AuPPh_3)Cl$	[83]	* $COs_5(CO)_{14}(COOEt)H$	[87]
* $CRu_5(CO)_{14}(AuPPh_3)Br$	[83]	* $COs_5(CO)_{14}(COOMe)I$	[87]
* $CRu_5(CO)_{14}(MeCO)(AuPPh_3)$	[84]	* $COs_5(CO)_{14}(NC_5H_4)H$	[88]
* $CRu_5(CO)_{14}(SEt)$	[77]	* $COs_5(CO)_{14}(OP(OMe)_2)H$	[89]
* $CRu_5(CO)_{13}(PPh_3)(AuPPh_3)$	[77]	* $COs_5(CO)_{13}(OP(OMe)_2)(P(OMe)_3)H$	[89]
* $CRu_5(CO)_{13}(PPh_3)(SEt)$	[77]	* $COs_5(CO)_{13}(OP(OMe)OP(P(OMe)_2)H$	[89]
I CAPPED SQUARE			
* $(CO)_{11}Co_4[SiCo(CO)_4]_2$	[90]	* $(CO)_{11}Co_4[GeCo(CO)_4]_2$	[91]
$(MeSi)Co_4(CO)_{11}[SiCo(CO)_4]$	[44]	* $(MeGe)Co_4(CO)_{11}[GeCo(CO)_4]$	[44]
$(MeGe)Co_4(CO)_{11}[SiCo(CO)_4]$	[44]	$(PhGe)Co_4(CO)_{11}[GeCo(CO)_4]$	[44]
* $(EtGe)Co_4(CO)_{11}[SiCo(CO)_4]$	[44]		
J M_2EM_3			
* $[GeCo_5(CO)_{16}]^-$	[92]		

* Clusters which have been characterised crystallographically

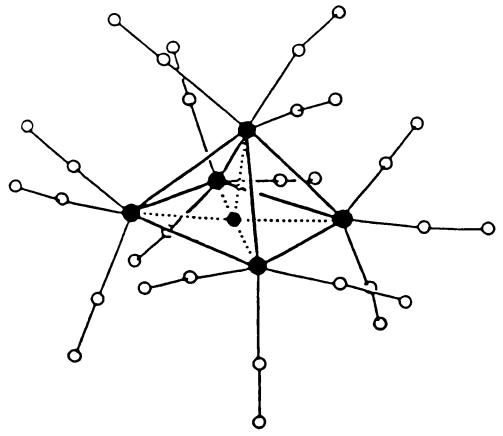

a) $CFe_5(CO)_{15}$

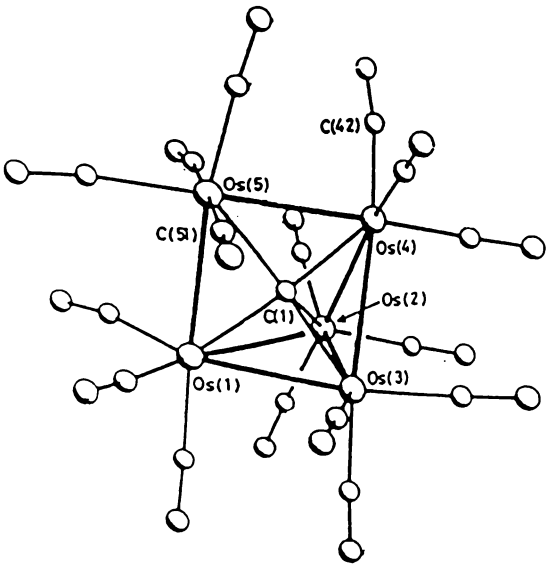

b) $COs_5(CO)_{16}$

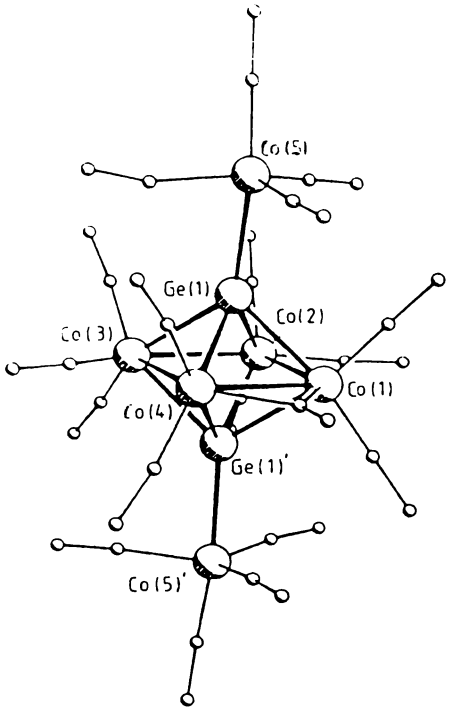

c) $(CO)_{11}Co_4[GeCo(CO)_4]_2$

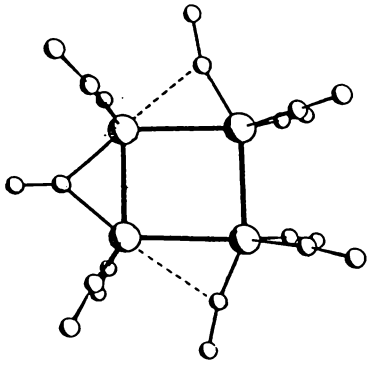

d) Distribution of carbonyls about the Co_4 plane in $(CO)_{11}Co_4[GeCo(CO)_4]_2$

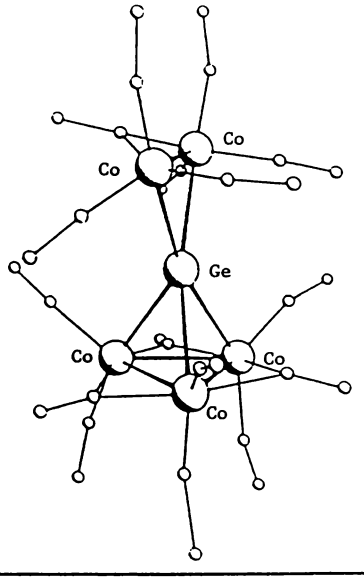

e) $[GeCo_5(CO)_{16}]^-$

Figure 1.5: Some clusters containing 'bare' five-coordinate group 14 atoms

In $CFe_5(CO)_{15}$, the C-Fe_{apical} bond (1.953(5) Å) is significantly longer than the C-Fe_{basal} bond, and as a result, the carbido atom lies 0.09(1) Å below the basal plane. This distance appears to increase with cluster charge, and in $[CFe_5(CO)_{14}]^{2-}$ the carbido atom lies 0.18(1) Å below the plane. A similar trend is observed for $COs_5(CO)_{15}$ and $[COs_5(CO)_{14}]^{2-}$, and in the Ru clusters $CRu_5(CO)_{15}$, $CRu_5(CO)_{14}(PPh_3)$ and $CRu_5(CO)_{13}(PPh_3)_2$, where replacement of CO ligands with PPh_3 (a weaker π-acceptor) effectively increases the charge on the cluster. Charge localistaion on C has been suggested as a possible cause.

The alternative structure for a μ_5-carbido transition metal cluster is the 'bridged butterfly' or *arachno*-pentagonal bipyramid (H), observed for $COs_5(CO)_{16}$ (figure 1.5b). As with the open butterfly structure, the carbido atom is closest to the 'wingtip' or apical Os atoms (1.98(2) Å). The bridged butterfly structure contains 76 valence electrons, and interchange between it and the 74 electron, square pyramid configuration, can occur with addition or loss of ligand(s):

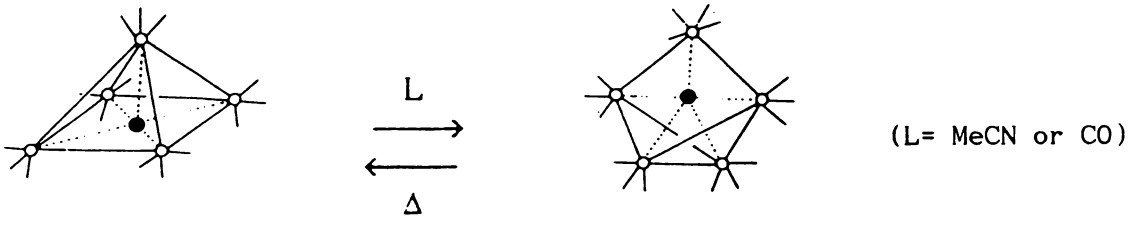

(L= MeCN or CO)

$CRu_5(CO)_{15}$ $CRu_5(CO)_{15}L$

Five-fold coordination is not known for Sn or Pb, but clusters containing μ_5-Si and μ_5-Ge have been reported. All but one of these compounds contain a distorted square of four Co atoms, bicapped by two μ_4-EY groups (figure 1.5c). The Co atoms in the M_4 plane are bonded to eight terminal carbonyls, two semi-bridging carbonyls and one fully bridging carbonyl (figure 1.5d). The E-Co bond lengths observed for these clusters are long (ranging from 2.39 Å to 2.43 Å in $(CO)_{11}Co_4[GeCo(CO)_4]_2$). These compounds have generally been produced from the *spiro*-$E[Co_2(CO)_7]_2$ compounds via reactions with REH_3 (eqns (1) and (2)) or by decarbonylation of extended-chain *spiro* clusters (3):

$$Ge[Co_2(CO)_7]_2 + RGeH_3 \rightarrow GeCo_4(CO)_{13}(GeRH) \xrightarrow{\downarrow Co_2(CO)_8} (RGe)Co_4(CO)_{11}[GeCo(CO)_4] \quad (1)$$

$$Si[Co_2(CO)_7]_2 + REH_3 \rightarrow (RE)Co_4(CO)_{11}[SiCo(CO)_4] \quad (2)$$

$$(CO)_6Co[ECo_2(CO)_7]_2 \xrightarrow{-CO} (CO)_{11}Co_4[ECo(CO)_4]_2 \quad (3)$$

The reaction of $RGeH_3$ with $Co_4(CO)_{12}$ has been found to provide the best route to $(CO)_{11}Co_4(GeR)_2$ (R = alkyl) compounds, but this route has not been investigated for $(CO)_xMGeH_3$ **[44]**.

A number of main group transition metal clusters are known to contain E_2M_4 square bipyramids, which indicates the high stability of this structure. These compounds commonly contain eight skeletal electron pairs (as do all examples listed here), rather than the seven skeletal electron pairs predicted for octahedral clusters. An analysis of the electronic structure of a hypothetical $(HP)_2Fe_4(CO)_{12}$ by Hoffmann *et al.* **[154]** indicates that the additional electron pair occupies an orbital formed from the low-lying HP---PH π^* antibonding molecular orbital and an $[Fe(CO)_3]_4$ combination which is approximately non-bonding.

The remaining 'bare' μ_5-Ge cluster, $[GeCo_5(CO)_{16}]^-$ **[92,93]**, has a unique structure formed by a $GeCo_3$ trigonal pyramid and a $GeCo_2$ triangle sharing a common Ge apex (**figure 1.5e**). In contrast with the earlier EM_3 trigonal pyramid-based structures, the $GeCo_3(CO)_9$ unit in $[GeCo_5(CO)_{16}]^-$ contains three bridging carbonyls about the Co_3 triangle. This feature is found in other $L_nECo_3(CO)_9$ trigonal pyramids with relatively bulky EL_n groups, and appears to be a response to steric crowding **[17]**. The synthesis and structure of $[GeCo_5(CO)_{16}]^-$ are discussed further in Chapter 3.

1.3.3 CLUSTERS IN WHICH E IS COORDINATED TO SIX M ATOMS

Transition metal clusters containing six-coordinate carbido atoms adopt either an octahedral or trigonal prismatic bonding configuration:

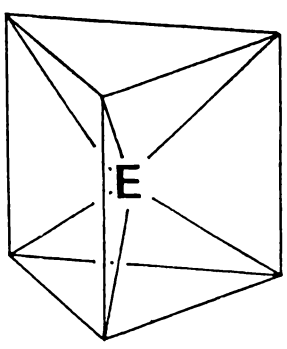

L TRIGONAL PRISMATIC

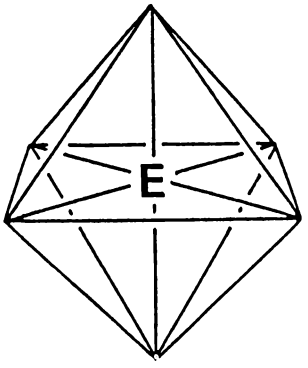

K OCTAHEDRAL

Clusters containing six-coordinate carbido atoms are listed in table 1.5

Both geometries, K and L, can be considered as microcosms of different metallic carbide stuctures. The octahedral structure of $CRu_6(CO)_{17}$ (figure 1.6a), can be compared with the face centred cubic packing of NbC. Similarly, the trigonal prismatic structure of $[CCo_6(CO)_{15}]^{2-}$ (figure 1.6b) is comparable with the hexagonal close packed structure of WC.

Table 1.4: Ideal radius ratios for clusters containing interstitial atoms (from reference [127])

Type of cavity	Number of vertices	r_E/r_M
Octahedron	6	0.414
Trigonal prism	6	0.528
Square antiprism	8	0.646
Cube	8	0.732
Icosahedron	12	0.902

Table 1.5: Clusters containing group 14 atoms coordinated to six transition metal atoms

CLUSTER	REF.	CLUSTER	REF.
K OCTAHEDRAL			
$[CRe_6(CO)_{19}]^{2-}$	[21]	$[CRu_6(CO)_{15}(NO)]^-$	[107]
* $[CRe_6(CO)_{18}(H)_2]^{2-}$	[94]	* $CRu_6(CO)_{14}(NO)_2$	[107]
* $[CRe_7(CO)_{22}]^-$	[95]	* $CRu_6(CO)_{15}(NO)AuPPh_3$	[107]
* $[CRe_7(CO)_{21}]^{3-}$	[186]	* $CRu_6(CO)_{15}(H)(NO)$	[108]
* $[CRe_7(CO)_{21}(H)]^{2-}$	[96]	$CRu_6(CO)_{16}(PPh_3)$	[109]
* $[CRe_7(CO)_{21}(AuPPh_3)]^{2-}$	[97]	* $CRu_6(CO)_{16}(PPh_2Et)$	[109]
$[CRe_7Rh(CO)_{23}]^{2-}$	[98]	$CRu_6(CO)_{16}(P(OMe)_3)$	[109]
* $[CRe_7Pt(CO)_{21}(C_4H_7)]^{2-}$	[98]	$CRu_6(CO)_{15}(PPh_3)_2$	[109]
$[CRe_7Rh(CO)_{21}(COD)]^{2-}$	[98]	$CRu_6(CO)_{15}(PPh_2Et)_2$	[109]
$[CRe_7Rh(CO)_{22}(PPh_3)]^{2-}$	[98]	$CRu_6(CO)_{15}(P(OMe)_3)_2$	[109]
$[CRe_7Ir(CO)_{21}(COD)]^{2-}$	[98]	$CRu_6(CO)_{14}(P(OMe)_3)_3$	[109]
$[CRe_7Pd(CO)_{21}(C_3H_5)]^{2-}$	[98]	$CRu_6(CO)_{13}(P(OMe)_3)_4$	[109]
$[CRe_7Pt(CO)_{21}(C_4H_7)]^{2-}$	[98]	* $CRu_6(CO)_{15}(PhCCH)$	[10]
$[CRe_7Pt(CO)_{21}(CH_3)_3]^{2-}$	[98]	* $CRu_6(CO)_{15}$(hexa-2,4-diene)	[10]
* $[CRe_8(CO)_{24}]^{2-}$	[99]	* $CRu_6(CO)_{14}$(bitropyl)	[10]
* $[CFe_6(CO)_{16}]^{2-}$	[100]	* $CRu_6(CO)_{11}(C_6H_6)_2$	[110]
* $[CFe_6(CO)_{15}(SO_2)]^{2-}$	[68]	* $[CRu_6(CO)_{16}]^{2-}$	[111]
* $[CFe_6(CO)_{15}(NO)]^-$	[101]	$CRu_6(CO)_{16}(H)_2$	[111]
* $CFe_6(CO)_{11}(NO)_4$	[101]	$[CRu_6(CO)_{16}CO_2Me]^-$	[111]
$[CFe_5Cr(CO)_{17}]^{2-}$	[70]	* $CRu_6(CO)_{16}Cu_2(MeCN)_2$	[10]
* $[CFe_5Mo(CO)_{17}]^{2-}$	[70]	* $CRu_5W(CO)_{17}(AuPEt_3)_2$	[105]
$[CFe_5W(CO)_{17}]^{2-}$	[70]	* $[COs_{10}(CO)_{24}]^{2-}$	[112]
* $[CFe_5Rh(CO)_{16}]^-$	[102]	* $[COs_{10}(CO)_{24}(H)]^-$	[113]
$[CFe_5Rh(CO)_{14}(COD)]^-$	[70]	* $[COs_{10}(CO)_{24}(NO)]^-$	[114]
$[CFe_5Ir(CO)_{14}(COD)]^-$	[70]	* $[COs_{10}(CO)_{23}(NO)]^-$	[114]
$[CFe_5Ni(CO)_{13}(COD)]^-$	[70]	$COs_{10}(CO)_{24}(H)_2$	[10]
$[CFe_5Ni(CO)_{15}]^{2-}$	[70]	* $[COs_{10}(CO)_{24}I]^-$	[10]
$[CFe_5Pd(CO)_{14}(C_3H_5)]^-$	[70]	* $COs_{10}(CO)_{24}I_2$	[10]
$[CFe_5Cu(CO)_{14}(MeCN)]^-$	[70]	* $[COs_{10}(CO)_{24}(AuBr)]^-$	[115]
* $CFe_5(CO)_{14}(AuPEt_3)^2$	[103]	* $[COs_{10}(CO)_{24}(AuPPh_3)]^-$	[116]
* $CFe_5(CO)_{14}(AuPPh_3)^2$	[104]	* $[COs_{10}(CO)_{24}(CuMeCN)]^-$	[116]
* $CFe_4Au_2(CO)_{12}(PEt_3)^2$	[82]	* $CCOs_{10}Au_4(CO)_{24}[P(C_6H_{11})_3]_3$	[117]
* $CFe_4CoRh(CO)_{16}$	[69]	$COs_{10}Au_4(CO)_{24}(PPh_3)_3$	[117]
$[CFe_4CoPd(CO)_{15}]^-$	[69]	$COs_{10}Au_4(CO)_{24}(PMe_2Ph)_3$	[117]
* $[CFe_3Rh_3(CO)_{15}]^-$	[19]	$[COs_{10}Au_5(CO)_{24}(PPh_3)_4]^+$	[117]
* $CRu_6(CO)_{17}$	[10]	* $[CCo_6(CO)_{14}]^-$	[9]
* $CRu_6(CO)_{16}(AuPMePh_2)_2$	[105]	* $[CCo_6(CO)_{13}]^{2-}$	[118]
$CRu_6(CO)_{14}(C_6H_6)$	[10]	* $[CRh_6(CO)_{13}]^{2-}$	[10]
* $CRu_6(CO)_{16}(CNBu^t)$	[106]	$[CRh_6(CO)_{13}(H)]^-$	[119]
$CRu_6(CO)_{14}(MeC_6H_5)$	[10]	* $[CRh_6(CO)_{11}(dppe)]^{2-}$	[119]
$CRu_6(CO)_{14}(Me_2C_6H_4)$	[10]	* $CRh_6Au_2(CO)_{13}(PPh_3)_2$	[120]
* $CRu_6(CO)_{14}(Me_3C_6H_3)$	[10]	* $[CRh_4Co_2(CO)_{13}]^{2-}$	[121]
L TRIGONAL PRISMATIC			
* $[CCo_6(CO)_{15}]^{2-}$	[122]	* $CRh_6(CO)_{15}[Au(PPh_3)]_2$	[124]
* $CCo_6(CO)_{12}S_2$	[10]	* $[CRh_6(CO)_{15}(AuPPh_3)]^-$	[124]
* $[CRh_6(CO)_{15}]^{2-}$	[10]	* $CRh_6(CO)_{15}Cu_2(MeCN)_2$	[125]
$[CRh_6(CO)_{15}(H)]^-$	[123]	* $CRh_8(CO)_{19}$	[10]
* $CRh_6(CO)_{15}[Ag(NCMe)]_2$	[124]	$[COs_{11}(CO)_{27}]^{2-}$	[126]
* $CRh_6(CO)_{15}[Ag(PPh_3)]_2$	[124]	$[COs_{11}Cu(CO)_{27}(NCMe)]^-$	[126]
* $CRh_6(CO)_{15}[Cu(PPh_3)]_2$	[124]		

* Clusters which have been characterised crystallographically

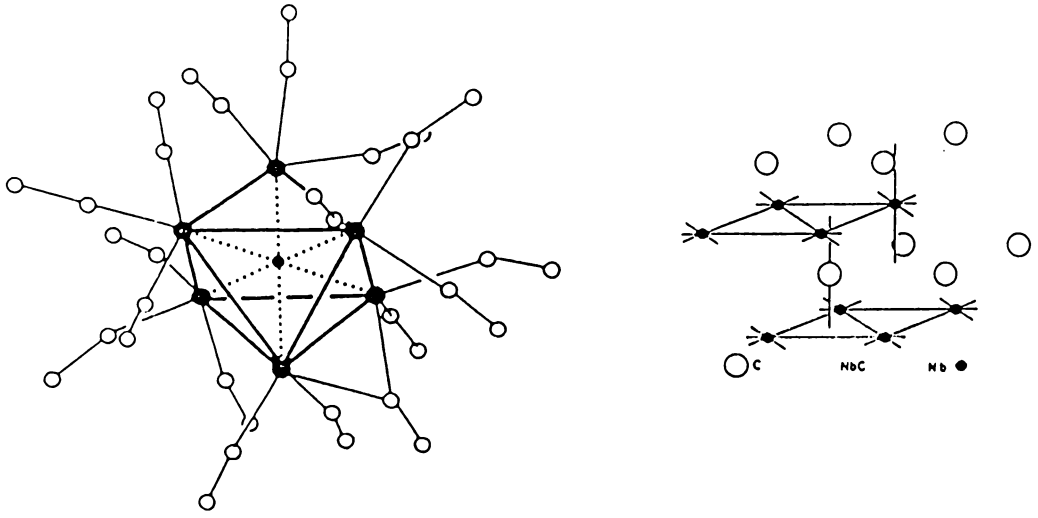

a) Octahedral structure of $CRu_6(CO)_{17}$ compared with the Face Centred Cubic Packing of NbC

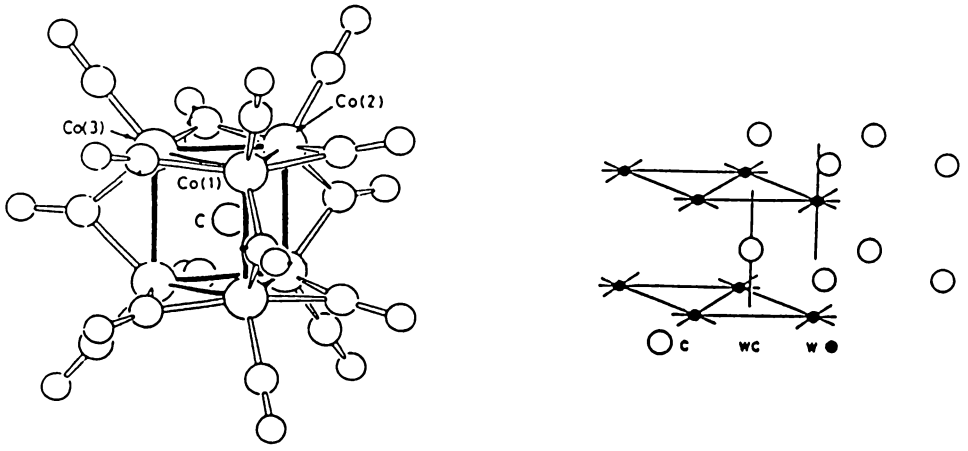

b) Trigonal prismatic structure of $[CCo_6(CO)_{15}]^{2-}$ compared with the Hexagonal Close Packing of WC

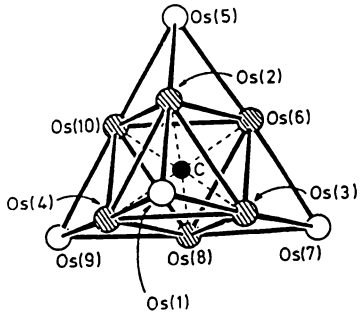

c) Skeletal core of $[COs_{10}(CO)_{24}]^{2-}$

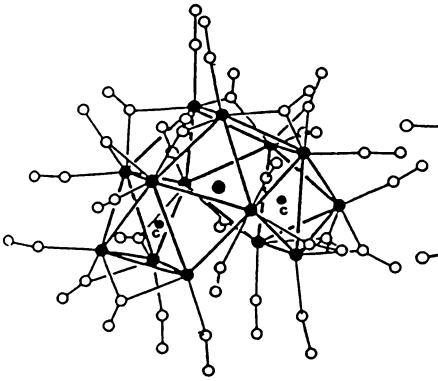

d) $[C_2Rh_{15}(CO)_{28}]^-$

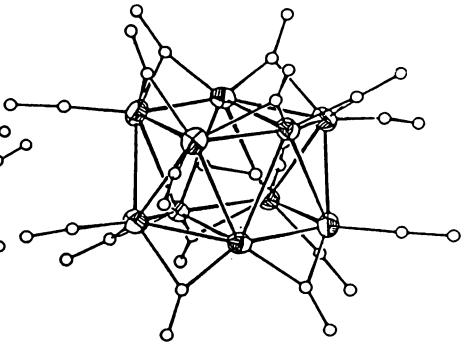

e) $[C_2Ni_{10}(CO)_{16}]^{2-}$

Figure 1.6: Some clusters containing 'bare' six-coordinate carbido atoms

The octahedral and trigonal prismatic geometries have distinct valence electron counts, 86 and 90 respectively. Thus the availability of electrons may explain why the octahedral configuration is more prevalent amongst transition metals belonging to the iron group, while the trigonal prismatic configuration is preferred by metals of the cobalt group. The choice of structure is also influenced by the size of the transition metal atom. The trigonal prismatic structure obviously contains a larger cavity for a given M-M bond length. The ideal r_E/r_M ratios (E = main group atom, M = transition metal atom, r_M = covalent radius of M) for a regular octahedron and a regular trigonal prism are 0.414 and 0.528 respectively (see **table 1.4**).

Interchange between the two configurations is known to occur with the addition or loss of electrons (ligands).

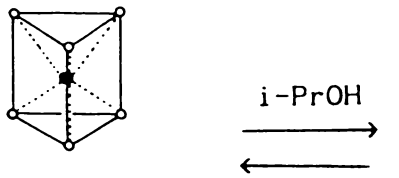

$[CRh_6(CO)_{15}]^{2-}$ $[CRh_6(CO)_{13}]^{2-}$ + 2CO

Oxidation of the trigonal prismatic $[CCo_6(CO)_{15}]^{2-}$ anion gives a distorted octahedral cluster, $[CCo_6(CO)_{14}]^-$. This is a rare example of a paramagnetic main group-transition metal cluster, having 87 valence electrons instead of the expected 86. The extension of one of the Co-Co bonds (2.916 Å) with respect to the others (mean 2.63 Å), has been attributed to the occupation of an antibonding orbital by the extra electron.

Interestingly, no COs_6 octahedral cluster is known. The only reported Os_6C structure is the edge-bridged square pyramid, $COs_6(CO)_{16}(MeCCMe)$. However larger clusters, such as the tricapped octahedral $[Os_{10}C(CO)_{24}]^{2-}$ anion (**figure 1.6c**), which contain COs_6 octahedral structures are known.

Many polycarbido species have been reported. In these clusters, the carbido atoms often occupy regular octahedral (*eg.* $[C_2Rh_{15}(CO)_{28}]^-$ [128] figure 1.6d) and trigonal prismatic (*eg.* $[C_2Ni_{10}(CO)_{16}]^{2-}$ [129] figure 1.6e) cavities. Polycarbido clusters have not been discussed as they are of little relevance to the rest of this work.

Six-fold coordination is not known for 'bare' Ge, Sn or Pb atoms. A $SiZr_6I_{12}$ cluster has been reported, containing a fully encapsulated Si atom within an octahedron of Zr atoms [155], and similar carbido clusters are also known. The chemistry of these compounds, however, has little in common with the carbonyl clusters discussed here.

1.3.4 CLUSTERS IN WHICH E IS COORDINATED TO MORE THAN SIX M ATOMS

Three different local bonding configurations are observed for 'bare' group 14 atoms coordinated to more than six transition metals:

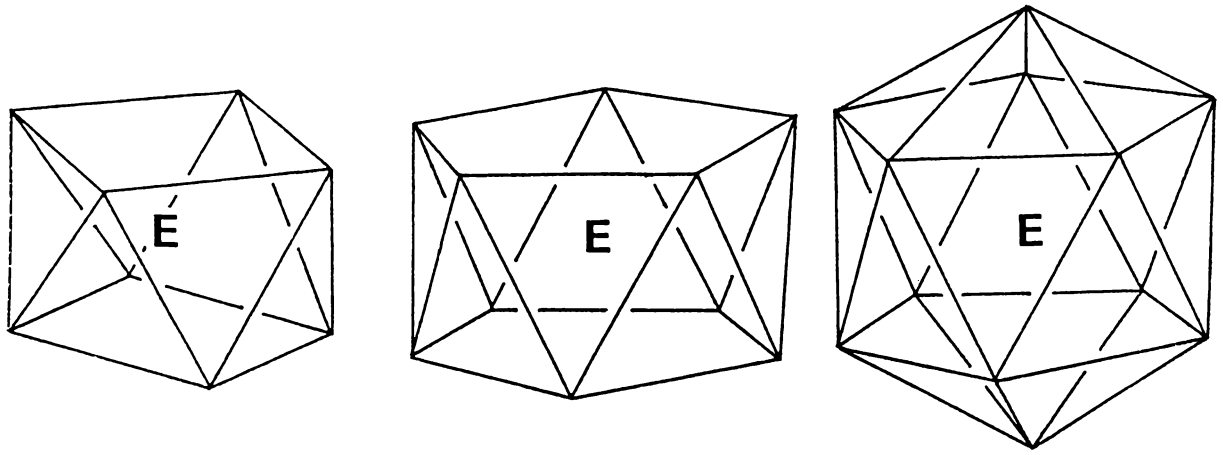

M SQUARE ANTIPRISMATIC *N PENTAGONAL ANTIPRISMATIC* *O ICOSAHEDRAL*

Group 14-transition metal clusters with these structures are listed in table 1.6.

The highest coordination number observed for encapsulated carbido atoms is eight. In these compounds the eight transition metal atoms describe a square antiprism with the carbido atom located at the centre. The cavity formed by a square antiprism is somewhat larger than the cavity within an octahedron or trigonal prism. This is probably partially responsible for the distortion of the square antiprism described by the Co atoms in $[CCo_8(CO)_{18}]^{2-}$ [9] (figure 1.7a). This distortion gives four normal (1.99 Å) and four elongated (2.15 Å) Co-C bonds. Electron counting reveals 114 valence electrons, in accord with Wades rules. This also corresponds with the 6N + 9 CVMO's predicted by Lauher.

This structure is also possessed by the $[CNi_8(CO)_{16}]^{2-}$ anion [130],

Table 1.6: Clusters containing group 14 atoms coordinated to more than six transition metal atoms

CLUSTER	REF.	CLUSTER	REF.
M SQUARE ANTIPRISMATIC			
* $[CCo_8(CO)_{18}]^{2-}$	[9]	* $[CNi_8(CO)_{16}]^{2-}$	[130]
* $[CNi_9Co_3(CO)_{20}]^{3-}$	[131]	* $[SiCo_9(CO)_{21}]^{2-}$	[132]
N PENTAGONAL ANTIPRISMATIC			
* $[GeNi_{10}(CO)_{20}]^{2-}$	[133]		
O ICOSAHEDRAL			
* $[GeNi_{12}(CO)_{22}]^{2-}$	[133]	* $[SnNi_{12}(CO)_{22}]^{2-}$	[133]

* Clusters which have been characterised crystallographically

as illustrated in figure 1.7b. $[CNi_8(CO)_{16}]^{2-}$ does not show the distortion observed for $[CCo_8(CO)_{18}]^{2-}$, which is consistent with the smaller size of the transition metal atom. It does, however, possess an extra 4 electrons; 6N + 11 CVMO'S. $[CNi_8(CO)_{16}]^{2-}$ was synthesised from $[CNi_9(CO)_{17}]^{2-}$ [130] by degradation under carbon monoxide. $[CNi_9(CO)_{17}]^{2-}$, itself contains a μ_8-CNi_8 square antiprism moiety, with another Ni atom capping one of the square faces (figure 1.7c). In this cluster, the carbido atom is displaced slightly towards the capping Ni atom, possibly due to a weak bonding interaction between the two.

A mixed metal cluster, $[CCo_3Ni_9(CO)_{20}]^{3-}$ [131], which also contains a μ_8-CM_8 moiety (figure 1.7d), was formed by the reaction of $[Ni_6(CO)_{12}]^{2-}$ with $ClCCo_3(CO)_9$. In this species, two alternate pairs of adjacent triangular faces of the square antiprism are capped by Ni atoms. The presence of the capping Ni atoms is not expected to effect the number of CVMO's, yet electron counting reveals 6N + 10 CVMO's. The antiprism itself shows a similar distortion to that of $[CCo_8(CO)_{18}]^{2-}$. The identity of the individual atoms composing the

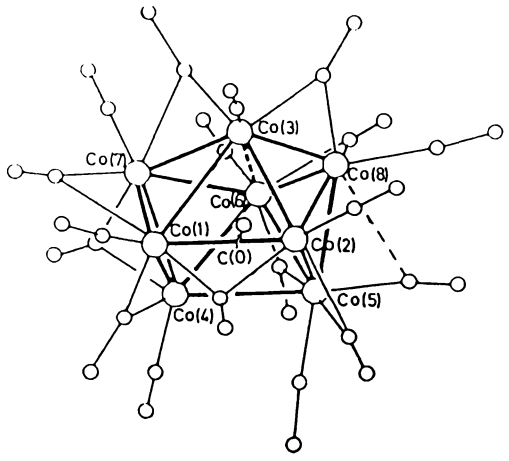

a) $[CCo_8(CO)_{18}]^{2-}$

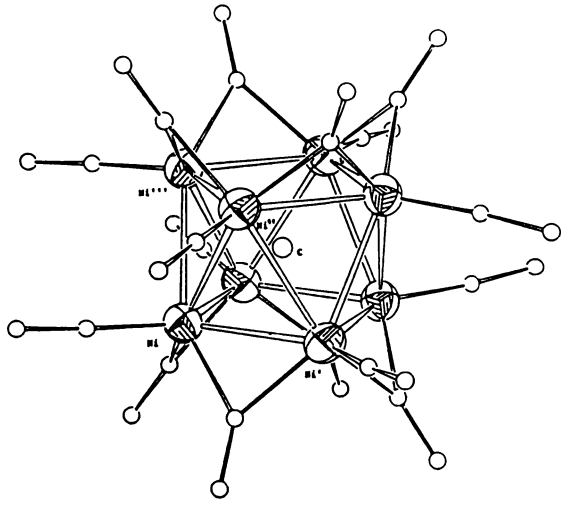

b) $[CNi_8(CO)_{16}]^{2-}$

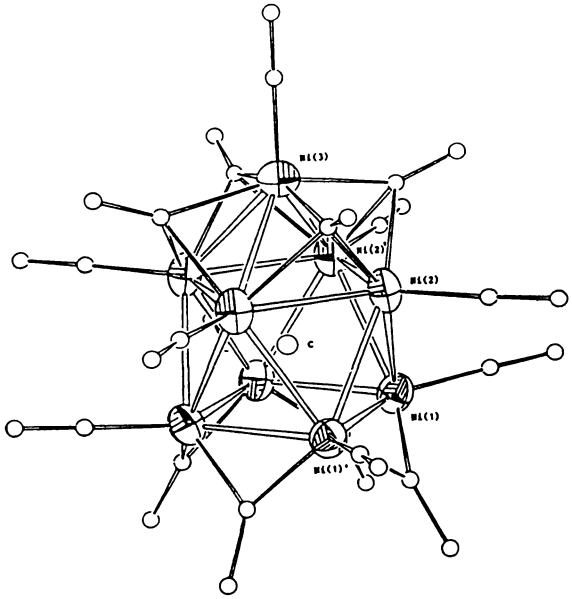

c) $[CNi_9(CO)_{17}]^{2-}$

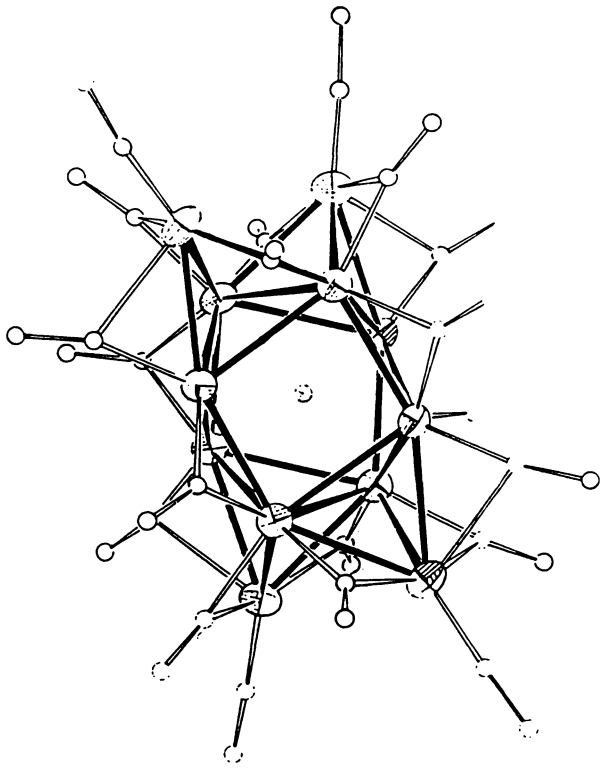

d) $[CCo_3Ni_9(CO)_{20}]^{3-}$

Figure 1.7: Clusters containing carbido atoms coordinated to more than six transition metals

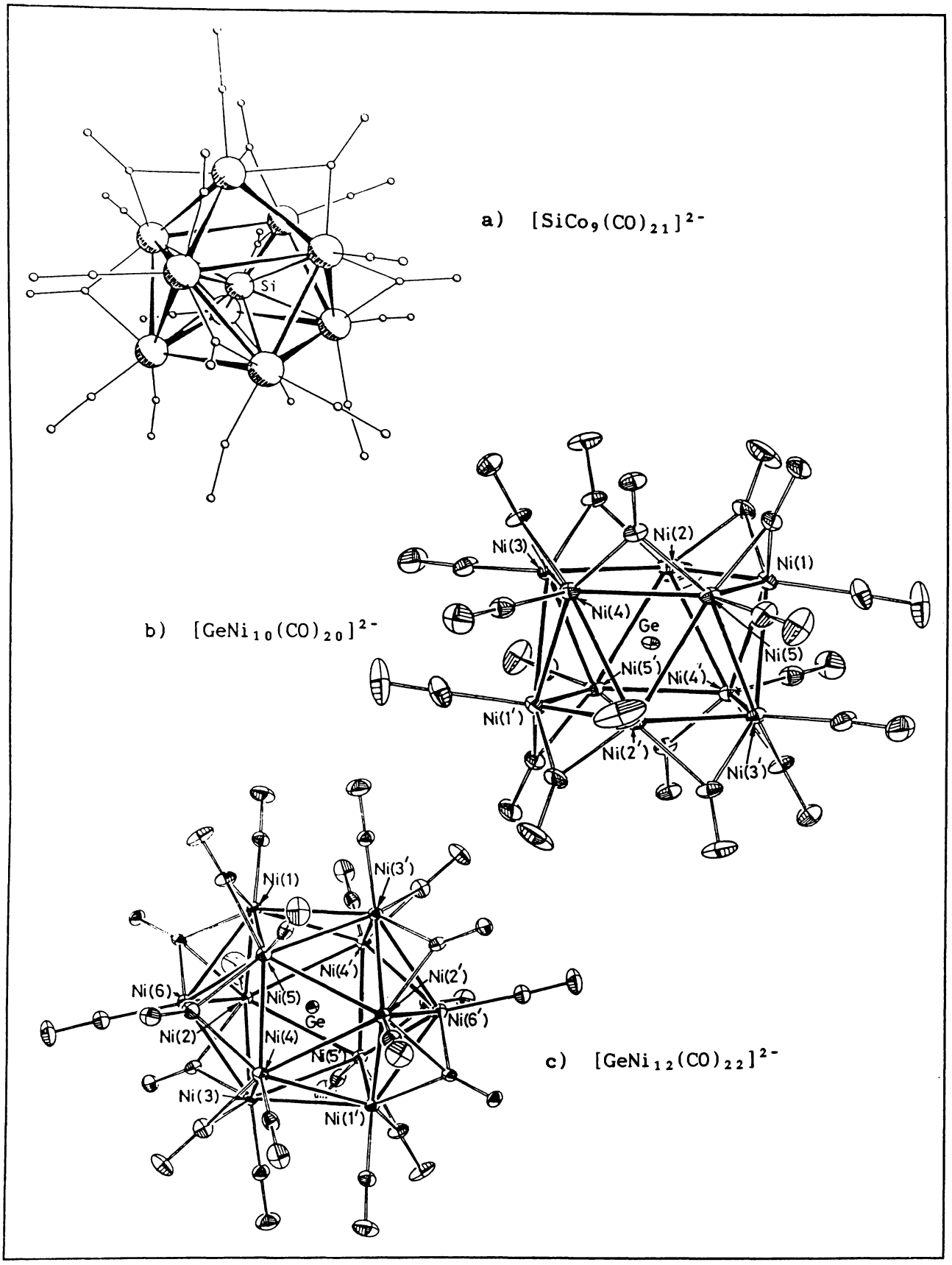

Figure 1.8: Clusters containing Si, Ge and Sn atoms coordinated to more than six transition metals

square antiprism is unclear, and the ratio of Ni to Co was determined by elemental analysis.

Obviously the relative sizes of the main group and transition metal atom plays a large part in determining whether a given structure will be stable. The small size of the Ni atom, which enables it to form these carbido-square antiprism structures, may also explain why no μ_6-CNi_6 octahedral or trigonal prismatic clusters are known.

$[SiCo_9(CO)_{21}]^{2-}$ **[64,132]** is the only reported cluster where Si is bonded to more than five transition metal atoms. This anion contains a fully encapsulated Si atom within a capped square antiprism of 9 Co atoms (**figure 1.8a**). Within the cluster, the Si atom also lies slightly above the geometric centre of the square antiprism of 8 Co atoms, suggesting a weak bonding interaction between the Si atom and the apical Co atom; the corresponding Si---Co distance is 2.529 Å. The ratio of covalent radii of Si and Co (0.83) is a lot larger than ideal (**table 1.4**), and this illustrates the remarkable flexibility of the square antiprism cage. The preparation and structure of this cluster are also discussed in Chapter Three. $[SiCo_9(CO)_{21}]^{2-}$ contains 129 valence electrons and is unique in that it is the only known paramagnetic structure that has one electron *fewer* than that expected for the observed geometry (130). The paramagnetism of this cluster has been confirmed by electron spin resonance (ESR) spectroscopy. At 77 K in CH_2Cl_2 a strong broad featureless absorption band was observed at g = 2.039. The magnitude of the observed g-shift is consistent with values reported for other reported paramagnetic transition metal clusters containing encapsulated main group atoms (*eg.* 2.0128 for $[CCo_6(CO)_{14}]^-$ **[9]** and 2.13 for $[C_2Co_{13}(CO)_{24}]^{4-}$ **[180]**).

It is obvious that larger structures are required to house fully encapsulated Ge and Sn atoms. In $[GeNi_{10}(CO)_{20}]^{2-}$, the Ge atom lies at the centre of a pentagonal antiprism of ten nickel atoms (**figure 1.8b**). This structure can also be regarded as a *trans-arachno* icosahedron. In $[GeNi_{12}(CO)_{22}]^{2-}$ and $[SnNi_{12}(CO)_{22}]^{2-}$ the central E atom is surrounded by a full icosahedron of twelve nickel atoms (**figure 1.8c**). These three anions have been isolated from the reactions of $GeCl_4$ or $SnCl_2.2H_2O$ with $[Ni_6(CO)_{12}]^{2-}$ **[133]**. The covalent radius ratios, r_E/r_M, for the Ge (1.06) and Sn (1.23) clusters are greater than the ideal value for an icosahedron (0.902, see **table 1.4**). A slight

elongation along one of the $[ENi_{12}(CO)_{22}]^{2-}$ pseudo-C_5 axes is more exaggerated for the Sn analogue, and is apparently required to accommodate the bulky Ge and Sn atoms.

A centred icosahedral structure has also been observed for $[SbRh_{12}(CO)_{27}]^{3-}$ [134]. Calculations by Mingos *et al.* [135] suggest that the preference for icosohedral over cuboctahedral or anti-cuboctahedral structures (found for $[Rh_{12}Pt(CO)_{24}]^{4-}$ [136] and $Pt_{15}(CO)_8(PBu^t_3)_6HX$ [137]) can be explained in terms of an absence of d valence electrons on the central main group atom.

1.4 ION PAIRING

Because virtually all of the reactions investigated in this thesis involve ionic species, careful consideration of the complex cation-anion-solvent interactions is warranted. Such interactions can have a wide bearing over the reaction products and the rate of reaction. For this reason relevant literature on ion pairing involving transition metal carbonyl anions is briefly reviewed below. For further information on ion pairing for metal carbonyl anions, readers are referred to reviews by Darensbourg [138] and by Horwitz and Shriver [139].

The range of ion pairing interactions that have been observed have been classified into three types depending on the degree of cation penetration of the anion ligand sphere:

a) Solvent Separated Ion Pairs.

The cation is surrounded by a coordination sphere of solvent molecules and the cation-anion interaction is minimal. The anion is essentially unperturbed by the cation. Solvent separated ion pairs exist in the presence of large mono-charged cations (*eg.* PPN^+) or when the cation is tightly bound by solvent molecules.

b) Contact or Tight Ion Pairs.

Carbonyl oxygen atoms on the anion are bound to the cation, as in $[(Co.salen^1)_2Na][Co(CO)_4]$ **[140]**:

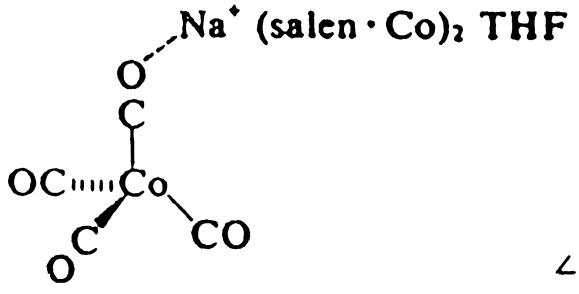

Na^+—Co 4.25 Å

$\angle Na^+$—O—C 142.1°

Solid-state structures characteristically show an angular $M^+\cdots O\text{-}C\text{-}M^-$ linkage. This allows maximum interaction with both the carbonyl π orbitals and the σ orbitals occupied by the lone pair of electrons on the oxygen. Polarisation of the carbonyl π-orbital electrons towards M^+ facilitates $d_\pi(M)\rightarrow\pi^*(CO)$ back-bonding. Therefore $M^+\cdots O\text{-}C\text{-}M^-$ contact ion pairs are readily detected by a drop in the carbonyl stretching frequency, ν_{CO}.

One might expect contact ion pair structures when the basicity of the anion rivals that of the solvent (*ie.* it is able to compete with the solvent for the cation). In this respect THF appears to be of similar basicity to carbonyl anions such as $[Co(CO)_4]^-$, $[Mn(CO)_5]^-$ and $[CpFe(CO)_2]^-$.

"Contact" may occur between more than two ions leading to *triple ions* or *ionic aggregates*. Edgell **[141]** suggested the possible presence of the $^-(CO)_3CoCO\cdots Na^+\cdots OCCo(CO)_3^-$ triple ion in THF, particularly at higher concentrations; and the triple ion $Tl[Co(CO)_4]_2^-$ has been reported to be spectroscopically observable in small amounts in THF, CH_3CN and CH_3NO_2 **[142]**. One would expect ion aggregates, if present, to be more important for larger cations such as Tl^+, and more nucleophilic metal carbonylates such as $[CpFe(CO)_2]^-$.

c) Direct Metal-Metal Interaction.

Complete penetration of the solvent sphere ultimately leads to

1 salen = N,N'-ethylenebis(salicylideniminato)

covalent bonding between the counter ion and the carbonylate metal center. However the degree of penetration of the ligand sphere and the consequent perturbation of the carbonylate may vary. This type of solution structure is most frequently observed with cations such as Zn^{2+}, Cd^{2+}, In^{3+}, Hg^{2+}, Tl^{+} or H^{+}. For $Hg[Co(CO)_4]_2$, no free $[Co(CO)_4]^-$ is observed, even in a strongly polar solvent such as DMF [153,143].

Infrared carbonyl stretching modes once again provide a useful tool for probing such interactions. As well as detecting structural rearrangements, direct M-M bonding between the cation and the carbonylate centre removes electron density from the anion metal atom, reducing its capacity for π-back donation to CO. This leads to an increase in ν_{CO}, in contrast with the effect observed for contact ion pairs.

These classifications of course describe what is a continuous progression of increasing interaction and are used purely for simplification. In fact, in a given situation, many types of interaction may be occurring and more than one may be important. The effects of the cation, anion and solvent in determining which of these structures are important, and the effects of ion pairing on reactivity are described below.

1.4.1 CATION, ANION AND SOLVENT EFFECTS

CATION EFFECTS

Generally, more electrophilic cations show a greater propensity to penetrate the anion carbonyl sphere. The solution structures of the $[Bu^n_4N]^+$, K^+, Na^+, Li^+ and Mg^{2+} salts of $[CpFe(CO)_2]^-$ in THF have been interpreted using infrared spectroscopy **[138]**. When the anion is purely in a symmetrical environment, as is the case for $[Bu^n_4N]^+$, two ν_{CO} absorption bands are seen at *ca.* 1865 and 1788 cm^{-1}. For K^+, Na^+, Li^+ and Mg^{2+}, the $Fe\text{-}C\text{-}O\cdots M^{n+}$ contact ion pairing is also observed, represented by a drop in the frequency of the bridged CO stretch in proportion to the charge/size ratio of the cation [1772 (K^+), 1770 (Na^+), 1745 (Li^+) and 1713 (Mg^{2+})]. The expected concomitant rise of the non-bridging carbonyl frequency is observed only for Mg^{2+}. Direct metal-metal interaction between the cation and the carbonylate centre has also been reported for Na^+, Li^+ and Mg^{2+}, characterised by two ν_{CO}

frequencies of higher energy than for the solvent separated ion pairs [1877, 1806 (Na^+); 1880, 1805 (Li^+); and 1918, 1854 (Mg^{2+})]. The Na^+ and Li^+ salts are interesting in that all three types of interaction are observed.

ANION EFFECTS

The extent of contact ion pairing is also related to the nucleophilicity of the anion. A series of increasing nucleophilicity (below) has been derived by Dessy, Pohl and King **[144]** from kinetic studies with organic halides, and this has been supported by electrochemical studies:

$$CpFe(CO)_2^- >> CpW(CO)_3^- > CpMo(CO)_3^- \simeq Mn(CO)_5^- > Co(CO)_4^-$$

Possibly more important in the case of contact ion pairing is the basicity **[145]** of the carbonyl groups. Infrared analysis of the contact/solvent-separated ion pairing ratio (in brackets) for THF solutions of the following Na^+ salts gave this sequence **[138]**:

$$CpM(CO)_3^- (>10) > Co(CO)_4^- (2) > Mn(CO)_5^- (\simeq 1) > V(CO)_6^- (<1)$$

(M = Cr, Mo, W)

Obviously the amount of contact ion pairing is dependent on the number of carbonyls available to disperse the negative charge. Substitution of carbonyl groups by poorer π-acceptors such as PR_3, $P(OR)_3$ or isonitriles increases the extent of contact ion pairing in $LMn(CO)_4^-$ and $LV(CO)_5^-$ **[138]**. Differing basicity or electrophilicity of carbonyl groups within asymmetric carbonylates can lead to site selectivity **[146,138]**.

SOLVENT EFFECTS

As previously mentioned, the effectiveness of the solvent at solvating the cation plays a large part in determining the ion paired structures present. This effectiveness is found to be related to the solvent polarity which can be measured in terms of the solvent dielectric constant (**table 1.7**).

Table 1.7: Dielectric constants for some common solvents (at 20°C unless otherwise stated) [147]

Solvent	Dielectric Constant
H_2O	78.54(25°C)
EtOH	24.30(25°C)
CH_2Cl_2	9.08
$CHCl_3$	4.81
Et_2O	4.34
C_6H_6	2.28
n-hexane	1.89

Altering the polarity of solvents by addition of small amounts of co-solvent is often used to distinguish the types of ion pairing present.

Edgell *et al.* have used vibrational spectroscopy to investigate the ion paired structures of $NaCo(CO)_4$ in a variety of solvents [148]. In strongly polar solvents such as DMF and DMSO, a single ν_{CO} infrared peak is observed near 1887 cm^{-1}. This peak corresponds to the triply degenerate C-O stretch expected for tetrahedral $[Co(CO)_4]^-$. Here solvent-separated ion pairs predominate and the $[Co(CO)_4]^-$ anion is unperturbed by the cation. As the polarity of the solvent decreases, more ν_{CO} bands are seen. In THF bands at 1855 cm^{-1} and 1895 cm^{-1} are observed as well as the peak at 1887 cm^{-1}. Edgell *et al.* conclude that $[Co(CO)_4]^-$ is predominantly in two kinds of environment; the solvent-separated environment described above, and a C_3 monodentate $Na^+\cdots O\text{-}C\text{-}Co(CO)_3^-$ 'contact' structure.

An unusual solvent-salt interaction recently reported by Attwood *et al.* [149] involves the *clathrate* effect wherein the salt ($NaMn(CO)_5$) tightly interacts with a specific number of solvent (15-crown-5 in toluene) molecules. In the solid state a dimer is seen with each Na bound to carbonyl oxygen atoms of two $[Mn(CO)_5]^-$ moieties and a 15-crown-5 molecule. In solution two immmiscible layers form, the lower layer containing the salt and a specific amount of solvent, and the upper layer containing pure solvent.

1.4.2 THE EFFECTS OF ION PAIRING ON REACTIVITY

Generally one would expect that the less closely associated a transition metal carbonyl anion is with its cation, the greater its

nucleophilicity in chemical reactions. This is called the "normal" counterion effect, and has been reported [144] for oxidative addition reactions of the form: $M(CO)_x^- + RX \rightarrow X^- + RM(CO)_x$; where RX is an alkyl halide and $M(CO)_x^-$ is $Fe(CO)_4^{2-}$, $Mn(CO)_5^-$, $Co(CO)_4^-$, $CpMo(CO)_3^-$ and $CpW(CO)_3^-$.

However if RX is an activated alkyl halide such as benzyl chloride or allyl chloride, an "inverse" counterion effect is observed with the weaker nucleophiles: $Co(CO)_4^-$, $Mn(CO)_5^-$ and $CpMo(CO)_3^-$. This has been explained in terms of cation assisted R-X bond cleavage when the RX molecules have some incipient carbonium ion character or some charge separation. A transition state has been suggested, where the cation is tightly bound to both the metal carbonyl and the RX group; not only facilitating cleavage of R-X but also acting as a template by bringing M and R into close proximaty [138]:

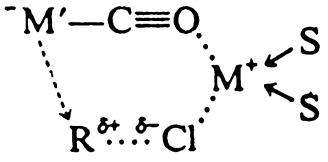

The cation may also affect anion reactivity by influencing the lability of ligands and hence the availability of open coordination sites. For example in $Na^+\cdots OCV(CO)_4PR_3^-$ (R = Ph, n-Bu) [150], close ion contact is thought to lead to a loss of V-P π-backbonding, facilitating ligand exchange reactions.

Very little is known about the effects of counterions on the reactivity of cluster anions. However one new dimension added by clusters is the possibility of cation interaction with the bridging carbonyls. The redox condensation of $Co(CO)_4^-$ and $Co_2(CO)_8$ to yield the trinuclear $Co_3(CO)_{10}^-$ anion has been shown to be counterion dependent. Optimum yields are obtained when Li^+ is the counterion and $Bu^n{}_2O$ the solvent. The solid state structure of the product shows Li^+ is tetrahedrally coordinated to oxygens from the $Bu^n{}_2O$, a μ_3-CO of one cluster anion and two μ_2-COs of other clusters. Here the Li^+ is thought to stabilise carbonyl bridging and in turn the cluster anion. Altering the ability of the cation to interact with the bridging carbonyls (*eg.* by replacing Li^+ with Na^+, or increasing the degree of solvation of Li^+ by changing the solvent) results in poorer yields.

Indeed, when THF was added to an Et_2O solution of $LiCo_3(CO)_{10}$, infrared studies showed that the μ_2-COs became terminal.

1.5 PRELIBATION[2]

The work presented in this thesis covers the reactions and the electrochemical and spectroscopic properties of cobalt and iron clusters, containing 'bare' silicon, germanium or tin atoms. The thesis is divided into six chapters. Chapters Two to Six describe essentially independent sections of experimental work, and each chapter is discussed individually.

Chapter Two describes the solvents and reagents, and the experimental and instrumental techniques used throughout this work, along with the preparations of group 14-transition metal clusters, investigated in later chapters. Possible routes for synthesising $Sn[Fe_2(CO)_8]_2$ have been examined in some detail, and this work is also included here.

Chapter Three describes the reactions of neutral *spiro* and trigonal pyramid-based μ_4-$EM_4(CO)_X$ clusters (E = Si, Ge, Sn and M = Co, Fe) with various transition metal carbonyl anions.

Chapter Four covers the reactions of the $[SiCo_9(CO)_{21}]^{2-}$ and $[GeCo_5(CO)_{16}]^-$ cluster anions.

In Chapter Five, the electrochemistry of the μ_4-$EM_4(CO)_X$ clusters, and other compounds containing *spiro* and trigonal pyramidal μ_4-EM_4 units, is investigated using cyclic voltammetry.

And Chapter Six discusses the infrared and Raman vibrational spectroscopy of the the μ_4-$EM_4(CO)_X$ clusters.

A fold-out section in Appendix A depicts the molecular structures of clusters frequently referred to in this thesis. The symbol ***(F #)*** is used in the text to refer readers to these diagrams.

2 "The wicked have a *prelibation* of that darkness they shall go to hereafter" T. Adams, 1633.

Chapter Two

Structures of compounds frequently refered to in this thesis are depicted in a fold-out section in Appendix A. The symbol *(F #)* is used in the text to refer readers to these diagrams.

CHAPTER 2 EXPERIMENTAL TECHNIQUES

2.1 GENERAL EXPERIMENTAL TECHNIQUES

Most of the compounds included in this work are unstable to oxidation if exposed to air. Some compounds, generally of high molecular mass, were stable enough to be handled in air for short periods of time. Most of the manipulations, however, were performed under vacuum or nitrogen atmosphere using standard Schlenk line techniques.

Manipulations of more volatile compounds, such as SiH_4 or GeH_4, were carried out on a conventional glass vacuum line. For long-term reactions involving volatile reagents, the reagents were sealed in 50 ml high pressure glass ampoules (10 atm maximum safe pressure) and stored in the dark. Sealed ampoules were opened using a thick-walled rubber sleeve, fitted with a tap adaptor. This could be connected to a vacuum line, enabling the top of the sealed ampoule to be broken without exposing the contents to the atmosphere.

All glassware was washed initially in concentrated base (methanolic KOH) then in concentrated acid (chromic acid). It was then rinsed thoroughly with water and dried in an oven before use. Joints and stopcocks subject to vacuum were lubricated using Apiezon 'M' and 'N' greases, respectively.

2.2 INSTRUMENTAL TECHNIQUES

2.2.1 INFRARED SPECTROSCOPY

Routine infrared spectra were run on a Pye Unicam PU9512. This instrument was suitable mainly for monitoring the progress of reactions. More accurate spectra were recorded using a Perkin-Elmer 180 spectrophotometer (4000-500 cm^{-1}) which allowed greater control over setting parameters and was capable of higher resolution.

Solution spectra were obtained using a solution cell of 0.1mm pathlength with KBr windows. Infrared spectra of solid samples were recorded either as a nujol mull between KBr windows or as a KBr disc. The region of interest was generally the carbonyl stretching region between 2200 cm^{-1} and 1700 cm^{-1}. Carbonyl stretching bands are sharp and intense with little mixing from other vibrational modes. This makes them particularly useful for identification (see also Chapter Six).

2.2.2 ELECTRON PROBE ANALYSIS

In electron probe analysis, X-ray emission was stimulated on the surface of the sample by a narrow beam of high energy electrons. The resulting X-ray emission was detected with an ORTEC Energy-dispersive X-ray Analyser. An associated JEOL JS-M35 scanning electron microscope was used to locate the area to be analysed.

The electron beam could be focussed onto an area as small as 10^{-8} cm^2, enabling analysis of extremely small samples and individual crystals. The results of analyses were only semi-quantitative, as matrix effects could not be properly corrected for, but were useful for detecting the elements present in the sample.

2.2.3 X-RAY DIFFRACTION

Sample crystals were sealed in thin-walled glass capillaries or coated in araldite and mounted with grease on a glass fibre. Preliminary precession photographs with Cu-Kα X-radiation were used to ascertain the quality of the crystal, possible space groups and lattice dimensions. A Ni filter was employed for zero and first upper-level photographs.

Full X-ray intensity data were collected at the University of Canterbury on a Nicolet P3 four circle automatic diffractommeter using Mo-Kα X-rays.

2.2.4 FAST ATOM BOMBARDMENT (FABS) MASS SPECTROSCOPY

FABS mass spectroscopy [156] is a useful technique for characterising ionic and high molecular weight compounds which are not normally amenable to mass spectroscopy. Problems associated with low sample volatility are overcome by a "sputtering" process. The sample is either dissolved or homogeneously dispersed, with the aid of a cosolvent, in a suitable solvent (or "matrix") of low volatility. When a cosolvent is used, this is later blown off with a stream of nitrogen. The sample is then impinged with a beam of fast or "hot" rare-gas atoms (usually argon or xenon), and clusters of matrix and sample molecules or ions are released. The matrix molecules evaporate away and the sample is thought to be ionised by collision in the gas phase.

The ions are accelerated and analysed as in a conventional mass spectrometer. Matrix peaks are observed in the mass spectra, but are at sufficiently low mass to not interfere with sample

characterisation.

For this work all samples were run using 3-nitrobenzyl alcohol (NOBA) as the matrix and CH_2Cl_2 as cosolvent.

2.2.5 UV-VISIBLE SPECTROSCOPY

Visible spectra were obtained using a Hitachi 150-20 spectrophotometer and data processor. Samples were dissolved in hexane and spectra were obtained using 10 mm pathlength silica cuvettes.

2.3 STARTING REAGENTS

2.3.1 SOLVENTS

ammonia - dried over sodium, stored in a 20 litre storage bulb on a vacuum line.

acetonitrile - used as supplied.

benzene - laboratory grade reagent dried over sodium wire.

chloroform - stolen from Geoff Mills without his knowledge.

dichloromethane - distilled under nitrogen atmosphere from phosphorus pentoxide.

diethyl ether and *tetrahydrofuran (THF)* - distilled under nitrogen atmosphere from sodium benzophenone.

pentane, *hexane* and *petroleum spirit* - distilled under nitrogen atmosphere from CaH_2.

2.3.2 REAGENTS

Et_4NCl, GeO_2, H_3PO_4, $LiAlH_4$, $NaBH_4$ - Used as supplied without further treatment.

$SiCl_4$ - Stored at 4°C, pumped before use to remove HCl, then distilled under vacuum.

$SnCl_4$ - Stored in a fume hood, pumped before use to remove HCl, then distilled under vacuum.

$Fe(CO)_5$ - Stored in the dark in a fume hood, pumped before use to remove CO, then distilled under vacuum.

$Co_2(CO)_8$, $Fe_2(CO)_9$, $Mn_2(CO)_{10}$ - Used as supplied. Stored under N_2 at 4°C.

2.4 PREPARATION OF STARTING COMPOUNDS

2.4.1 GROUP 14 HYDRIDES

GeH_4 - Monogermane was prepared on a vacuum line by the reduction of

GeO_2 with borohydride [157]. A mixture of NaOH (20 g), GeO_2 (10 g) and $NaBH_4$ (18 g) in 250 ml of distilled water was added slowly under vacuum to 500 ml of 50% H_3PO_4 solution. The mixture was added below the surface of the acid using an extended separating funnel. A vigorous reaction followed, liberating GeH_4 along with small amounts of Ge_2H_6 and other higher oligomers.

$$[HGeO_3]^- + [BH_4]^- + 2H^+ \rightarrow GeH_4 + H_3BO_3$$

When the reaction had died down, the products were released into the vacuum line through a $CaCl_2$ column. The GeH_4 was separated from the other products by fractionation. The volatile mixture was passed through successively colder traps, selectively condensing out the various components. Water vapour and the higher germanes were trapped out in a CCl_4 slush bath (-22°C) and an ethanol slush bath (-117°C) respectively. The GeH_4 product was collected in a liquid nitrogen trap (-196°C).

SiH_4 - Monosilane was prepared on a vacuum line by the reduction of $SiCl_4$ with $LiAlH_4$ in diethyl ether. A large excess of $LiAlH_4$ was used to ensure complete reduction. $LiAlH_4$ was purified by extraction into diethyl ether under nitrogen, using a Soxhlet extractor. 20 ml of this solution was more than sufficient to completely react with 1.2 ml $SiCl_4$ (10 mmol). The $LiAlH_4$ solution was transfered to a flask using a syringe, and the $SiCl_4$ distilled onto this under vacuum. Ether vapour was separated from the gaseous products using a chloroform slush bath (-63°C) and the SiH_4 was collected in a liquid nitrogen trap (-196°C).

Any excess SiH_4 was destroyed by NaOH in a waste trap.

2.4.2 TRANSITION METAL CARBONYL ANIONS

$[Et_4N][Co(CO)_4]$ - [158] $Co_2(CO)_8$ (1.71 g, 5 mmol) in 50 ml THF was reduced using 25 g of 1% Na amalgam under nitrogen atmosphere.

$$Co_2(CO)_8 + 2Na(Hg) \rightarrow 2Na^+ + 2[Co(CO)_4]^-$$

After stirring the reaction mixture for 3 hours, a solution of

Et_4NCl (1.6 g, 8.7 mmol) in 50 ml of CH_2Cl_2 was added. The mixture was then stirred for a further 10 minutes and NaCl was precipitated.

$$[Co(CO)_4]^- + Et_4NCl \rightarrow [Et_4N][Co(CO)_4] + NaCl$$

The supernatant liquid was decanted, filtered and the solvent evaporated off. It was not possible to completely remove the THF under vacuum. This was achieved by recrystallising the product from CH_2Cl_2.

Note:

1 This synthesis reportedly fails under rigorously anhydrous conditions [159] and there is some indication that NaOH plays an active role [160].
2 Contamination with mercury compounds is unavoidable. $[Hg\{Co(CO)_4\}_3]^-$ (ν_{CO} (solid) 2035s 1970-1950vs,br cm^{-1}) and $Hg[Co(CO)_4]_2$ (ν_{CO} (solid) 2075s 2040m 2010sh 1970vs cm^{-1}) have been detected in this system [160]. $[Hg\{Co(CO)_4\}_3]^-$ is also known to react with halides which displace $[Co(CO)_4]^-$ to give $[Hg\{Co(CO)_4\}_2X]^-$ (ν_{CO} (solid) 2060s 2010sh 1970vs cm^{-1}) [161]. Therefore $[Hg\{Co(CO)_4\}_2Cl]^-$ may be present following addition of Et_4NCl.

The $[PPN]^+$ and $[PhMe_3N]^+$ salts of $[Co(CO)_4]^-$ were prepared in an analogous manner to $[Et_4N][Co(CO)_4]$ using PPNCl and $PhMe_3NBr$ in place of Et_4NCl.

$Na_2[Fe(CO)_4]$ - Several methods for preparing $[Fe(CO)_4]^{2-}$ have been presented in the literature. The two routes outlined below were used in this work:

(i) Sodium reduction in liquid ammonia [162]: In a typical preparation sodium (0.22 g, 9.5 mmol) was dissolved in liquid ammonia (the equivalent of 17 litres of $NH_{3(g)}$ at STP) giving a solution of approximately 0.1 $moll^{-1}$. Iron pentacarbonyl (0.5 ml, 3.8 mmol) was condensed into the reaction vessel in small aliquots and the reaction allowed to proceed, with occasional stirring, at -63°C (chloroform slush bath). Completion of the reaction was

indicated by the disappearance of the blue colour characteristic of alkali metals in liquid ammonia. The resulting yellow suspension was cooled to -196°C and the incondensibles removed under vacuum. The vessel was then allowed to warm and the ammonia was removed. The products were pumped for 24 hours to ensure complete removal of the ammonia and any remaining $Fe(CO)_5$.

Relatively pure $Na_2Fe(CO)_4$ is a pale pink/brown colour. Darker colouration indicates contamination with polynuclear anions such as $[Fe_2(CO)_8]^{2-}$ and $[Fe_3(CO)_{11}]^{2-}$ which are red and brown respectively.

Note:

1 Only 80-85% of the stoichiometric quantity of iron pentacarbonyl is required to react completely with the available sodium. Side reactions involving the formation of hydrogen and sodium amide have been detected. A reaction involving Na and CO has also been suggested to account for the paucity of CO in the product gases.
2 The concentration of Na in ammonia should be as low as practicable, preferably less than 0.1 mol l^{-1}.
3 Ammonia and unreacted $Fe(CO)_5$ should be removed as soon as posssible once the blue colour has been discharged.

(ii) Sodium reduction in dioxane **[163]**: A two-necked round bottomed flask, fitted with a reflux condenser was attached to a Schlenk line via the condenser. The flask was charged with sodium (2.0 g, 46 mmol), benzophenone (1.82 g, 10 mmol) and 120 ml of dry dioxane. The solution was refluxed under nitrogen using a heating mantle, and was regularly stirred. When the deep purple colour of the benzophenone ketyl appeared, a nitrogen flushed dropping funnel containing iron pentacarbonyl (6.2 ml, 46 mmol) was attached to the flask. The iron pentacarbonyl was added dropwise over 2.5 h until the blue colour of the refluxing solution was discharged. The resulting white suspension was heated at reflux for a further 45 min, and then allowed to cool to room temperature. Hexane (120 ml) was added to complete the precipitation of $Na_2[Fe(CO)_4](dioxane)_{1.5}$. The solvent was removed by filtering the product under nitrogen through a glass frit. The white product was then washed with two 80ml portions of hexane and dried under vacuum. $Na_2[Fe(CO)_4](dioxane)_{1.5}$ was obtained in yields of 90-95%.

$[Et_4N]_2[Fe_2(CO)_8]$ - [164] $Fe_2(CO)_9$ (1 g, 2.7 mmol) was added to methanolic KOH (25_ml, 1 mol l^{-1}) and the mixture stirred until a deep red solution was obtained, indicating the presence of the potassium salt. The resulting solution was filtered and a solution of Et_4NCl (0.7 g, 4 mmol) in aqueous KOH (10 ml, 1 mol l^{-1}) was added dropwise producing a deep red precipitate. This was washed three times with 20 ml of water and dried under vacuum.

$Na_2[Fe_2(CO)_8]$ Three different routes were used to prepare $Na_2[Fe_2(CO)_8]$:

(i) and (ii) - $Na_2[Fe(CO)_4]$ and $Na_2[Fe(CO)_4](dioxane)_{1.5}$, prepared as outlined above, were both reacted with iron pentacarbonyl to give $Na_2[Fe_2(CO)_8]$:

$$Na_2[Fe(CO)_4] + Fe(CO)_5 \rightarrow Na_2[Fe_2(CO)_8] + CO$$

In both cases this reaction was performed *in situ*. Once the formation of $Na_2[Fe(CO)_4]$ was complete, an equivalent amount of $Fe(CO)_5$ again, was added over a 2 h period in small aliquots. Reaction was allowed to proceed for a further 2 h to ensure completion. The products were then worked up as previously described for the respective $Na_2[Fe(CO)_4]$ syntheses.

(iii) Sodium reduction in naphthalene/THF **[165]**: A nitrogen flushed Schlenk flask containing a magnetic stirrer bar was charged with sodium (0.26 g, 11.3 mmol) and placed in an ice bath. A solution of naphthalene (1.49 g, 11.6 mmol) in 75 ml THF was added to the flask and the mixture was stirred for 2 h at 0°C, producing a deep green solution. A nitrogen flushed dropping funnel was then attached to the flask.

$Fe(CO)_5$ (1.5 ml, 11.5 mmol) was condensed into another Schlenk flask containing 30 ml THF. This solution was decanted into the dropping funnel under nitrogen. The deep green Na/naphthalene was cooled to -63.5°C (chloroform slush bath) and the $Fe(CO)_5$ solution was added dropwise over 30 min with vigorous stirring. The green solution became red and an orange precipitate was formed. The reaction mixture was stirred for a further hour before being allowed

to warm to room temperature. Pentane (30 ml) was then added and the mixture stirred for 30 min and filtered through a glass frit. The orange precipitate was washed with three 30 ml portions of pentane and dried under vacuum.

Note: $Na_2[Fe_2(CO)_8]$ prepared using THF as the solvent invariably retained tightly coordinated solvent molecules (ie. $Na_2[Fe_2(CO)_8].xTHF$).

$[Et_4N][Fe(CO)_3NO]$ and *$[PPN][Fe(CO)_3NO]$* - $Hg[Fe(CO)_3NO]_2$ was prepared [163] and used to produce $[Et_4N][Fe(CO)_3NO]$ and $[PPN][Fe(CO)_3NO]$ as required.

$Fe(CO)_5$ (7 ml, 0.052 mol) was distilled under vacuum into a 100 ml Schlenk flask. The flask was then flushed with nitrogen and charged with KNO_2 (4.3 g, 0.05 mol) and methanol (25 ml). This mixture was reacted at 35°C for 16 h with continuous stirring to give $K[Fe(CO)_3NO]$, and then allowed to cool to room temperature.

$$Fe(CO)_5 + KNO_2 \rightarrow K[Fe(CO)_3NO] + CO_{(g)} + CO_{2(g)}$$

Mercury(II) chloride (3.67 g, 0.014 mol) was heated in water (35 ml) until completely dissolved and added to the $K[Fe(CO)_3NO]$ solution. This mixture was stirred for 1 h during which time $Hg[Fe(CO)_3NO]_2$ was precipitated:

$$K[Fe(CO)_3NO] + HgCl_2 \rightarrow Hg[Fe(CO)_3NO]_{2(s)} + 2KCl$$

The brown precipitate was removed by filtering under suction and the crude product extracted in CH_2Cl_2 (50 ml). The solvent was removed under vacuum and the product washed with pentane (20 ml) to remove any $[HgFe(CO)_4]_n$ present.

When required, $[Et_4N][Fe(CO)_3NO]$ or $[PPN][Fe(CO)_3NO]$ were obtained by stirring $Hg[Fe(CO)_3NO]_2$ in diethyl ether over sodium amalgam until the red colour was discharged, and then adding Et_4NCl or PPNCl.

$[Et_4N][Mn(CO)_5]$ - This was prepared by reduction of $Mn_2(CO)_{10}$ by Na

amalgam [167], as in the synthesis of $[Et_4N][Co(CO)_4]$. The product was found to be very air-sensitive. The infrared spectrum of the products in CH_2Cl_2 showed νCO peaks at 2090w, 2050m, 2044m, 2008m, 2078br, 1894s, 1856s cm^{-1}. The latter two peaks can be assigned to $[Mn(CO)_5]^-$. The other peaks are apparently due to traces of $Mn_2(CO)_{10}$ and $[Mn_3(CO)_{14}]^-$. The $Mn_2(CO)_{10}$ is formed by oxidation of $[Mn(CO)_5]^-$. In the presence of $[Mn(CO)_5]^-$, $Mn_2(CO)_{10}$ then reacts to give $[Mn_3(CO)_{14}]^-$.

2.4.3 $EM_4(CO)_x$ COMPOUNDS

$Ge[Co_2(CO)_7]_2$ - [42] GeH_4 and $Co_2(CO)_8$ in a 1-1.5:2 ratio were sealed in an ampoule with 5 ml of hexane. The ampoule was stored in the dark for at least 14 days before being opened.

$$GeH_4 + 2Co_2(CO)_8 \rightarrow Ge[Co_2(CO)_7]_2 + 2H_2 + 2CO$$

The product was recrystallised from hexane before use.

$Si[Co_2(CO)_7]_2$ - This was prepared in an analagous manner to $Ge[Co_2(CO)_7]_2$, using SiH_4 in place of GeH_4 [63].

$Ge[Fe_2(CO)_8]_2$ - This was provided by Skelte Anema. The preparation of $Ge[Fe_2(CO)_8]_2$ has been reported in references [38] and [25].

$Si[Fe_2(CO)_8]_2$ - [38,25] $Fe_2(CO)_9$ (0.85 g, 2.34 mmol), SiH_4 (1.0 mmol) and hexane (7ml) were sealed under vacuum in a 50ml glass ampoule at 30°C. After 7 days the ampoule was opened and the contents transferred to a Schlenk flask. $Si[Fe_2(CO)_8]_2$ was isolated (~64% yield) from the products by chromatography on silica plates using hexane as the solvent.

$Sn[Fe_2(CO)_8]_2$ - The preparation of $Sn[Fe_2(CO)_8]_2$ is discussed below in section 2.5.

$Pb[Fe_2(CO)_8]_2$ - [48,49] A methanolic solution of lead(II) acetate trihydrate (0.24 g 0.6 mmol) was added dropwise to a solution of $[Et_4N]_2[Fe_2(CO)_8]$ (0.6 g, 1.0 mmol) in methanol (20 ml). After 1 h,

the solution was filtered and the solid $[Et_4N]_2[\{(CO)_8Fe_2\}Pb\{Fe(CO)_4\}_2]$ was dried under vacuum. $[Et_4N]_2[\{(CO)_8Fe_2\}Pb\{Fe(CO)_4\}_2]$ (0.25 g, 0.22 mmol) was stirred with $[Cu(MeCN)_4][PF_6]$ (0.16 g, 0.43 mmol) in CH_2Cl_2 (30 ml) for 24 h. The solvent was removed under vacuum and $Pb[Fe_2(CO)_8]_2$ was extracted in hexane.

$(CO)_5MnGeCo_3(CO)_9$ - This preparation is described in section 3.2.3.1.

2.4.4 GROUP 14 TRANSITION METAL CARBONYL ANIONS

$[Et_4N][GeCo_5(CO)_{16}]$ - [92,32] A nitrogen flushed Schlenk flask containing a solution of $Ge[Co_2(CO)_7]_2$ (0.14 g 0.2 mmol) and $[Et_4N][Co(CO)_4]$ (0.13 g, 0.4mmol) in CH_2Cl_2 (20 ml) was heated at 35-40°C for 3 h. Either the crude product was reacted further *in situ*, or $[Et_4N][GeCo_5(CO)_{16}]$ was extracted into diethyl ether and purified by recrystallisation.

$[Et_4N][Ge_2Co_7(CO)_{21}]$ - [32] Crude $[Et_4N][GeCo_5(CO)_{16}]$ (*ca.* 0.4 mmol) was prepared and reacted *in situ* with $Co_2(CO)_8$ (0.15 g, 0.4 mmol) in THF (20 ml). The reaction mixture was stirred at 45-50°C for 8 h. The solvent was then removed under vacuum and the product extracted with diethyl ether (20 ml).

$[Et_4N][Ge_2Fe_2Co_5(CO)_{22}]$ - [33] $Ge[Co_2(CO)_7]_2$ (0.20 g, 0.29 mmol) was reacted with $[Et_4N][Fe_2(CO)_8]$ (0.17 g, 0.29 mmol) in 15 ml CH_2Cl_2 under nitrogen atmosphere. The reaction was stirred for 4 h at room temperature. The solvent was then evaporated off and the $[Et_4N][Ge_2Fe_2Co_5(CO)_{22}]$ extracted with diethyl ether (20 ml).

$[Et_4N]_3[SiCo_9(CO)_{21}][Co(CO)_4]$ - This preparation is described in section 3.2.1. The $[PPN]^+$ and $[PhMe_3N]^+$ salts of $[SiCo_9(CO)_{21}]^{2-}$ were prepared in an analagous manner to $[Et_4N]_3[SiCo_9(CO)_{21}][Co(CO)_4]$, using $[PPN][Co(CO)_4]$ and $[PhMe_3N][Co(CO)_4]$ in place of $[Et_4N][Co(CO)_4]$.

2.4.5 MISCELLANEOUS

$[Bu_4N][ClO_4]$ - $AgClO_4$ (2.12 g, 10.2 mmol) was stirred with Bu_4NI (3.78 g, 10.2 mmol) in CH_2Cl_2 (100 ml) under nitrogen atmosphere for 24 h. The reaction mixture was filtered to remove $AgI_{(s)}$ which had formed as a fine yellow precipitate. The crude product was recrystallised by cooling a solution of ethyl acetate and CH_2Cl_2 and then by cooling a heated (40°C) ethyl acetate solution. $[Bu_4N][ClO_4]$ was isolated in moderate yields.

$[Cu(CH_3CN)_4][PF_6]$ - [168] HPF_6 (5 ml of 60-65% solution, *ca.* 57 mmol) was added in 2 ml portions to a stirred suspension of copper(I) oxide (2 g, 14 mmol) in acetonitrile (40 ml). $[Cu(CH_3CN)_4][PF_6]$ was formed in an exothermic reaction:

$$Cu_2O + 2HPF_6 \xrightarrow{CH_3CN} 2[Cu(CH_3CN)_4][PF_6] + H_2O$$

The reaction mixture was stirred for a further 5 min then filtered hot through a glass frit. The filtrate showed a bluish tinge due to Cu^{2+} impurities. Pure white $[Cu(CH_3CN)_4][PF_6]$ was obtained from successive recrystallisations from acetonitrile (50 ml) by adding diethyl ether (50 ml) and cooling.

Ph_3PAuCl - An EtOH solution of $HAuCl_4$ was treated with 2 molar equivalents of PPh_3 in EtOH. The reaction mixture was stirred until the yellow colour disappeared. The white crystalline product was filtered off and dried in air.

$[(Ph_3PAu)_3O][BF_4]$ - Silver(I) oxide was prepared by treating an aqueous solution of $AgNO_3$ (0.63 g, 3.7 mmol) with excess $NaOH_{(aq)}$. The Ag_2O precipitate was washed with water, ethanol and acetone. It was then transferred along with $NaBF_4$ (0.63 g, 6.5 mmol) to a solution of Ph_3PAuCl (0.5 g, 1 mmol) in 65 ml acetone. The mixture was stirred for an hour and the acetone removed under vacuum. The residue was redissolved in 15 ml $CHCl_3$ and filtered. Diethyl ether was added to precipitate the product [169].

$(C_5H_5)_2Co$ - [170,171] Cobaltocene was synthesised from cobalt(II) chloride and dicyclopentadiene in a three stage preparation:

(i) $(C_5H_6)_2 \rightarrow 2C_5H_6$

(ii) $NaH + C_5H_6 \rightarrow NaC_5H_5 + H_2$

(iii) $CoCl_2 + 2NaC_5H_5 \rightarrow (C_5H_5)_2Co + 2NaCl$

(i) Cyclopentadiene was prepared by cracking dicyclopentadiene at 160-170°C. This was carried out by heating an excess of the dimer in the presence of iron filings. The reaction was carried out in a fume hood and the reaction vessel was fitted with a distillation column. As it formed the cyclopentadiene, with a boiling point of 42°C, distilled over into a flask cooled with ice. When a sufficient quantity had been collected the flask was stoppered and stored in a freezer until required (see note 1).

(ii) NaH (2.4 g of 60% in mineral oil, 1.44 g, 60 mmol) was placed in a 250 ml flask which had been flushed with N_2. Then diethyl ether (25 ml) was added, the mixture swirled and allowed to settle and the ether decanted off. This procedure, repeated twice, was carried out to remove the oil in which the NaH was stored. Tetrahydrofuran (100 ml) was added and then C_5H_6 slowly from a syringe. The resulting mixture was stirred for 90 minutes to give a pale pink solution of NaC_5H_5 in THF ready for use.

(iii) The solution of sodium cyclopentadienide in THF was added to a nitrogen flushed flask containing anhydrous cobalt(II) chloride (3.89 g, 30 mmol) (see note 2) and fitted with a reflux condensor. An exothermic reaction ensued during which the reaction mixture turned dark purple in colour. The mixture was boiled for two hours under reflux to ensure complete reaction, and then cooled to room temperature before the solvent was removed under vacuum. The flask was flushed with $N_{2(g)}$ and a sublimation tongue was attached. Dark-violet crystals were obtained by sublimation at 60 - 200°C (see note 3).

Note:

1 Cyclopentadiene dimerises slowly ($t_{1/2} \approx 12$ hours at room temperature) and should be stored in the dark at low temperatures and used as soon as possible.

2 It is imperative that the anhydrous cobalt(II) chloride is as dry as possible. This was achieved by heating pink hydrated $CoCl_2$ at 160°C under vacuum for 2-3 days. The product should be pure blue with no pink tinge.

3 Cobaltocene is normally very air sensitive but relatively large crystals, as obtained by sublimation, are stable for brief periods in air. Otherwise Cp_2Co is best stored and handled under a N_2 atmosphere.

$(C_5H_5)Fe(CO)_2I$ - [172] Iodine (3 g, 11.8 mmol) was added to $[(C_5H_5)Fe(CO)_2]_2$ (3 g, 8.5 mmol) in 15 ml $CHCl_3$ in a flask flushed with nitrogen. The black mixture was heated under reflux for 30 min then allowed to cool to room temperature. The reaction mixture was then washed in two portions with a 20 ml aqueous solution of 7 g of sodium thiosulphate 5-hydrate to remove excess iodine. The aqueous layer was decanted off and the $CHCl_3$ removed under vacuum. The dry black product was washed with three 10 ml portions of hexane. It was then dissolved in CH_2Cl_2 and filtered to remove any iron(III) oxide.

2.5 PREPARATION OF $Sn[Fe_2(CO)_8]_2$

2.5.1 REACTION OF $SnCl_4$ WITH $[Et_4N]_2[Fe_2(CO)_8]$

(i) Reactant Ratio of 1 : 1

$SnCl_4$ (0.1 ml, 0.87 mmol) was condensed into a flask containing an equimolar amount of $[Et_4N]_2[Fe_2(CO)_8]$ (0.52 g, 0.87 mmol) and 20 ml of CH_2Cl_2 under vacuum. The red reaction mixture was allowed to warm to room temperature and magnetically stirred under a nitrogen atmosphere. The reaction progress was monitored regularly using infrared spectroscopy in the carbonyl stretching region, and after 45 minutes, appeared to have gone to completion. The reaction was monitored for a further 4 h with no apparent change.

The solvent was removed under vacuum and the green hexane-soluble fraction extracted using three 50 ml portions of hexane. When the

solvent was removed from the extracts under vacuum a small amount of oily residue remained with the products, hence the overall weight of this fraction could not be determined. An infrared spectrum of the hexane-soluble fraction showed weak peaks due to $Sn[Fe_2(CO)_8]_2$ (ν_{CO} (hexane) 2072m, 2044s, 2027ms, 2010s cm^{-1}), a strong peak at 2042 cm^{-1} due to $Fe_3(CO)_{12}$, and weaker peaks at 1998 cm^{-1} and 2021 cm^{-1}.

The hexane soluble products were concentrated and passed through a column packed with silica gel (60-120 mesh), using hexane as eluant. Green $Fe_3(CO)_{12}$ (0.040 g, 14% based on Fe) was the first product eluted followed by $Sn[Fe_2(CO)_8]_2$. The amount of $Sn[Fe_2(CO)_8]_2$ recovered was too small to be measured. The weak peaks observed at 1998 cm^{-1} and 2021 cm^{-1} in the initial infrared spectrum were not observed after the solution was passed through the column. These were probably associated with a yellow/orange oily product which remained attached to the column.

The remaining, hexane insoluble, products were dissolved in CH_2Cl_2 and filtered leaving a small amount of white precipitate attached to the inside of the reaction vessel. This was insoluble in both CH_2Cl_2 and THF.

The red CH_2Cl_2 fraction was found to contain a mixture of products and these were difficult to separate. An ether extraction was found to be largely comprised of a red product (ν_{CO} (CH_2Cl_2) 2064w, 1997s, 1972m, 1940sh, 1718w cm^{-1}). Attempts were made to grow crystals of this product by cooling the ether solution and also by hexane diffusion into an ether solution. The latter method resulted in the formation of strongly twinned red rhombohedral-shaped crystals and preliminary X-ray diffraction studies indicated a triclinic unit cell with the following dimensions:

$$a = 8.63\text{Å} \quad \alpha = 93.73°$$
$$b = 9.19\text{Å} \quad \beta = 83.18°$$
$$c = 8.55\text{Å} \quad \gamma = 96.39°$$
$$U = 668\ \text{Å}^3$$

By comparison with $[Et_4N]^+$ salts of other anionic transition-metal carbonyl clusters, a sensible density would be *ca.* 1.7 g cm^{-3}. This would indicate a molecular weight of *ca.* 683/Z.

This product was identified as $[Et_4N][HFe_3(CO)_{11}]$ which has an M_r

of 606.9 and ν_{CO} (CH_2Cl_2) 2070w, 2000vs, 1972s, 1946m, 1718w cm^{-1} [173]. This would suggest the space group P1 with Z = 1, which is very rare, or $P\bar{1}$ with both anion and cation disordered about a centre of symmetry. Alternatively one or more of the cell axes may have higher multiplicity since the photographs were weak and some rows of spots may have been missed.

Electron probe analysis of a sample crystal was consistent with this assignment with iron being the only element observed.

An infrared spectrum of the remaining brown CH_2Cl_2 fraction showed peaks corresponding to a small amount of $[HFe_3(CO)_{11}]^-$ plus peaks at 2041s, 1959sh, 1936s,br cm^{-1}. Yellow plate-like crystals, a white polycrystalline product and a small amount of red oily residue were obtained by cooling the CH_2Cl_2 solution. The white product exhibited no infrared bands in the carbonyl stretching region, and was assumed to be Et_4NCl. X-ray diffraction studies of the yellow crystals indicated that they had monoclinic symmetry with the unit cell dimensions below. The space group appears to be $P2_1$, for which Z = 2 is appropriate. The density of the crystalline product was determined by flotation in a solution of $ZnBr_2$.

$$a = 8.18\text{Å} \quad \alpha = 90°$$
$$b = 11.92\text{Å} \quad \beta = 97°$$
$$c = 10.53\text{Å} \quad \gamma = 90°$$
$$U = 1019.55\ \text{Å}^3,\ D_M = 1.82\ \text{g cm}^{-3},\ M_r \simeq 1121/Z$$

This product was identified as $[Et_4N][Cl_3SnFe(CO)_4]$, Mr = 523.13, ν_{CO} 2036, 1954, 1937 cm^{-1} [174].

(ii) Reactant ratio of 1 : 2

The previous reaction was repeated with a $SnCl_4$: $[Fe_2(CO)_8]^{2-}$ ratio of 1 : 2. $SnCl_4$ (0.05 ml, 0.43 mmol) was condensed onto $[Et_4N]_2[Fe_2(CO)_8]$ (0.51 g, 0.85 mmol) and 10 ml CH_2Cl_2 under vacuum. The flask was flushed with nitrogen and stirred at room temperature for 45 minutes. The products were worked up as described in reaction (i). The hexane fraction contained only a small amount of the yellow oily product with weak infrared peaks at 2021 cm^{-1} and 1998 cm^{-1}. No $Sn[Fe_2(CO)_8]_2$ or $Fe_3(CO)_{12}$ were recovered.

The red CH_2Cl_2 fraction was found to contain $[HFe_3(CO)_{11}]^-$ and the white product noted in the previous section. No $[Cl_3SnFe(CO)_4]^-$ was

observed.

A small amount of the white insoluble product reported in reaction (i) remained in the reaction vessel.

(iii) Reactant Ratio of 3 : 2

$SnCl_4$ (0.05 ml, 0.43 mmol) was condensed onto $[Et_4N]_2[Fe_2(CO)_8]$ (0.17 g, 0.29 mmol) in CH_2Cl_2 (10 ml), and stirred at room temperature for 45 minutes as in parts (i) and (ii).

The hexane soluble products were extracted in three 50 ml portions and concentrated. An infrared spectrum of this fraction revealed significant amounts of $Sn[Fe_2(CO)_8]_2$ and $Fe_3(CO)_{12}$. Weak peaks were also observed at 1998 cm^{-1} and 2021 cm^{-1}.The hexane fraction was chromatographed to give $Sn[Fe_2(CO)_7]_2$ (0.019 g, 0.024 mmol, 6% of Sn, 17% of Fe) and 0.018 g $Fe_3(CO)_{12}$ (0.036 mmol, 18% of Fe).

An infrared spectrum of the yellow/brown CH_2Cl_2 fraction (0.48 g) only contained bands due to $[Cl_3SnFe(CO)_4]^-$. When this solution was concentrated and cooled, yellow crystals of $[Et_4N][Cl_3SnFe(CO)_4]$ formed, along with some of the white product assumed to be Et_4NCl.

The insoluble white precipitate was again present in the reaction vessel, in larger proportions than for the two previous reactions.

2.5.2 REACTION OF $SnCl_4$ WITH $Na_2[Fe_2(CO)_8].THF$

(i) Reactant Ratio of 1 : 1

$SnCl_4$ (0.1 ml, 0.86 mmol) was condensed under vacuum into a Schlenk flask containing a solution of $Na_2[Fe_2(CO)_8].THF$ (0.39 g, 0.86 mmol, prepared by Na/naphthalene reduction of $Fe(CO)_5$) in THF (35 ml). The reaction mixture was permitted to warm to room temperature and was stirred for an hour. The solvent was then removed under vacuum. Three 50 ml hexane extracts were taken, then combined and concentrated. An infrared spectrum revealed $Fe_3(CO)_{12}$, $Sn[Fe_2(CO)_8]_2$ and peaks at 1998 cm^{-1} and 2021 cm^{-1}, as in section 2.5.1. The hexane solution was run on a silica gel column, yielding $Fe_3(CO)_{12}$ (0.098 g, 34% of Fe) and $Sn[Fe_2(CO)_8]_2$ (0.046 g, 6.8% of Sn, 15% of Fe).

An infrared spectrum of the hexane-insoluble products in CH_2Cl_2 revealed $[HFe_3(CO)_{11}]^-$ and $[Cl_3SnFe(CO)_4]^-$ plus a weak unidentified peak at 2096 cm^{-1}.

(ii) Reactant Ratio of 1 : 2

This reaction was repeated using 0.05 ml of $SnCl_4$ (0.43 mmol) and 0.39 g $Na_2[Fe_2(CO)_8].THF$ (0.86 mmol) and the products were worked up as described in the previous section. Infrared spectra of the hexane soluble fraction exhibited the same array of peaks as seen for reaction (i). However, the proportion of $Fe_3(CO)_{12}$ in the hexane fraction was markedly reduced and the peaks at 2021 cm^{-1} and 1998 cm^{-1} were relatively more intense. These observations were reflected in the yields obtained after chromatography: $Fe_3(CO)_{12}$ (0.042 g, 15% of Fe) and $Sn[Fe_2(CO)_8]_2$ (0.058 g, 17% of Sn, 19% of Fe).

An infrared spectrum of the hexane insoluble products again contained bands due to $[HFe_3(CO)_{11}]^-$ and $[Cl_3SnFe(CO)_4]^-$ plus a weak peak at 2096 cm^{-1}.

(iii) Reactant ratio of 1 : 4

$SnCl_4$ (0.05 ml, 0.43 mmol) was reacted with $Na_2[Fe_2(CO)_8].THF$ (0.78 g, 1.72 mmol) in THF (50 ml) as described above.

$Fe_3(CO)_{12}$ (0.75 g, 0.15 mmol, 13%of Fe) and $Sn[Fe_2(CO)_8]_2$ (0.075 g 0.095 mmol, 22% of Sn, 11% of Fe) were isolated on workup. The 2021 cm^{-1} and 1998 cm^{-1} peaks were also detected in the hexane fraction by infrared spectroscopy.

An infrared spectrum of the hexane insoluble products contained bands due to $[HFe_3(CO)_{11}]^-$ and $[Cl_3SnFe(CO)_4]^-$ with a weak peak at 2096 cm^{-1}.

2.5.3 REACTION OF SnI_4 WITH $Na_2[Fe_2(CO)_8].THF$

A 1 : 4 ratio of SnI_4 (0.583 g, 0.93 mmol) and $Na_2[Fe_2(CO)_8].THF$ (1.69 g, 3.72 mmol, prepared from $Na_2[Fe_2(CO)_8].(dioxane)_{1.5}$) were stirred in 40 ml THF at room temperature and under a nitrogen atmosphere for 1 hour. The solvent was then removed under vacuum and a 50 ml hexane fraction was removed. This extract was colourless and initially showed no carbonyl infrared bands. When concentrated from 50 ml to *ca.* 2 ml ν_{CO} bands were observed at 2022 cm^{-1} and 1998 cm^{-1} along with a very weak band at 2045 cm^{-1}. There was no evidence that $Sn[Fe_2(CO)_8]_2$ had been formed.

An infrared spectrum of the hexane-insoluble fraction, run in CH_2Cl_2, showed carbonyl stretches at 2050w, 2004sh, 1998vs, 1979vs, 1898s and 1790w,br cm^{-1}. This spectrum can be assigned to

$[(CO)_8Fe_2]Sn[Fe(CO)_4]_2^{2-}$ (ν_{CO} (CH_2Cl_2) 2050w, 2003s, 1990s, 1975vs, 1899s, 1793br cm^{-1}) [31]. A component of the very strong peak at 1998 cm^{-1} may be due to the presence of a small amount of $[HFe_3(CO)_{11}]^-$ in the CH_2Cl_2 fraction.

2.5.4 REACTION OF $SnCl_4$ WITH $Na_2[Fe_2(CO)_8]$

(i) Reactant Ratio of 1 : 2 in Benzene

Na (0.096 g, 4.18 mmol) was dissolved in dried liquid ammonia (*ca.* 4 litres at STP) on a vacuum line. $Fe(CO)_5$ (0.23 ml, 1.74 mmol) was added in small portions by condensation and allowed to react at -63°C (using a chloroform slush bath). The reaction was stirred occasionally until all the sodium had reacted. This was indicated by the disappearance of the blue colour. The same amount of $Fe(CO)_5$ again was added over ~1 h and stirred for ~2 h at -63°C to ensure complete reaction. The ammonia was then evaporated off and the $Na_2[Fe_2(CO)_8]$ left under vacuum for 24 hours to ensure complete removal. A 90% yield (1.57 mmol) was assumed.

Benzene (40 ml) was then condensed onto the $[Fe_2(CO)_8]^{2-}$ followed by $SnCl_4$ (0.09 ml, 0.78 mmol). The reaction mixture was allowed to warm to room temperature and was stirred for 1 h. The reaction vessel was transferred to a Schlenk line where it was flushed with nitrogen and the products worked up. An infrared spectrum of the yellow solution revealed $[Cl_3SnFe(CO)_4]^-$ as the main component with lesser amounts of $Fe_3(CO)_{12}$ and $Sn[Fe_2(CO)_8]_2$. There were also unidentified peaks at 2086 cm^{-1} and 2105 cm^{-1}. Three 50 ml hexane extracts were concentrated and passed through a silica gel column. An orange product remained attached to the column and $Sn[Fe_2(CO)_8]_2$ and $Fe_3(CO)_{12}$ were isolated from the eluent. The yield of $Sn[Fe_2(CO)_8]_2$ was very low (0.025 g, 0.031 mmol, ~4% of Sn)

(ii) Reactant ratio of 1 : 4 in Benzene

Sodium (0.30 g, 13 mmol) plus a total of 1.4 ml $Fe(CO)_5$ (10.6 mmol) were used to produce $Na_2[Fe_2(CO)_8]$ (*ca.* 4.78 mmol). This was stirred with $SnCl_4$ (0.14 ml, 1.19 mmol) in benzene (100 ml) for 1 h, as described above. The products were worked up giving $Sn[Fe_2(CO)_8]_2$ (0.132 g, 0.17 mmol, ~14% of Sn). A CH_2Cl_2 infrared spectrum of the hexane insoluble fraction contained bands due to $[Cl_3SnFe(CO)_4]^-$ and weaker bands due to $[HFe_3(CO)_{11}]^-$.

(iii) Reactant ratio of 1 : 4 in THF

Run One: Sodium (0.30 g, 13 mmol) plus $Fe(CO)_5$ (1.3 ml, 9.83 mmol) were used to prepare $Na_2[Fe_2(CO)_8]$ (*ca.* 8.87 mmol). THF (100 ml) was condensed onto this, followed by $SnCl_4$ (0.125 ml, 1.1 mmol). These were reacted as described in section (i).

On work up, The hexane soluble fraction was found to contain 0.139 g $Sn[Fe_2(CO)_8]_2$ (0.35 mmol, ~16% of Sn). The hexane insoluble products again consisted of $[Cl_3SnFe(CO)_4]^-$ with lesser amounts of $[HFe_3(CO)_{11}]^-$.

Run Two: Sodium (0.26 g, 11.3 mmol) and $Fe(CO)_5$ (1.2 ml, 9 mmol) were used to prepare $Na_2[Fe_2(CO)_8]$ (*ca.* 8.17 mmol). This was allowed to react with $SnCl_4$ (0.23 ml, 2 mmol) in THF (100 ml) for 3 h. The longer reaction time appeared to have minimal effect on the products of the reaction. $Sn[Fe_2(CO)_8]_2$ (0.26 g, 0.32 mmol) was isolated in a yield of ~16% based on Sn.

2.5.5 REACTION OF $SnCl_4$ WITH $Na_2[Fe(CO)_4].(dioxan)_{1.5}$ (1 : 8 ratio)

$Na_2[Fe(CO)_4].(dioxan)_{1.5}$ (2.27 g, 6.56 mmol) was added to a white suspension of $SnCl_4$ (0.093 ml, 0.81 mmol) in 50 ml THF. The mixture was stirred under a nitrogen atmosphere and monitored using infrared spectroscopy. The reaction proceeded slowly. After 20 hours the solvent was removed under vacuum and the products extracted using $CHCl_3$. A remaining insoluble pink precipitate (*ca.* 0.7 g) was found to contain some unreacted $[Fe(CO)_4]^{2-}$. The $CHCl_3$ was removed from the soluble products under vacuum and the hexane-soluble fraction extracted in two 20 ml portions. An infrared spectrum of the green/brown hexane solution showed the unidentified peaks at 2020m and 1995s cm^{-1}, with a small peak at 2045 cm^{-1} due to $Fe_3(CO)_{12}$. There was no evidence that $Sn[Fe_2(CO)_8]_2$ had been formed.

An infrared spectrum of the remaining yellow/brown $CHCl_3$-soluble fraction contained peaks due to $[Cl_3SnFe(CO)_4]^-$.

2.5.6 REACTION OF $SnCl_4$ WITH $Na_2[Fe(CO)_4]$ (1 : 8 Ratio)

$Fe(CO)_5$ (0.89 ml, 6.9 mmol) was distilled in small portions into a solution of Na (0.40 g, 17.3 mmol) in liquid ammonia (*ca.* 4 litres at STP) under vacuum. This was reacted at -63°C to give $Na_2[Fe(CO)_4]$ as described in section 2.4.3.

When the synthesis was completed, the reaction vessel was transferred to a Schlenk line where it was flushed with nitrogen. To this was added a white suspension of $SnCl_4$ (0.10 ml, 0.87 mmol) in THF (10 ml). The mixture was stirred for 20 hours, the solvent removed under vacuum, and the products extracted in two 15 ml portions of $CHCl_3$. An infrared spectrum revealed that $[Cl_3SnFe(CO)_4]^-$ was again the dominant product. Also present were small amounts of $Sn[Fe_2(CO)_8]_2$ and $Fe_3(CO)_{12}$.

The solvent was removed under vacuum and the hexane soluble products were isolated using two 20 ml extracts. The hexane fractions were then concentrated and passed through a silica gel column. $Fe_3(CO)_{12}$ was isolated and an orange product remained attached to the column. $Sn[Fe_2(CO)_8]_2$ could not be isolated in appreciable yields.

2.5.7 REACTION OF $SnCl_4$ WITH THE PRODUCTS OF SODIUM/AMALGAM REDUCTION OF $Fe(CO)_5$

$Fe(CO)_5$ (1.3 ml, 9.96 mmol) was condensed on to THF (50 ml) over a 1% sodium/mercury amalgam. The mixture was stirred for 3 hours at room temperature under a nitrogen atmosphere. The pale yellow solution gradually went red and a fine pale yellow-pink precipitate formed. An infrared spectrum of the red THF solution showed strong peaks at 1918 cm^{-1} and 1852 cm^{-1} indicating that a large amount of $[Fe_2(CO)_8]^{2-}$ had been formed in the reaction. Peaks were also present at 1998w 1988vw 1892sh 1875s 1830sh cm^{-1}, which could not be identified. The weak peak at 1998 cm^{-1} with a shoulder at 1988 cm^{-1} were probably due to $[HFe_3(CO)_{11}]^-$ and the weak shoulder at 1892 cm^{-1} may represent $[HFe(CO)_4]^-$ (ν_{CO} (solid) 2015w 1937sh 1897vs cm^{-1}) [175]. A solid-state infrared spectrum of the precipitate contained a strong broad peak at *ca.* 1765 cm^{-1} confirming that $Na_2[Fe(CO)_4]$ had been formed. A broad feature centred at *ca.* 1880 cm^{-1}, consistent with the solution spectrum, was also seen.

The precipitate and the red solution were stirred to a slurry and decanted off the amalgam into $SnCl_4$ (0.14 ml, 1.19 mmol) in THF (20 ml). The mixture was then stirred overnight under a nitrogen atmosphere. Two 50 ml $CHCl_3$ extractions were made and these were found to contain $Sn[Fe_2(CO)_8]_2$ and $[HFe_3(CO)_{11}]^-$.

$Sn[Fe_2(CO)_8]_2$ was separated from the ionic products by the addition of silica gel to the combined $CHCl_3$ extracts. The mixture was

stirred for 15 minutes and then filtered through a glass frit. The gel was then washed with a further 200 ml CH_2Cl_2 and the filtrates combined. The solvents were removed by evaporation and spectroscopically pure $Sn[Fe_2(CO)_8]_2$ (0.603 g, 0.76 mmol) was produced with a yield of 64% based on Sn. This reaction is somewhat capricious, as is common with complex systems involving transition metal carbonyl anions. When the preparation was repeated, yields varied between 35 and 64%.

2.5.8 DISCUSSION

Compounds of the form $E[Fe_2(CO)_8]_2$ (E = Si,Ge,Sn) have all been described in the literature. In most cases these have been isolated in low yields as side products from unlikely reactions [38]. $Si[Co_2(CO)_7]_2$ and $Ge[Co_2(CO)_7]_2$, which are structurally similar, have in the past provided useful starting points for further cluster synthesis. It seems likely that $E[Fe_2(CO)_8]_2$ compounds will be similarly useful. Therefore the synthesis of $Sn[Fe_2(CO)_8]_2$ was investigated as part of an effort at Waikato University to provide more rational syntheses and improved yields of $E[Fe_2(CO)_8]_2$ compounds.

$Sn[Fe_2(CO)_8]_2$ was first synthesised and structurally characterised in 1967 [48,38]. It was initially prepared by vigorous reaction of Bu_3SnCl with $Fe(CO)_5$. $Sn[Fe_2(CO)_8]_2$ was obtained in ≤16% yield, along with organotin iron carbonyl compounds. Higher yields (25%) were obtained by reacting $SnCl_4$ with "$[Fe(CO)_4]^{2-}$" in a 1 : 8 ratio. This report was very brief and a personal communication later revealed that the $[Fe(CO)_4]^{2-}$ had been prepared by sodium/amalgam reduction of $Fe(CO)_5$. There was some indication that the $[Fe(CO)_4]^{2-}$ used was impure (see later).

Work (concurrent to this investigation) has shown that reacting EH_4 (E = Si,Ge) with $Fe_2(CO)_9$ provides a useful means of obtaining good yields of $Si[Fe_2(CO)_8]_2$ (61%) and $Ge[Fe_2(CO)_8]_2$ (43%) [38,25]. Stannane (SnH_4), however, is much less stable than SiH_4 and GeH_4. Skelte Anema has shown that, although yields of up to 21% can be obtained, the synthesis of $Sn[Fe_2(CO)_8]_2$ from SnH_4 and $Fe_2(CO)_9$ is unreliable.

An attempt was therefore made to prepare $Sn[Fe_2(CO)_8]_2$ from $SnCl_4$ and $[Fe_2(CO)_8]^{2-}$ in a salt elimination reaction. This appeared to provide a logical route for this synthesis. Attempts were also made to

repeat the $SnCl_4$/"$[Fe(CO)_4]^{2-}$" preparation described by Cotton *et al.* using $Na_2[Fe(CO)_4]$ of good purity.

When $SnCl_4$ was reacted with $[Et_4N]_2[Fe_2(CO)_8]$, a molar ratio of 3 : 2 provided the optimum yield of $Sn[Fe_2(CO)_8]_2$ (~6% based on Sn). When the stoichiometric ratio of 1 : 2 was employed, no $Sn[Fe_2(CO)_8]_2$ was produced. The fate of the tin in this reaction is not clear but may have been associated with the insoluble white precipitate remaining in the reaction vessel. Virtually all of the iron in the products was present as $[HFe_3(CO)_{11}]^-$. The hydrogen atom in $[HFe_3(CO)_{11}]^-$ was probably derived from adventitious H_2O present in the solvent. In later reactions where THF was employed as the solvent, $[HFe_3(CO)_{11}]^-$ may also have been produced by photolytic or radical induced abstraction of hydrogen from the solvent **[176]**. For example:

$$[Fe_3(CO)_{12}]^{-\cdot} + C_4H_8O \xrightarrow{h\nu} [HFe_3(CO)_{11}]^- + [C_4H_7O\cdot] + CO$$

$$[Fe(CO)_4]^{-\cdot} + C_4H_8O \rightarrow [HFe(CO)_4]^- + [C_4H_7O\cdot]$$

$$[HFe(CO)_4]^- + Fe(CO)_5 \rightarrow [HFe_3(CO)_{11}]^- + 3CO$$

When the proportion of $SnCl_4$ to $[Fe_2(CO)_8]^{2-}$ in the reactants was increased (to 1 : 1 then 3 : 2), $Sn[Fe_2(CO)_8]_2$ was produced but only in small yields. A large proportion of the tin ended up as $[Cl_3SnFe(CO)_4]^-$ and was not involved in further reaction. When a reactant ratio of 3 : 2 was used, this species also accounted for the bulk of the iron in the products.

$[Et_4N]^+$ is not a particularly suitable cation for this salt elimination reaction, and the excess $SnCl_4$ that is required for the formation of $Sn[Fe_2(CO)_8]_2$ may be necessary to promote the removal of Cl^- from other $SnCl_4$ molecules, giving $[SnCl_6]^{2-}$. As the $[Et_4N]^+$ salt, this species could account for the insoluble white precipitate mentioned above.

The high lattice energy and insolubility of NaCl makes Na^+ a much more suitable cation for salt elimination. When $SnCl_4$ was reacted with $Na_2[Fe_2(CO)_8]$ in THF (section 2.5.2) higher yields of $Sn[Fe_2(CO)_8]_2$ were generally obtained. Also, an excess of $SnCl_4$ was no longer required for the production of $Sn[Fe_2(CO)_8]_2$.

The yield of $Sn[Fe_2(CO)_8]_2$ was found to increase as the proportion of $[Fe_2(CO)_8]^{2-}$ increased from reactions (i) to (iii). The reaction in

part (iii) contained the same tin to iron ratio (1 : 8) as the $SnCl_4$/"$[Fe(CO)_4]^{2-}$" preparation described by Cotton *et al.* [177], however the yield based on tin (~22%) was still less than they reported (25%).

One possible problem associated with using THF as the solvent is that this combines exothermically with $SnCl_4$ to form a white suspension of $SnCl_4$.2THF, and the presence of the coordinated solvent molecules may hinder the reaction with $[Fe_2(CO)_8]^{2-}$.

SnI_4 is a weaker Lewis acid than $SnCl_4$ and therefore does not form SnI_4.2THF. Also, the Sn-I bond is weaker than the Sn-Cl bond, and it was expected that this would facilitate the formation of $Sn[Fe_2(CO)_8]_2$.

In fact, when SnI_4 was reacted with $Na_2[Fe_2(CO)_8]$, formation of $Sn[Fe_2(CO)_8]_2$ was not detected and $[(CO)_8Fe_2]Sn[Fe(CO)_4]^{2-}$ was identified as the dominant product. This species was not observed in any of the other reactions. It appears that this forms because Sn(IV) is more readily reduced to give Sn(II):

$$SnI_4 \rightarrow SnI_2 + 2I^-$$

Although the yield of $[(CO)_8Fe_2]Sn[Fe(CO)_4]_2^{2-}$ was not measured, infrared spectroscopy indicates that this species was by far the major product. $[(CO)_8Fe_2]Sn[Fe(CO)_4]_2^{2-}$ has previously been synthesised in 59% yield by reacting tin(II) acetate with $[Et_4N][Fe_2(CO)_8]$ [31]. If the yield from the current reaction is optimised this reaction, or one involving SnI_2, may provide an improved route for synthesising $[(CO)_8Fe_2]Sn[Fe(CO)_4]_2^{2-}$.

In section 2.5.4 (i) and (ii), benzene was used as the solvent for the reaction of $SnCl_4$ with $Na_2[Fe_2(CO)_8]$ (prepared via sodium reduction of $Fe(CO)_5$ in ammonia). Benzene does not form an adduct with $SnCl_4$. Also, being less polar than THF. However, by comparing reactions (ii) and (iii) it can be seen that replacement of the solvent had minimal effect on the reaction. When the reaction time was extended to 3 h (reaction (iii) run two) this also had little effect on the reaction.

$[Cl_3SnFe(CO)_4]^-$ was a major product in all of the reactions described in section 2.5.4. This suggests that there is a deficit of iron in the reactions. This may be due to the purity of the $Na_2[Fe_2(CO)_8]$ formed via the Na/NH_3 reduction method. If conversion of $[Fe(CO)_4]^{2-}$ to $[Fe_2(CO)_8]^{2-}$ had not gone to completion, any remaining

$[Fe(CO)_4]^{2-}$ would have been only slightly soluble in THF and would not have had time to react. This could also explain why the yields are lower than for similar reactions using $Na_2[Fe_2(CO)_8]$ prepared by the sodium/naphthalene reduction method (section 2.5.2).

As mentioned earlier, a comunication recieved from Cotton indicated that $Na_2[Fe(CO)_4]$ used for the "$SnCl_4/[Fe(CO)_4]^{-}$" synthesis had been prepared by Na/amalgam reduction of $Fe(CO)_5$. This "$Na_2[Fe(CO)_4]$" had formed a red solution in THF. Pure $Na_2[Fe(CO)_4]$, however, is white and only slightly soluble in THF, so this was not the only reduction product. The red colour of the THF solution suggests that higher nuclearity iron carbonyl anions are also present. It has been shown that the reduction of $Fe(CO)_5$ in THF is very complicated. $[Fe(CO)_4]^{2-}$ and $[Fe_2(CO)_8]^{2-}$ are both likely to be formed, along with $[HFe(CO)_4]^{-}$ and $[HFe_3(CO)_{11}]^{-}$ via the reaction of transient $[Fe(CO)_4]^{-\cdot}$ and $[Fe_3(CO)_{12}]^{-\cdot}$ radical anions with THF **[176]**. In this case there is also the possibility of contamination with mercury.

An attempt was made to repeat the "Cotton" synthesis using $Na_2[Fe(CO)_4](dioxan)_{1.5}$ (section 2.5.5). Even with an extended reaction time (20 h *cf.* 3 h), no $Sn[Fe_2(CO)_8]_2$ was detected amongst the products.

By reducing $Fe(CO)_5$ with sodium in liquid ammonia it is possible to prepare very pure $Na_2[Fe(CO)_4]$. This was reacted with $SnCl_4$ in a 8:1 ratio (section 2.5.6). A very small amount of $Sn[Fe_2(CO)_8]_2$ was detected in the products, but in other respects there was little difference between this reaction and the one involving $Na_2[Fe(CO)_4].(dioxane)_{1.5}$ (section 2.5.6). Therefore the source of $[Fe(CO)_4]^{2-}$ was probably not a significant factor in the previous reaction. It seems that impurities in the synthesis described by Cotton *et al.* must have influenced the reaction.

The greatest yield of $Sn[Fe_2(CO)_8]_2$ (35-64%) was presented by the reaction of $SnCl_4$ with the products of a sodium amalgam reduction of $Fe(CO)_5$ (section 2.5.7). The products of this reduction contained both $[Fe(CO)_4]^{2-}$ and $[Fe_2(CO)_8]^{2-}$, with a little $[HFe_3(CO)_{11}]^{-}$ and other unidentified species. From the previous reactions it is evident that $Sn[Fe_2(CO)_8]_2$ is not obtained in high yields when $SnCl_4$ is reacted with $[Fe(CO)_4]^{2-}$ or $[Fe_2(CO)_8]^{2-}$ alone. It also seems unlikely that reacting $SnCl_4$ with a combination of these two anions would be any more successful. Therefore an explanation for the high yield obtained in

section 2.5.7 must rest with other species present in the products of the sodium amalgam reduction.

When $[Co(CO)_4]^-$ is prepared by sodium amalgam reduction (section 2.4.3) $Hg[Co(CO)_4]_2$ and $[Hg\{Co(CO)_4\}_3]^-$ are also known to be formed. Similar mercury contamination may be occuring when $Fe(CO)_5$ is reduced, and this may be responsible for the unidentified infrared peaks. A polymeric $[HgFe(CO)_4]_n$ species is known but this was not detected [178]. It is also probable that traces of finely suspended amalgam were transferred when the reduction products were decanted.

Because this system is very complex it is difficult to ascertain exactly what species are involved and what factors are important for this synthesis. However it is apparent from the preceeding reactions that agents able to abstract Cl^- from $SnCl_4$ promote this reaction, and that the preparation of $Sn[Fe_2(CO)_8]_2$ is more successful when $SnCl_4$ is reacted with $[Fe_2(CO)_8]^{2-}$ rather than $[Fe(CO)_4]^{2-}$. As mentioned in section 2.4.3, $[Hg\{Co(CO)_4\}_3]^-$ is known to react with halides releasing $[Co(CO)_4]^-$. It could be envisaged that if similar iron containing species were present in the products of the $Fe(CO)_5$ sodium amalgam reduction (eg. $[Hg\{Fe_2(CO)_8\}_n]^{x-}$) that these might promote the formation of $Sn[Fe_2(CO)_8]_2$ by providing both a source of $[Fe_2(CO)_8]^{2-}$ and an agent for abstracting Cl^- from $SnCl_4$ ($HgCl_2$). This would satisfy both requirements. A detailed investigation of the products of the $Fe(CO)_5$ sodium amalgam reduction is obviously required for a fuller understanding of the processes involved. This may be very complex task, based on previous investigations of the redox processes of iron carbonyls in THF [176].

In the meantime, the original aim of this work has been realised in that a reasonably reproducible recipe for moderate yields of $Sn[Fe_2(CO)_8]_2$ has been established.

Chapter Three

Structures of compounds frequently refered to in this thesis are depicted in a fold-out section in Appendix A. The symbol *(F #)* is used in the text to refer readers to these diagrams.

CHAPTER 3 REACTIONS OF $EM_4(CO)_x$ (E = Si, Ge, Sn; M = Co, Fe) WITH TRANSITION METAL CARBONYL ANIONS

3.1 INTRODUCTION

3.1.1 SYNTHESIS AND STRUCTURE OF $EM_4(CO)_x$ CLUSTERS

Three types of skeletal structure are adopted by $EM_4(CO)_x$ (E = Si, Ge, Sn; M = Co, Fe) clusters:

(i) *$E[Co(CO)_4]_4$; E is bonded to four terminal $-Co(CO)_4$ groups.* This structure requires 72 valence electrons and is known for E = Ge and Sn.

(ii) *$E[M_2(CO)_x]_2$; E bridges two $M_2(CO)_x$ moieties forming two mutually perpendicular EM_2 triangles with a common apex, E.* This is refered to as a *spiro* structure which describes the arrangement about the central E atom. This structure requires 68 valence electrons and is known for E = Si, Ge when M = Co ***(F 1)***; and for E = Si, Ge, Sn when M = Fe ***(F 2)***.

(iii) *$(CO)_4CoEC_3(CO)_9$; E is bonded to a terminal $Co(CO)_4$ group and also triply bridges a $Co_3(CO)_9$ moiety forming a ECo_3 trigonal pyramid.* This structure requires 66 valence electrons and is known for E = Si, Ge ***(F 5)***.

Each of the EM_4 structures has a distinct electron count, the number of valence electrons decreasing with increasing closure. Electronic considerations preclude the formation of $E[Fe(CO)_x]_4$ or $(CO)_xFeEFe_3(CO)_y$ clusters, although the $[(CO)_4FeSiFe_3(CO)_{10}]^-$ and $[(CO)_4FeGeFe_3(CO)_{10}]^-$ anions (discussed in chapter 5) do have structures similar to (iii).

The "all-terminal" compounds, $Ge[Co(CO)_4]_4$ and $Sn[Co(CO)_4]_4$ have been formed by reacting EX_4 (X = halogen) with $[Co(CO)_4]^-$ **[42,53,181]**. A similar reaction is not observed for silicon. It has been suggested that the smaller covalent radius of silicon would mean that an equivalent "$Si[Co(CO)_4]_4$" cluster would be very sterically crowded.

The first *spiro* cluster to be reported, $Sn[Fe_2(CO)_8]_2$, was synthesised and structurally characterised in 1967 **[177,48]** (see

section 2.5.8). $Ge[Fe_2(CO)_8]_2$ was reported a short time later [182]. Over the years the germanium compound has been variously prepared from $GeCl_4/[Fe(CO)_4]^{2-}$, $Me_3NH^+GeCl_3^-/Fe(CO)_5$, $(CH_2{=}CH)_4Ge/Fe_2(CO)_9$ [40] and $Ge[Mn(CO)_2(MeCp)]_2/Fe_2(CO)_9$ [183] systems, always in low yield. The silicon analogue, $Si[Fe_2(CO)_8]_2$ has also been briefly reported from the reaction of $SiCl_3H$ with $Fe_2(CO)_9$ [184]. However, the most efficient method for synthesising *spiro* clusters is via the reaction of EH_4 with $Co_2(CO)_8$ or $Fe_2(CO)_9$. This method has been used to prepare $Si[Fe_2(CO)_8]_2$ [63,39], $Ge[Fe_2(CO)_8]_2$ [38], $Si[Co_2(CO)_7]_2$ and $Ge[Co_2(CO)_7]_2$ [38,26] (see chapter 2). Unfortunately SnH_4 is too unstable to be useful in this type of reaction, however a convenient alternative method for preparing $Sn[Fe_2(CO)_8]_2$ has been established in Chapter 2. A $Sn[Co_2(CO)_7]_2$ species is not known.

At first glance the bridging E atom in $E[Fe_2(CO)_8]_2$ appears to be replacing one of the three bridging carbonyls on $Fe_2(CO)_9$, yet the E-bridged $Fe_2(CO)_8$ units adopt a configuration where all carbonyls are terminal. This may reflect ligand packing effects. It also permits lengthening of the Fe-Fe bond (*cf.* $Fe_2(CO)_9$) to accommodate the group 14 atom and to minimise Fe-E-Fe angular strain. In table 3.1 it can be seen that the Fe-Fe bondlength increases as E becomes larger. This structure has also been reported for $Pb[Fe_2(CO)_8]_2$, showing that it can accommodate the very large Pb atom [31].

In contrast, the $Fe_2(CO)_8$ moiety in $[(CO)_8Fe_2]E[Fe(CO)_4]_2^{2-}$ (E = Sn, Pb) *(F 3)* [31,49] is bridged by two CO groups, as well as the Pb atom, providing a better analogy with $Fe_2(CO)_9$. In this case the carbonyl-bridged configuration may allow more efficient dissipation of the negative charge.

The electronic requirement for a bridging carbonyl group at each end of the *spiro*-$E[Co_2(CO)_7]_2$ clusters leads to less efficient ligand packing and an uncomfortably short Co-Co bond. This is associated with significant asymmetry in the bridging carbonyl groups and the ECo_2 triangles, along with distortion of the dihedral angle between the two ECo_2 triangles from 90° (see Chapter 1 and table 3.1).

The strain inherent in these $E[Co_2(CO)_7]_2$ clusters may account for the non-existance of a tin analogue. The size of the Sn atom would prevent the completion of a triangle with two Co atoms already bridged by a carbonyl group.

Table 3.1: Structural features of *spiro*-E[$M_2(CO)_x$]$_2$ Clusters

Cluster	E-M(Å)	ΔE-M(Å)[a]	M-M(Å)	M-E-M°[c]	Dihedral angle°	ref
Si[$Fe_2(CO)_8$]$_2$	2.347	[b]	2.792	73	89	[38]
Ge[$Fe_2(CO)_8$]$_2$	2.400	0.014	2.825	72	89	[40]
Sn[$Fe_2(CO)_8$]$_2$	2.54	0.02	2.87	69	87	[48]
Si[$Co_2(CO)_7$]$_2$	2.288	0.025	2.528	67	81	[39]
Ge[$Co_2(CO)_7$]$_2$	2.361	0.037	2.56	66	84	[42]

[a] average difference in E-M bondlength within each EM_2 triangle, [b] EM_2 triangles are symmetrical to within bondlength errors, [c] internal angle within the EM_2 triangle

Similar arguments based on angular strain can be used to explain why Sn is also not able to adopt structures of the third type. The Sn atom is too large and the -EM_3 trigonal pyramid too constraining for such a structure to be favourable. However, for the smaller main group atoms, the -EM_3 trigonal pyramid structure appears to be particularly stable.

Figure 3.1: Decarbonylation Reactions of $GeCo_4(CO)_x$ Clusters

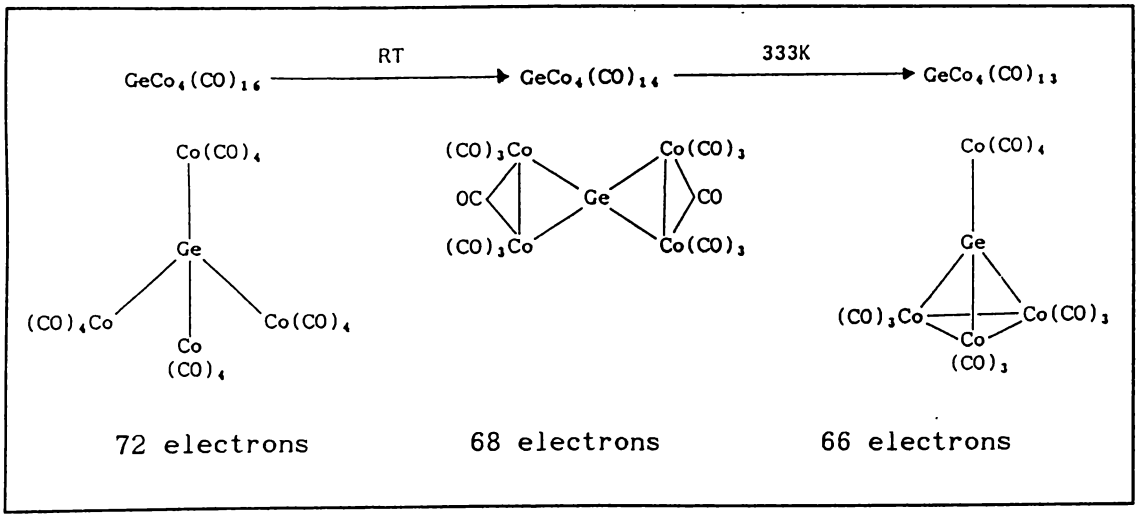

All three structures, (i), (ii) and (iii), have been reported for Ge when M = Co, and are all produced in the $GeBr_4/[Co(CO)_4]^-$ and $GeH_4/Co_2(CO)_8$ reactions. These three compounds are related by successive decarbonylation reactions, with a corresponding increase in clusterification (Co-Co bond formation). See figure 3.1.

A similar relationship is observed between $Si[Co_2(CO)_7]_2$ and $(CO)_4CoSiCo_3(CO)_9$. When $(CO)_4CoSiCo_3(CO)_9$ and $(CO)_4CoGeCo_3(CO)_9$ were first prepared by Schmid, the reactions of $[Co(CO)_4]^-$ with SiI_4 [185] and $GeBr_4$ [179] respectively were performed at elevated temperatures. Under these conditions the more open structures would have been unstable and were therefore not observed.

3.1.2 REACTIONS WITH TRANSITION METAL CARBONYL ANIONS

The reactions of $EM_4(CO)_x$ clusters with transition metal carbonyl anions that have been reported to date, vary from simple addition or substitution reactions to complex systems involving the formation of higher nuclearity clusters.

An addition reaction is observed when $(CO)_4CoGeCo_3(CO)_9$ is reacted with $[Co(CO)_4]^-$, giving $[GeCo_5(CO)_{16}]^-$ ***(F 7)*** as the main product [92,93]. The $[GeCo_7(CO)_{20}]^-$ anion in ***(F 8)*** has also been isolated from this system [32]. $[GeCo_5(CO)_{16}]^-$ is also formed when the *spiro*-$Ge[Co_2(CO)_7]_2$ cluster is reacted with $[Co(CO)_4]^-$, but heat is required for this reaction to proceed. Hence this reaction still appears to go via $(CO)_4CoGeCo_3(CO)_9$, which is produced in an initial thermal decarbonylation step:

$$Ge[Co_2(CO)_7]_2 \xrightarrow{\Delta} (CO)_4CoGeCo_3(CO)_9 + CO$$

$$(CO)_4CoGeCo_3(CO)_9 + [Co(CO)_4]^- \rightarrow [GeCo_5(CO)_{16}]^- + CO$$

$[GeCo_5(CO)_{16}]^-$ is one of only a handful of compounds yet reported which contain a Ge atom coordinated to five metal atoms. The steric and electronic effects of increased coordination are manifested in unusually long Ge-Co bonds and short Co-Co bonds (2.53 Å) in the $-GeCo_3$ trigonal pyramid. In the $GeCo_2$ triangle, the average Ge-Co bond length is 2.46 Å, compared with typical values of *ca.* 2.36 Å for other compounds containing $GeCo_2$ triangles. Similarly, in the $-GeCo_3$ trigonal pyramid, the Ge-Co bonds range from 2.33 to 2.51 Å, compared

with an average value of 2.28 Å in $(CO)_4CoGeCo_3(CO)_9$.

In view of the strain inherent in this cluster, it seems reasonable that this species might readily lose the bridged $Co_2(CO)_7$ group in a reaction with $Co_4(CO)_{12}$ which is already present in the reaction mixture. This could account for the formation of $[GeCo_7(CO)_{20}]^-$:

$$[GeCo_5(CO)_{16}]^- + Co_4(CO)_{12} \rightarrow [GeCo_7(CO)_{20}]^- + Co_2(CO)_8$$

When $Ge[Co_2(CO)_7]_2$ is reacted with $[Mn(CO)_5]^-$ [93,28] a substitution reaction is observed. This gives a trigonal pyramid-type structure with a $Mn(CO)_5$ group in the terminal position. Heat is again required for this reaction to proceed, and the formation of $(CO)_4CoGeCo_3(CO)_9$ ***(F 5)*** by thermal decarbonylation has been assumed to be the first step:

$$Ge[Co_2(CO)_7]_2 \xrightarrow{\Delta} (CO)_4CoGeCo_3(CO)_9 + CO$$

$$(CO)_4CoGeCo_3(CO)_9 + [Mn(CO)_5]^- \rightarrow (CO)_5MnGeCo_3(CO)_9 + [Co(CO)_4]^-$$

A similar process is observed when $Ge[Co_2(CO)_7]_2$ is reacted with $[Fe(CO)_2Cp]^-$, although the product has only been tentatively characterised as $Cp(CO)_2FeGeCo_3(CO)_9$ by infrared spectroscopy.

The work of Gerlach [187] and other authors [188,189] suggests the following displacement series:

$$[Fe(CO)_2Cp]^- > [Mn(CO)_5]^- > [Fe(CO)_4]^{2-} > [Co(CO)_4]^-$$

where a terminal transition metal carbonyl group bonded to a group 14 atom can be displaced by a transition metal carbonyl anion preceeding it in the series.

This series corresponds with the order of relative nucleophilicities, discussed in section 1.4.1.

The reaction of $Ge[Co_2(CO)_7]_2$ with $[Fe_2(CO)_8]^{2-}$ proceeds at room temperature giving $[Ge_2Co_5Fe_2(CO)_{22}]^-$ in good yield [33]. This structure incorporates two $-EM_3$ trigonal pyramids linked through the Ge atoms to a $Co(CO)_3$ unit in a mutually *trans* configuration ***(F 10)***.

It has been suggested that this reaction proceeds via an

initial substitution-addition reaction, producing a "$[GeCo_3Fe_2(CO)_{17}]^-$" species, similar in structure to $[GeCo_5(CO)_{16}]^-$. This could then combine with unreacted $Ge[Co_2(CO)_7]_2$ in a similar reaction to that proposed for $[GeCo_5(CO)_{16}]^-$ and $Co_4(CO)_{12}$, above. This would give $[Ge_2Co_5Fe_2(CO)_{22}]^-$ as shown:

$$Ge[Co_2(CO)_7]_2 + [Fe_2(CO)_8]^{2-} \rightarrow "[GeCo_3Fe_2(CO)_{17}]^-" + [Co(CO)_4]^- + CO$$

$$"[GeCo_3Fe_2(CO)_{17}]^-" + Ge[Co_2(CO)_7]_2 \rightarrow [Ge_2Co_5Fe_2(CO)_{22}]^- + Co_2(CO)_8 + CO$$

A cluster with a similar structure, $[Ge_2Co_7(CO)_{21}]^-$ ***(F 9)***, has been prepared by reacting $[GeCo_5(CO)_{16}]^-$ with $Co_2(CO)_8$ under forcing conditions [150,32]. A similar reaction mechanism could be envisaged if an initial reaction between $[GeCo_5(CO)_{16}]^-$ and $Co_2(CO)_8$ releases $(CO)_4GeCo_3(CO)_9$:

$$[GeCo_5(CO)_{16}]^- + Co_2(CO)_8 \rightarrow (CO)_4CoGeCo_3(CO)_9 + [Co_3(CO)_{10}]^-$$

$$[GeCo_5(CO)_{16}]^- + (CO)_4CoGeCo_3(CO)_9 \rightarrow [Ge_2Co_7(CO)_{21}]^- + Co_2(CO)_8$$

The structure of $[GeCo_5(CO)_{16}]^-$ containing a five-coordinate Ge atom is apparently too sterically hindered to be adopted by the smaller Si atom. When $Si[Co_2(CO)_7]_2$ was reacted with $[Co(CO)_4]^-$ at 40°C by Sims, the high nuclearity $[\mu_8\text{-}SiCo_9(CO)_{21}]^{2-}$ ***(F 12)*** cluster, containing a fully encapsulated Si atom, was formed [64,132]. An identical reaction, also requiring heat, was observed for $(CO)_4CoSiCo_3(CO)_9$.

Another product has been isolated in very low yield from these reactions. This compound was tentatively characterised as the uncapped square antiprism, $[SiCo_8(CO)_{18}]^{2-}$ on the basis of its infrared spectrum.

The cavity formed by a regular capped square-antiprism of Co atoms (r = 1.35 Å) would be expected to have a radius of *ca.* 0.85 Å. Hence for $[SiCo_9(CO)_{21}]^{2-}$, expansion of the Co cage is required to accommodate the Si atom (r = 1.12 Å). This accounts for the unusually long basal intra-planar Co-Co bonds (mean 2.808 Å) and exceptional upper plane Co-Co bonds (mean 2.940 Å), observed. This illustrates that the square antiprism cage is remarkably flexible. It is interesting that a cubic structure, which contains a larger cavity, is not adopted. Presumably the larger number of M-M bonds in the

antiprism, and the stability of the EM_3 tetrahedral unit (of which the square antiprism is composed) are responsible.

The formation of $[SiCo_9(CO)_{21}]^{2-}$ is surprisingly specific, yet it is difficult to envisage a mechanism for its synthesis. An attempted quantitative analysis, although inconclusive, tended to indicate that a $Si[Co_2(CO)_7]_2$ to $[Co(CO)_4]^-$ ratio of between 4 : 2 and 4 : 3 is optimum for the synthesis of the $[SiCo_9(CO)_{21}]^{2-}$ dianion. Perhaps the overiding factor is the remarkable stability of this structure.

$[SiCo_9(CO)_{21}]^{2-}$ is also the major product in the reactions of $Si[Co_2(CO)_7]_2$ with $[Mn(CO)_4]^-$ and $[Fe_2(CO)_8]^{2-}$ **[33]**. An initial substitution reaction occurs, releasing $[Co(CO)_4]^-$. This then reacts to form $[SiCo_9(CO)_{21}]^{2-}$, swamping other possible reactions.

3.1.3 AIMS

As mentioned above, the synthesis of the $[SiCo_9(CO)_{21}]^{2-}$ dianion is surprisingly specific, yet a mechanism for this reaction is not obvious. This reaction was further investigated and attempts were made to find other products which might give some indication of the processes involved in this synthesis. In particular, it was hoped that the product tentatively identified as $[SiCo_8(CO)_{18}]^{2-}$ could be fully characterised.

$[SiCo_9(CO)_{21}]^{2-}$ is also the major product when $Si[Co_2(CO)_7]_2$ is reacted with the $[Mn(CO)_5]^-$ and $Fe_2(CO)_8]^{2-}$ anions. However, the reactions of $(CO)_4CoSiCo_3(CO)_9$ with these anions have not been investigated. $(CO)_4CoSiCo_3(CO)_9$, having a terminal $-Co(CO)_4$ group is more likely to undergo $(CO)_4CoGeCo_3(CO)_9$-type substitution reactions, and under conditions less conducive to the formation of $[SiCo_9(CO)_{21}]^{2-}$. Similarly, it was thought that reacting $(CO)_4CoGeCo_3(CO)_9$ with $[Mn(CO)_5]^-$ might provide higher yields of $(CO)_5MnGeCo_3(CO)_9$ than previously obtained from the reaction involving $Ge[Co_2(CO)_7]_2$.

The $[Fe(CO)_3NO]^-$ anion is isolelectronic with $[Co(CO)_4]^-$, and is also known to undergo condensation reactions with neutral metal carbonyl clusters **[190,191]**:

$$[Fe(CO)_3(NO)]^- + Ru_3(CO)_{12} \rightarrow [FeRu_3(CO)_{12}(NO)]^- \quad (1)$$

$$[Fe(CO)_3(NO)]^- + CFe_5(CO)_{15} \rightarrow [CFe_6(CO)_{13}(NO)_2]^{2-} + [CFe_5(CO)_{13}(NO)]^- \quad (2)$$

It was therefore of interest to compare the reactions of $[Fe(CO)_3NO]^-$

with $E[Co_2(CO)_7]_2$ clusters to the analagous reactions of $[Co(CO)_4]^-$.

The reactions of $(CO)_4CoECo_3(CO)_9$ clusters with the polynuclear anion, $[Co_6(CO)_{15}]^{2-}$ were also investigated. It was thought that this might provide a direct route to high nuclearity clusters, and in particular a $SiCo_{10}$ bicapped square antiprism. $[Co_6(CO)_{15}]^{2-}$ is known to decompose to $[Co(CO)_4]^-$ and $Co_4(CO)_{12}$ in the presence of excess CO. Therefore $[Co_6(CO)_{15}]^{2-}$ was reacted with the trigonal pyramid-type clusters *(F 5)* rather than the *spiro*-$E[Co_2(CO)_7]_2$ clusters *(F 1)*.

Finally, since methods of preparing $E[Fe_2(CO)_8]_2$ clusters in good yield have now become available (see chapter two) it was of interest to see if these clusters would also be useful as precursors for synthesising larger clusters. To this end, these clusters were reacted with $[Co(CO)_4]^-$, $[Mn(CO)_5]^-$ and $[Fe_2(CO)_8]^{2-}$.

3.2 EXPERIMENTAL

3.2.1 PREPARATION OF $[SiCo_9(CO)_{21}]^{2-}$

The synthesis of $[SiCo_9(CO)_{21}]^{2-}$ *(F 12)* was initially reported by Sims [64,132] and has more recently been investigated by Barris [33]. A general preparation is included below. In the current investigation, further compounds have been isolated from this system and characterised.

General Preparation

$Si[Co_2(CO)_7]_2$ (0.2 g, 0.3 mmol) and $Et_4NCo(CO)_4$ (0.1 g, 0.3 mmol) in 20 ml CH_2Cl_2 are stirred at *ca.* 35°C (oil bath) in a Schlenk flask under a nitrogen atmosphere. The red-brown solution goes darker as the reaction proceeds, and the formation of fine dark coloured crystals is usually observed towards the end of the reaction. The reaction takes *ca.* 18 hours to go to completion, which is indicated by the disappearance of the infrared peak at 2085 cm^{-1}, due to $Si[Co_2(CO)_7]_2$.

$[SiCo_9(CO)_{21}]^{2-}$ (ν_{CO} (CH_2Cl_2) 2054w, 2004s,br, 1955br,sh, 1791w,br cm^{-1}) (figure 3.2) is the major reaction product. Also present are $Co_4(CO)_{12}$ and an excess of $[Co(CO)_4]^-$. The solvent is evaporated and the $Co_4(CO)_{12}$ extracted in 20 ml of ether. When a CH_2Cl_2 solution of the remaining product is cooled to *ca.* -30°C, dark rectangular prismatic crystals of the mixed salt, $[Et_4N]_3[SiCo_9(CO)_{21}][Co(CO)_4]$

form in good yields (up to *ca.* 80%, based on the number of moles of Co atoms).

A small amount of a white insoluble residue also forms on the inside of the reaction vessel during the reaction. It appears that this residue accounts for the deficit of Si in the reaction products.

When $PPNCo(CO)_4$ is used in place of $Et_4NCo(CO)_4$ the reaction proceeds at a faster rate, going to completion in 11.5 h. This can be explained by reduced ion pairing between $[Co(CO)_4]^-$ and the larger, less electrophillic $[PPN]^+$ cation. The $[PPN]_2[SiCo_9(CO)_{21}]$ product crystallises without incorporating $[Co(CO)_4]^-$, but is still difficult to separate from $[Co(CO)_4]^-$ present in the product mixture. The crystalline product also appears to be less stable than the $[Et_4N]^+$ equivalent.

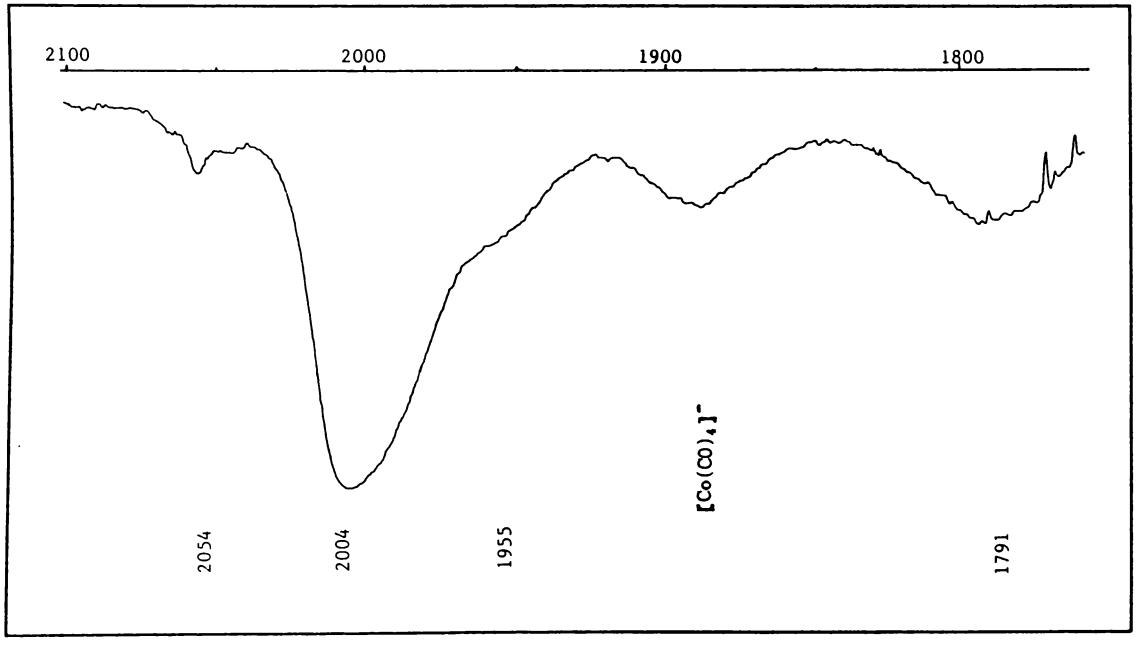

Figure 3.2: Infrared Spectrum of $[SiCo_9(CO)_{21}]^{2-}$ (CH_2Cl_2)

Notes:

1 The initial preparation reported by Sims was performed at 40°C. Reduced temperature was found to decrease the proportion of $Co_4(CO)_{12}$ produced.

2 It is difficult to completely remove the THF used in preparing $[Et_4N][Co(CO)_4]$ (see chapter two). If even small amounts of THF are

present in the preparation of $[SiCo_9(CO)_{21}]^{2-}$, this increases decomposition of $Si[Co_2(CO)_7]_2$ giving larger amounts of $Co_4(CO)_{12}$. Further reaction also produces dark green $[Co_6(CO)_{15}]^{2-}$, identified by comparison of its infrared spectrum with that reported for $Cs_2[Co_6(CO)_{15}]$ (see **table 3.2**). The peak at ~1888 cm^{-1} in the observed spectra was $[Co(CO)_4]^-$ present as an impurity.

Table 3.2 : Infrared Spectra of $[Co_6(CO)_{15}]^{2-}$

Observed Spectra (in CH_2Cl_2)	(in THF)	$Cs_2[Co_6(CO)_{15}]$ (in THF) [9]
2049w	2038w	2042m
1980s	1977s	1982s
1953sh	1953m	1959sh
	1897sh	
1888m	1884m	
1771w	1776w	1778s
1725w	1736m	1737s
	1707sh	1685m

3.2.1.1 FABS Mass Spectroscopic Investigation of $[Et_4N]_3[SiCo_9(CO)_{21}][Co(CO)_4]$

A FABS mass spectrum was obtained using a crystalline sample of $[Et_4N]_3[SiCo_9(CO)_{21}][Co(CO)_4]$. This showed fragmentation peaks of what appears to be two different clusters (**figure 3.3** and **table 3.3**).

A peak corresponding to the parent ion, $[SiCo_9(CO)_{21}]^-$ can be seen at m/e = 1147. A stepwise loss of CO groups from $[SiCo_9(CO)_{21}]^-$ produces a series of peaks corresponding to $[SiCo_9(CO)_n]^-$ (n = 21 to 12) fragments. The loss of one Co atom gives a similar succession of decarbonylated $[SiCo_8(CO)_n]^-$ (n = 18 to 15, 13 to 11) fragments. Smaller species containing Si with 3, 4 or 5 Co atoms can also be seen.

The highest peak in the mass spectrum occurs beyond that of $[SiCo_9(CO)_{21}]^-$. This is also related to a succession of decarbonylated fragments. The growth rate of these peaks and the pattern of peak

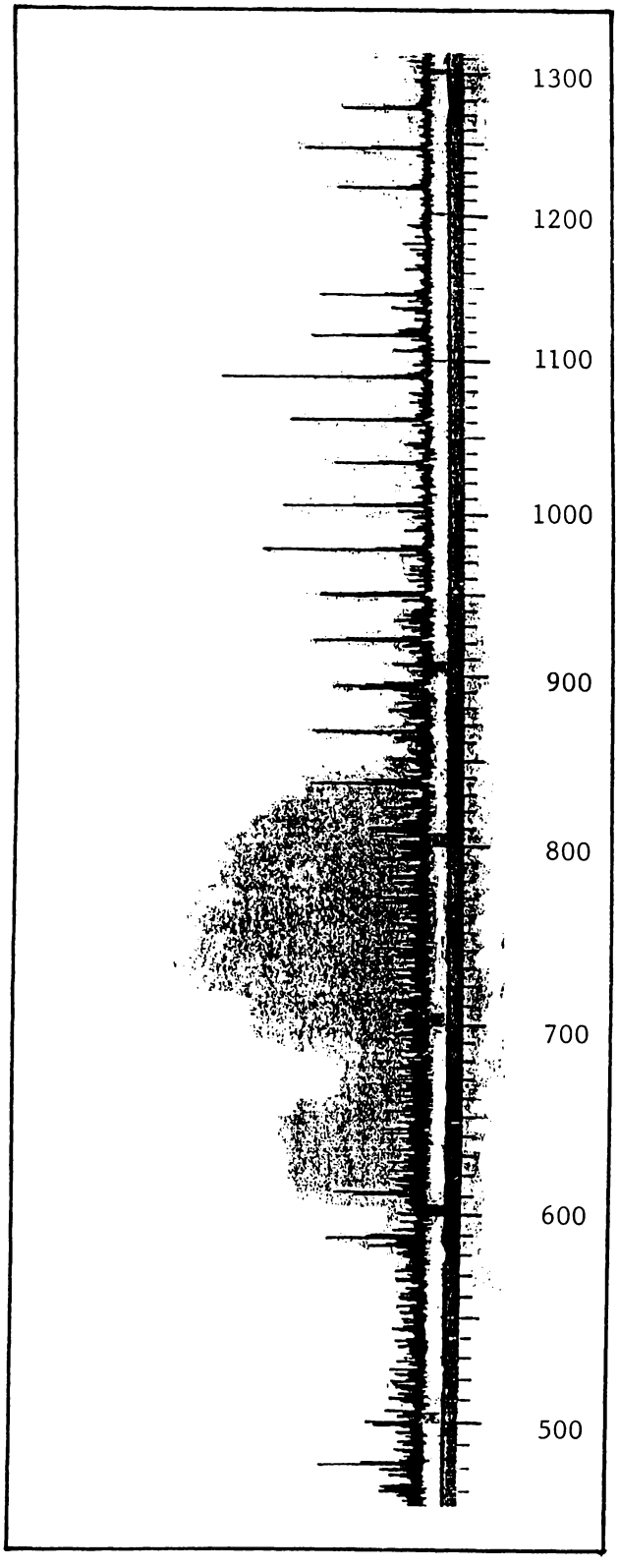

figure 3.3: FABS mass spectroscopic fragmentation pattern for $[Et_4N]_3[SiCo_9(CO)_{21}][Co(CO)_4]$ sample.

Table 3.3: FABS mass spectroscopic fragmentation pattern for $[Et_4N]_3[SiCo_9(CO)_{21}][Co(CO)_4]$ sample.

m/e	Int.	Possible Assignments		
		Fragments containing Si	Fragments contining non-carbonyl C	Other
1274	28		$[CCo_{10}(CO)_{24}]^-$	
1246	40		$[CCo_{10}(CO)_{23}]^-$	
1218	30		$[CCo_{10}(CO)_{22}]^-$	
1190	6		$[CCo_{10}(CO)_{21}]^-$	
1162	8		$[CCo_{10}(CO)_{20}]^-$	
1147	35	$[SiCo_9(CO)_{21}]^-$		
1134	13		$[CCo_{10}(CO)_{19}]^-$	
1119	38	$[SiCo_9(CO)_{20}]^-$		
1106	12		$[CCo_{10}(CO)_{18}]^-$	
1091	70	$[SiCo_9(CO)_{19}]^-$		
1078	6		$[CCo_{10}(CO)_{17}]^-$	
1063	45	$[SiCo_9(CO)_{18}]^-$		
1035	32	$[SiCo_9(CO)_{17}]^-$		
1007	47	$[SiCo_9(CO)_{16}]^-$		
1004	12	$[SiCo_8(CO)_{18}]^-$		
979	53	$[SiCo_9(CO)_{15}]^-$		
976	11	$[SiCo_8(CO)_{17}]^-$		
951	35	$[SiCo_9(CO)_{14}]^-$		
948	10	$[SiCo_8(CO)_{16}]^-$		
935	12		$[CCo_9(CO)_{14}]^-$	
923	38	$[SiCo_9(CO)_{13}]^-$		
920	10	$[SiCo_8(CO)_{15}]^-$		
907	13		$[CCo_9(CO)_{13}]^-$	
895	30	$[SiCo_9(CO)_{12}]^-$		
879	13		$[CCo_9(CO)_{12}]^-$	
864	39	$[SiCo_8(CO)_{13}]^-$		
851	13		$[CCo_9(CO)_{11}]^-$	
836	38	$[SiCo_8(CO)_{12}]^-$		
823	15		$[CCo_9(CO)_{10}]^-$	
808	20	$[SiCo_8(CO)_{11}]^-$		
792	18		$[CCo_8(CO)_{11}]^-$	
770	17		$[CCo_6(CO)_{14}]^-$	
742	18		$[CCo_6(CO)_{13}]^-$	
612	30	$[SiCo_8(CO)_4]^-$	$[CCo_4(CO)_{14}]^-$	
588	32	$[SiCo_9(CO)]^-$	$[CCo_5(CO)_{10}]^-$	
585	18	$[SiCo_8(CO)_3]^-$		
500	19	$[SiCo_8]^-$		
481	33		$[CCo_7(CO)_2]^-$	
457-459	>100	$[SiCo_3(CO)_9]^-$		$[Co_3(CO)_{10}]^-$ (Matrix)$_3^-$
453	33		$[CCo_7(CO)]^-$	
450	27		$[CCo_6(CO)_2]^-$	
435	45	$[SiCo_5(CO)_4]^-$		$[Co_5(CO)_5]^-$
351	100	$[SiCo_5(CO)]^-$		$[Co_5(CO)_2]^-$
348	30	$[SiCo_4(CO)_3]^-$		$[Co_4(CO)_4]^-$
332	20		$[CCo_4(CO)_3]^-$	
329	52		$[CCo_3(CO)_5]^-$	
317	50	$[SiCo_3(CO)_4]^-$		$[Co_3(CO)_5]^-$
304-306	>>100		$[CCo_4(CO)_2]^-$	(Matrix)$_2^-$
289	42			$[Co_3(CO)_4]^-$
276	35		$[CCo_4(CO)]^-$	
261	25	$[SiCo_3(CO)_2]^-$		$[Co_3(CO)_3]^-$
258	24	$[SiCo_2(CO)_4]^-$		$[Co_2(CO)_5]^-$

intensities differ from that of the $[SiCo_9(CO)_{21}]^-$ fragmentation products. Also, the m/e for the highest peak is not consistent with likely recombination products involving $[SiCo_9(CO)_{21}]^-$ and the matrix, a matrix fragment or a cluster fragment. This suggests that these peaks represent an impurity in the sample. The position of the highest peak (m/e = 1274) is consistent with either $[SiCo_{10}(CO)_{23}C]^-$ or $[CCo_{10}(CO)_{24}]^-$. The spectrum is too weak and not sufficiently resolved to detect whether Si is present from the isotope pattern. The formation of a $[SiCo_{10}(CO)_{23}C]^-$ species would involve the loss of an O atom from a carbonyl group. No reports of C-O cleavage ocurring in the mass spectrometer have been found in the literature and there is no evidence of an entire $[SiCo_{10}(CO)_{24}]^-$ ion in the spectrum. Therefore this peak has been assigned to $[CCo_{10}(CO)_{24}]^-$, present as an impurity. Peaks consistent with fragments containing non-carbonyl C atoms can be seen throughout the spectrum.

The exceptionally strong peaks at m/e = 306 and 459 appear to represent the association of two and three matrix molecules (as indicated in the table). These were also seen in other negative ion FABS mass spectra.

3.2.1.2 Characterisation of $[CCo_8(CO)_{18}]^{2-}$

Another product, apparently more soluble in CH_2Cl_2, has previously been isolated from the $[SiCo_9(CO)_{21}]^{2-}$ synthesis in very low concentrations following successive crystallisations of $[Et_4N]_3[SiCo_9(CO)_{21}][Co(CO)_4]$. This product was tentatively characterised as $[SiCo_8(CO)_{18}]^{2-}$, on the basis of its carbonyl infrared spectrum in CH_2Cl_2. In the current investigation, this compound was again isolated and identified as $[CCo_8(CO)_{18}]^{2-}$ ***(F 11)***.

$[Et_4N]_2[CCo_8(CO)_{18}]$

$[Et_4N]_2[CCo_8(CO)_{18}]$ was isolated from the products of the $[Et_4N]_3[SiCo_9(CO)_{21}][Co(CO)_4]$ preparation. Infrared spectra were obtained in CH_2Cl_2 and THF. These are comparable with the spectrum reported for $[CCo_8(CO)_{18}]^{2-}$ **(table 3.4)**.

Attempts were made to grow crystals suitable for X-ray diffraction studies by cooling a CH_2Cl_2 solution and by slow diffusion of hexane into a CH_2Cl_2 solution at 4°C. In the latter case, brown crystals formed which were extremely thin (almost transparent) in one dimension.

Table 3.4: Infrared Spectra of $[CCo_8(CO)_{18}]^{2-}$

$[CCo_8(CO)_{18}]^{2-}$ (in THF) [9]	Observed Spectra (in THF)	(in CH_2Cl_2)
2055vw	2050w	2043w
1990vs	1990s	1990s,br
1950w	1950sh	1950sh
1810m	1808w,br	1790w,br

This made them almost impossible to handle and unsuitable for crystallography.

Co was the only element detected when two crystals were analysed using electron probe analysis. However this is not unambiguous as the detection of Si is approaching the limit of this technique. Si may have been present even though it was not detected.

$[PPN]_2[CCo_8(CO)_{18}]$

This anion was also isolated as the $[PPN]^+$ salt, following successive recrystallisations of $[PPN]_2[SiCo_9(CO)_{21}]$. An attempt was made at growing crystals by cooling a CH_2Cl_2 solution and by slow diffusion of hexane into a CH_2Cl_2 solution at *ca.* -17°C. Brown plate-like crystals were obtained by the latter method. A sample of these was used for FABS mass spectroscopy.

The mass spectrum was very weak but showed a distinct series of successively decarbonylated ions in the high mass region (table 3.5). The highest of these (m/e = 960) could be attributed to $[CCo_8(CO)_{17}]^-$. It is not unusual in mass spectra of transition metal carbonyl compounds for the highest ion to be the parent minus a CO group. On this basis, the sample was identified as $[PPN]_2[CCo_8(CO)_{18}]$.

A suitable crystal was sealed in a glass capilliary and a preliminary X-ray diffraction study was made. A triclinic unit cell was found, for which $P\bar{1}$ is the most common space group.The density was

Table 3.5: FABS Mass Spectrum of $[CCo_8(CO)_{18}]^{2-}$ (high mass region)

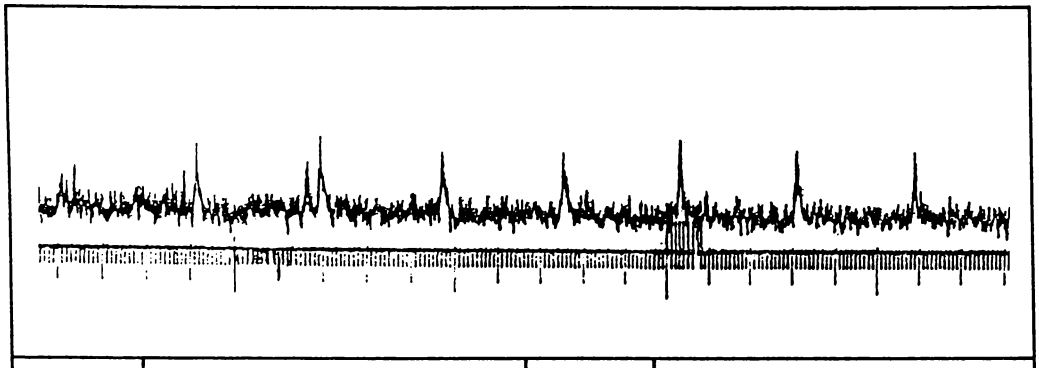

m/e	Possible Assignment	m/e	Possible Assignment
960	$[CCo_8(CO)_{17}]^-$	817	$[CCo_7(CO)_{14}]^-$
932	$[CCo_8(CO)_{16}]^-$	792	$[CCo_8(CO)_{11}]^-$
904	$[CCo_8(CO)_{15}]^-$	789	$[CCo_7(CO)_{13}]^-$
876	$[CCo_8(CO)_{14}]^-$	764	$[CCo_8(CO)_{10}]^-$
848	$[CCo_8(CO)_{13}]^-$	761	$[CCo_7(CO)_{12}]^-$
820	$[CCo_8(CO)_{12}]^-$		

assumed to be *ca.* 1.46 g cm^{-3}, by comparison with $[PPN]_2[Ni_5(CO)_{12}]$ [193].

$$a = 15.56\ \text{Å} \qquad \alpha = 93.47°$$
$$b = 11.94\ \text{Å} \qquad \beta = 91.10°$$
$$c = 25.91\ \text{Å} \qquad \gamma = 107.89°$$
$$U = 4568\ \text{Å},\ M_r = 4018/z$$

For the $P\bar{1}$ space group Z usually equals 2. This would indicate a molecular weight of 2009, which is reasonably consistent with $[PPN]_2[CCo_8(CO)_{18}]$ (M_r = 2064.55). Full X-ray crystallographic characterisation was not pursued.

Crystals of the $[PPN]^+$ salt were also used for cyclic voltammetric studies (see chapter five). The voltammograms obtained were also consistent with what has previously been reported for the

$[CCo_8(CO)_{18}]^{2-}$ dianion.

3.2.1.3 Characterisation of $[Et_4N][Cl_2SiCo_7(CO)_{21}]$

$[Et_4N][Cl_2SiCo_7(CO)_{21}]$ (figure 3.5) was isolated as a side product from one particular preparation of $[Et_4N]_3[SiCo_9(CO)_{21}][Co(CO)_4]$.

The Cl atoms in $[Cl_2SiCo_7(CO)_{21}]^-$ must be derived from Et_4NCl present as an impurity in the $[Et_4N][Co(CO)_4]$. At the time it was suspected that some Et_4NCl was present in the sample because of the relatively low solubility of the "$[Et_4N][Co(CO)_4]$" in CH_2Cl_2.

Relatively pure $[Et_4N][Cl_2SiCo_7(CO)_{21}]$ was extracted in diethyl ether from the other products of the reaction, following the removal of $Co_4(CO)_{12}$ in hexane. Rectangular black plate-like crystals were obtained by slow diffusion of hexane into the diethyl ether solution at 4°C. A suitable crystal was used for full X-ray crystallographic characterisation.

Electron probe analysis of sample crystals indicated a Cl : Si : Co ratio of 1.7 : 1.5 : 7 (table 3.6). This is reasonably consistent with the $[Cl_2SiCo_7(CO)_{21}]^-$ formulation. Four different shaped crystals were analysed, all giving similar values. This confirmed that $[Et_4N][Cl_2SiCo_7(CO)_{21}]$ comprises at least a large part of the ether-soluble fraction.

Table 3.6: Electron Probe Analysis of $[Et_4N][Cl_2SiCo_7(CO)_{21}]$

ELEMENT	SHELL	WEIGHT %	ATOMIC %
Cl	K	11.7	16.6
Si	K	8.1	14.5
Co	K	80.2	68.9

Infrared Spectrum

The infrared spectrum of $[Et_4N][Cl_2SiCo_7(CO)_{21}]$ (shown in figure 3.4) exhibits seven peaks in the carbonyl stretching region (ν_{CO} (CH_2Cl_2) 2099vw, 2070w, 2048vs, 2026s, 2004m, 1865vw, 1824w cm^{-1}). The two weak peaks at 1865 and 1824 cm^{-1} can be assigned to bridging

carbonyl stretching modes, and the remaining five peaks to terminal carbonyl vibrations. In the solid state, the overall symmetry of the anion is very low (C_1), and in solution the symmetry is unlikely to be any higher. Therefore one might expect to see up to 16 infrared active terminal CO stretching modes, with an additional 3 for the bridging CO's. It is obvious that the observed spectrum is far simpler than this, and it is probably best to regard the two ends of the anion as independent. In table 3.7, the infrared spectrum of $[Et_4N][Cl_2SiCo_7(CO)_{21}]$ is compared with spectra of anionic monosubstituted derivatives of $Co_4(CO)_{12}$, and with spectra of clusters containing a μ_3-$CCo_3(CO)_9$ moiety. The $[Et_4N][Cl_2SiCo_7(CO)_{21}]$ infrared peaks at 2070, 2026, 2004 and 1824 cm^{-1} can clearly be assigned to the $-Co_4(CO)_{11}$ portion of the cluster. The remaining terminal carbonyl stretches, along with a component of the 2026 cm^{-1} peak, correspond quite closely with those reported for $Cl_3SiOCCo_3(CO)_9$ and $Br_3SiOCCo_3(CO)_9$. Note that a much closer correlation is observed with the spectrum of the neutral $PhCCo_3(CO)_9$ compound than with that of the $[PhCCo_3(CO)_9]^-$ anion. On the other hand, the carbonyl stretches attributed to the $-Co_4(CO)_{11}$ end of the cluster closely resemble those of anionic $[Co_4(CO)_{11}X]^-$ compounds. This suggests that the charge is localised mainly within the $-Co_4(CO)_{11}$ group.

$[GeCo_7(CO)_{20}]^-$ *(F 8)* also contains both a $-Co_4(CO)_{11}$ and a triply bridged $Co_3(CO)_9$ moiety. For $[GeCo_7(CO)_{20}]^-$, peaks equivalent to the two weak high frequency stretching modes of $[Et_4N][Cl_2SiCo_7(CO)_{21}]$ were not reported. It also appears that the 2026 cm^{-1} peak has been split into its $-Co_4(CO)_{11}$ and $Co_3(CO)_9$ components.

X-ray Crystallographic Study of $[Et_4N][Cl_2SiCo_7(CO)_{21}]$

The crystal of $[Et_4N][Cl_2SiCo_7(CO)_{21}]$ obtained as described above, was coated in araldite. Preliminary precession photographs using Cu-Kα radiation indicated that the crystal had monoclinic symmetry, and belonged to the non-standard $P2_1/n$ space group (a special setting of $P2_1/c$). This was confirmed by successful solution. Intensity data were collected for 5251 unique reflections, for which $4°<2\theta<45°$, on a Nicolet diffractometer at the University of Canterbury. Of these 2626 had $I>3\sigma(I)$ and were employed in all calculations. Mo-Kα radiation and a θ-2θ scan technique were used. Standard reflections monitored at

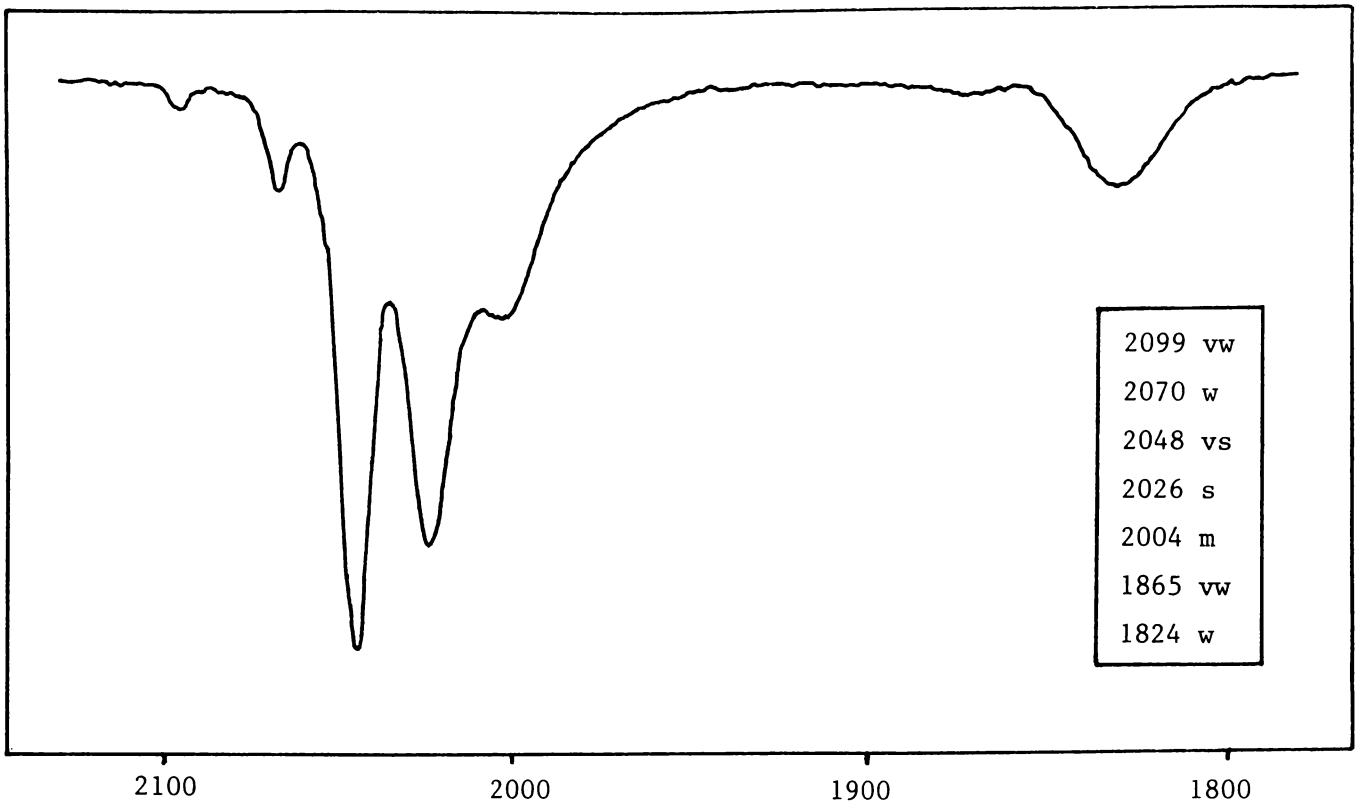

Figure 3.4: Infrared spectrum of $[Et_4N][Cl_2SiCo_7(CO)_{21}]$ (CH_2Cl_2 solution)

Table 3.7: Infrared spectrum of $[Et_4N][Cl_2SiCo_7(CO)_{21}]$ compared with spectra reported for $[Co_4(CO)_{11}Y]^-$ and $YCo_3(CO)_9$ species.

$[Co_4(CO)_{11}Y]^-$		$[Cl_2SiCo_7(CO)_{21}]^-$	$[GeCo_7(CO)_{20}]^-$	$X_3SiOCCo_3(CO)_9$		$PhCCo_3(CO)_9$	$[PhCCo_3(CO)_9]^-$*
Y = COMe [196]	Y = I [198]		[32]	X = Cl [211]	X = Br [93]	[192]	[204]
		2099vw		2104w	2105w	2101m	~2044w
2057w	2070vw	2070w					
		2048vs	2054s	2056s	2061vs	2054vs	~1992vs
2010vs	2020s	2026s	2033s 2028s	2040s	2040vs	2039s	~1974s
1986s	2000sh	2004m	1990w	2020w	2025m,sh	2020w	~1948vw
					1982w		
		1865vw					
1818m	1835ms	1824w	1825w				

* Numerical values were not reported. Peak positions were inferred from a reproduction of the infrared spectrum and from comments made in reference [204]

regular intervals showed that no crystal decomposition had occured. Lattice dimensions were obtained from 22 high-angle reflections

Data were corrected for Lorentz polarisation effects, and for absorption by an ϕ-scan technique (transmission factors, 0.942 maximum and 0.555 minimum).

Table 3.8: Crystal Data for $[Et_4N][Cl_2SiCo_7(CO)_{21}]$

Formula: $C_{29}H_{20}Co_7Cl_2NO_{21}Si$	
Mr = 1229.99	
Monoclinic space group $P2_1/n$ (Non-std $P2_1/c$)	
a = 9.110(4) Å	
b = 22.472(9) Å	β = 95.28(4)°
c = 21.01(1) Å	
U = 4284(3) Å^3	D_{calc} = 1.91 g cm^{-3}
Z = 4	
F(000) = 2424	μ(Mo-Kα) = 29 cm^{-1}
T = 148 K	λ(Mo-Kα) = 0.71073 Å
Crystal dimensions: 0.76 x 0.34 x 0.02 mm	

The coordinates of the 7 Co atoms and the Si atom were obtained using the TREF routine of SHELXS86. Subsequent difference maps located the Si, Cl, C, N and O atoms. In the final cycles of full-matrix least-squares refinement, the Co atoms were assigned anisotropic temperature factors and the H atoms were included in calculated positions. The refinement converged to R = 0.0595, R_w = 0.0573 with 8.5 reflections per parameter and $w = 1.6334(\sigma^2(F) + 0.000852F^2)^{-1}$. The positional parameters were obtained from this refinement cycle. The final difference map revealed no electron density greater than 0.8 e Å^{-3}.

Positional and thermal parameters and tables of calculated and observed structure factors are given in the Appendix **B**.

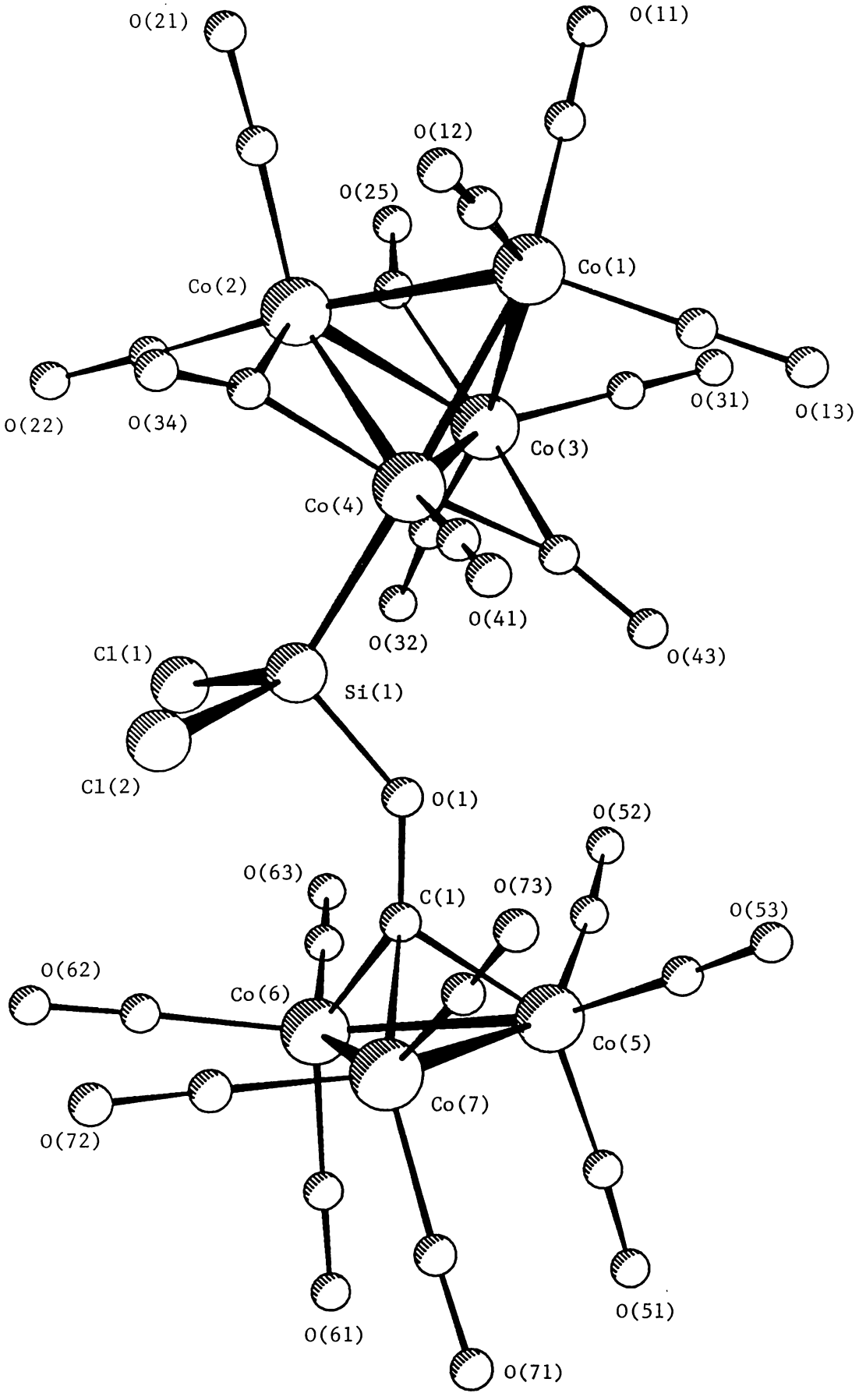

Figure 3.5: Crystal structure of $[Cl_2SiCo_7(CO)_{21}]^-$

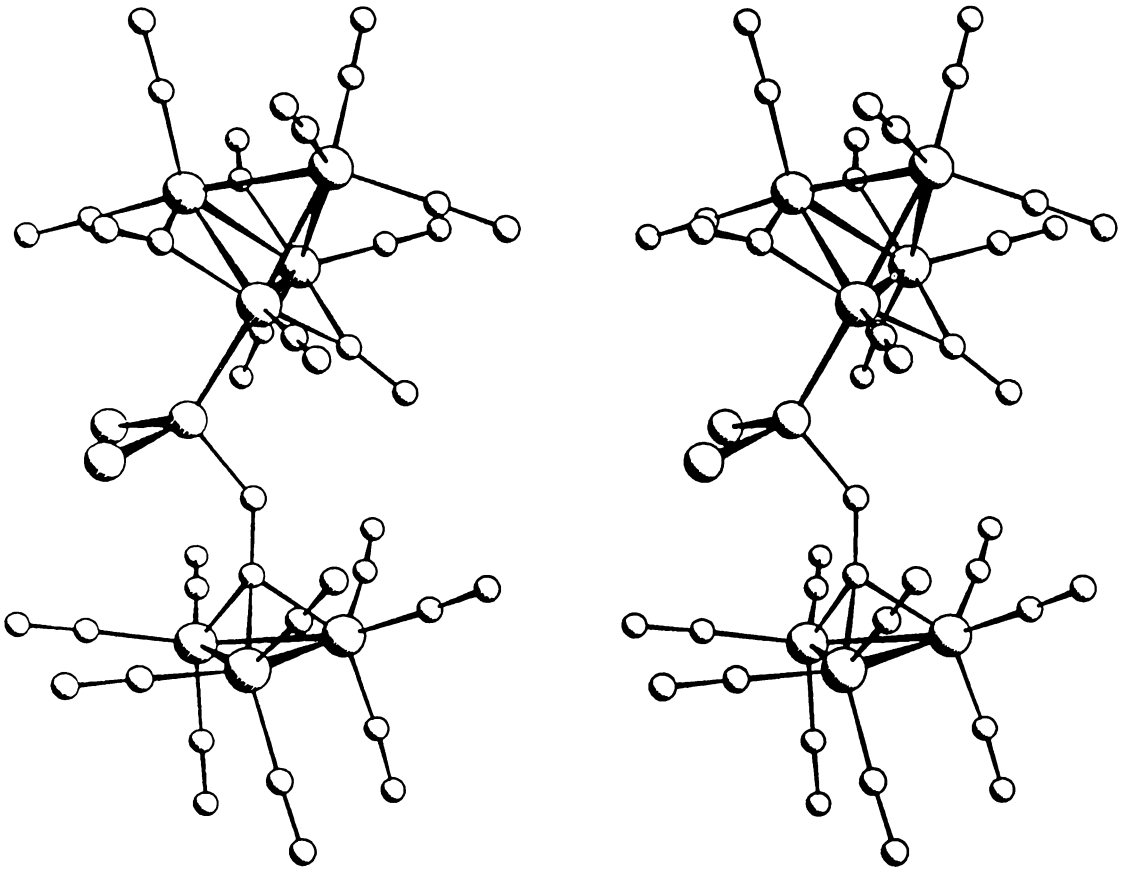

Figure 3.6: Stereo view of $[Cl_2SiCo_7(CO)_{21}]^-$

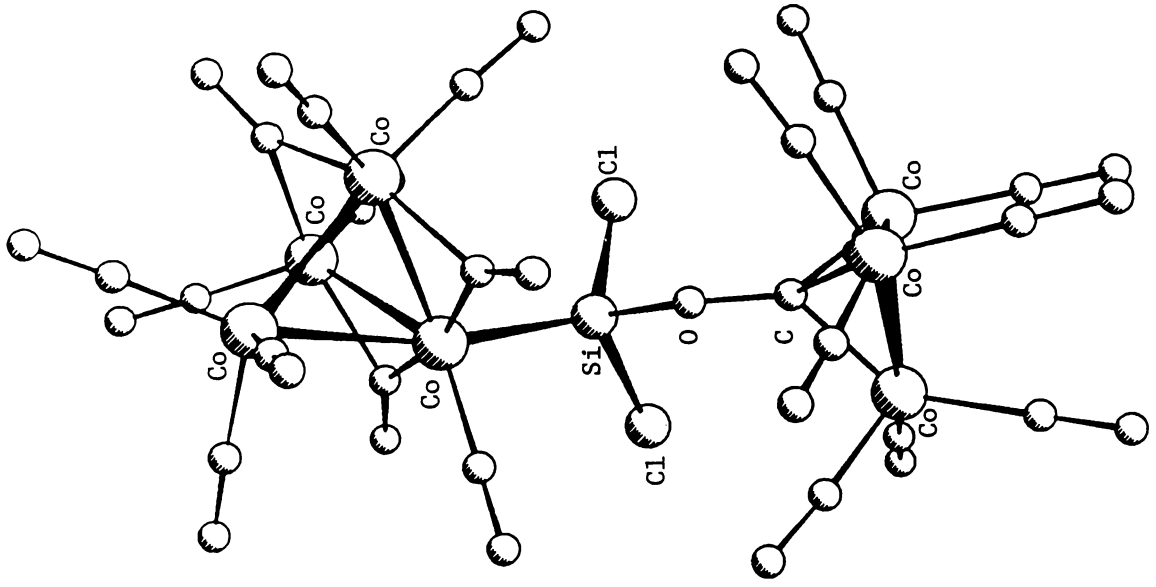

Figure 3.7: Another perspective of $[Cl_2SiCo_7(CO)_{21}]^-$

3.2.1.4 Structure of $[Et_4N][Cl_2SiCo_7(CO)_{21}]$

The $[Cl_2SiCo_7(CO)_{21}]^-$ cluster essentially consists of $Co_4(CO)_{12}$ with a terminal CO group replaced by a $-Si(Cl)_2-$ unit which is also bound to the O atom on a CO group, triply bridging a $Co_3(CO)_9$ moiety. Perspective diagrams of the anion are shown in **figures 3.5, 3.6,** and **3.7.** The atom numbering system employed in **figure 3.5** is used throughout this discussion. Selected bond lengths and bond angles are presented in **tables 3.9** and **3.10** respectively.

The $-Co_4(CO)_{11}$ portion of the $[Cl_2SiCo_7(CO)_{21}]^-$ cluster adopts the C_{3v} configuration of $Co_4(CO)_{12}$, with three μ_2-CO groups which bridge the edges of a Co_3 triangle. This basal triangle is capped by an apical Co atom with all-terminal carbonyls. The Co_{basal}-Co_{basal} and Co_{basal}-Co_{apical} bonds are comparable in length with the appropriate bonds in related compounds, and the overall mean Co-Co length within the tetrahedron is almost identical to that in $Co_4(CO)_{12}$ (see **table 3.11**).

In $[Cl_2SiCo_7(CO)_{21}]^-$, the $-Si(Cl)_2OCCo_3(CO)_9$ group is coordinated to a basal cobalt atom, Co(4) in an axial position; approximately *trans* to the apical Co. The longest Co-Co bond (2.529(3) Å) is that located *trans* to the Si-Co bond. The presence of the $-Si(Cl)_2OCCo_3(CO)_9$ substituent also induces significant

Table 3.9: Selected Bond Lengths for $[Et_4N][Cl_2SiCo_7(CO)_{21}]$ (Å)

Co(1) ---Co(2)	2.520(3)	Co(4) ---Si(1)	2.215(5)
Co(1) ---Co(3)	2.517(3)	Si(1) ---Cl(1)	2.088(6)
Co(1) ---Co(4)	2.529(3)	Si(1) ---Cl(2)	2.099(7)
Co(2) ---Co(3)	2.466(3)	Si(1) ---O(1)	1.67(1)
Co(2) ---Co(4)	2.466(3)	O(1) ---C(1)	1.30(2)
Co(3) ---Co(4)	2.445(3)	Co(5) ---C(1)	1.93(2)
Co(5) ---Co(6)	2.477(3)	Co(6) ---C(1)	1.89(2)
Co(5) ---Co(7)	2.477(3)	Co(7) ---C(1)	1.91(2)
Co(6) ---Co(7)	2.494(3)		

Table 3.10: Selected Bond Angles for $[Et_4N][Cl_2SiCo_7(CO)_{21}]$ (degrees)

Co(2) -Co(1) -Co(3)	58.6(1)	Co(2) -Co(1) -Co(4)	58.5(1)
Co(3) -Co(1) -Co(4)	57.9(1)	Co(1) -Co(2) -Co(3)	60.6(1)
Co(1) -Co(2) -Co(4)	60.9(1)	Co(3) -Co(2) -Co(4)	59.4(1)
Co(1) -Co(3) -Co(2)	60.7(1)	Co(1) -Co(3) -Co(4)	61.3(1)
Co(2) -Co(3) -Co(4)	60.3(1)	Co(1) -Co(4) -Co(2)	60.6(1)
Co(1) -Co(4) -Co(3)	60.8(1)	Co(1) -Co(4) -Si(1)	166.5(2)
Co(2) -Co(4) -Co(3)	60.3(1)	Co(2) -Co(4) -Si(1)	110.3(2)
Co(3) -Co(4) -Si(1)	106.5(2)	Co(6) -Co(5) -Co(7)	60.5(1)
Co(6) -Co(5) -C(1)	48.9(5)	Co(7) -Co(5) -C(1)	49.4(5)
Co(5) -Co(6) -Co(7)	59.8(1)	Co(5) -Co(6) -C(1)	50.3(5)
Co(7) -Co(6) -C(1)	49.2(5)	Co(5) -Co(7) -Co(6)	59.8(1)
Co(5) -Co(7) -C(1)	50.2(5)	Co(6) -Co(7) -C(1)	48.7(5)
Co(4) -Si(1) -Cl(1)	119.6(3)	Co(4) -Si(1) -Cl(2)	116.4(2)
Co(4) -Si(1) -O(1)	111.2(4)	Cl(1) -Si(1) -Cl(2)	101.8(3)
Cl(1) -Si(1) -O(1)	102.8(4)	Cl(2) -Si(1) -O(1)	102.9(5)
Si(1) -O(1) -C(1)	140(1)	Co(5) -C(1) -Co(6)	80.8(7)
Co(5) -C(1) -Co(7)	80.4(7)	Co(5) -C(1) -O(1)	124(1)
Co(6) -C(1) -Co(7)	82.1(7)	Co(6) -C(1) -O(1)	136(1)
Co(7) -C(1) -O(1)	132(1)		

asymmetry in the two carbonyls which bridge to the Si-bonded Co atom. These two bridging carbonyls are displaced towards the substituted metal centre, while the third bridging carbonyl remains reasonably symmetric:

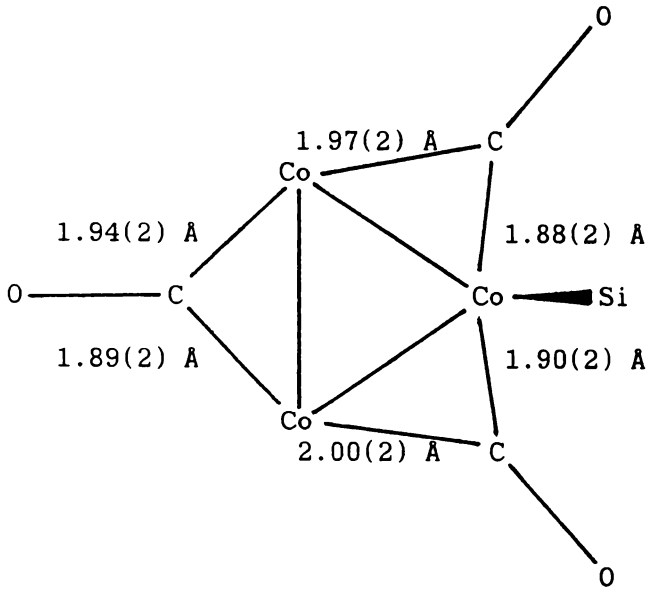

Most of the monosubstituted derivatives of $Co_4(CO)_{12}$, for which structures have been reported, adopt the same configuration with substitution occuring at the apical position on a basal Co (eg. $Co_4(CO)_{11}PR_3$, where R = Ph, Me [194,195]; and $[Co_4(CO)_{11}X]^-$, where X = COMe, COOMe [196,197]). The exception is $[Co_4(CO)_{11}I]^-$ [198], in which the iodine is attached to the apical Co atom, although a small amount of the basal isomer was detected in the crystal.

Table 3.11: Comparative Bond Distances in $Co_4(CO)_{12}$ and its Monosubstituted Derivatives

Co-Co bond	$[Cl_2SiCo_7(CO)_{21}]^-$	$Co_4(CO)_{12}$	$Co_4(CO)_{11}X$		$[Co_4(CO)_{11}X]^-$	
			X = PPh_3	X = PMe_3	X = I	X = COMe
ba-ax	2.522		2.530	2.565	2.52	2.562
ba-ba	2.459		2.482	2.480	2.47	2.461
mean	2.491	2.492	2.506	2.522	2.493	2.512

For $[Co_4(CO)_{11}I]^-$, the greater electronegativity of I appears to be the factor favouring apical substitution. Strong σ-donors prefer coordination to the basal Co atoms where more carbonyl groups are available to distribute the excess charge.

The three Co atoms at the other end of the $[Cl_2SiCo_7(CO)_{21}]^-$ cluster, form an almost regular triangle. The interatomic distances and angles of the $-OCCo_3(CO)_9$ moiety are comparable with those found in other oxymethylidine clusters of this type (eg. $Et_3NB(H)_2OCCo_3(CO)_9$ [199], $Et_3NB(Cl)_2OCCo_3(CO)_9$ [200], $Cp_2Ti(Cl)OCCo_3(CO)_9$ [201] and $(CO)_4CoSi(Cl)_2OCCo_3(CO)_9$ [202]). The C(1)-O(1) and Si(1)-O(1) bonds are both relatively short (1.30(2) Å and 1.67(1) Å respectively) , suggesting some form of delocalised π-bonding. The Si(1)-O(1)-C(1) angle of 140(1)° is also very large, but this is probably due to steric repulsion between the bulky groups at either end of the Si-O-C linkage.

Bonding about the Si atom is essentially tetrahedral, although the the bulkiness of the $Co_4(CO)_{11}$ group causes some distortion. The mean Si-Cl bond length (2.094 Å) approximates the sum of the covalent radii of Si and Cl (1.12 and 0.99 Å, respectively). The Si-Co bond, however, is surprisingly short (2.215(5) Å). This compares with Si-Co bond lengths of 2.249(8) and 2.254(3) Å in $(CO)_4CoSi(Cl)_2OCCo_3(CO)_9$ and $(CO)_4CoSiCl_3$ respectively.

For the terminal carbonyl groups, the M-C and C-O bond lengths range from 1.75(2) to 1.82(2) Å and from 1.12(2) to 1.18(2) Å respectively. While the Co-C bond distances for terminal carbonyls coordinated to the basal Co_3 triangle in the $Co_4(CO)_{11}$ moiety lie to the short end of the Co-C range, these are not significantly different from the other Co-C bond lengths.

3.2.2 REACTIONS OF $SiCo_4(CO)_x$

3.2.2.1 $(CO)_4CoSiCo_3(CO)_9$ and $[Fe_2(CO)_8]^{2-}$

$(CO)_4CoSiCo_3(CO)_9$ (0.30 g, 0.48 mmol) was stirred at room temperature with $[Et_4N]_2[Fe_2(CO)_8]$ (0.28 g, 0.48 mmol) in 20 ml of CH_2Cl_2 under a nitrogen atmosphere. The infrared spectrum of $[Et_4N]_2[Fe_2(CO)_8]$ as a nujol mull [203] contains two broad bands in the carbonyl stretching region (1920s,br, 1852s,br cm^{-1}) each having several shoulders. However $[Et_4N]_2[Fe_2(CO)_8]$ is only slightly soluble in CH_2Cl_2 and these peaks could not be observed. The $(CO)_4CoSiCo_3(CO)_9$ ν_{CO} infrared peaks at 2085 and 2043 cm^{-1} were therefore used to monitor

the reaction.

A rapid reaction occurred during which the purple solution became brown. After 10 minutes the $(CO)_4CoSiCo_3(CO)_9$ infrared bands had disappeared, and an infrared spectrum showed peaks at 2060w, 2023vs, 1996s, 1889m cm^{-1}.

The solution was filtered through a glass frit and the solvent was removed under vacuum. An initial extraction in hexane (40 ml) contained mainly $Co_4(CO)_{12}$, with weak peaks at 2023 and 2000 cm^{-1}. These latter peaks diminished in intensity when the sample was placed under vacuum. They also appeared to be associated with a yellow product which collected in the muck trap. This product was identified as $Fe(CO)_5$ (ν_{CO} (hexane) 2022s, 2003s, 1997s, 1964w cm^{-1}; ν_{CO} (CH_2Cl_2) 2020s, 1994s,br cm^{-1}).

An infrared spectrum of the ether soluble fraction showed peaks at 2064vw, 2004vs, 1969w, 1928w, 1812w cm^{-1}. This product was identified as $[Et_4N][FeCo_3(CO)_{12}]$ (figure 3.8). The observed infrared spectrum is compared with that reported for $[Et_4N][FeCo_3(CO)_{12}]$ in table 3.12.

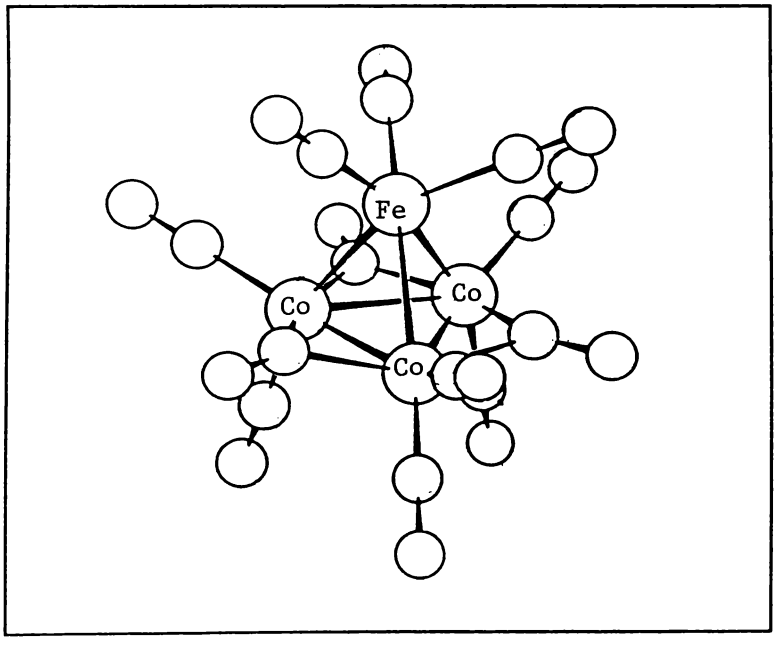

Figure 3.8: Structure of $[FeCo_3(CO)_{12}]^-$

The remaining products, not soluble in ether, were redissolved in CH_2Cl_2. An infrared spectrum showed a very strong $[Co(CO)_4]^-$ band at

Table 3.12: Infrared Spectra of $[FeCo_3(CO)_{12}]^-$

Observed Spectrum (in CH_2Cl_2)	$[FeCo_3(CO)_{12}]^-$ (in MeCN) [205]
2064vw	2066w
2004vs	2008s
1969w	1974m
1928w	1932m
1812w	1815m

1889 cm^{-1}, and weak peaks at 2004 and 1790 cm^{-1}. The latter peaks were attributed to $[SiCo_9(CO)_{21}]^{2-}$ (ν_{CO} (CH_2Cl_2) 2054w, 2004s,br, 1955br,sh, 1791w,br cm^{-1} [132]).

3.2.2.2 $(CO)_4CoSiCo_3(CO)_9$ and $[Et_4N][Mn(CO)_5]$

$(CO)_4CoSiCo_3(CO)_9$ (0.225 g, 0.35 mmol) was added to $[PPN][Mn(CO)_5]$ (0.262 g, 0.36 mmol) in CH_2Cl_2 (60 ml) and stirred under nitrogen atmosphere. A rapid reaction ensued during which the $[Mn(CO)_5]^-$ infrared peaks at 1894 cm^{-1} and 1856 cm^{-1} disappeared, to be replaced by a strong $[Co(CO)_4]^-$ peak at 1889 cm^{-1} plus a peak at 2011 cm^{-1} with a shoulder at 1981 cm^{-1}. The three prominent $(CO)_4CoSiCo_3(CO)_9$ infrared bands at 2087s, 2047vs, 2031s cm^{-1} also shifted slightly to lower frequencies. After 15 min the reaction appeared to have gone to completion. The solution was stirred for a further 20 min with no apparent change.

The solution was filtered through a glass frit and the CH_2Cl_2 solvent removed under vacuum. Two 40 ml hexane extracts were combined and the solvent removed under vacuum. A cold finger containing continuously running water was inserted into the Schlenk flask and $Mn_2(CO)_{10}$ (0.004 g, 0.010 mmol, 6% of Mn) was removed by sublimation over 6 h, under continuous vacuum at room temperature. An infrared spectrum of the remaining hexane fraction contained very weak bands characteristic of $Co_4(CO)_{12}$, plus another product with peaks at 2115w, 2077m, 2044s, 2024m cm^{-1} (figure 3.9). This compound was identified as

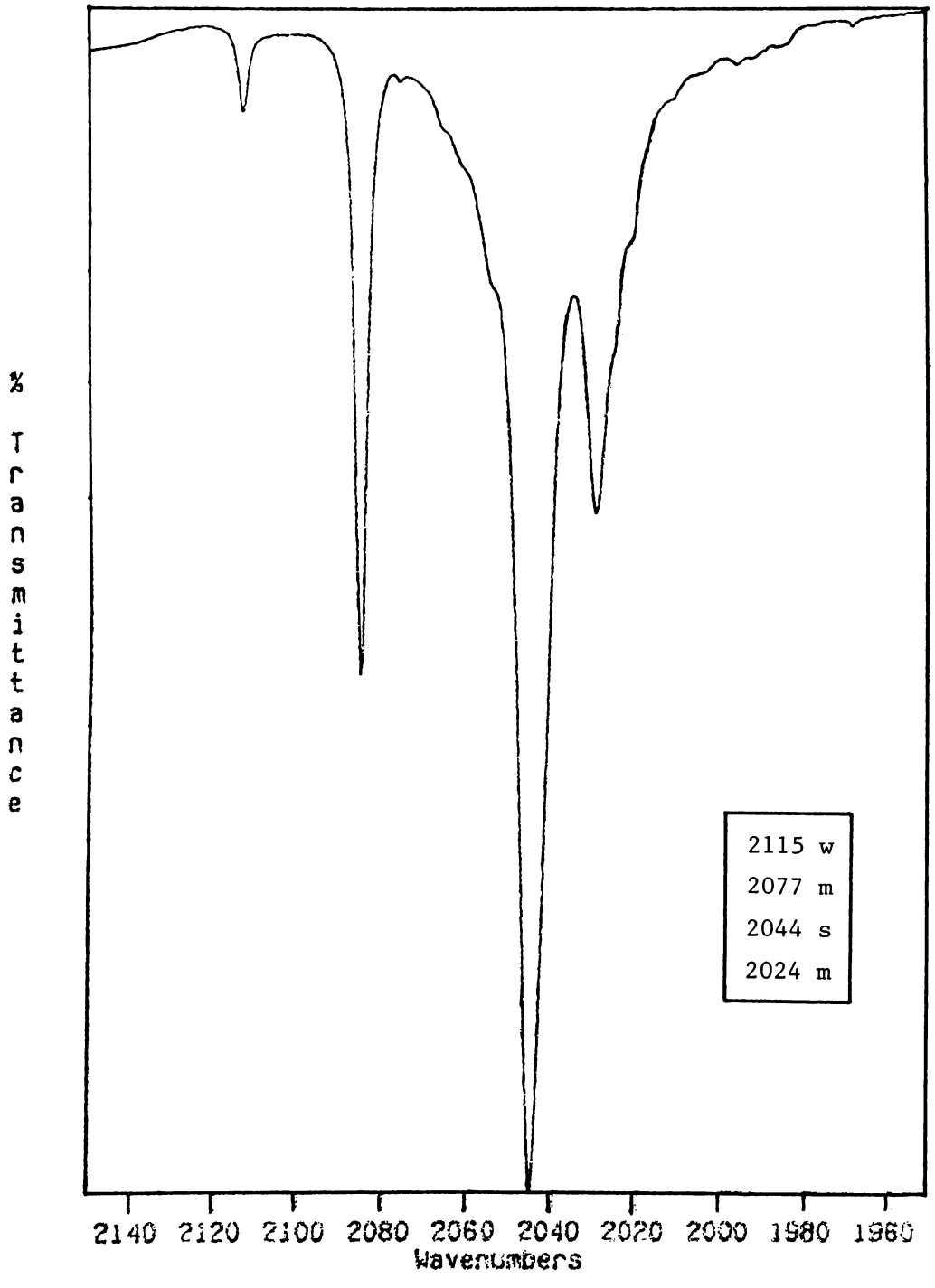

Figure 3.9: Infrared spectrum of $(CO)_5MnSiCo_3(CO)_9$ (hexane solution)

$(CO)_5MnSiCo_3(CO)_9$ *(F 5)* (0.098 g, 0.15 mmol, 42% of Mn, 31% of Co) on the basis of its infrared spectrum and FABS mass spectrum (shown below). The cyclic voltammogram of this compound, included in chapter five, is also consistent with this assignment.

A positive-ion FABS mass spectrum was obtained using a crystalline sample of this compound. The highest peak (m/e = 624) is consistent with the $[SiCo_3Mn(CO)_{13}]^+$ ion. That is, the parent minus a carbonyl group. As already mentioned, this is not uncommon.

Table 3.13: FABS Mass Spectrum of $(CO)_5MnSiCo_3(CO)_9$

m/e	Int.	Possible Assignments
624	8	$[SiCo_3Mn(CO)_{13}]^+$
596	42	$[SiCo_3Mn(CO)_{12}]^+$
568	27	$[SiCo_3Mn(CO)_{11}]^+$
540	20	$[SiCo_3Mn(CO)_{10}]^+$
512	15	$[SiCo_3Mn(CO)_9]^+$
484	14	$[SiCo_3Mn(CO)_8]^+$
205	25	$[SiCo_3]^+$, $[Co_3(CO)]^+$
202	22	$[SiCo_2(CO)_2]^+$, $[Co_2(CO)_3]^+$
167	100	$[SiMn(CO)_3]^+$, $[Mn(CO)_4]^+$

An ether extract (80 ml) from the hexane-insoluble products (0.104 g) showed infrared bands at 2096vw, 2066vw, 2007s, 1978sh, 1935w,br, 1823w,br cm^{-1}, with a peak at 1989 cm^{-1} representing $[Co(CO)_4]^-$. An attempt was made to grow crystals by slow diffusion of hexane into a diethyl ether solution at 4°C. The product came down as an oily red residue, from which one red rhombohedral-shaped crystal was retrieved.

This crystal was coated in araldite and used for preliminary X-ray diffraction studies. A triclinic unit cell was detected, for which $P\bar{1}$ is the most common space group. The density was assumed to be *ca.*

1.68 g cm^{-3}, by comparison with $[PPN][NCo_6(CO)_{18}]$ (see below).

a = 14.08 Å	α = 108.25°
b = 38.19 Å	β = 91.06°
c = 9.35 Å	γ = 98.05°
U = 4719 $Å^3$,	M_r = 4775/Z

For the $P\bar{1}$ space group it is most common for Z to equal 2. This would suggest a molecular weight of 2387.

Unfortunately, this crystal decomposed before it could be used for full crystallographic characterisation. Despite many attempts, further crystals could not be grown.

The remaining products, not soluble in ether (0.262 g) were redissolved in CH_2Cl_2. An infrared spectrum revealed mainly $[Co(CO)_4]^-$ (*ca.* 0.39 mmol, 27% of Co) with very weak peaks at 2000 and 1790 cm^{-1}, probably due to $[SiCo_9(CO)_{21}]^{2-}$ ***(F 12)***.

3.2.2.3 $(CO)_4CoSiCo_3(CO)_9$ and $[Et_4N]_2[Co_6(CO)_{15}]$

$(CO)_4CoSiCo_3(CO)_9$ (0.048 g, 0.076 mmol) was added to a solution of $[Et_4N]_2[Co_6(CO)_{15}]$ (0.079 g, 0.076 mmol) in CH_2Cl_2 (30 ml) and stirred under a nitrogen atmosphere. The reaction was monitored using infrared spectroscopy.

No change was detected in the infrared spectrum of the reaction mixture over 24 h. The solution was heated to 35-40°C using an oil bath. A reaction proceeded slowly with infrared peaks emerging at 2054 cm^{-1} and 2004 cm^{-1}. After 20 h the distinctive $(CO)_4CoSiCo_3(CO)_9$ peak at 2047 cm^{-1}, and the $[Co_6(CO)_{15}]^{2-}$ peak at 1980 cm^{-1} were no longer evident. The reaction mixture was filtered and the products worked up.

An initial extraction in hexane (50 ml) was found to contain $Co_4(CO)_{12}$ (0.023 g, 0.040 mmol, 21% of Co). The remaining products (0.084 g) were dissolved in CH_2Cl_2. An infrared spectrum contained bands characteristic of $[SiCo_9(CO)_{21}]^{2-}$ and $[Co(CO)_4]^-$.

3.2.2.4 $Si[Co_2(CO)_7]_2$ and $[Fe(CO)_3NO]^-$

$Si[Co_2(CO)_7]_2$ was reacted with the $[Et_4N]^+$ and $[PPN]^+$ salts of

$[Fe(CO)_3NO]^-$:

(i) $Si[Co_2(CO)_7]_2$ (0.231 g, 0.35 mmol) was stirred under nitrogen with $[PPN][Fe(CO)_3NO]$ (0.094 g, 0.31 mmol) in CH_2Cl_2 (30 mmol). Infrared specroscopy was used to monitor the progress of the reaction. As the reaction proceeded the brown solution became darker. After 8 h the infrared bands corresponding to the two reactants had disappeared and the reaction appeared to have gone to completion. The reaction mixture was monitored for a further 4 h with no apparent change. An infrared spectrum of the products exhibited carbonyl stretching bands at 2100w, 2066s, 2056s, 2020s,br, 2000s, 1888s, 1860sh, 1801mw, 1761w cm^{-1}.

The reaction mixture was filtered under nitrogen through a glass frit and the solvent removed under vacuum. A white insoluble precipitate remained in the reaction vessel. An initial hexane extract (80 ml) contained predominantly $Co_4(CO)_{12}$ (0.106 g, 0.19 mmol, 54% of Co), with weak peaks at 2024 and 2001 cm^{-1} due to $Fe(CO)_5$.

Two extractions (50 ml) in diethyl ether were found to contain $[PPN][NCo_6(CO)_{15}]$ (**figure 3.10**) (ν_{CO} (THF) 2060vw,sh, 2015-2010vs, 1895vw,sh, 1860vs, 1830w cm^{-1} **[206]**), and a small amount of $[PPN][FeCo(CO)_{12}]$ (**figure 3.8**) (ν_{CO} (CH_2Cl_2) 2062vw, 2004vs, 1969w, 1928w, 1813w cm^{-1} [205]). These two compounds could not be completely separated and this meant $[PPN][NCo_6(CO)_{15}]$ was not identified as a product until a suitable crystal was obtained and used for full X-ray crystallographic characterisation. Details of this investigation are given below. Even after full crystallographic characterisation it was not possible to distinguish $[NCo_6(CO)_{15}]^-$ from possible $[NCo_{6-n}Fe_n(CO)_{15-n}(NO)_n]^-$ anions. However, electron probe analysis of the same crystal confirmed that Co was the only transition metal present. Also there were no obvious NO stretches in the infrared spectrum.

The crystal of $[PPN][NCo_6(CO)_{15}]$ used for X-ray crystallography was obtained by diffusion of hexane into the ether solution at 4°C. The products came down as a mixture of dark irregular chunky crystals of $[PPN][NCo_6(CO)_{15}]$, and red square plates to blocks of the product identified as $[PPN][FeCo_3(CO)_{12}]$.

To confirm the identity of $[PPN][FeCo_3(CO)_{12}]$, sample crystals were subject to electron probe analysis. This indicated a P : Fe : Co ratio of 3.3 : 1.1 : 3, compared with an expected ratio of 2 : 1 : 3 (table 3.14). The ratio of Fe to Co is reasonably accurate, but the analysis

of P is near the limits of this technique and is therefore not as reliable.

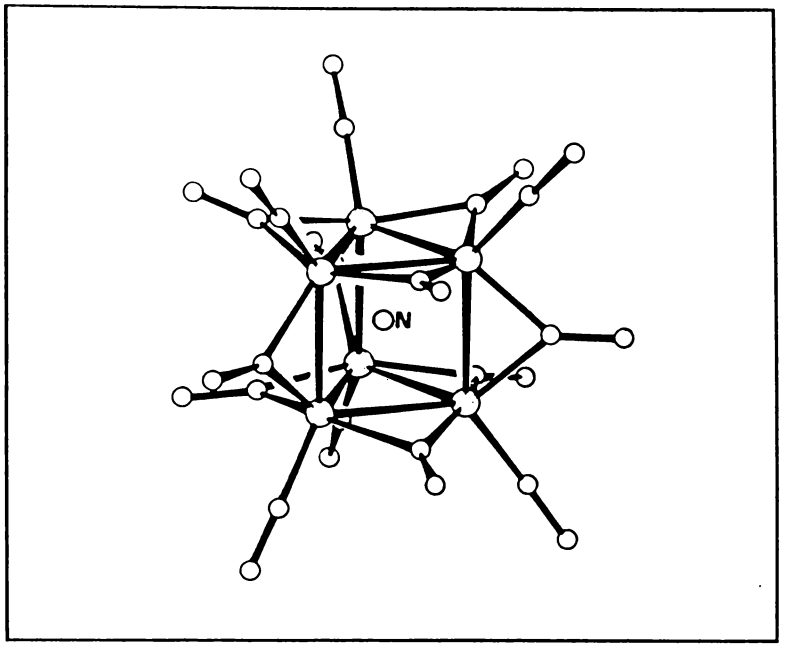

Figure 3.10: Structure of $[NCo_6(CO)_{15}]^-$

Table 3.14: Electron Probe Analysis of $[PPN][FeCo_3(CO)_{12}]$

ELEMENT	SHELL	WEIGHT %	ATOMIC %
P	K	30.3	45.0
Fe	K	18.5	15.3
Co	K	51.1	39.8

A crystal of $[PPN][FeCo_3(CO)_{12}]$ was coated in araldite and used for preliminary X-ray diffraction studies. The setting photographs were weak but indicated orthorhombic symmetry with $P2_12_12_1$ the probable space group. 1.68 g cm^{-3} was taken as a reasonable value for the density, by comparison with $[PPN][NCo_6(CO)_{15}]$ (see below).

$$a = 14.0\ \text{Å}$$
$$b = 31.8\ \text{Å}$$
$$c = 10.9\ \text{Å}$$
$$U = 4852\ \text{Å}^3 \quad M_r = 4910/Z$$

For the $P2_12_12_1$ space group it is most likely for Z to equal 4. This implies a molecular weight of 1228, which is reasonably consistent with $[PPN][FeCo_3(CO)_{12}]$ (M_r = 1107).

The remaining products, not soluble in ether, (0.259 g) were dissolved in CH_2Cl_2. An infrared spectrum revealed mainly $[Co(CO)_4]^-$ (~0.412 mmol, 33% of Co) with very weak peaks at 2002 cm-1 and 1790 cm^{-1}, probably due to $[SiCo_9(CO)_{21}]^{2-}$.

The weak peaks at 2100, 1801 and 1761 reported above were not observed once the reaction products were worked up. These peaks appeared to be associated with yellow residue which collected in the muck trap when the solvent was removed under vacuum. The volatility of this species suggests a low molecular weight, and it was assumed to be $Fe(CO)_2(NO)_2$ which exhibits two ν_{CO} infrared bands between 2100 and 2040 cm^{-1}, and two ν_{NO} bands between 1810 and 1750 cm^{-1} **[207]**.

(ii) $Si[Co_2(CO)_7]_2$ (0.205 g, 0.31 mmol) and $[Et_4N][Fe(CO)_3NO]$ (0.094 g, 0.31 mmol) were reacted in CH_2Cl_2 (30 ml) under nitrogen atmosphere. The reaction was monitored regularly using infrared spectroscopy, and after 10 h had gone to completion. At this stage the products were worked up as described for the previous section.

The proportion of $Co_4(CO)_{12}$ produced in this reaction (0.055 g, 0.096 mmol, 31% of Co) was significantly less than in the previous reaction. There was also a marked decrease in the amount of $[SiCo_9(CO)_{21}]^{2-}$ contained in the CH_2Cl_2 fraction (0.124 g). An infrared spectrum of the products contained in the diethyl ether fraction again revealed $[NCo_6(CO)_{15}]^-$ along with larger amounts of $[FeCo_3(CO)_{12}]^-$.

When hexane was slowly diffused into the diethyl ether solution at 4°C, the products again came down as a mixture of red plate-like $[Et_4N][FeCo_3(CO)_{12}]$ crystals and dark brown $[Et_4N][NCo_6(CO)_{15}]$ crystals. Partial separation of these products was achieved by placing the crystals in hexane and adding CCl_4 until a portion of the sample (predominantly $[Et_4N][FeCo_3(CO)_{12}]$) remained suspended. The

hexane/CCl_4 mixture was decanted off, and the suspended crystals retrieved by adding more hexane. An infrared spectrum of these crystals confirmed $[Et_4N][FeCo_3(CO)_{12}]$ as one of the products.

A suitable crystal of $[Et_4N][NCo_6(CO)_{15}]$ was mounted in a glass capilliary and used for preliminary X-ray diffraction studies. The unit cell was found to have tetragonal symmetry with unit cell dimensions:

$$a = b = 16.92 \text{ Å}, \; c = 21.51 \text{ Å}$$
$$U = 6157 \text{ Å}^3$$

Assuming Z = 8, a density of 1.98 g cm^{-3} can be calculated using the unit cell volume and the molecular weight of $[Et_4N][NCo_6(CO)_{15}]$ (M_r = 917.68). This value is sensible when compared with the density of 1.97 g cm^{-3}, reported for $[Et_4N][Ge_2Co_7(CO)_{21}]$ [32].

X-ray Crystallographic Study of [PPN][$NCo_6(CO)_{15}$]

The crystal of $[PPN][NCo_6(CO)_{15}]$ obtained above, was coated in araldite. Preliminary precession photographs using Cu-Kα radiation indicated that the crystal had triclinic symmetry, for which $P\bar{1}$ is the most common space group. This was confirmed by successful solution. Intensity data were collected for 6832 unique reflections, for which $4° < 2\theta < 38°$, on a Nicolet diffractometer at the University of Canterbury. 4565 reflections with $I > 2\sigma(I)$ were employed in all calculations. Mo-Kα radiation and a Wyckoff scan technique were used. Standard reflections monitored at regular intervals showed that no crystal decomposition had occured. Lattice dimensions were obtained from 25 high-angle reflections

Data were corrected for Lorentz polarisation effects, and for absorption (transmission factors, 0.82 maximum and 0.75 minimum).

The coordinates of the Co atoms were obtained using the Patterson method. The C, N, and P atoms were located by subsequent full-matrix least squares refinement cycles. Assigning the encapsulated atom as nitrogen provided the most reasonable temperature factor. Substituting C, Si or O for the nitrido atom gave unrealistic values. In later refinement cycles the Co atoms were assigned anisotropic temperature factors. Without locating the H atoms, the refinement converged to R = 0.0944, R_w = 0.0944 with 12.2 reflections per parameter. At this

stage the identity of the sample was realised and further refinement was not pursued.

Table 3.15: Crystal Data for $[PPN][NCo_6(CO)_{15}]$

Formula: $C_{51}H_{30}Co_6N_2O_{15}P_2$	
M_r = 1326.4	
Triclinic space group $P\bar{1}$	
a = 19.466(9) Å	α = 96.54(3)°
b = 8.987(3) Å	β = 109.59(3)°
c = 15.468(6) Å	γ = 90.51(3)°
U = 2529(2) $Å^3$	Dcalc = 1.68 g cm^{-3}
Z = 2	
F(000) = 1324	μ(Mo-Kα) = 21.3 cm^{-1}
λ(Mo-Kα) = 0.71073 Å	
Crystal dimensions: 1.15 x 0.34 x 0.11 mm	

Unfortunately Martinengo *et al.* [206] have already reported an accurate crystal structure of $[PPN][NCo_6(CO)_{15}]$: a = 19.686(8) Å, b = 9.065(5) Å, c = 15.737(7) Å, α = 95.69(6)°, β = 69.99(6)°, γ = 81.31(6)°; which was refined to give R = 0.056.

3.2.3 REACTIONS OF $GeCo_4(CO)_x$

3.2.3.1 $(CO)_4CoGeCo_3(CO)_9$ and $[Et_4N][Mn(CO)_5]$

$(CO)_4CoGeCo_3(CO)_9$ (0.36 g, 0.5 mmol) and $[Et_4N][Mn(CO)_5]$ (0.4 g, 0.5 mmol) in CH_2Cl_2 (20 ml) were magnetically stirred under nitrogen. The reaction was monitored for 30 min using infrared spectroscopy. During this time the $[Mn(CO)_5]^-$ infrared bands diminished and a strong $[Co(CO)_4]^-$ band appeared at 1889 cm^{-1}.

The solution was filtered and the solvent removed under vacuum. The hexane soluble products were extracted in two 50 ml portions. These were combined and the hexane removed under vacuum. Any $Mn_2(CO)_{10}$

present was removed from the hexane fraction by sublimation onto a cold finger containing running water at room temperature. An infrared spectrum of the remaining hexane soluble fraction conformed with the spectrum previously reported for $(CO)_5MnGeCo_3(CO)_9$ (ν_{CO} 2115w, 2078m, 2041vs, 2022ms cm^{-1} [28]). This product was isolated in 72% yield (0.235 g, 0.36 mmol).

An infrared spectrum of the hexane-insoluble fraction revealed $[Co(CO)_4]^-$ (ν_{CO} (CH_2Cl_2) 1889 cm^{-1}) and a small amount of $[GeCo_5(CO)_{16}]^-$ (ν_{CO} (CH_2Cl_2) 2078w, 2053m, 2025vs, 2000sh, 1820w cm^{-1}).

3.2.3.2 $(CO)_4CoGeCo_3(CO)_9$ and $[Et_4N]_2[Co_6(CO)_{15}]$

$(CO)_4CoGeCo_3(CO)_9$ (0.074 g, 0.110 mmol) was added to a solution of $[Et_4N]_2[Co_6(CO)_{15}]$ (0.100 g, 0.097 mmol) in CH_2Cl_2 (30 ml) and stirred under a nitrogen atmosphere. The reaction was monitored using infrared spectroscopy.

A reaction proceeded slowly at room temperature with infrared peaks emerging at 2054 cm^{-1} and 2026 cm^{-1}. After 80 h the distinctive $(CO)_4CoGeCo_3(CO)_9$ peak at 2042 cm^{-1}, and the $[Co_6(CO)_{15}]^{2-}$ peak at 1980 cm^{-1} were no longer evident. The reaction mixture was filtered and the products worked up.

An initial extraction in hexane (*ca.* 50 ml) was found to contain $Co_4(CO)_{12}$ (0.036 g, 0.064 mmol, 25% of Co). The major product, extracted in diethyl ether (*ca.* 50 ml), was identified as $[GeCo_5(CO)_{16}]^-$ ***(F 7)*** from its infrared spectrum. This was retrieved in near quantitative yield (0.098 g, 0.104 mmol, 94% of Ge, 51% of Co). The only ether insoluble product was found to be $[Co(CO)_4]^-$ (0.020 g, 0.066 mmol, 6% of Co).

3.2.3.3 $Ge[Co_2(CO)_7]_2$ and $Na_2[Fe(CO)_4]$

$Ge[Co_2(CO)_7]_2$ (0.20 g, 0.29 mmol) and $Na_2[Fe(CO)_4]$ (0.07 g, 0.33 mmol, prepared by Na/NH_3 reduction of $Fe(CO)_5$) in CH_2Cl_2 (20 ml) were stirred under nitrogen. The reaction was monitored regularly using infrared spectroscopy.

Over three days the $Ge[Co_2(CO)_7]_2$ underwent a gradual decarbonylation reaction giving $(CO)_4CoGeCo_3(CO)_9$, but no further reaction was detected. The pale pink $Na_2[Fe(CO)_4]$ appeared to remain insoluble in CH_2Cl_2.

The reaction mixture was heated under reflux for 24 h with still no

apparent change. THF (4 ml) was added to help solubilise the $Na_2[Fe(CO)_4]$ but instead lead to rapid decomposition of the $(CO)_4CoGeCo_3(CO)_9$ producing $[Co(CO)_4]^-$ (ν_{CO} (CH_2Cl_2) 1889 cm^{-1}) and some $Co_4(CO)_{12}$ (ν_{CO} (CH_2Cl_2) 2062s, 2052s, 2038w, 2028w, 1865m cm^{-1}).

3.2.3.4 $Ge[Co_2(CO)_7]_2$ and $[Et_4N][Fe(CO)_3NO]$

A nitrogen flushed Schlenk flask was charged with $Ge[Co_2(CO)_7]_2$ (0.130 g, 0.19 mmol) and $[Et_4N][Fe(CO)_3NO]$ (0.056 g, 0.19 mmol) in CH_2Cl_2 (30 ml). The reaction mixture was magnetically stirred at room temperature and monitored using infrared spectroscopy. As the reaction progressed, the brown solution gradually darkened. After 11 h the infrared peaks corresponding to the two reactants had disappeared and new peaks were now evident at (ν_{CO} (CH_2Cl_2) 2100w, 2076vw, 2033s, 2017s, 1997sh, 1953w, 1890m, 1801m and 1761vw cm^{-1}).

The reaction mixture was filtered and the solvent removed under vacuum. A hexane extraction was attempted but no hexane soluble products were detected. The bulk of the products were found to be soluble in diethyl ether.

An infrared spectrum of the products contained in an ether extract (*ca.* 80 ml) showed peaks at ν_{CO} (CH_2Cl_2) 2072w, 2034vs, 2015s, 1997w,sh, 1980w,sh, 1948w, 1889m cm^{-1}. Crystals were grown by slow diffusion of hexane into the concentrated ether solution. The crystalline product showed infrared bands at ν_{CO} (CH_2Cl_2) 2072w, 2015vs, 1948w, 1916m, 1605vw cm^{-1} **(figure 3.11)**.

Sample crystals were subject to electron probe analysis, which detected Ge, Fe and Co in a ratio of approximately 2 : 2 : 5 **(table 3.16)**. Two different crystals were investigated, both giving similar signals.

Table 3.16: Electron Probe Analysis of Unknown Product

ELEMENT	SHELL	WEIGHT %	ATOMIC %
Ge	K	26.2	22.1
Fe	K	18.6	20.5
Co	K	55.2	57.4

Figure 3.11: Infrared spectrum of unidentified product (CH_2Cl_2 solution)

A weakly-diffracting crystal of this compound was investigated using X-ray crystallography. Preliminary diffraction studies indicated a unit cell belonging to the $P2_12_12_1$ space group. A value of 1.93 g cm^{-3} was used for the density by comparison with $[Et_4N][Ge_2Co_5Fe_2(CO)_{22}]$ [33].

$$a = 11.69 \text{ Å}$$
$$b = 11.81 \text{ Å}$$
$$c = 21.00 \text{ Å}$$
$$U = 2899 \text{ Å}^3, \; M_r = 3370/Z$$

A data set was collected using a fragment of this crystal but the quality was poor and a solution could not be obtained. With retrospect the unit cell may have been monoclinic, with the unique angle being very close to 90°. If this were the case, then only half of the required data set had been collected, and this had been done with the unique angle constrained to 90°. Not surprisingly, attempts to find a solution in the $P2_1/n$ space group failed.

In the supernatant decanted from these crystals, the infrared bands at 2034, 1997, 1980, 1957 and 1889 cm^{-1} had increased in intensity. The latter peak can be attributed to $[Co(CO)_4]^-$, but the other compounds present were not able to be isolated or characterised.

$[Co(CO)_4]^-$ (ν_{CO} (CH_2Cl_2) 1989 cm^{-1}) was the only ether-insoluble product detected. The infrared peaks reported above at 2100, 1801 and 1761 cm^{-1}) were not observed once the products were worked up. These correspond with the product identified as $Fe(CO)_2(NO)_2$ in the reaction of $Si[Co_2(CO)_7]_2$ with $[Fe(CO)_3NO]^-$.

3.2.3.5 $Ge[Co_2(CO)_7]_2$ and $[CpNi(CO)]_2$

$Ge[Co_2(CO)_7]_2$ (0.55 g, 0.78 mmol) was added to $[CpNi(CO)]_2$ (0.12 g, 0.39 mmol) in CH_2Cl_2 (80 ml). The red solution was stirred for 5 h under a nitrogen atmosphere. During this period no change was detected in the carbonyl infrared spectrum of the reaction mixture.

The solution was heated at 35-40°C using an oil bath. A slow reaction ensued during which the distinctive $Ge[Co_2(CO)_7]_2$ infrared peak at 2061 cm^{-1} gradually diminished in intensity, while strong peaks emerged at 2054 cm^{-1} and 2026 cm^{-1}. After 48 h the 2061 cm^{-1} peak had disappeared and the peak at 1847 cm^{-1}, with contributions from both

$Ge[Co_2(CO)_7]_2$ and $[CpNi(CO)]_2$, was barely visible.

A yellow-green hexane extraction (*ca.* 100 ml) of the products showed infrared bands at 2085w, 2051m, 2045m, 2032vs, 1971s, 1898vw and 1854vw cm^{-1}, representing a mixture of compounds.

An attempt was made to separate these unidentified products by sublimation onto a cold finger containing running water, under continuous vacuum. Unfortunately the entire hexane soluble fraction proved volatile at room temperature. When the products that had collected on the cold finger were redissolved in hexane, the strong infrared peak at 1971 cm^{-1} was no longer present and the 2032 cm^{-1} peak was significantly weaker. It was later discovered that a yellow compound had collected in the muck trap. This was assumed to be $CpCo(CO)_2$ (red liquid, ν_{CO} (CS_2) 2028, 1967 cm^{-1} **[207]**), which is very volatile and could account for the two missing peaks.

The remaining hexane fraction was chromatographed on a silica gel plate, using hexane as eluant. Five bands were observed, each of which was isolated and redissolved using CH_2Cl_2. These products are listed in order of decreasing mobility:

(i) Yellow; ν_{CO} (hexane) 2080m, 2050s, 2032w, 2010m 1968w cm^{-1} (figure 3.12).

(ii) Pink; ν_{CO} (hexane) 1892w, 1844s cm^{-1}. Identified as unreacted $[CpNi(CO)]_2$ (red; ν_{CO} ($CHCl_3$) 1891(1.9), 1841(10) **[208]**).

(iii) Green; ν_{CO} (hexane) 2085m, 2045vs, 2021s, 1854s cm^{-1}. Identified as $CpNiCo(CO)_5$ (green, ν_{CO} (cyclohexane) 2084m, 2045vs, 2024s, 1855s cm^{-1} **[209]**).

(iv) Brown; barely moved on the plate and was difficult to redissolve; ν_{CO} (hexane) 2032 cm^{-1}.

Unfortunately the the amounts of the unidentified yellow and brown phases retrieved were barely sufficient to obtain weak solution infrared spectra. The volatility of these products suggests a relatively low molecular weight. No further efforts were made to characterise these compounds.

The bulk of the products of this reaction (not soluble in hexane) were dissolved in diethyl ether. An infrared spectrum in CH_2Cl_2 exhibited carbonyl stretches at 2077w, 2054m, 2026vs, 2004sh, 1965sh, 1867w, 1822w cm^{-1}. The 1867 cm^{-1} peak could not be identified, but the

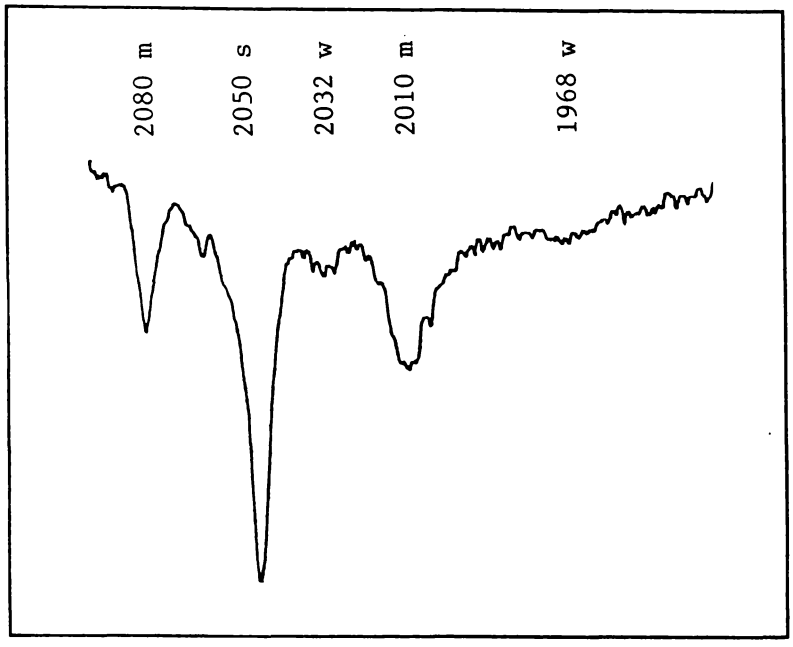

Figure 3.12: Carbonyl region infrared spectrum of product (i)

remaining peaks were attributed to $[GeCo_5(CO)_{16}]^-$ ***(F 7)*** (ν_{CO} (CH_2Cl_2) 2078w, 2053m, 2025vs, 2000sh, 1820w cm^{-1}).

Attempts were made to crystallise the diethyl ether fraction by cooling an ether solution, and by slow diffusion of hexane into an ether solution at 4°C. In each case the product came down as an oily residue. When Et_4NCl (0.02 g) was added to the solution some crystals were obtained by cooling. These were used for electron probe analysis, which detected Ge and Co in an atomic ratio of 1 : 4.8 (**table 3.17**). Three different shaped crystals were analysed, all giving similar values. This supports $[GeCo_5(CO)_{16}]^-$ as the major product of this reaction.

Table 3.17: Electron Probe Analysis of "$[GeCo_5(CO)_{16}]^-$"

ELEMENT	SHELL	WEIGHT %	ATOMIC %
Ge	K	20.5	17.3
Co	K	79.5	82.7

3.2.4 REACTIONS OF $E[Fe_2(CO)_8]_2$ *(F 2)*

3.2.4.1 $Si[Fe_2(CO)_8]_2$ and $[Co(CO)_4]^-$

(i) $Si[Fe_2(CO)_8]_2$ (0.030 g, 0.043 mmol) was added to a solution of $Et_4N[Co(CO)_4]$ (0.014 g, 0.045 mmol) in CH_2Cl_2 (10 ml) under nitrogen atmosphere. Changes in the reaction mixture were monitored using infrared spectroscopy.

The solution was stirred for 20 h at room temperature with no apparent reaction. The reaction vessel was heated to 35-40°C using an oil bath. Over 78 h the yellow colour of the reaction mixture faded and the solution became slightly murky. The intensity of the $Si[Fe_2(CO)_8]_2$ infrared bands gradually diminished and a weak band emerged at 2000 cm^{-1}. The $[Co(CO)_4]^-$ infrared peak at 1889 cm^{-1} remained strong throughout.

The reaction mixture was filtered through a glass frit. Small blue-green crystals remained attached to the inside of the reaction vessel. These were assumed to be some Co(II) or Fe(II) species and were not investigated further.

The solvent was removed from the filtrate under vacuum. A hexane extract was found to contain $Co_4(CO)_{12}$ with a trace amount of unreacted $Si[Fe_2(CO)_8]_2$.

The remaining products, dissolved in CH_2Cl_2, contained a new compound (ν_{CO} (CH_2Cl_2) 2077w, 2000s, 1985sh, 1955vw, 1827vw cm^{-1}). This dark-coloured product was produced in very low yield (an estimated 2-4%) and the infrared bands were dwarfed by the peak at 1889 cm^{-1} representing unreacted $[Co(CO)_4]^-$.

An attempt was made to crystallise the unidentified product, but the very low yield, the amount of $[Co(CO)_4]^-$ also present and gradual decomposition prevented further characterisation.

(ii) $Si[Fe_2(CO)_8]_2$ (0.061 g, 0.086 mmol) and $Et_4N[Co(CO)_4]$ (0.026 g, 0.086 mmol) in CH_2Cl_2 (10 ml) were sealed under vacuum in a 50 ml glass ampoule and heated at *ca.* 40°C. After 4 days the ampoule was opened and the contents worked up as described above.

The reaction proceeded in a similar manner to that described in (i). $Co_4(CO)_{12}$ (0.003 g, 0.005 mmol) was isolated as the only hexane soluble product. An infrared spectrum of the hexane insoluble fraction (0.028 g) showed the same pattern of peaks as those observed in reaction (i). Small blue-green crystals and an insoluble grey

precipitate were also produced.

(iii) A Schlenk flask charged with $Si[Fe_2(CO)_8]_2$ (0.043 g, 0.061 mmol) in CH_2Cl_2 (15 ml) was heated at 35-40°C for 4 days under nitrogen atmosphere. No reaction was observed and no change in the infrared spectrum could be detected.

Two crystals of Et_4NCl were added and the solution stirred at 35-40°C for a further 4 days. The yellow colour of the reaction mixture faded and the solution became slightly murky.

The products were worked up as described in (i). Infrared spectra of the hexane and CH_2Cl_2 fractions indicated a reaction similar to those observed in (i) and (ii). Small amounts of $Co_4(CO)_{12}$ and the unidentified species (ν_{CO} (CH_2Cl_2) 2077w, 2000s, 1985sh, 1955vw, 1827vw cm^{-1}) had been formed, and the $[Co(CO)_4]^-$ had remained largely unreacted.

3.2.4.2 $Sn[Fe_2(CO)_8]_2$ and $[Co(CO)_4]^-$

(i) $Sn[Fe_2(CO)_8]_2$ (0.044 g, 0.056 mmol) was added to $[Et_4N][Co(CO)_4]$ (0.017 g, 0.056 mmol) in CH_2Cl_2 (20 ml) and stirred under nitrogen atmosphere. The reaction was monitored using infrared spectroscopy.

No changes were detected in the infrared spectrum after 16 h. The reaction mixture was heated to 35-40°C using an oil bath, and stirred for 48 h. During this time the $Sn[Fe_2(CO)_8]_2$ infrared peaks diminished and weak peaks emerged at 2024 and 2005 cm^{-1}. The $[Co(CO)_4]^-$ infrared peak at 1889 cm^{-1} remained strong throughout.

The reaction mixture was filtered through a glass frit leaving small blue-green crystals in the reaction vessel. A hexane extract (*ca.* 40 ml) of the products contained $Co_4(CO)_{12}$ with a trace of unreacted $Sn[Fe_2(CO)_8]_2$. An infrared spectrum of the products contained in a 40 ml diethyl ether extract showed a $[Co(CO)_4]^-$ peak at 1889 cm^{-1} and unidentified peaks at 2080w, 2024s, 2005vs, 2000sh, 1934w cm^{-1}. This compound was produced in very low yield and gradually decomposed, preventing further characterisation.

A CH_2Cl_2 extract (*ca.* 40 ml) of the remaining ether-insoluble products exhibited only one ν_{CO} infrared band at 1889 cm^{-1}, representing unreacted $[Co(CO)_4]^-$ (0.011 g, 0.037 mmol, 66% of Co).

(ii) $Sn[Fe_2(CO)_8]_2$ (0.052 g, 0.066 mmol) in CH_2Cl_2 (15 ml) was stirred

under nitrogen atmosphere at 35-40°C for 2 days. No reaction was observed and no change could be detected by infrared spectroscopy.

$K[Co(CO)_4]$ (0.014 g, 0.066 mmol) in CH_2Cl_2 (10 ml) was added and the mixture stirred for 3 days at 35-40°C. The products were then worked up as described in (i).

$Co_4(CO)_{12}$ appeared to be the only species produced in this reaction. This was recovered along with unreacted $Sn[Fe_2(CO)_8]_2$ in the hexane fraction. Unreacted $K[Co(CO)_4]$ (0.008 g, 0.039 mmol) was isolated by CH_2Cl_2 extraction.

3.2.4.3 $Si[Fe_2(CO)_8]_2$ and $[Fe_2(CO)_8]^{2-}$

$Si[Fe_2(CO)_8]_2$ (0.080 g, 0.11 mmol) and $[Et_4N]_2[Fe_2(CO)_8]$ (0.066 g, 0.11 mmol) in CH_2Cl_2 (20 ml) were stirred at room temperature under nitrogen atmosphere. The ν_{CO} infrared peaks of $Si[Fe_2(CO)_8]_2$ were used to monitor reaction progress.

No reaction was detected after 5 h so the reaction mixture was heated to 35-40°C using an oil bath. After 30 min the distinctive $Si[Fe_2(CO)_8]_2$ infrared band at 2050 cm^{-1} was no longer evident and a strong peak had emerged at ~1990 cm^{-1}. The reaction was monitored for a further 3 h during which time the 1990 cm^{-1} peak diminished and a peak at 1949 cm^{-1} became very intense. At this stage the reaction was terminated and the products worked up.

The solution was filtered through a glass frit, and the solvent removed under vacuum. A hexane extraction was attempted but no hexane soluble products were detected. An infrared spectrum of the products contained in a diethyl ether extract (*ca.* 60 ml) showed peaks at 2063w, 2016w, 1996vs, 1972s, 1957vw, 1720w cm^{-1}. $[HFe_3(CO)_{11}]^-$ (ν_{CO} (CH_2Cl_2) 2070w, 2000vs, 1972s, 1946m, 1718w cm^{-1} **[173]**) was identified as the main compound present. The species responsible for the very weak peaks at 2016 and 1957 cm^{-1} could not be isolated or characterised.

A CH_2Cl_2 extract of the remaining ether-insoluble products exhibited infrared bands at 2018w, 2005m, 1995sh, 1948s, 1894sh cm^{-1}. This species was identified as $[Fe_4(CO)_{13}]^{2-}$ (ν_{CO} (acetone) 2067vw, 2021w, 2009w, 1990sh, 1949s, 1896sh cm^{-1} **[203]**).

3.2.4.4 $Sn[Fe_2(CO)_8]_2$ and $[Fe_2(CO)_8]^{2-}$

$Sn[Fe_2(CO)_8]_2$ (0.092 g, 0.12 mmol) and $[Et_4N]_2[Fe_2(CO)_8]$ (0.069 g,

0.12 mmol) in CH_2Cl_2 (20 ml) were stirred at 35-40°C under nitrogen atmosphere. Infrared spectroscopy was used to monitor the reaction.

After 15 min, $Sn[Fe_2(CO)_8]_2$ infrared bands were no longer evident and strong peaks at ~1990 and ~1972 cm^{-1} indicated that $[HFe_3(CO)_{11}]^-$ had been formed. The solution was removed from the heat, filtered through a glass frit, and the solvent evaporated off. No hexane soluble species were detected. $[HFe_3(CO)_{11}]^-$, extracted in diethyl ether (*ca.* 60 ml), was identified as the major product by its infrared spectrum. Weak unidentified peaks at 2018 and 1957 cm^{-1} (comparable with those observed in section 3.2.4.3) were also present in this spectrum.

The remaning products, not soluble in diethyl ether, were redissolved in CH_2Cl_2 (*ca.* 40 ml). An infrared spectrum revealed $[Fe_4(CO)_{13}]^{2-}$ along with an unidentified peak at 1894 cm^{-1}. These two products could not be separated.

3.2.4.5 $Si[Fe_2(CO)_8]_2$ and $[Mn(CO)_5]^-$

$Si[Fe_2(CO)_8]_2$ (0.12 g, 0.17 mmol) was stirred for 5 h with $[PPN][Mn(CO)_5]$ (0.13 g, 0.17 mmol) in CH_2Cl_2 (10 ml) under nitrogen atmosphere. The infrared spectrum of the solution was monitored but no reaction was detected.

The reaction vessel was heated to 35-40°C using an oil bath. A slow reaction ensued, during which the yellow solution turned red. The reaction was allowed to proceed until the $[Mn(CO)_5]^-$ infrared peaks at 1894 and 1856 cm^{-1} had disappeared. After 48 h the solution was removed from the heat and filtered through a glass frit. The solvent was evaporated under vacuum. A hexane extract (*ca.* 40 ml) was found to contain $Mn_2(CO)_{10}$ (ν_{CO} (hexane) 2044s, 2013vs, 2001w, 1994w, 1982m cm^{-1}). The remaining product was insoluble in hexane and diethyl ether, and exhibited four infrared bands in the carbonyl stretching region (ν_{CO} (CH_2Cl_2) 2028w, 1996s, 1958vs, 1911s cm^{-1}). An attempt was made to grow a crystal of this species, suitable for X-ray diffraction studies by: cooling a CH_2Cl_2 solution; slow diffusion of hexane into a CH_2Cl_2 solution; and by slow diffusion of diethyl ether into a CH_2Cl_2 solution. No suitable crystals were obtained.

A FABS mass spectrum was obtained using a crystalline sample of the unidentified product. The position of the highest peak (m/e = 797) and the fragmentation pattern suggests that this compound is $[CFe_6(CO)_{16}]^{2-}$ [100] (figure 3.13).

Table 3.18: FABS Mass Spectrum of $[PPN]_2[CFe_6(CO)_{16}]$

m/e	Int.	Possible Assignments
797	55	$[CFe_6(CO)_{16}]^-$
768	13	$[CFe_6(CO)_{15}]^-$
740	63	$[CFe_6(CO)_{14}]^-$
684	17	$[CFe_6(CO)_{12}]^-$
656	77	$[CFe_6(CO)_{11}]^-$
628	100	$[CFe_6(CO)_{10}]^-$, $[CFe_5(CO)_{12}]^-$
616	18	$[Fe_5(CO)_{12}]^-$, $[Fe_4(CO)_{14}]^-$
600	52	$[CFe_6(CO)_9]^-$, $[CFe_5(CO)_{11}]^-$
588	27	$[Fe_5(CO)_{11}]^-$, $[Fe_4(CO)_{13}]^-$
532	15	$[Fe_5(CO)_9]^-$, $[Fe_4(CO)_{11}]^-$
516	14	$[CFe_6(CO)_6]^-$, $[CFe_5(CO)_8]^-$, $[CFe_4(CO)_{10}]^-$
504	22	$[Fe_5(CO)_8]^-$, $[Fe_4(CO)_{10}]^-$, $[Fe_3(CO)_{12}]^-$
488	28	$[CFe_6(CO)_5]^-$, $[CFe_5(CO)_7]^-$, $[CFe_4(CO)_9]^-$
476	18	$[Fe_5(CO)_7]^-$, $[Fe_4(CO)_9]^-$, $[Fe_3(CO)_{11}]^-$
460	26	$[CFe_6(CO)_4]^-$, $[CFe_5(CO)_6]^-$, $[CFe_4(CO)_8]^-$
448	43	$[Fe_5(CO)_6]^-$, $[Fe_4(CO)_8]^-$, $[Fe_3(CO)_{10}]^-$
432	75	$[CFe_6(CO)_3]^-$, $[CFe_5(CO)_5]^-$, $[CFe_4(CO)_7]^-$
421	40	$[HFe_5(CO)_5]^-$, $[HFe_4(CO)_7]^-$, $[HFe_3(CO)_9]^-$
404	57	$[CFe_6(CO)_2]^-$, $[CFe_5(CO)_4]^-$, $[CFe_4(CO)_6]^-$, $[CFe_3(CO)_8]^-$
393	37	$[HFe_5(CO)_4]^-$, $[HFe_4(CO)_6]^-$, $[HFe_3(CO)_8]^-$
364	10	$[Fe_5(CO)_3]^-$, $[Fe_4(CO)_5]^-$, $[Fe_3(CO)_7]^-$
348	16	$[CFe_6]^-$, $[CFe_5(CO)_2]^-$, $[CFe_4(CO)_4]^-$, $[CFe_3(CO)_6]^-$
306	>100	$(Matrix)_2^-$

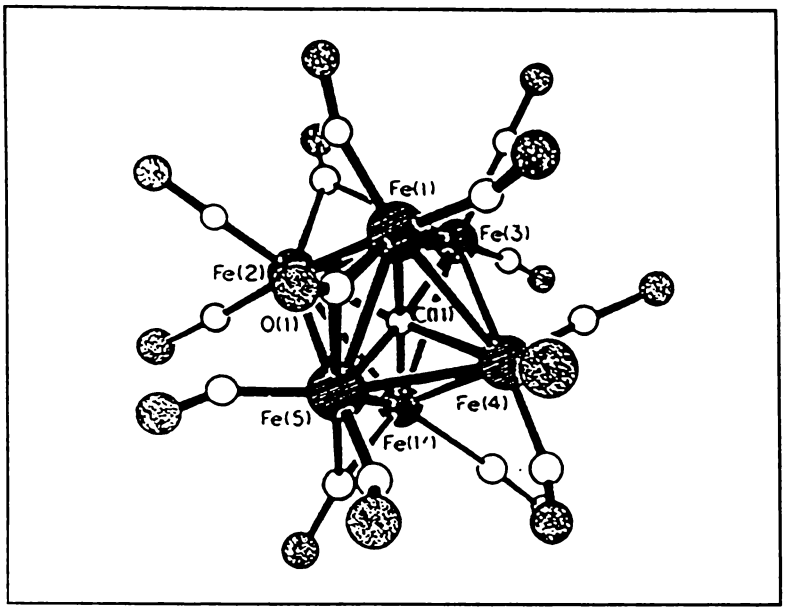

Figure 3.13: Structure of $[CFe_6(CO)_{16}]^-$

Two series of peaks, each showing a pattern typical of successive CO loss, can be seen in the mass spectrum. The first series represents the loss of CO or $Fe(CO)_x$ groups from the parent ion. Note that it is not possible to distinguish the loss of an Fe atom (m = 56) from the loss of two CO groups (m = 28). The second series, beginning with $[Fe_5(CO)_{12}]^-$, represents fragments where the carbido atom has also been lost.

The infrared spectrum observed for the ether fraction is compared with spectra reported for $[CFe_6(CO)_{16}]^{2-}$ in table 3.19.

Table 3.19: Infrared Spectra of $[CFe_6(CO)_{16}]^{2-}$

Observed Spectrum (in CH_2Cl_2)	$[CFe_6(CO)_{16}]^{2-}$ (in acetone)	[210] (in THF)
2028w	2028w	2028vw
1996sh		
1958vs	1964vs	1961vs
1911sh	1930w,sh	1931w,sh
		1772w,br

3.2.4.6 $Ge[Fe_2(CO)_8]_2$ and $[Mn(CO)_5]^-$

$Ge[Fe_2(CO)_8]_2$ (0.10 g, 0.13 mmol) was added to $[PPN][Mn(CO)_5]$ (0.099 g, 0.13 mmol)) in CH_2Cl_2 (10 ml) in a nitrogen flushed Schlenk flask. The solution was stirred at 35-40°C and the reaction was followed using infrared spectroscopy.

After 2 days the distinctive $[Mn(CO)_5]^-$ peaks were no longer visible. The solution was removed from the heat and filtered through a glass frit. The solvent was evaporated under vacuum. $Mn_2(CO)_{10}$ was removed in a hexane extract (*ca.* 40 ml). The remaining product exhibited identical carbonyl infrared stretches to the species identified as $[CFe_6(CO)_{16}]^{2-}$ in section 3.2.4.5.

A crystalline sample of this species was obtained by cooling the CH_2Cl_2 solution. This was used for electron probe analysis. This indicated a P to Fe ratio of 1 : 1 (see **table 3.20**). As mentioned previously, the detection of P is near the limits of this technique, and the proportion of P in the sample may not be very accurate. Significant amounts of Ge and Mn were not detected.

Table 3.20: Electron Probe Analysis of "$[CFe_6(CO)_{16}]^{2-}$"

ELEMENT	SHELL	WEIGHT %	ATOMIC %
P	K	37.4	51.8
Fe	K	62.6	48.2

3.3 DISCUSSION

3.3.1 PREPARATION OF $[SiCo_9(CO)_{21}]^-$

Four previously unreported products have been detected in the reaction of $Si[Co_2(CO)_7]_2$ with $[Co(CO)_4]^-$. Two of these compounds, $[Co_6(CO)_{15}]^-$ and $[Cl_2SiCo_7(CO)_{21}]^-$ were derived from impurities present in the reactants.

When THF is present in the reaction mixture, $Si[Co_2(CO)_7]_2$ decomposes rapidly and $[Co_6(CO)_{15}]^-$ is produced along with $Co_4(CO)_{12}$ and $[Co(CO)_4]^-$. The other species, $[Cl_2SiCo_7(CO)_{21}]^-$ is apparently the product of a reaction between $Si[Co_2(CO)_7]_2$ and Cl^-. The infrared spectrum of this product compares favourably with the spectrum reported

for a previously unidentified product formed when $Si[Co_2(CO)_7]_2$ is reacted with Et_4NCl (see table 3.21). In this case, other unidentified products were also present so a clean spectrum was not obtained. This earlier reaction appears to provide a reasonable yield of $[Cl_2SiCo_7(CO)_{21}]^-$ and if further investigated could prove a useful route for its synthesis, should anyone see fit to produce more $[Et_4N][Cl_2SiCo_7(CO)_{21}]$.

Table 3.21: Infrared Spectra of $[Et_4N][Cl_2SiCo_7(CO)_{21}]$

Observed Spectrum (in CH_2Cl_2)	$Si[Co_2(CO)_7]_2/Et_4NCl$ reaction product (in CH_2Cl_2) [33]
2099vw	
2070w	2070
2048vs	2051
2026s	2032
2004m	2000
	1965
1865vw	
1824w	

The mechanism for the formation of $[Cl_2SiCo_7(CO)_{21}]^-$ is liable to be very complex. $Cl_3SiOCCo_3(CO)_9$, which is structurally related to $[Cl_2SiCo_7(CO)_{21}]^-$, has been described from the reaction of $SiCl_4$ with $[Co(CO)_4]^-$ [211]. The proposed reaction scheme involved the combining of three $Cl_3SiOCCo(CO)_3$ units to produce $Cl_3SiOCCo_3(CO)_9$, possibly releasing $Cl_3SiOSiCl_3$. A similar process may be operating in the current reaction, however at this stage there is no evidence on which to propose a reaction mechanism, and speculation would probably be of little use.

A carbido cluster, $[CCo_8(CO)_{18}]^{2-}$ ***(F 11)*** was also isolated in very low yield from the products of this synthesis. This compound, consisting of a square antiprism of Co atoms containing an

encapsulated carbido atom, was originally prepared by the reaction of $[CCo_6(CO)_{15}]^{2-}$ with $Co_4(CO)_{12}$ [9]. $[CCo_8(CO)_{18}]^{2-}$ has previously been isolated from the $[SiCo_9(CO)_{21}]^{2-}$ synthesis [33], but was tentatively identified as the silicon analogue, $[SiCo_8(CO)_{18}]^{2-}$.

Peaks consistent with a $[CCo_{10}(CO)_{24}]^{-}$ ion were also detected by FABS mass spectroscopy. This probably corresponds with a bicapped analogue of $[CCo_8(CO)_{18}]^{2-}$, although such a cluster has not been previously reported. A bicapped square antiprism should contain 142 electrons, which suggests a neutral $CCo_{10}(CO)_{24}$ species, although like $[SiCo_9(CO)_{21}]^{2-}$, this compound may not be electron precise.

This compound is believed to be a very minor product, despite a relatively strong signal in the mass spectrum. There was no evidence for a $CCo_{10}(CO)_{24}$ species in the infrared spectra or cyclic voltammograms (see chapter 5) of $[SiCo_9(CO)_{21}]^{2-}$. It is possible that the carbido cluster was concentrated in the particular sample that was used for mass spectroscopy. Alternatively, the strong signal may reflect the relative stabilities of this compound and $[SiCo_9(CO)_{21}]^{2-}$. A bicapped square antiprism with an encapsulated carbido atom would be more symmetrical and less strained than $[SiCo_9(CO)_{21}]^{2-}$, and hence less likely to fragment.

The fact that carbido clusters were detected in the synthesis of $[SiCo_9(CO)_{21}]^{2-}$, suggests that some interaction may be occuring between the silicon atom and electron rich carbonyl oxygen atoms. For example:

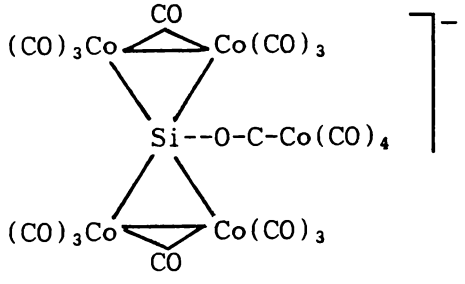

Silicon is a stronger Lewis acid than germanium, and examples of this sort of Si-O-C-M interaction have been well documented [212,213].

For example:

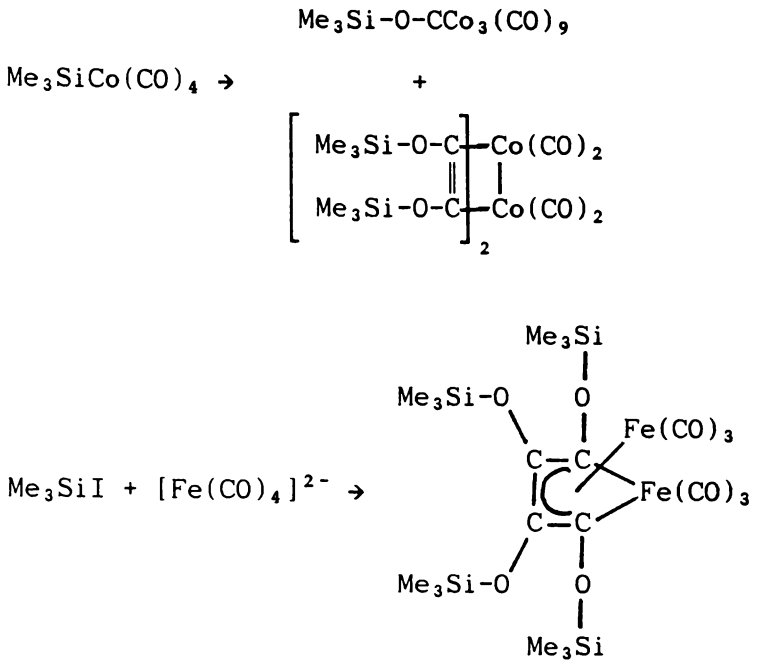

The $[Cl_2SiCo_7(CO)_{21}]^-$ cluster, described above, is another example of this type of compound.

The eventual fate of the Si atom in a reaction of this sort is not clear. Such reactions tend to be complex and unpredictable. However this kind of process could account for the loss of Si and for the formation of the carbido clusters as well as providing the extra Co atoms required for forming $[SiCo_9(CO)_{21}]^{2-}$.

Germanium is a weaker Lewis acid than silicon and is less likely to undergo this type of reaction.

3.3.2 OTHER REACTIONS OF $ECo_4(CO)_x$

It has previously been reported that, when heated, $Si[Co_2(CO)_7]_2$ reacts with $[Fe_2(CO)_8]^{2-}$ producing mainly $[SiCo_9(CO)_{21}]^{2-}$ [33], along with a small amount of a second product. $[SiCo_9(CO)_{21}]^{2-}$ was thought to have been produced by the reaction of $[Co(CO)_4]^-$, displaced from the $Si[Co_2(CO)_7]_2$ by $[Fe_2(CO)_8]^{2-}$. The analogous reaction between $(CO)_4CoSiCo_3(CO)_9$ and $[Fe_2(CO)_8]^{2-}$, reported here, proceeds very rapidly at room temperature. Under these conditions the formation of $[SiCo_9(CO)_{21}]^{2-}$ is not favoured and very little was detected in the products. The major product of this reaction was identified as $[FeCo_3(CO)_{12}]^-$ (figure 3.8). A relatively large amount of $Fe(CO)_5$ also

appeared to be produced. In this reaction, Si-O-C-M interactions could also be used to account for the net loss of Si in the soluble products.

In retrospect the second product of the $Si[Co_2(CO)_7]_2/[Fe_2(CO)_8]^{2-}$ reaction also appears to be $[FeCo_3(CO)_{12}]^-$. The infrared spectrum reported for this species is very similar to that observed here for $[FeCo_3(CO)_{12}]^-$ (table 3.22), and the unit cell dimensions that were obtained are also consistent with $[Et_4N][FeCo_3(CO)_{12}]$. At the time a much larger cluster was suspected because an electron probe analysis had indicated a Si to Fe to Co ratio of 1 : 5 : 8. This may have been obtained from a non-representative crystal.

Table 3.22: Infrared Spectra of $[FeCo_3(CO)_{12}]^-$

$Si[Co_2(CO)_7]_2$ reaction product (CH_2Cl_2) [33]	$(CO)_4CoSiCo_3(CO)_9$ reaction product (CH_2Cl_2)	$[FeCo_3(CO)_{12}]^-$ [205] (MeCN)
	2064vw	2066w
2002s	2004vs	2008s
1984w,sh	1969w	1974m
	1928w	1932m
1814w,br	1812w	1815m

When $(CO)_4CoSiCo_3(CO)_9$ was reacted with $[Mn(CO)_5]^-$, a typical metal exchange reaction was observed. Replacement of the terminal $-Co(CO)_4$ unit occurred rapidly at room temperature producing $(CO)_5MnSiCo_3(CO)_9$ in reasonable yield (~30%). A small amount of $[SiCo_9(CO)_{21}]^{2-}$ also appeared to be formed by the reaction of displaced $[Co(CO)_4]^-$.

Another product of this reaction was recovered in an ether extraction. The solubility of this product in diethyl ether and the position of the ν_{CO} peaks, particularly the bridging carbonyl stretching mode at 1823 cm^{-1}, suggest a single negative charge. The unit cell parameters obtained from X-ray diffraction studies indicate a molecular weight of approximately 4775/Z (assuming a density of 1.68 g cm^{-3} as observed for $[PPN][NCo_6(CO)_{18}]$). For the $P\bar{1}$ space group it is most common for Z to equal 2. This implies a molecular weight of

approximately 2317.

There is insufficient information to make any sort of prediction about the structure of this compound. However the available data suggests a very large cluster with up to 14 metal atoms. It must be noted that only a single crystal was ever obtained, and that this crystal may not have been representative of the ether fraction as a whole.

The analogous reaction of $(CO)_4CoGeCo_3(CO)_9$ with $[Mn(CO)_5]^-$ was undertaken in an attempt to obtain greater yields of $(CO)_5MnGeCo_3(CO)_9$. The original preparation of $(CO)_5MnGeCo_3(CO)_9$ **[93]** involved refluxing a CH_2Cl_2 solution of $Ge[Co_2(CO)_7]_2$ with $[Mn(CO)_5]^-$ for 2.5 h. This reaction was thought to proceed via the formation of $(CO)_4CoGeCo_3(CO)_9$. Problems arise because the $[Mn(CO)_5]^-$ anion is readily oxidised and heating the reaction mixture at 40°C for 2.5 h frequently leads to the formation of large amounts of $Mn_2(CO)_{10}$ and little $(CO)_5MnGeCo_3(CO)_9$. A second reaction between $Ge[Co_2(CO)_7]_2$ and $[Co(CO)_4]^-$ to give $[GeCo_5(CO)_{16}]^-$ *(F 7)* also occurs more rapidly under these conditions. The reaction between $[Mn(CO)_5]^-$ and preformed $(CO)_4CoGeCo_3(CO)_9$ proceeds faster and at lower temperatures, thereby reducing the production of $Mn_2(CO)_{10}$ and $[GeCo_5(CO)_{16}]^-$ and providing $(CO)_5MnGeCo_3(CO)_9$ in high yield (~70%).

The reactions between $E[Co_2(CO)_7]_2$ clusters and $[Co_6(CO)_{15}]^{2-}$ did not prove particularly useful. It was hoped that these reactions might provide routes to high nuclearity group 14-transition metal clusters. Despite the apparent deficit of CO in these reactions, $[Co_6(CO)_{15}]^{2-}$ merely acted as a source of $[Co(CO)_4]^-$ and $Co_4(CO)_{12}$. The products of these reactions were the same as those observed when $Si[Co_2(CO)_7]_2$ and $Ge[Co_2(CO)_7]_2$ were reacted directly with $[Co(CO)_4]^-$.

The reaction between $Ge[Co_2(CO)_7]_2$ and $[Co_6(CO)_{15}]^{2-}$ produced $[GeCo_5(CO)_{16}]^-$ in near quantitative yield:

$$3CO + [Co_6(CO)_{15}]^{2-} + Ge[Co_2(CO)_7]_2 \rightarrow [GeCo_5(CO)_{16}]^- + Co_4(CO)_{12} + [Co(CO)_4]^-$$

Three extra CO groups are required for this reaction to proceed. This may account for the deficit of cobalt (~18%) in the soluble products of this reaction. A small amount of decomposition may be allowing this reaction to proceed. $[SiCo_9(CO)_{21}]^{2-}$ is produced from the reaction of $Si[Co_2(CO)_7]_2$ and $[Co_6(CO)_{15}]^{2-}$ in a similar fashion.

Despite being isoelectronic with $[Co(CO)_4]^-$, the reactions of $[Fe(CO)_3NO]^-$ with $Si[Co_2(CO)_7]_2$ and $Ge[Co_2(CO)_7]_2$ have more in common with those of $[Fe_2(CO)_8]^{2-}$.

As is the case with the $[Mn(CO)_5]^-$ and $[Fe_2(CO)_8]^{2-}$ anions, when $[Fe(CO)_3NO]^-$ is reacted with $Si[Co_2(CO)_7]_2$ some displacement of $[Co(CO)_4]^-$ occurs and a small amount of $[SiCo_9(CO)_{21}]^{2-}$ is produced. However the reaction with $[Fe(CO)_3NO]^-$ occurs readily at room temperature and under these conditions the major products of this reaction are $[FeCo_3(CO)_{12}]^-$ and $[NCo_6(CO)_{15}]^-$, neither of which retains the Si atom. $[FeCo_3(CO)_{12}]^-$ was also identified as a product of the analogous $[Fe_2(CO)_8]^{2-}$ reaction.

It is not unusual for nitrido clusters to be formed by the reaction of $[Fe(CO)_3NO]^-$ with transition metal clusters. For example, the reaction with $Fe_3(CO)_{12}$ produces the $[NFe_4(CO)_{12}]^{2-}$ "butterfly" cluster [190]. Although there are numerous reports of reactions involving the conversion of a coordinated NO ligand to a nitrido ligand [214] the details of NO bond cleavage remain vague. The nitrido atom may have been formed by reaction with an adjacent CO group, with CO_2 elimination. Alternatively the NO bond cleavage may occur on the cluster surface, giving oxido and nitrido ligands, followed by elimination of the oxygen as CO_2. The Si atom may also play a role in abstracting the nitrosyl oxygen. This could also help explain the loss of the Si.

Table 3.23: Infrared Spectra of Unidentified Product

Observed Spectrum (in CH_2Cl_2)	$[Ge_2Co_5Fe_2(CO)_{22}]^-$ (in CH_2Cl_2) [33]	$[GeCo_5(CO)_{16}]^-$ (in CH_2Cl_2) [92]
2072w	2071w	2078w
2015vs	2016vs	2052m
1948w	1946w	2025vs
1916m	1913m	2000sh
	1810w	1820w
1605vw		

The product isolated from the reaction between $Ge[Co_2(CO)_7]_2$ and $[Et_4N][Fe(CO)_3NO]$ appeared to retain the Ge atom. An electron probe analysis detected Ge, Fe and Co in an approximate ratio of 2 : 2 : 5. The infrared spectrum of this compound (**table 3.23**) is remarkably similar to that reported for $[Ge_2Co_5Fe_2(CO)_{22}]^{2-}$ ***(F 10)*** (the product of the reaction between $Ge[Co_2(CO)_7]_2$ and $[Fe_2(CO)_8]^{2-}$). It exhibits almost identical terminal carbonyl stretching modes, but there is no evidence of a bridging carbonyl gorup, equivalent to that bridging the two Fe atoms in $[Ge_2Co_5Fe_2(CO)_{21}]^{2-}$ (1810 cm^{-1}). Instead there appears to be a very weak nitrosyl stretching mode at 1605 cm^{-1}. This suggests a $[Ge_2Fe_2Co_5(CO)_{19}(NO)_2]^-$ anion with one of the following structures:

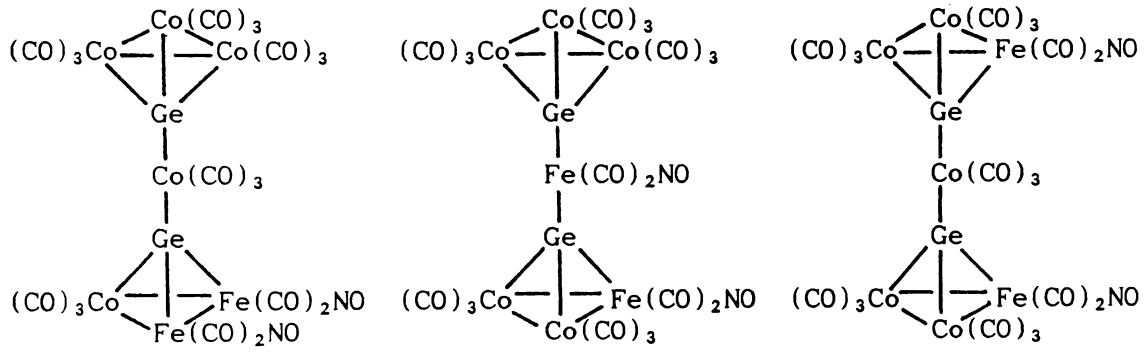

It has been suggested that $[Ge_2Co_7(CO)_{21}]^-$ ***(F 9)*** and $[Ge_2Co_5Fe_2(CO)_{22}]^-$ ***(F 10)***, which also have this type of structure, are formed via the reaction of an intermediate $[GeM_5(CO)_x]^-$ anion with a neutral $GeM_4(CO)_x$ cluster (see section 3.1.2). A similar mechanism could account for the formation of the proposed "$[GeCo_3Fe_2(CO)_{14}(NO)_2]^-$" species. For example:

$$Ge[Co_2(CO)_7]_2 + [Fe(CO)_3NO]^- \rightarrow GeCo_3Fe(CO)_{12}NO$$

$$GeCo_3Fe(CO)_{12}NO + [Fe(CO)_3NO]^- \rightarrow "[GeCo_3Fe_2(CO)_{14}(NO)_2]^-"$$

$$"[GeCo_3Fe_2(CO)_{14}(NO)_2]^-" + GeCo_3Fe(CO)_{12}NO \rightarrow [Ge_2Co_5Fe_2(CO)_{19}(NO)_2]^- + CoFe(CO)_7NO$$

X-ray diffraction studies indicated a molecular weight of approximately 3370/Z. For the $P2_12_12_1$ space group it is rare for Z not to equal 4. This implies a molecular weight of *ca.* 843. As indicated above, there was some ambiguity over the space group and even the

symmetry of the unit cell. If the suggested monoclinic $P2_1/c$ space group is chosen, Z may also equal 2 providing the anion has internal symmetry, giving a molecular weight of *ca.* 1686. In either case the calculated molecular weight is not in very good agreement with that of the proposed "$[GeCo_3Fe_2(CO)_{14}(NO)_2]^-$" anion (Mr = 1274).

If a simple addition reaction were occurring, it is possible that a $[Et_4N][GeCo_4Fe(CO)_{15}NO]$ (Mr = 944) species is being produced. However, when the infrared spectrum of the iso-structural $[GeCo_5(CO)_{16}]^-$ anion is compared with that of the unidentified product, significant differences are apparent (**table 3.23**). Also, the Co : Fe ratio for this species is higher than that detected by electron probe analysis.

It is also feasible for $[Fe(CO)_3NO]^-$ to displace two Co groups, giving $[Et_4N][(CO)_7Co_2GeFe(CO)_3NO]$ (Mr = 687).

In the end it is hard to go past the remarkable similarity between the infrared spectra of the unidentified product and $[GeCo_5Fe_2(CO)_{22}]^-$, and a "$[GeCo_3Fe_2(CO)_{14}(NO)_2]^-$" cluster seems the most likely alternative.

No reaction was observed between $Ge[Co_2(CO)_7]_2$ (or $(CO)_4CoGeCo_3(CO)_9$) and $[Fe(CO)_4]^{2-}$. It was hoped that $[Fe(CO)_4]^{2-}$ would displace a $-Co(CO)_4$ group producing a $[(CO)_4FeGeCo_3(CO)_9]^-$ anion or a neutral $(CO)_9Co_3GeFe(CO)_4GeCo_3(CO)_9$ species by reaction with further $(CO)_4CoGeCo_3(CO)_9$. The displacement series in section 1.4.1 suggests that this should occur.

The main impediment to reaction appeared to be the solubility of $Na_2[Fe(CO)_4]$ in CH_2Cl_2. In more polar solvents (eg. THF) the $ECo_4(CO)_x$ clusters decompose.

Earlier metal exchange reactions involving $H_3GeM(CO)_x$, $MeH_2GeM(CO)_x$ and $Me_2HGeM(CO)_x$ species were found to proceed in diethyl ether when no reaction was observed in hydrocarbon solvents [215]. It has been suggested that the ether promotes dissociation of the terminal $M(CO)_x$ group, facilitating attack by other more nucleophilic transition metal carbonyl anions. $Na_2[Fe(CO)_4]$ is unlikely to be any more soluble in ether, but it may add on to a bare Ge easier than having to actively displace a $-Co(CO)_4$ group.

It would probably be worth repeating not only this but other metal exchange reactions in diethyl ether. Unfortunately this possibility was only realised following the completion of most of this work, but is

worth bearing in mind for future studies.

To date there is no convenient accepted method for synthesising the $[CpNi(CO)]^-$ anion, and controversy exists over some reported syntheses [216]. Although not strictly within the scope of this work, $Ge[Co_2(CO)_7]_2$ was reacted with the neutral $[CpNi(CO)]_2$ dimer. It was interesting that $[GeCo_5(CO)_{16}]^-$ ***(F 7)*** was identified as the major product, even though the presence of $[Co(CO)_4]^-$ was not detected at any stage. The counterion for $[GeCo_5(CO)_{16}]^-$ was not identified, but possibilities include $[Cp_2Co]^+$ and $[Cp_2Ni]^+$.

$CpNiCo(CO)_5$ and $CpCo(CO)_2$ were also identified as products of this reaction. Two other hexane soluble compounds were isolated but not in sufficient quantities to permit characterisation.

3.3.3 REACTIONS OF $E[Fe_2(CO)_8]_2$ CLUSTERS

The reactions of $E[Fe_2(CO)_8]_2$ clusters with transition metal carbonyl anions, $[Co(CO)_4]^-$, $[Mn(CO)_5]^-$ and $[Fe_2(CO)_8]^{2-}$, also did not produce the high nuclearity group 14-transition metal clusters that were hoped for.

No reaction was detected between $[Co(CO)_4]^-$ and $Si[Fe_2(CO)_8]_2$ or $Sn[Fe_2(CO)_8]_2$. When $[Et_4N][Co(CO)_4]$ was heated for long periods with $Si[Fe_2(CO)_8]_2$ or $Sn[Fe_2(CO)_8]_2$ a reaction was observed, however in both cases Cl^- proved to be the reacting species. This came from very small amounts of Et_4NCl present in the $[Et_4N][Co(CO)_4]$. The reaction of $Si[Fe_2(CO)_8]_2$ was able to be reproduced by heating the cluster with a trace amount of Et_4NCl. Furthermore, no reaction was observed when $Sn[Fe_2(CO)_8]_2$ was heated with $K[Co(CO)_4]$, aside from the gradual decomposition of $[Co(CO)_4]^-$ to $Co_4(CO)_{12}$.

In the reactions of $Si[Fe_2(CO)_8]_2$ and $Sn[Fe_2(CO)_8]_2$ with Cl^-, the clusters were gradually consumed and unidentified products were detected in very low yield. The individual products of these two reactions showed distinctly different infrared spectra and different solubilities. However both were only obtained in very low yield and gradually decomposed. This prevented further characterisation.

When $Si[Fe_2(CO)_8]_2$ and $Ge[Fe_2(CO)_8]_2$ were heated with $[Mn(CO)_5]^-$, both reactions produced $Mn_2(CO)_{12}$ and a product identified as $[CFe_6(CO)_{16}]^{2-}$ (**figure 3.13**). The formation of $[CFe_6(CO)_{16}]^{2-}$ is perhaps not so surprising when we consider that it has previously been synthesied by heating $[Mn(CO)_5]^-$ with $Fe(CO)_5$ **[100]**. This reaction

initially produces $[MnFe_2(CO)_{12}]^-$, which when heated gives $[CFe_6(CO)_{16}]^-$. $[MnFe_2(CO)_{12}]^-$ can also be produced by reacting $[Mn(CO)_5]^-$ with $Fe_2(CO)_9$ [217]. Considering the similarity between the E-bridged ends of the *spiro*-$E[Fe_2(CO)_8]_2$ clusters and $Fe_2(CO)_9$, it seems reasonable that reaction with $[Mn(CO)_5]^-$ would also produce $[MnFe_2(CO)_{12}]^-$ and with heating, $[CFe_6(CO)_{16}]^{2-}$. Note that $[MnFe_2(CO)_{12}]^-$ was not detected in either of the above reactions, but then reaction only occurred when the solutions were heated.

The reactions of $Si[Fe_2(CO)_8]_2$ and $Sn[Fe_2(CO)_8]_2$ with $[Fe_2(CO)_8]^{2-}$ similarly failed to produce clusters containing group 14 atoms. No reaction was observed at room temperature, and when the reaction mixtures were heated to ~40°C, $[HFe_3(CO)_{11}]^-$ and $[Fe_4(CO)_{13}]^{2-}$ were produced. Unidentified weak infrared peaks were seen at ~2016 and ~1957 cm^{-1} in the ether fractions of both reactions, but this product could not be isolated or characterised.

The fact that no new group 14-transition metal clusters were isolated from the reactions of $E[Fe_2(CO)_8]_2$ was disappointing. In the case of $[Co(CO)_4]^-$ this was perhaps not so surprising. $[Co(CO)_4]^-$ follows $[Fe(CO)_4]^{2-}$ in the displacement series, which makes any reactions involving metal substitution unlikely. However the general lack of success in these reactions may be attributable to a number of factors:

a) The *spiro*-$E[Fe_2(CO)_8]_2$ clusters are less strained than their cobalt counterparts, and therefore probably less reactive (see introduction).

b) The greater number of CO ligands and larger intra-triangle M-E-M angles would mean that the group 14 atom is better shielded in the $E[Fe_2(CO)_8]_2$ clusters than in their $E[Co_2(CO)_7]_2$ counterparts. It would therefore be less susceptable to attack.

c) Unlike the $ECo_4(CO)_x$ compounds, the $E[Fe_2(CO)_8]_2$ clusters do not have and cannot readily form terminal $-M(CO)_x$ groups, which act as sites for reaction. $E[Fe_2(CO)_8]_2$ clusters cannot condense down to form analogues of $(CO)_4CoECo_3(CO)_9$.

d) The difficulty in forming EFe_3 trigonal pyramids may in itself be a hinderance, since ECo_3 units form the basis for higher nuclearity group 14-cobalt clusters.

e) Finally, the loss of the group 14 atom in such reactions occurs much more frequently than originally anticipated. This unfortunately

seems to be a common feature of reactions involving group 14-transition metal clusters and transition metal carbonyl anions. As mentioned above, E-O-C-M interactions could be involved, although this is less likely for Ge and Sn. In any event, the mechanism involved in the removal of the main group atom is likely to be very complex and probably differs in each case. Presumably the group 14 atom eventually ends up amongst the insoluble residues remaining in the reaction vessel. No attempts were made to characterise these insoluble products.

3.3.4 CONCLUSIONS

Unfortunately these reactions of $EM_4(CO)_x$ clusters with transition metal anions did not produce the high nuclearity group 14-transition metal clusters that were hoped for. The main reason for this appeared to be the loss of the main group atom during reaction. This is more of a problem with Si than with Ge, and more of a problem for the $EFe_4(CO)_x$ clusters than for their $ECo_4(CO)_x$ counterparts. An understanding of how the main group atom is lost is crucial to understanding the mechanisms involved in these reactions. This is likely to be a very complicated process and probably varies from reaction to reaction.

When this problem is added to those associated with the generally unpredictable, messy and often capricious nature of reactions involving transition metal anions and group 14-transition metal clusters, this does not appear to be as good a method for cluster synthesis as originally anticipated.

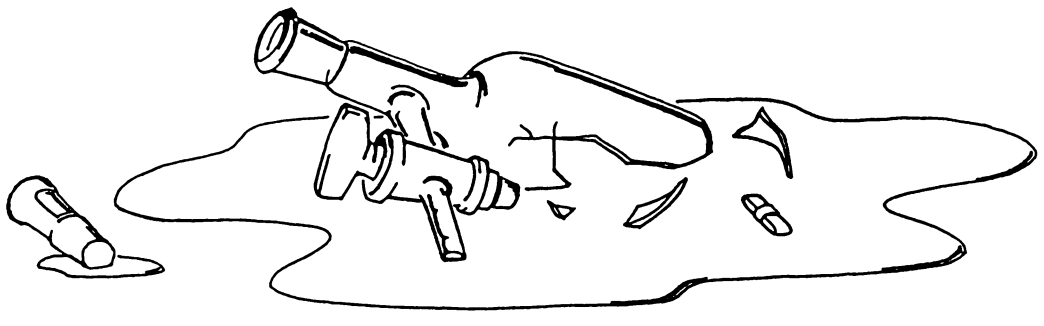

Chapter Four

Structures of compounds frequently refered to in this thesis are depicted in a fold-out section in Appendix A. The symbol *(F #)* is used in the text to refer readers to these diagrams.

CHAPTER 4 REACTIONS OF THE GROUP 14 TRANSITION METAL CLUSTER ANIONS: $[SiCo_9(CO)_{21}]^{2-}$ AND $[GeCo_5(CO)_{16}]^-$

4.1 INTRODUCTION

4.1.1 REDOX CONDENSATION REACTIONS OF CLUSTER ANIONS

Reactions of anionic transition metal clusters with cationic or neutral species have to date provided a generally successful strategy for synthesising clusters of increased nuclearity [13].

Protonation Reactions

A number of high nuclearity clusters reported in the literature have been formed by the protonation of anionic clusters. The small size of H^+ apparently allows it to add to the metal core, when other electrophiles tend to be attracted to sites of highest electron density in the ligand sphere. For many multiply charged anions, the degree of protonation can be controlled by the selection of acid and solvent. For example, the protonation of $[Os_5(CO)_{15}]^{2-}$ [218], $[Os_6(CO)_{18}]^{2-}$ [219], $[Os_7(CO)_{20}]^{2-}$ [13], $[Os_8(CO)_{22}]^{2-}$ [13] and $[Os_{10}C(CO)_{24}]^{2-}$ [113], with sulphuric acid in CH_2Cl_2 or THF gives the corresponding monohydrides. However in acetonitrile, dihydrides are produced.

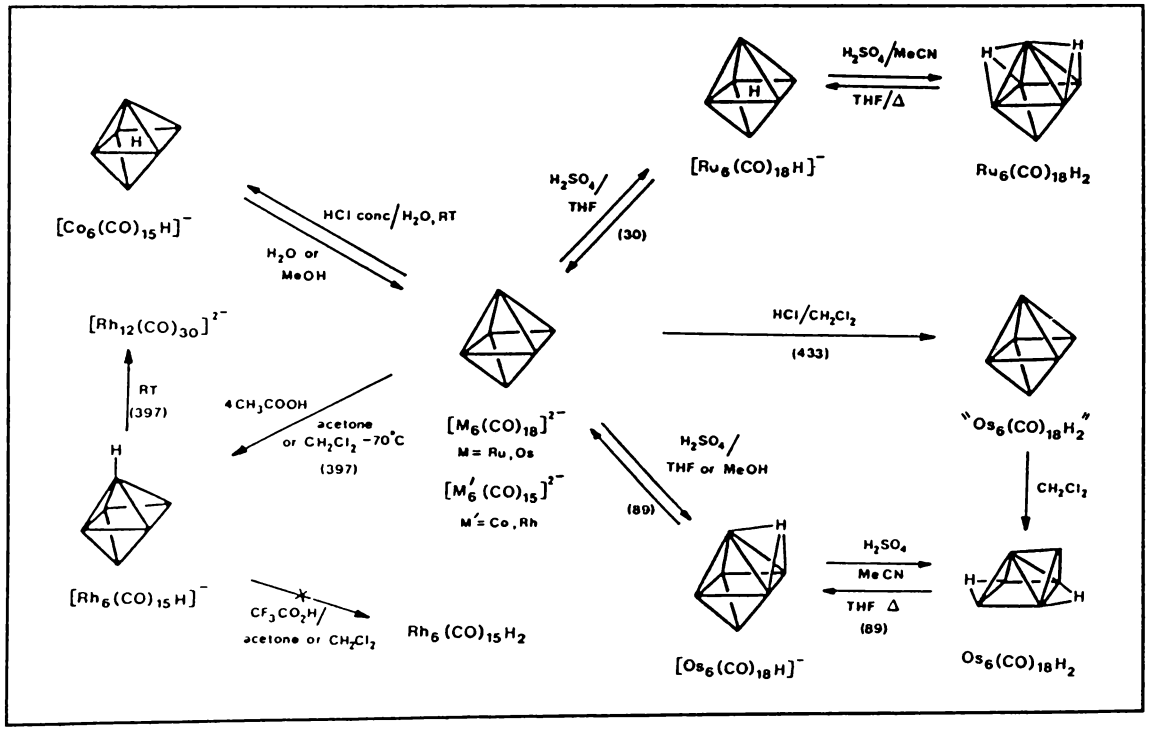

Figure 4.1: Protonation reactions of $[M_6(CO)_{18}]^{2-}$ (M = Ru, Os) and $[M_6(CO)_{15}]^{2-}$ (M = Co, Rh) (from reference [13])

It is not possible to predict the site that a hydride atom will occupy, even in a homologous series of compounds (see **figure 4.1**). However there is some evidence indicating a preference for sites of highest electron density **[13]**. In the literature, protonation most frequently occurs at an edge-bridging site. A few clusters with face-capping hydrides are known (eg. $Ru_6(CO)_{18}H_2$ **[220]**), and terminal hydride ligands have been reported for $Os_6(CO)_{19}H_2$ **[221]** and $[Rh_6(CO)_{15}H]^-$ **[222]**. A number of clusters with interstitial hydrides are also known (*eg.* $[Co_6(CO)_{15}H]^-$ and $[Ru_6(CO)_{18}H]^-$ in **figure 4.1**).

The addition of protons to anionic carbonyl clusters does not affect the number of skeletal electrons, yet in some cases protonation is accompanied structural rearrangements (*eg.* $Os_6(CO)_{18}H_2$ in **figure 4.1**) or by unexpected chemical transformations **[223]**:

$$3[Ni_6(CO)_{12}]^{2-} + 2H^+ \rightarrow 2[Ni_9(CO)_{18}]^{2-} + H_2$$

$$2[Ni_9(CO)_{18}]^{2-} + H^+ \rightarrow [Ni_{12}(CO)_{21}H]^{3-} + Ni(CO)_4 + 3Ni + CO$$

$$[Ni_{12}(CO)_{21}H]^{3-} + H^+ \rightleftharpoons [Ni_{12}(CO)_{21}H_2]^{2-}$$

and **[5]**:

$$[Fe_4(CO)_{13}]^{2-} + H^+ \rightarrow [HFe_4(CO)_{13}]^-$$

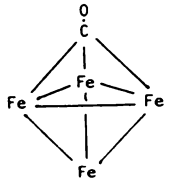

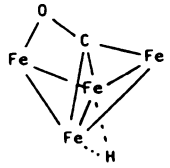

Addition of NO^+

The treatment of carbonyl cluster anions with the nitrosonium ion, NO^+, can result in CO substitution **[224,214]**:

$$[NFe_4(CO)_{12}]^- + NO^+ \rightarrow NFe_4(CO)_{11}(NO) + CO$$

$$[CRe_7(CO)_{21}]^{3-} + NO^+ \rightarrow [CRe_7(CO)_{20}(NO)]^{2-} + CO$$

or in M-M bond cleavage [214,225]:

$$[H_3Os_4(CO)_{12}]^- + NO^+ \xrightarrow[CH_2Cl_2]{} H_3Os_4(CO)_{12}(NO)$$

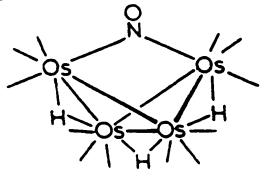

$$[COs_{10}(CO)_{24}]^{2-} + NO^+ \rightarrow [COs_{10}(CO)_{24}(NO)]^-$$

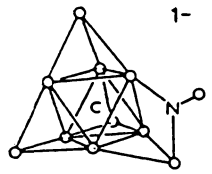

The product of the latter reaction, $[COs_{10}(CO)_{24}(NO)]^-$, contains a μ_2-NO, but undergoes decarbonylation over a period of 10 days to give $[COs_{10}(CO)_{23}(NO)]^-$, with a terminal nitrosyl group.

The high oxidation potential of NO^+ means that less robust clusters are frequently destroyed by the nitrosonium ion. Protonation of cluster anions has also been observed with NO^+, even under "anhydrous" conditions [214]:

$$[NRu_4(CO)_{12}]^- + NO^+ \rightarrow HRu_4N(CO)_{12}$$

Reactions with Metal Cations

Several condensation reactions involving salts of Ag(I), Au(I), Hg(I), Hg(II) and Tl(III) with anionic clusters have been reported [13]. These reactions produce conglomerates in which the introduced metal atom bridges two or more cluster units, each essentially retaining their initial metal cluster geometry. For example [226,227]:

$$2[RuCo_3(CO)_{12}]^- + HgBr_2 \rightarrow [RuCo_3(CO)_9]_2Hg + 6CO + 2Br^-$$

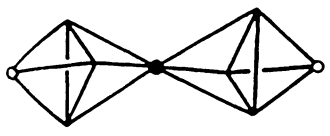

$$[Os_3(CO)_{11}H]^- + HgBr_2 \rightarrow Os_9Hg_3(CO)_{33}$$

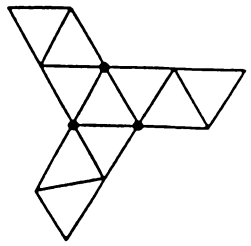

The synthesis of $[C_2Os_{20}(CO)_{48}Hg]^{2-}$ from the reaction of $[COs_{10}(CO)_{24}]^{2-}$ with RHgY (R = C_6F_5, C_6H_5, Cl, CF_3COO; Y = CF_3COO, Cl) has been shown to proceed via the formation of the $[COs_{10}(CO)_{24}(HgR)]^-$, intermediate, which undergoes condensation when left standing for up to a week [228]. Spectroscopic evidence suggests that in $[COs_{10}(CO)_{24}(HgR)]^-$, the RHg group adopts a μ_3-face-capping position.

Reactions with Cationic Mononuclear Metal Complexes

Reactions with $[(MeCN)_4M]^+$ (M = Cu, Ag) and $[R_3PM]^+$ (M = Cu, Ag, Au) fragments have provided a general method for incorporating an additional metal atom into the core of anionic clusters [13]. The resulting coordinated $[(MeCN)M]^+$ and $[R_3PAu]^+$ units provide no skeletal electrons to the cluster, and therefore should not induce any structural rearrangements. This however is not always the case (eg. $Os_8(CO)_{22}(AuPPh_3)_2$ [229]).

Evans and Mingos [230] have shown that for R_3PM fragments, the metal orbitals with predominantly d-character are filled, and that the bonding characteristics of these fragments are determined primarily by the hybrid (s-z) orbital (a_1 symmetry) and higher lying degenerate pair of p_x and p_y orbitals (e symmetry) (**figure 4.2**). In the case of R_3PAu, the p_x and p_y orbitals are much higher in energy and play only a secondary role in bonding. Thus the R_3PAu unit can be considered to be isolobal with a hydrido ligand. Much has been made of this analogy in the literature. It has been suggested that gold derivatives of clusters may be used to predict the position of hydrogen atoms in the corresponding hydrides [231]. In most cases, gold derivatives have proved to be structural analogues of the corresponding hydrides, but there are many exceptions (*eg.* $HCoRu_3(CO)_{13}$ and $Ph_3PAuCoRu_3(CO)_{13}$ [232]).

According to Mingos [233], the R_3PAu fragment effectively functions as $[R_3PAu]^+$, and provides an increment of 12 to the polyhedral electron

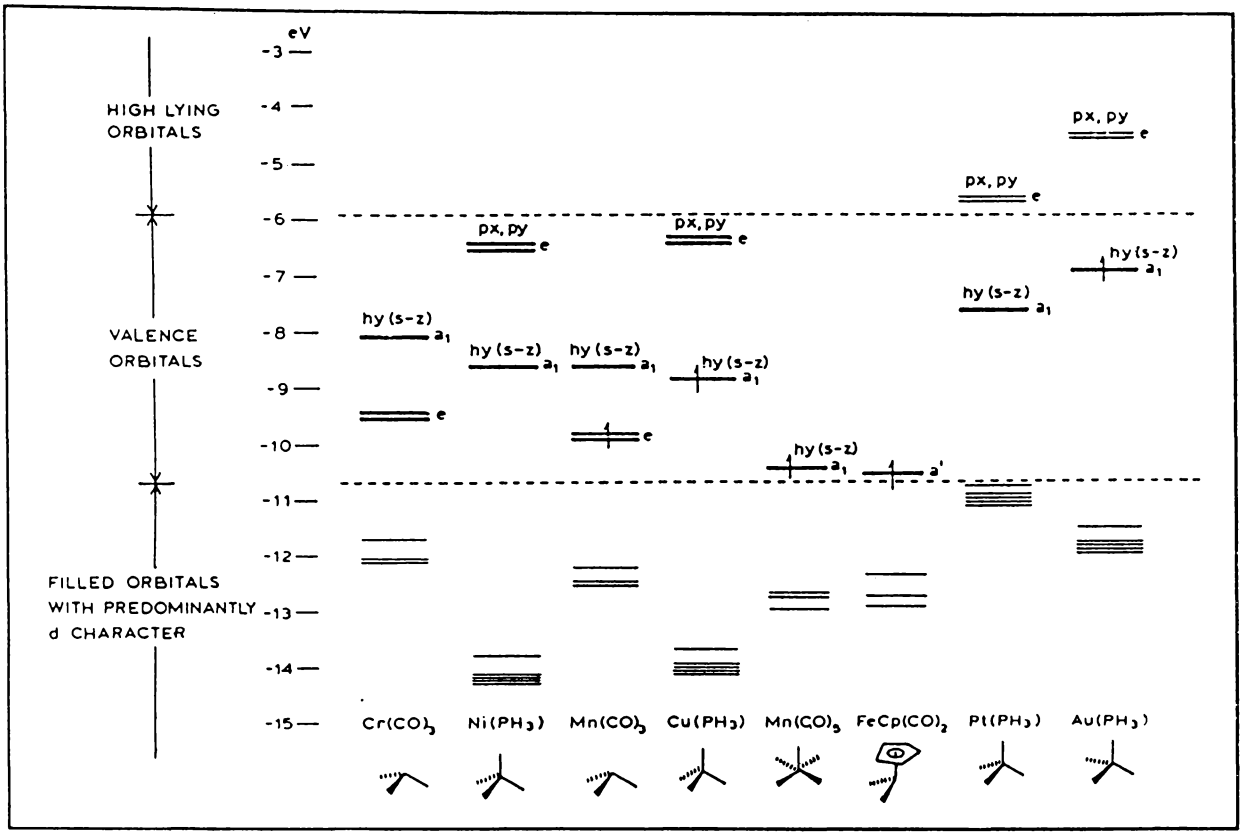

Figure 4.2: Relative energies of the frontier molecular orbitals for some transition metal fragments (from reference [233])

count in both the face-capping and edge-bridging bonding modes. In comparison, face-capping and edge-bridging metal carbonyl units lead to increments of 12 and 14 respectively. Therefore gold containing clusters have two fewer electrons per edge-bridging R_3PAu group than predicted by electron counting principles.

The ability of the R_3PAu fragment to adopt μ_2- and μ_3-bonding modes, in both cases increasing the polyhedral electron count by 12, can account for the stereochemical non-rigidity of many gold containing clusters. ^{31}P and ^{13}C n.m.r. spectra of $CRh_6(CO)_{13}(AuPPh_3)_2$ indicate that in solution, the Ph_3PAu fragments migrate all over the Rh frame in a manner reminiscent of CO, even at very low temperatures [120]. Therefore it is not surprising that in crystallographic studies, the bonding geometry of R_3PAu appears to be influenced mainly by the need to reduce non-bonding interactions.

In contrast, the copper fragments have a stronger preference for face-capping positions, and there are several instances where $[R_3PAu]^+$and $[LCu]^+$ bind differently to the same cluster (*eg.*

$CRh_6(CO)_{15}(ML)$, ML = $CuPPh_3$, $AuPPh_3$ [234]; $H_3Ru_3(CO)_9(ML)$, ML = $CuPPh_3$, $CuPPh_2Me$, CuNCMe, $AuPPh_3$ [234]; $[COs_{10}(CO)_{24}(ML)]^-$, ML = CuNCMe, $AuPPh_3$ [116]). In LCu, the valence hybrid (s-z), p_x and p_y orbitals are lower in energy, providing a better isolobal analogy with the $2a_1$ and 2e frontier orbitals of $Mn(CO)_3$ [230]. This accounts for the preference for μ_3-bonding. Clusters containing edge-bridging μ_2-CuL groups, however, are known and several cases have been reported recently (*eg.* $Ru_3(CO)_9(C_2Bu^t)(CuPPh_3)$ [116] and $H_3Os_3(CO)_{10}(CuPPh_3)$ [235]).

Reactions with Neutral Metal Complexes

Carbonyl cluster anions also undergo condensation reactions with neutral metal complexes, particularly when the neutral metal complex is coordinatively unsaturated or readily generates a coordinatively unsaturated fragment. Frequently unsaturation in the neutral metal complex is achieved by the displacement of halide atoms. For example, $[CCo_3Ni_9(CO)_{20}]^{3-}$ is one of the products formed when $[Ni_6(CO)_{12}]^{2-}$ is reacted with $ClCCo_3(CO)_9$ [131].

Tachikawa *et al.* have described a number of square pyramidal CFe_4M, and octahedral CFe_5M and CFe_4M_2 clusters, formed by reacting $[CFe_4(CO)_{12}]^{2-}$ and $[CFe_5(CO)_{14}]^{2-}$ with unsaturated metal fragments (figure 4.3) [236]. In each of these cases, the incoming metal atom completes a previously incomplete metal polyhedron. Tachikawa *et al.* also noted that similar condensation reactions did not occur for monoanionic species like $[CFe_4Rh(CO)_{14}]^-$, and attributed this to insufficient electron density on the cluster.

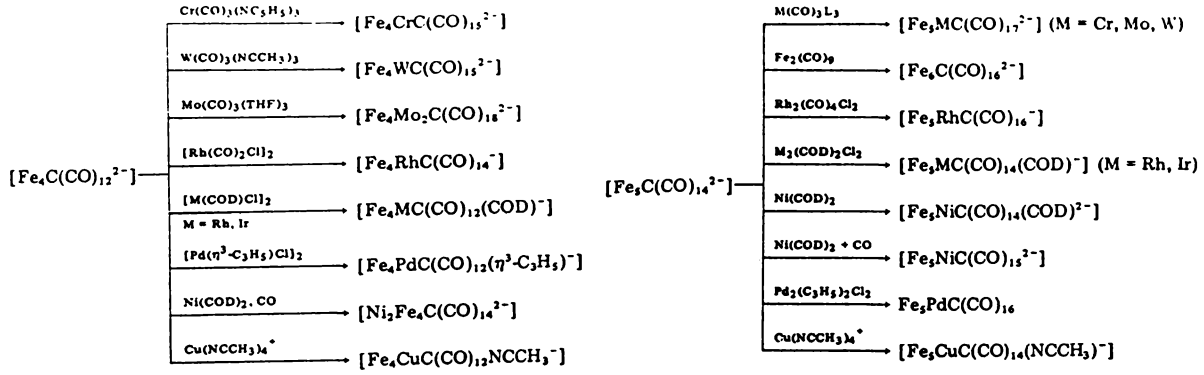

Figure 4.3: Some reactions of $[CFe_4(CO)_{12}]^{2-}$ and $[CFe_5(CO)_{14}]^{2-}$ with unsaturated metal fragments

4.1.2 REACTIONS OF $[SiCo_9(CO)_{21}]^{2-}$ AND $[GeCo_5(CO)_{16}]^-$

The $[SiCo_9(CO)_{21}]^{2-}$ and $[GeCo_5(CO)_{16}]^-$ anions are shown in figure 4.4, and their structures are discussed in more detail in section 3.1.2.

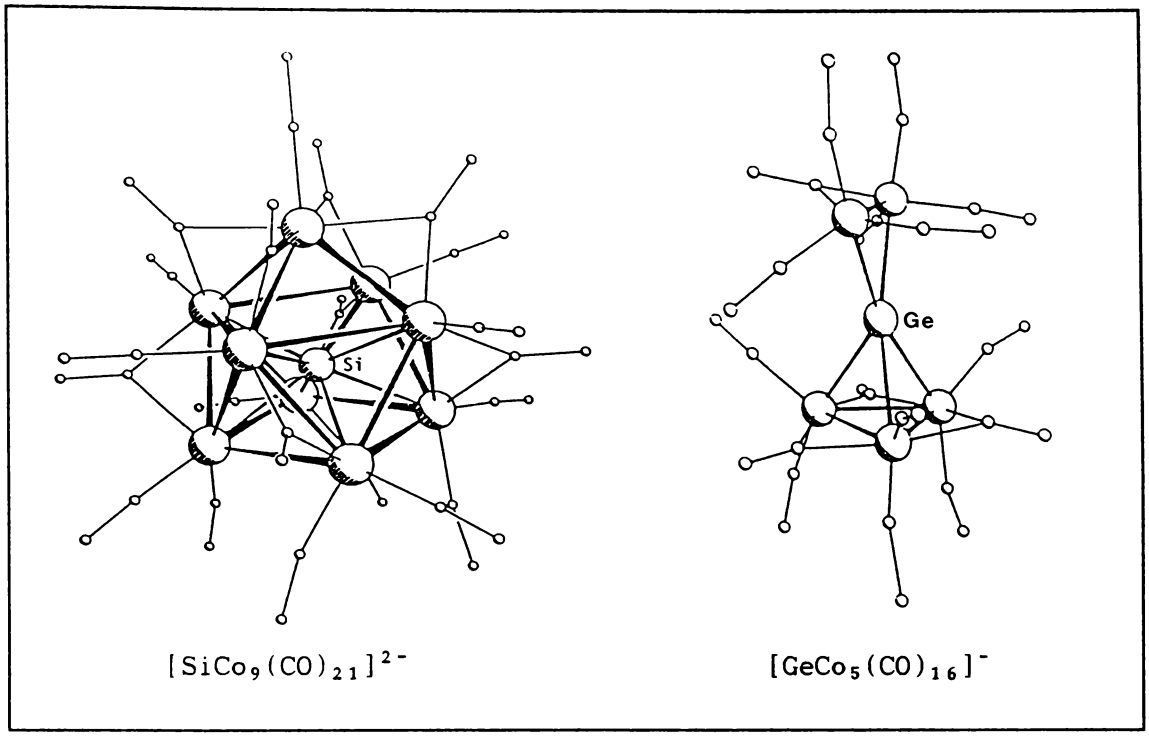

Figure 4.4: Structures of $[SiCo_9(CO)_{21}]^{2-}$ and $[GeCo_5(CO)_{16}]^-$

$[SiCo_9(CO)_{21}]^{2-}$ is unique in that it is the only cluster known to contain a fully encapsulated Si atom. The surrounding Co atoms describe a square antiprism with the remaining Co capping one of the square faces. Since this structure appears quite stable, it seems feasible that the uncapped $SiCo_8$ and bicapped $SiCo_{10}$ analogues could also be synthesised; possibly by removing the capping Co atom on $[SiCo_9(CO)_{21}]^{2-}$, or by capping the second square face. Stable uncapped square antiprism structures have been reported for $[CCo_8(CO)_{18}]^{2-}$ [9] and $[CNi_8(CO)_{16}]^{2-}$ [130], and bicapped square antiprism structures for $[PRh_{10}(CO)_{22}]^{3-}$ [237] and $[SRh_{10}(CO)_{22}]^{2-}$ [238].

In $[GeCo_5(CO)_{16}]^-$, the Ge atom is coordinated to five Co atoms. It caps a $Co_3(CO)_9$ moiety as well as bridging a $Co_2(CO)_7$ unit. It may also be possible to increase the nuclearity of $[GeCo_5(CO)_{16}]^-$ by introducing more metal atoms to the metal core. Higher nuclearity

clusters containing fully encapsulated Ge atoms have been reported ($[GeNi_{10}(CO)_{22}]^{2-}$ and $[GeNi_{10}(CO)_{20}]^{2-}$ [133]).

To date, the only reaction of $[GeCo_5(CO)_{16}]^-$ to be investigated is that with $Co_2(CO)_8$, yielding $[Ge_2Co_7(CO)_{21}]^-$ [32]. This reaction is thought to proceed via the initial formation of $(CO)_4CoGeCo_3(CO)_9$, which then reacts with further $[GeCo_5(CO)_{16}]^-$ (see section 3.1.2).

The reactions of $[SiCo_9(CO)_{21}]^{2-}$ with H^+, Hg^{2+} and $[Ph_3PAu]^+$ have been investigated, but the products of each of these reactions have not been fully characterised [33].

The reaction between $[SiCo_9(CO)_{21}]^{2-}$ and Ph_3PAuCl was found to produce a black insoluble product. An electron probe analysis of the $[Et_4N]^+$ salt indicated a Si : Co : Au : P ratio of approximately 3 : 39 : 1 : 1. An extremely small single crystal was isolated, from which the crystal system and unit cell dimensions were determined (orthorhombic, a = 10.6 Å, b = 41.0 Å, c = 11.4 Å, U = 4954 $Å^3$, D_M = 1.82 g cm^{-3}, M_r = 5431/Z).

When $[SiCo_9(CO)_{21}]^{2-}$ was reacted with $HgCl_2$, a product was isolated, which gradually decomposed over *ca.* 10 h to produce a green Co(II) precipitate. The carbonyl infrared spectrum of this species is relatively simple (ν_{CO} (CH_2Cl_2) 2098w, 2038sh, 2029s, 1815w,br cm^{-1} [33]), suggesting a reasonably symmetrical structure. The peak positions also suggest a single negative charge.

A spectroscopically identical product was obtained from the reaction of $[SiCo_9(CO)_{21}]^{2-}$ with H_3PO_4. This product was also unstable, decomposing before it could be fully characterised. It is possible that hydrogen and mercury add on to the $[SiCo_9(CO)_{21}]^{2-}$ cluster in a similar manner (*ie.* as H^+ and XHg^+). The unstable $[COs_{10}(CO)_{24}(HgR)]^-$ cluster described above, is the only reported case where RHg+ adds onto a cluster in this fashion. It is also possible that H^+ and Hg^{2+} are disrupting the $[SiCo_9(CO)_{21}]^{2-}$ capped square antiprism to give identical products.

4.1.3 AIMS

In the current study, the attempted protonation of $[SiCo_9(CO)_{21}]^{2-}$ was repeated using different combinations of acid and solvent. It was hoped that a dihydride could be isolated and characterised. This would in turn give support to the argument that, in previous reactions, H^+ and XHg^+ were adding onto the $[SiCo_9(CO)_{21}]^{2-}$ cluster, rather than

disrupting it.

Further attempts were also made to characterise the unidentified product formed in the reaction between $[SiCo_9(CO)_{21}]^{2-}$ and Ph_3PAuCl. Other possible condensation reactions involving the electrophiles, $[BuNCAu]^+$, $[(MeCN)Cu]^+$ and NO^+, were also investigated in the hope of synthesising and fully characterising novel high nuclearity carbonyl clusters.

Cp_2Co was originally reacted with $[SiCo_9(CO)_{21}]^{2-}$ in an attempt to reduce the cluster (section 5.2.4.3). however, this appears to result in a condensation reaction and was therefore included in this chapter.

An unsaturated metal fragment, suitable for condensation reactions can be generated by elimination of the halide atom from the neutral $CpFe(CO)_2I$ complex. The addition of the $[CpFe(CO)_2]^+$ fragment onto organic compounds is well documented **[240,241,242]**, and it was thought that this application could be extended to transition metal cluster chemistry. Both $[SiCo_9(CO)_{21}]^{2-}$ and $[GeCo_5(CO)_{16}]^-$ were reacted with $CpFe(CO)_2I$ in the presence of $TlBF_4$ (added to expedite the elimination of the halide).

$[GeCo_5(CO)_{16}]^-$ was also reacted with $[CpNi(CO)]_2$. It was thought that this reaction might proceed in a similar manner to the reaction with $Co_2(CO)_8$ (outlined above), and could provide clarification of the mechanism involved. A condensation reaction was also considered feasible. $[CpNi(CO)]_2$ is known to act as a source of CpNi in reactions with $Os_3(CO)_{12}$ and $HRu_3(CO)_9(C_6H_9)$, producing $Cp_3Ni_3Os_3(CO)_9$ **[243]** and $CpNiRu_3(CO)_8(C_6H_9)$ **[244]** respectively. Alternatively, a Ni atom could displace a Co on $[GeCo_5(CO)_{16}]^-$. Exchange reactions of this type have been described by Vahrenkamp for neutral clusters containing EM_3 trigonal pyramids **[30,5]**. The yields from these reactions tend to be low and the substitution mechanism is not well understood.

It was also considered possible that the cationic metal fragments might react by abstracting $[Co(CO)_4]^-$ from $[GeCo_5(CO)_{16}]^-$ or $[SiCo_9(CO)_{21}]^{2-}$. In the latter case, this might lead to the formation of an uncapped analogue of $[SiCo_9(CO)_{21}]^{2-}$.

4.2 EXPERIMENTAL

4.2.1 REACTIONS OF $[SiCo_9(CO)_{21}]^{2-}$ *(F 12)*

4.2.1.1 $[SiCo_9(CO)_{21}]^{2-}$ and Ph_3PAuCl

The $[Et_4N]^+$ and $[PPN]^+$ salts of $[SiCo_9(CO)_{21}]^{2-}$ were reacted with

Ph_3PAuCl.

(i) $[Et_4N]_3[SiCo_9(CO)_{21}][Co(CO)_4]$ (0.10 g, 0.06 mmol) was reacted with three molar equivalents of Ph_3PAuCl (0.09 g, 0.18 mmol) in CH_2Cl_2 (20 ml). The reaction mixture was stirred in a Schlenk flask under nitrogen atmosphere, and the progress of the reaction was followed using infrared spectroscopy.

A rapid initial reaction was observed during which the $[Co(CO)_4]^-$ ν_{CO} peak at 1889 cm^{-1} disappeared and peaks at 2052s, 1984m and 1960s cm^{-1} were produced. These peaks are consistent with those reported for $Ph_3PAuCo(CO)_4$ (ν_{CO} (hexane) 2055s, 1986m, 1960s cm^{-1} [239]). The ν_{CO} infrared peaks due to $[SiCo_9(CO)_{21}]^{2-}$ slowly decreased in intensity, and after 5 h, all the $[SiCo_9(CO)_{21}]^{2-}$ appeared to have reacted. $Ph_3PAuCo(CO)_4$ was the only soluble product observed by infrared spectroscopy. The CH_2Cl_2 solution was decanted, leaving a dark brown crystalline product (I) in the bottom of the reaction vessel. This species also proved insoluble in THF, MeCN and methanol.

A solid-state infrared spectrum of a sample of product I showed the following infrared vibrations: ν_{CO} (KBr disc) 2028vw, 1965s, 1907sh, 1890sh, 1760m, 1740m cm^{-1} (**figure 4.5**). Distinctive $[Et_4N]^+$ peaks were also seen at ~1160, ~990 and ~775 cm^{-1}, but no Ph_3P infrared bands were detected.

A crystalline sample was also used for negative ion FABS mass spectroscopy. It must be noted that FABS mass spectroscopy requires that the sample is dispersed throughout the matrix. Because of the low solubility of product I, it is possible that the sample preparation technique and the "sputtering" process may have enhanced the signals from minor product(s), marginally more soluble in the cosolvent/matrix mixture. That is, the mass spectrum may not be representative of the bulk of the sample.

As in the mass spectrum of $[Et_4N]_3[SiCo_9(CO)_{21}][Co(CO)_4]$ (Chapter 3.2.1.1), the fragmentation pattern of product I (**table 4.1**) exhibits two series of peaks which appear to represent different compounds. The best assignment for the highest peak in the mass spectrum (m/e = 1277) appears to be $[CCo_{11}(CO)_{22}]^-$, containing a carbido atom. This peak is related to a succession of weak peaks representing $[CCo_{11}(CO)_n]^-$ (n = 22 to 17) and $[CCo_9(CO)_n]^-$ (n = 18 to 7) fragments. Note that Si has the same mass as a CO group so it is possible that Si is also

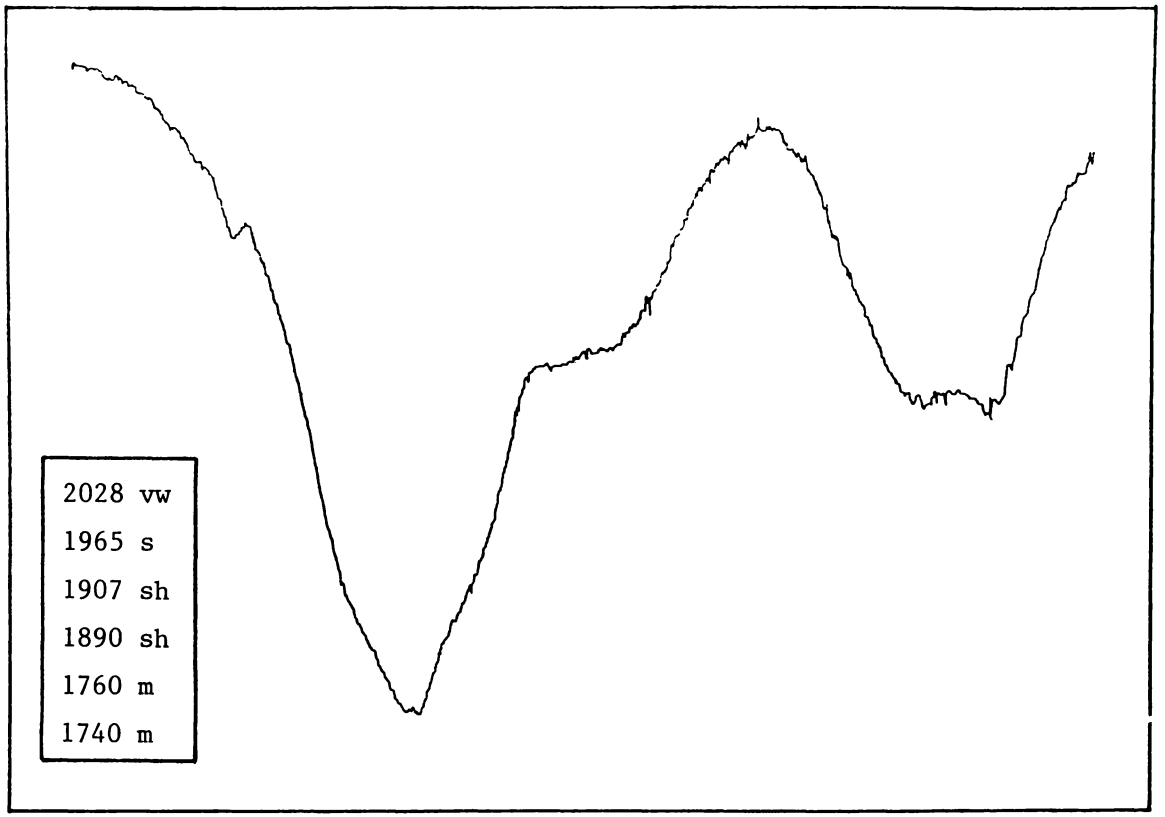

Figure 4.5: Solid-state infrared spectrum of product I (KBr disc)

Table 4.1: FABS mass spectroscopic fragmentation pattern for product I

m/e	Int.	Possible Assignments		
		Fragments containing Si	Fragments contining non-carbonyl C	Other
1277	4		$[CCo_{11}(CO)_{22}]^-$	
1249	3		$[CCo_{11}(CO)_{21}]^-$	
1221	2		$[CCo_{11}(CO)_{20}]^-$	
1193	1		$[CCo_{11}(CO)_{19}]^-$	
1175	28	$[SiCo_9(CO)_{22}]^-$		
1165	1		$[CCo_{11}(CO)_{18}]^-$	
1147	70	$[SiCo_9(CO)_{21}]^-$		
1137	1		$[CCo_{11}(CO)_{17}]^-$	
1119	100	$[SiCo_9(CO)_{20}]^-$		
1091	74	$[SiCo_9(CO)_{19}]^-$		
1063	34	$[SiCo_9(CO)_{18}]^-$		
1047	2		$[CCo_9(CO)_{18}]^-$	
1035	31	$[SiCo_9(CO)_{17}]^-$		
1019	1		$[CCo_9(CO)_{17}]^-$	
1007	25	$[SiCo_9(CO)_{16}]^-$		
991	4		$[CCo_9(CO)_{16}]^-$	
979	26	$[SiCo_9(CO)_{15}]^-$		
976	3	$[SiCo_8(CO)_{17}]^-$		
963	4		$[CCo_9(CO)_{15}]^-$	
951	26	$[SiCo_9(CO)_{14}]^-$		
948	3	$[SiCo_8(CO)_{16}]^-$		
935	6		$[CCo_9(CO)_{14}]^-$	
923	21	$[SiCo_9(CO)_{13}]^-$		
920	4	$[SiCo_8(CO)_{15}]^-$		
907	5		$[CCo_9(CO)_{13}]^-$	
895	18	$[SiCo_9(CO)_{12}]^-$		
892	4	$[SiCo_8(CO)_{14}]^-$		
879	4		$[CCo_9(CO)_{12}]^-$	
867	13	$[SiCo_9(CO)_{11}]^-$		
864	6	$[SiCo_8(CO)_{13}]^-$		
851	3		$[CCo_9(CO)_{11}]^-$	
839	11	$[SiCo_9(CO)_{10}]^-$		
836	4	$[SiCo_8(CO)_{12}]^-$		
823	7		$[CCo_9(CO)_{10}]^-$	
811	10	$[SiCo_9(CO)_9]^-$		
808	4	$[SiCo_8(CO)_{11}]^-$		
795	4		$[CCo_9(CO)_9]^-$	
783	6	$[SiCo_9(CO)_8]^-$		
780	4	$[SiCo_8(CO)_{10}]^-$		
767	4		$[CCo_9(CO)_8]^-$	
755	5	$[SiCo_9(CO)_7]^-$		
752	4	$[SiCo_8(CO)_9]^-$		
739	3		$[CCo_9(CO)_7]^-$	
727	4	$[SiCo_9(CO)_6]^-$		
646	5		$[CCo_6(CO)_{10}]^-$	
616	4	$[SiCo_9(CO)_2]^-$		
590	3		$[CCo_6(CO)_8]^-$	
587	3	$[SiCo_9(CO)]^-$		
562	3		$[CCo_6(CO)_7]^-$	
544	4	$[SiCo_4(CO)_{10}]^-$		$[Co_4(CO)_{11}]^-$
534	6		$[CCo_6(CO)_6]^-$	
516	3	$[SiCo_4(CO)_9]^-$		$[Co_4(CO)_{10}]^-$
488	3	$[SiCo_4(CO)_8]^-$		$[Co_4(CO)_9]^-$
457-459	11	$[SiCo_4(CO)_6]^-$		$[Co_3(CO)_{10}]^-$ (Matrix)$_3^-$
450	3		$[CCo_6(CO)_3]^-$	
401	4	$[SiCo_3(CO)_7]^-$		$[Co_3(CO)_8]^-$
353	5			
304-306	49		$[CCo_4(CO)_2]^-$	(Matrix)$_2^-$

present. Unfortunately the spectrum is not sufficiently resolved to permit detection of Si from the isotope pattern.

The second series of peaks is much more intense and the fragments do not contain a carbido atom. The parent ion has m/e = 1175, which is consistent with either $[SiCo_9(CO)_{22}]^-$ or $[Co_9(CO)_{23}]^-$. In the preliminary investigation of this reaction [33], Si was detected in product I by electron probe analysis. Therefore $[SiCo_9(CO)_{22}]^-$ was assumed to be the parent ion. A stepwise loss of CO groups from $[SiCo_9(CO)_{22}]^-$ produces a series of peaks corresponding to $[SiCo_9(CO)_n]^-$ (n = 22 to 6) fragments. The loss of one Co atom gives a similar succession of decarbonylated fragments: $[SiCo_8(CO)_n]^-$ (n = 17 to 9).

It is unlikely that these two series of peaks relate to the same compound (eg. $[CSiCo_{11}(CO)_{21}]^{n-}$) because the formation of the m/e = 1175 fragment would require the loss of a CCo_2 fragment without the loss of any CO groups.

The peak at m/e = 459 is consistent with a $[Ph_3PAu]^-$ fragment, however this peak, along with the exceptionally strong peak at m/e = 306 were also observed in other negative ion FABS mass spectra reported in this work. These peaks appear to represent the combination of two and three matrix molecules.

(ii) The reaction was repeated by layering Ph_3PAuCl (0.026 g, 0.054 mmol) in benzene on top of a CH_2Cl_2 solution of $[Et_4N]_3[SiCo_9(CO)_{21}][Co(CO)_4]$ (0.030 g, 0.018 mmol) in a 10 mm-diameter Schlenk tube at -63.5°C (chloroform slush bath). At this temperature the benzene freezes. The slush bath was removed and the contents of the Schlenk flask allowed to slowly warm to 4°C in a refrigerator. As the benzene melted, the benzene solution of Ph_3PAuCl gradually diffused into the CH_2Cl_2 solution, allowing the Ph_3PAuCl to react with the $[Et_4N]_3[SiCo_9(CO)_{21}][Co(CO)_4]$. In this way the reaction was slowed down in the hope that, as the insoluble product formed, it would crystallise out giving crystals suitable for X-ray diffraction studies. However the crystals produced were badly twinned, consisting of very thin superimposed plates.

(iii) Reaction (ii) was repeated using $[PPN]_2[SiCo_9(CO)_{21}]$ (0.04 g, 0.018 mmol). The $[PPN]^+$ salt of I also precipitated as a black

polycrystalline solid. Crystals of a quality suitable for X-ray diffraction studies were not obtained.

4.2.1.2 $[SiCo_9(CO)_{21}]^{2-}$ and (BuNC)AuCl

The $[Et_4N]^+$, $[PPN]^+$ and $[PhMe_3N]^+$ salts of $[SiCo_9(CO)_{21}]^{2-}$ were reacted with (BuNC)AuCl.

(i) A nitrogen flushed Schlenk flask was charged with $[Et_4N]_3[SiCo_9(CO)_{21}][Co(CO)_4]$ (0.077 g, 0.045 mmol) and (BuNC)AuCl (0.028 g, 0.090 mmol) in CH_2Cl_2 (20 ml). The reaction mixture was magnetically stirred at room temperature and the reaction was monitored using infrared spectroscopy.

In a rapid initial reaction, the $[Co(CO)_4]^-$ peak at 1889 cm^{-1} disappeared and was replaced by a broad feature at *ca.* 1970 cm^{-1}, on the side of the $[SiCo_9(CO)_{21}]^{2-}$ peak at 2004 cm^{-1}. In a slower reaction, the $[SiCo_9(CO)_{21}]^{2-}$ 2004 and 1790 cm^{-1} peaks shifted to higher frequency and a new peak emerged at ~2040 cm^{-1}. During the next 30 h the entire spectrum gradually shifted back to lower frequency. The 2052 cm^{-1} peak disappeared and the $[Co(CO)_4]^-$ peak reappeared at 1889 cm^{-1}. There appeared to be a certain amount of decomposition during this reaction, indicated by a drop in the intensities of the infrared spectra, and by the formation of an off-white precipitate. Some precipitation of $Au_{(s)}$ also occured on the inside of the reaction vessel. After 30 h the reaction appeared to have ceased. The solution was stirred for a further 8 h to ensure completion before being worked up.

The reaction mixture was filtered through a glass frit and the solvent removed under vacuum. A hexane extract (*ca.* 40 ml) appeared to contain a trace amount of $(BuNC)AuCo(CO)_4$ (ν_{CO} (hexane) 2148, 2055, 1964 cm^{-1}). The remaining products were redissolved in CH_2Cl_2. An infrared spectrum of this fraction revealed ν_{CO} peaks at 2150m, 1991s, 1824vw, 1790w cm^{-1} (**figure 4.6**), with a $[Co(CO)_4]^-$ peak at 1889 cm^{-1}.

The CH_2Cl_2 fraction was crystallised by slowly diffusing hexane into the CH_2Cl_2 solution at room temperature. This produced a mixture of white crystals (probably Et_4NCl and $[Et_4N][Co(CO)_4]$) and a black crystalline solid (unknown II). Partial separation of these products was achieved by placing the crystals in hexane and adding CCl_4 until a

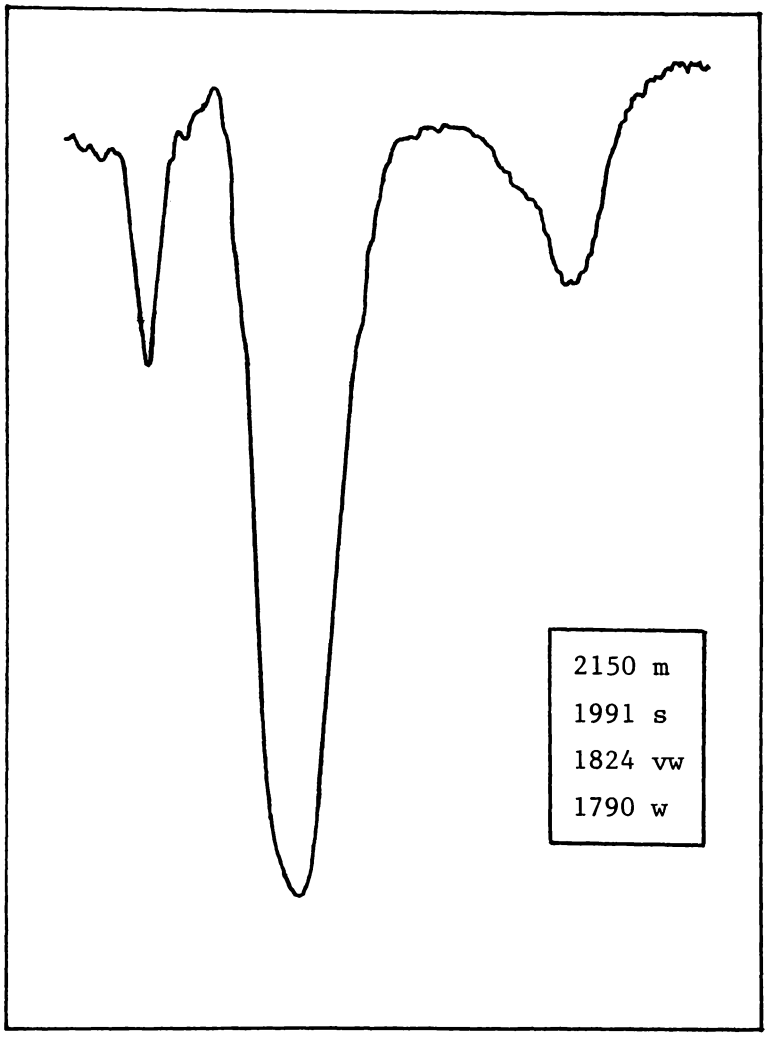

Figure 4.6: Infrared spectrum of product II (CH_2Cl_2 solution)

portion of the crystals (predominantly white) remained suspended. The hexane/CCl_4 mixture, with suspended crystals, was decanted off, and the remaining crystals redissolved in CH_2Cl_2. Attempts were made to grow crystals of II suitable for X-ray diffraction studies by cooling a CH_2Cl_2 solution, and by slow diffusion of hexane into a CH_2Cl_2 solution at 4°C; all without success.

(ii) $[Et_4N]_3[SiCo_9(CO)_{21}][Co(CO)_4]$ (0.077 g, 0.045 mmol) was reacted with (BuNC)AuCl (0.028 g, 0.090 mmol) in CH_2Cl_2 (20 ml) as described in (i). The reaction mixture was magnetically stirred for 1.5 h, until the predominant ν_{CO} infrared peak at 2004 cm^{-1} had shifted to *ca.* 2013 cm^{-1}. At this stage, the solution was filtered under nitrogen and the products were worked up.

A hexane extract contained $(BuNC)AuCo(CO)_4$. The remaining product(s) were found to be soluble in diethyl ether. This fraction was redissolved in CH_2Cl_2. An infrared spectrum revealed ν_{CO} peaks at 2155m, 2039w, 2012vs and 1798m,br cm^{-1}. This solution was stored in a fridge for *ca.* 24 h. During this period, the predominant ν_{CO} infrared peak returned to *ca.* 2000 cm^{-1}. Some decomposition had occured, but $[Co(CO)_4]^-$ was not detected in the infrared spectrum. The solution was left at room temperature for a further 24 h. A carbonyl infrared spectrum revealed product II, but the spectrum was less intense, indicating further decomposition. $[Co(CO)_4]^-$ was not detected.

(iii) $[PPN]_2[SiCo_9(CO)_{21}]$ (0.067 g, 0.030 mmol) was reacted with (BuNC)AuCl (0.019 g, 0.060 mmol) in CH_2Cl_2 (20 ml) as described in (i). The reaction proceeded in a similar manner and the products were worked up as previously described. Attempts were made to crystallise the $[PPN]^+$ salt of II by cooling a CH_2Cl_2 solution, and by slowly diffusing hexane into a CH_2Cl_2 solution at 4°C. No crystals suitable for X-ray diffraction studies were obtained.

(iv) $[PhMe_3N]_2[SiCo_9(CO)_{21}]$ (0.090 g, 0.052 mmol) and (BuNC)AuCl (0.033 g, 0.105 mmol) in CH_2Cl_2 (20 ml) were stirred under nitrogen, and the infrared spectrum of the solution monitored at regular intervals. $[PhMe_3N]_2[SiCo_9(CO)_{21}]$ is insoluble in CH_2Cl_2 and this appeared to prevent any reaction. No change was detected in the

infrared spectrum of the CH_2Cl_2 solution over a 40 h period.

The reaction vessel was placed in an oil bath and heated at 35-40°C for 8 h with continuous stirring. Still no reaction was detected. The CH_2Cl_2 solution was decanted, and a solid state infrared spectrum (KBr disc) of the insoluble species remaining in the reaction vessel revealed only unreacted $[PhMe_3N]_2[SiCo_9(CO)_{21}]$.

4.2.1.3 $[SiCo_9(CO)_{21}]^{2-}$ and $[(MeCN)_4Cu][PF_6]$

A nitrogen flushed Schlenk flask was charged with $[Et_4N]_3[SiCo_9(CO)_{21}][Co(CO)_4]$ (0.35 g, 0.2 mmol) in CH_2Cl_2 (50 ml) andchilled to -30°C (1,1,1,-trichloroethane slush bath). This solution was treated with $[(MeCN)_4Cu][PF_6]$ (0.15g, 0.4 mmol) in CH_2Cl_2 (20 ml) and stirred for 2 min at -30°C. A solution of Ph_3P (0.22 g, 0.82 mmol) in CH_2Cl_2 (20 ml) was then added. At this stage, an infrared spectrum of the solution indicated that the $[Co(CO)_4]^-$ had been consumed and new weak ν_{CO} peaks could be seen at 2030 and 1956 cm^{-1}.

After 15 min the reaction vessel was removed from the slush bath and allowed to gradually warm to room temperature. The infrared spectrum of the solution was monitored regularly. As the reaction proceeded, the intensity of the $[SiCo_9(CO)_{21}]^{2-}$ ν_{CO} peaks began to diminish and a reddish precipitate formed.

After an hour the solution was filtered through a glass frit and the reaction products were worked up. No hexane soluble products were detected. An infrared spectrum of the products contained in a diethyl ether extract (*ca.* 20 ml) revealed peaks at 2078vw, 2030s and 1956w cm^{-1}. However this product was retrieved in very low yield and decomposed over *ca.* 4 h at room temperature, preventing further characterisation. The remaining ether-insoluble fraction was redissolved in CH_2Cl_2 and an infrared spectrum revealed only unreacted $[SiCo_9(CO)_{21}]^{2-}$.

4.2.1.4 $[SiCo_9(CO)_{21}]^{2-}$ and Cp_2Co

$[Et_4N]_3[SiCo_9(CO)_{21}][Co(CO)_4]$ (0.120 g, 0.070 mmol) was treated with a solution of Cp_2Co (0.013 g, 0.069 mmol) in CH_2Cl_2 (40 ml) in a nitrogen flushed Schlenk flask.

After 5 min an infrared spectrum of the solution revealed that the weak $[SiCo_9(CO)_{21}]^{2-}$ ν_{CO} peak at 2055 cm^{-1} had disappeared, and a new peak had emerged at 2031 cm^{-1} with a shoulder at 2040 cm^{-1}. The rest

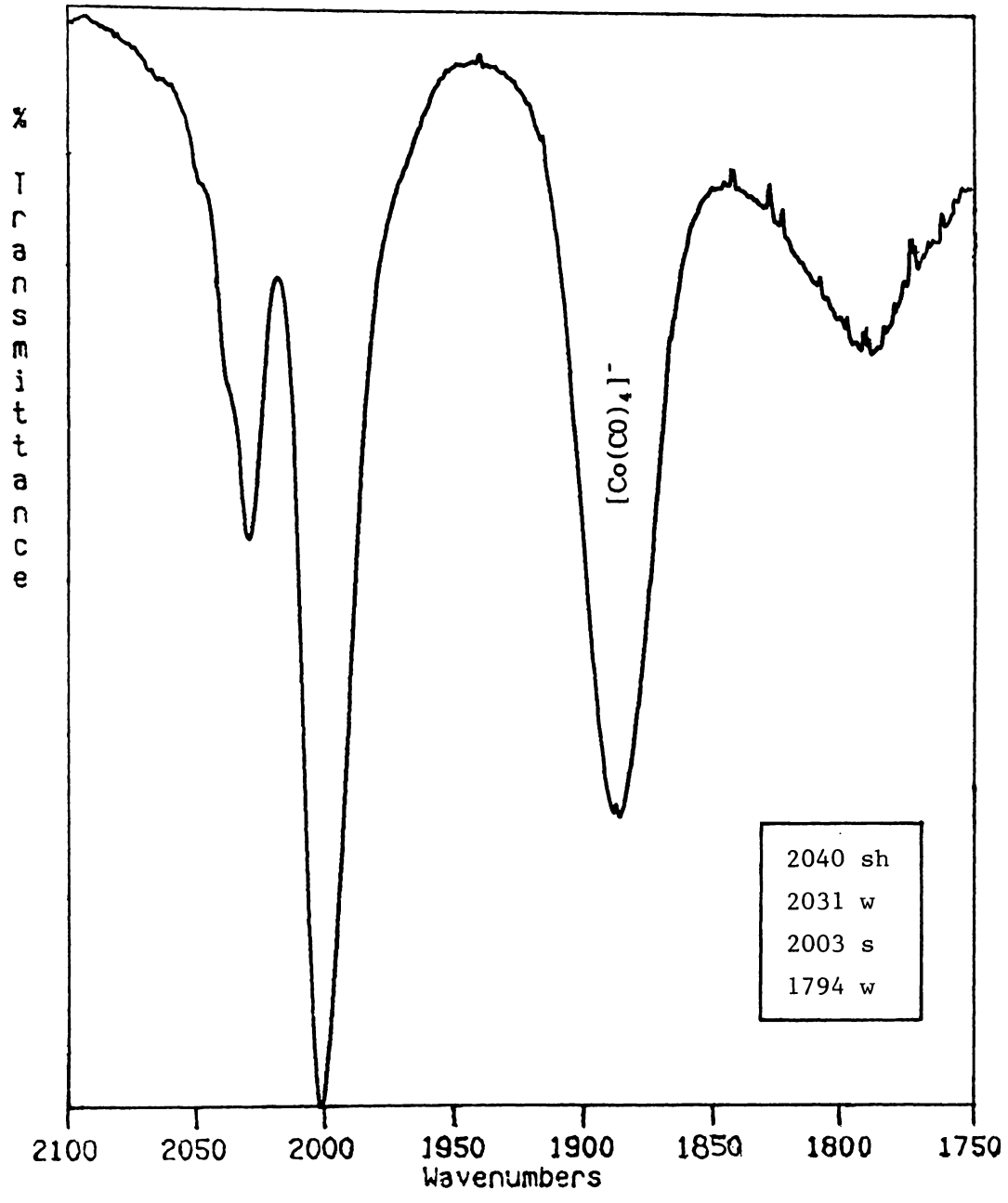

Figure 4.7: Infrared spectrum of product III (CH_2Cl_2 solution)

of the spectrum remained essentially unchanged. The reaction mixture was stirred for 1 h but no further reaction was detected.

The solution was then filtered and the CH_2Cl_2 solvent was removed under vacuum. No hexane-soluble or ether-soluble products were detected. The products also proved difficult to redissolve in CH_2Cl_2 and the addition of excess PPNCl was required to effect dissolution. A infrared spectrum of the product (III) showed ν_{CO} peaks at 2040sh, 2031w, 2003s and 1794mw,br cm^{-1} (figure 4.7), with a $[Co(CO)_4]^-$ peak at 1889 cm^{-1}.

Hexagonal brown plate-like crystals of this product were grown by slowly diffusing hexane into a CH_2Cl_2 solution at 4°C. These crystals were found to decompose rapidly in air. A preliminary X-ray diffraction analysis of a sample crystal revealed a hexagonal unit cell belonging to the $P6_3/m$ space group:

$$a = b = 28.87\ \text{Å},\ c = 27.78\ \text{Å}$$
$$\alpha = \beta = 90°,\ \gamma = 120°$$
$$U = 20047\ \text{Å}^3$$

Attempts to collect a full intensity data set were thwarted by decomposition of the crystal.

4.2.1.5 $[SiCo_9(CO)_{21}]^{2-}$ and H_2SO_4

(i) A drop of concentrated sulphuric acid (89%) was added to a solution containing $[Et_4N]_3[SiCo_9(CO)_{21}][Co(CO)_4]$ (0.25 g, 0.145 mmol) in CH_2Cl_2 (30 ml). The mixture was stirred in a Schlenk flask under nitrogen at room temperature. Reaction progress was monitored using infrared spectroscopy.

The ν_{CO} infrared peaks due to $[SiCo_9(CO)_{21}]^{2-}$ and $[Co(CO)_4]^-$, slowly diminished as the reaction proceeded. After 5 h the $[Co(CO)_4]^-$ ν_{CO} peak at 1889 cm^{-1} had dissappeared, and the $[SiCo_9(CO)_{21}]^{2-}$ ν_{CO} peaks were relatively weak. New peaks could also be seen at 2062w, 2052w, 2037sh, 2029s cm^{-1}. It took approximately 12 h for the reaction to finally go to completion.

A hexane extract of the reaction products was found to contain $Co_4(CO)_{12}$ only. An infrared spectrum of the remaining product (IV) in CH_2Cl_2 revealed ν_{CO} peaks at 2098w, 2038sh, 2029s, 1815w,br cm^{-1} (figure 4.8). This product proved to be unstable, gradually

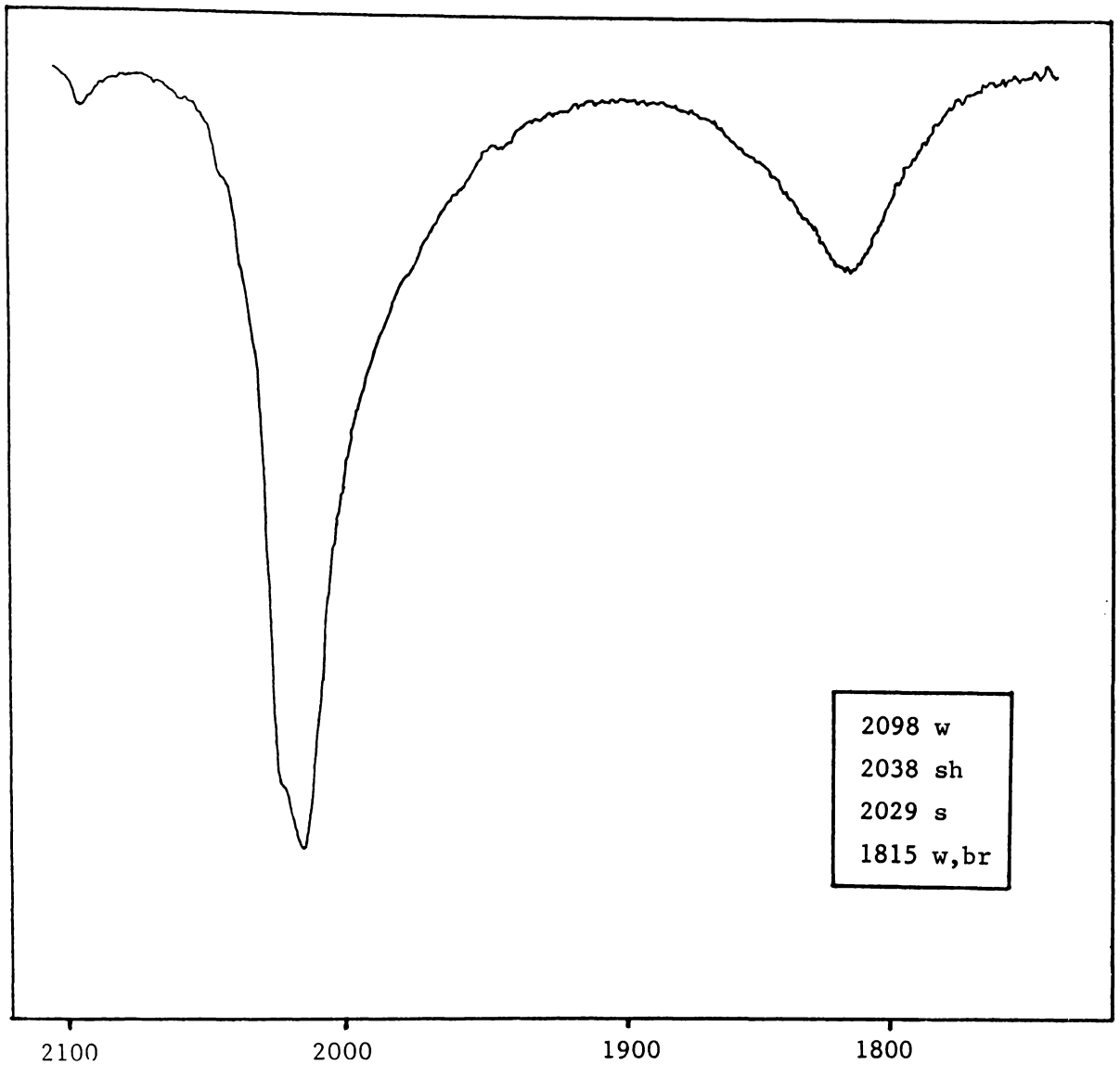

Figure 4.8: Infrared spectrum of product IV (CH_2Cl_2 solution)

decomposing even at -17°C to give a pink solid. Attempts to grow crystals of the product by cooling a CH_2Cl_2 solution and by slow diffusion of hexane into a CH_2Cl_2 solution were unsuccessful.

(ii) A drop of concentrated sulphuric acid (89%) was added to a solution of $[Et_4N]_3[SiCo_9(CO)_{21}][Co(CO)_4]$ (0.205 g, 0.119 mmol) in acetonitrile (30 ml). The reaction mixture was stirred under a nitrogen atmosphere, and the reaction was followed using infrared spectroscopy.

The $[Co(CO)_4]^-$ derived from the mixed salt was consumed in a rapid initial reaction. After 20 min, the $[Co(CO)_4]^-$ ν_{CO} peak at 1889 cm^{-1} had disappeared. $[SiCo_9(CO)_{21}]^{2-}$ reacted more slowly with the acid. As this reaction proceeded, the colour of the solution faded and a white precipitate formed. After 4 h only a very weak $[SiCo_9(CO)_{21}]^{2-}$ peak at 2004 cm^{-1} was evident in the ν_{CO} infrared spectrum. No ν_{CO} infrared active products were detected.

4.2.1.6 $[SiCo_9(CO)_{21}]^{2-}$ and $NOBF_4$

The $[Et_4N]^+$ and $[PPN]^+$ salts of $[SiCo_9(CO)_{21}]^{2-}$ were reacted with NO^+.

(i) $[Et_4N]_3[SiCo_9(CO)_{21}][Co(CO)_4]$ (0.170 g, 0.10 mmol) in CH_2Cl_2 (20 ml) was added to a nitrogen flushed Schlenk flask containing three molar equivalents of $NOBF_4$ (0.35 g, 0.30 mmol). The mixture was stirred at room temperature and the reaction monitored using infrared spectroscopy. The $NOBF_4$, which is only slightly soluble in CH_2Cl_2, reacted slowly with $[SiCo_9(CO)_{21}]^{2-}$. After 4 h the distinctive $[SiCo_9(CO)_{21}]^{2-}$ infrared bands at 2004 and 1790 cm^{-1} had disappeared, along with the $[Co(CO)_4]^-$ band at 1889 cm^{-1}.

The reaction mixture was filtered through a glass frit and the CH_2Cl_2 solvent removed under vacuum. An infrared spectrum of the products contained in an hexane extract (*ca.* 40 ml) showed carbonyl stretching modes characteristic of $Co_4(CO)_{12}$ (ν_{CO} (hexane) 2064s, 2055s, 2039w, 2028w, 1867m cm^{-1}), with very weak peaks at 2191, 1810 and 1793 cm^{-1}.

The remaining product (0.104 g) was found to be soluble in ether. An infrared spectrum, using CH_2Cl_2 as the solvent revealed ν_{CO} peaks at 2106w, 2032s, 1980vw,sh, 1801 cm^{-1} (**figure 4.9**). No peaks were

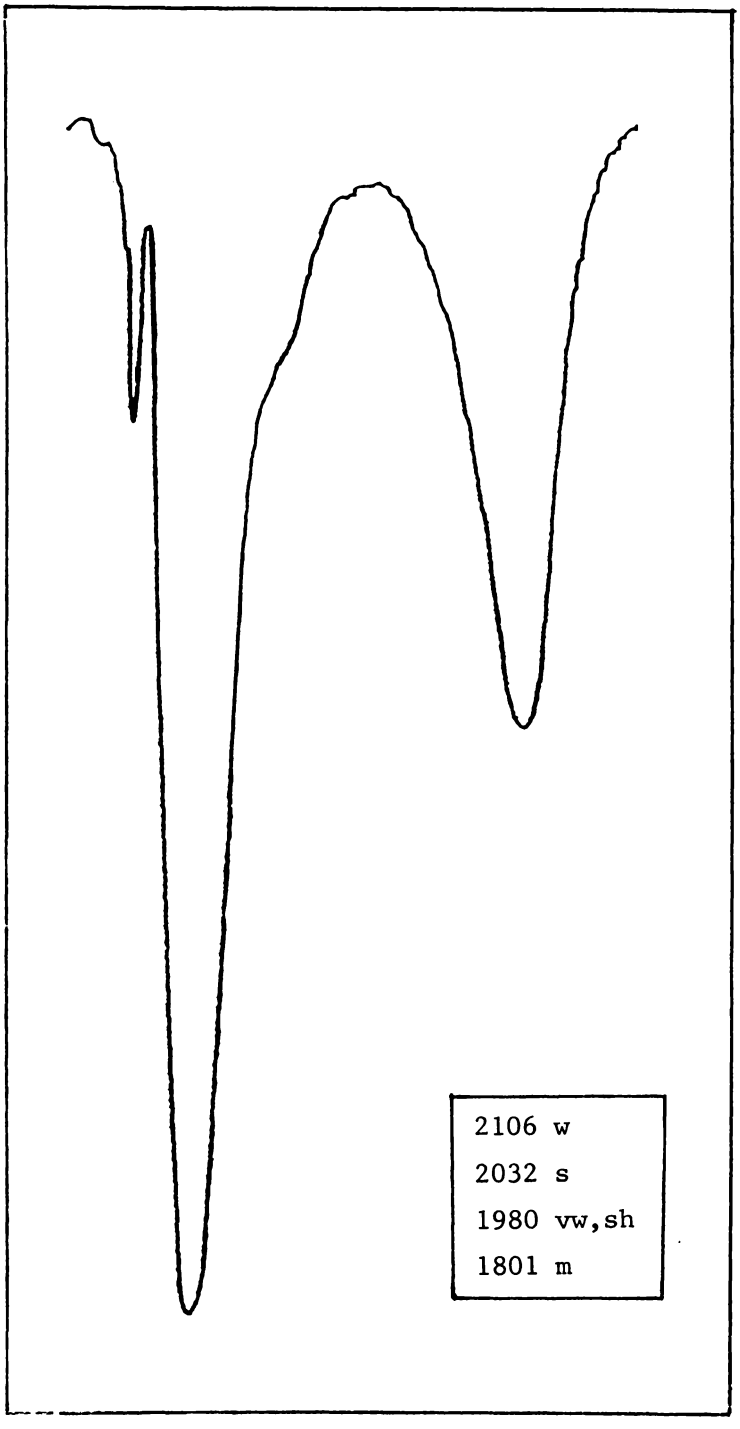

Figure 4.9: Infrared spectrum of product V (CH_2Cl_2 solution)

observed that could be assigned to NO stretching. This species is refered to as compound V.

Attempts were made to grow crystals of V by: cooling a diethyl ether solution; cooling a CH_2Cl_2 solution; and slowly diffusing hexane into an ether solution at 4°C. Small dark brown plate-like crystals were obtained by the latter method. A sample crystal was sealed in a glass capilliary and used for preliminary X-ray diffraction studies. A tetragonal unit cell was detected. 1.97 g cm^{-3} was taken as a reasonable value for the density, by comparison with $[Et_4N][Ge_2Co_7(CO)_{21}]$ [32].

$$a = 16.65 \text{ Å}$$
$$b = 16.65 \text{ Å}$$
$$c = 15.13 \text{ Å}$$
$$U = 4194 \text{ Å}^3, M_r = 4976/Z$$

This crystal was too small and too weakly diffracting to be suitable for full X-ray crystallographic analysis.

(ii) $[PPN]_2[SiCo_9(CO)_{21}]$ (0.222 g, 0.10 mmol) was reacted with $NOBF_4$ (0.023 g, 0.20 mmol) as described in (i). The reaction proceeded in a similar manner, producing $Co_4(CO)_{12}$ plus the unidentified product V. Attempts were made to grow crystals of the $[PPN]^+$ salt of V by: a) cooling a diethyl ether solution; b) cooling a CH_2Cl_2 solution; c) slow diffusion of hexane into a diethyl ether solution at 4°C; d) slow diffusion of diethyl ether into a CH_2Cl_2 solution at 4°C. No crystals suitable for X-ray diffraction studies were obtained.

(iii) $[Et_4N]_3[SiCo_9(CO)_{21}][Co(CO)_4]$ (0.100 g, 0.059 mmol) was reacted with excess $NOBF_4$ (0.038 g, 0.33 mmol) in CH_2Cl_2 (20 ml). As the reaction proceeded, the black-brown colour of the solution faded a little, and the solution became slightly murky, indicating decomposition. The solution was stirred for 8 h and the product worked up as previously described. $Co_4(CO)_{12}$ and V (0.026 g) were again isolated, but in reduced yields.

4.2.1.7 $[SiCo_9(CO)_{21}]^{2-}$ and $CpFe(CO)_2I$

$TlBF_4$ (0.26 g, 0.9 mmol) was added to a solution of $CpFe(CO)_2I$

(0.09 g, 0.3 mmol) in CH_2Cl_2 (*ca.* 10 ml). This was followed by the immediate addition of $[Et_4N]_3[SiCo_9(CO)_{21}][Co(CO)_4]$ (0.17 g, 0.1 mmol) in CH_2Cl_2 (*ca.* 20 ml). The reaction mixture was stirred magnetically under a nitrogen atmosphere and monitored using infrared spectroscopy.

After 3 h the $[Co(CO)_4]^-$ infrared peak at 1885 cm^{-1} had disappeared and a very fine pale green precipitate had begun to form (probably TlI with some Fe^{2+} or Co^{2+} species giving it the green tinge). The reaction mixture was stirred for a further 3 days until the $CpFe(CO)_2I$ peak at 2040 cm^{-1} was no longer evident. During this period a moderately strong peak emerged at ~2030 cm^{-1}, reaching maximum intensity after 48 h, then disappearing over the following 24 h. This species may have been $CpCo(CO)_2$ (ν_{CO} (CH_2Cl_2) 2032, 1971 cm^{-1}, see section 3.2.3.5), with the 1971 cm^{-1} peak concealed behind the $[SiCo_9(CO)_{21}]^{2-}$ spectrum.

After three days the infrared spectrum of the solution still closely resembled that of $[SiCo_9(CO)_{21}]^{2-}$, with additional weak peaks at 2064, 2020 and 1958 cm^{-1}. the reaction mixture was filtered under gravity through a glass frit, but the pale green precipitate could not be completely removed. The CH_2Cl_2 solvent was removed under vacuum and the hexane soluble products extracted. An infrared spectrum of the hexane fraction showed ν_{CO} peaks at 2068w, 2040m, 2016m, 2001s, 1978m, 1965w cm^{-1}. These peaks can be assigned to $CpCoFe(CO)_6$ (ν_{CO} (hexane) 2071(10), 2018(16.7), 2015, 2000(3.5), 1982(15.3), 1959(1.5), 1855, 1848, 1836, 1831(0.8) cm^{-1} **[245]**), plus unreacted $CpFe(CO)_2I$ (ν_{CO} (hexane) 2040, 2001 cm^{-1}).

A diethyl ether extraction (*ca.* 40 ml) was attempted, but no ether-soluble products were detected. The remaining ether-insoluble fraction was redissolved in CH_2Cl_2. An infrared spectrum revealed only unreacted $[SiCo_9(CO)_{21}]^{2-}$. Some of the insoluble pale green precipitate also remained.

4.2.2 REACTIONS OF $[GeCo_5(CO)_{16}]^-$ *(F 7)*

4.2.2.1 $[GeCo_5(CO)_{16}]^-$ and Ph_3PAuCl

Ph_3PAuCl (0.084 g, 0.17 mmol) was added to a solution of $[Et_4N][GeCo_5(CO)_{16}]$ (0.084 g, 0.17 mmol) in CH_2Cl_2 (*ca.* 30 ml) in a nitrogen flushed Schlenk flask. Changes in the reaction mixture were monitored using infrared spectroscopy.

The solution was stirred for 24 h at room temperature with no apparent reaction. The flask was heated at 35-40°C using an oil bath, and the solution was stirred for a further 6 h. During this period, weak peaks emerged at 1960 and 1889 cm^{-1}. At this stage the reaction was terminated and the reaction mixture was worked up.

The solution was filtered through a glass frit and the CH_2Cl_2 solvent was removed under vacuum. A hexane extract (*ca.* 40 ml) was found to contain a small amount of $Ph_3PAuCo(CO)_4$ (ν_{CO} (hexane) 2055s, 1986m, 1956s cm^{-1} [239]). An infrared spectrum of the remaining products, redissolved in CH_2Cl_2, revealed unreacted $[GeCo_5(CO)_{16}]^-$ plus a very weak $[Co(CO)_4]^-$ peak at 1889 cm^{-1}.

4.2.2.2 $[GeCo_5(CO)_{16}]^-$ and $[CpNi(CO)]_2$

$[Et_4N][GeCo_5(CO)_{16}]$ (0.148 g, 0.16 mmol) was added to $[CpNi(CO)]_2$ (0.032 g, 0.10 mmol) in CH_2Cl_2 (*ca.* 30 ml). The dark red solution was stirred for 24 h under a nitrogen atmosphere. During this period, no change was detected in the carbonyl infrared spectrum of the reaction mixture.

The reaction vessel was heated at 35-40°C (oil bath) with continuous stirring. As the reaction progressed, the distinctive $[GeCo_5(CO)_{16}]^-$ and $[CpNi(CO)]_2$ infrared peaks at 2033-2028 and 1841 cm^{-1} respectively, diminished in intensity and new peaks emerged at 1971 cm^{-1} and 1889 cm^{-1}.

After 2 days the reaction was terminated. The reaction mixture was filtered through a glass frit and the solvent was removed under vacuum. An initial hexane extract (*ca.* 40 ml) was found to contain $CpCo(CO)_2$ (ν_{CO} (CS_2) 2028, 1967 cm^{-1} [207]) plus unreacted $[CpNi(CO)]_2$. The remaining hexane-insoluble products were redissolved in CH_2Cl_2. A carbonyl infrared spectrum revealed a strong $[Co(CO)_4]^-$ peak at 1889 cm^{-1}, with an unidentified shoulder at ~1870 cm^{-1}, and a trace of unreacted $[GeCo_5(CO)_{16}]^-$.

4.2.2.3 $[GeCo_5(CO)_{16}]^-$ and $CpFe(CO)_2I$

$TlBF_4$ (0.05 g, 0.17 mmol) was added to a solution of $CpFe(CO)_2I$ (0.05 g, 0.17 mmol) in CH_2Cl_2 (*ca.* 10 ml). This was immediately followed by the addition of $[Et_4N][GeCo_5(CO)_{16}]$ (0.14 g, 0.15 mmol) in CH_2Cl_2 (*ca.* 20 ml). The reaction mixture was stirred under a nitrogen atmosphere and monitored using infrared spectroscopy.

As the reaction proceeded, the infrared peaks at ~2053 and ~1998 cm^{-1} increased in intensity and weak new shoulders appeared at ~2069 and ~2100 cm^{-1}. A very weak peak at 1889 cm^{-1}, initially due to residual $[Co(CO)_4]^-$ from the preparation of $[Et_4N][GeCo_5(CO)_{16}]$, at first disappeared but then reappeared after *ca.* 2 h. The reaction mixture was left stirring for a further 24 h, with no apparent change, before being worked up.

The solution was filtered through a glass frit and the CH_2Cl_2 solvent was removed under vacuum. An infrared spectrum of the products contained in a hexane extraction (*ca.* 40 ml), exhibited ν_{CO} bands at 2065vs, 2054s, 2011s, 1996sh, 1978sh, 1958sh, 1856m, 1810mw, 1774m cm^{-1}. These peaks were attributed to $Co_4(CO)_{12}$ (ν_{CO} (hexane) 2064s, 2055s, 2039w, 2028w, 1867m cm^{-1}), $CpFeCo(CO)_6$ (ν_{CO} (hexane) 2071(10), 2018(16.7), 2015, 2000(3.5), 1982(15.3), 1959(1.5), 1855, 1848, 1836, 1831(0.8) cm^{-1} **[245]**), and $[CpFe(CO)_2]_2$ (ν_{CO} (CH_2Cl_2) 1998(10), 1959(6.7), 1802, 1795(10) cm^{-1} **[246]**)

A subsequent diethyl ether extraction was concentrated and placed in a refrigerator overnight. By morning, small black plate-like crystals had formed. An infrared spectrum of sample crystals, redissolved in CH_2Cl_2, showed ν_{CO} bands at 2053m, 2033s, 2028s, 1998m, 1822m cm^{-1}. This product was later identified as $[GeCo_7(CO)_{20}]^-$ (ν_{CO} (CH_2Cl_2) 2054s, 2033s, 2028s, 1990w, 1825m,br cm^{-1} **[32]**), as shown in **(F 8)**.

A suitable crystal was sealed in a glass capilliary and investigated using X-ray crystallography. Preliminary diffraction studies indicated a monoclinic unit cell belonging to the $P2_1/c$ space group. A density of 1.89 g cm^{-3} was determined by flotation in a solution of aqueous $ZnBr_2$.

$$a = 12.73\ Å \qquad \alpha = 90°$$
$$b = 18.76\ Å \qquad \beta = 103°$$
$$c = 16.95\ Å \qquad \gamma = 90°$$
$$U = 3945\ Å^3,\ M_r = 4491/Z$$

If Z is assumed to equal 4, this would indicate a mass of approximately 1127, which is consistent with the $[Et_4N][GeCo_7(CO)_{20}]$ formulation (M_r = 1175.48). A crystal structure has been previously reported for

$[Et_4N][GeCo_7(CO)_{20}]$ by Duffy *et al.* [32] (Monoclinic, space group $P2_1/c$, a = 12.761(7) Å, b = 18.415(3) Å, c = 17.675(4) Å, β = 102.91(3)°, U = 4048 $Å^3$, D_{calc} = 1.93 g cm^{-3}).

The remaining ether-insoluble products were redissolved in CH_2Cl_2. An infrared spectrum of this fraction indicated that $[Co(CO)_4]^-$ and unreacted $[GeCo_5(CO)_{16}]^-$ were the only carbonylates present.

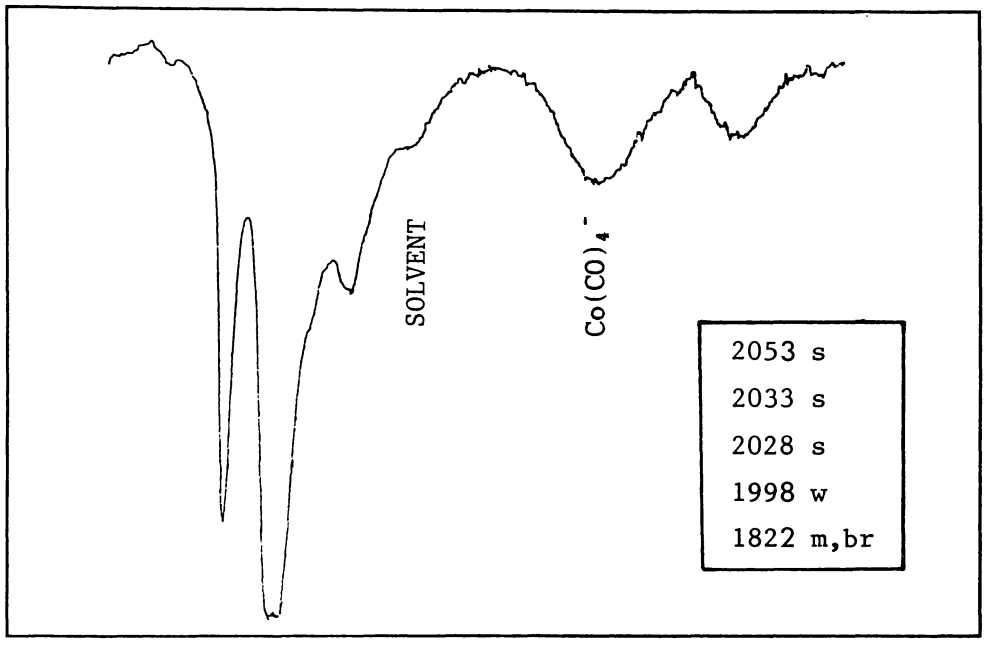

Figure 4.10: Infrared spectrum of $[GeCo_7(CO)_{20}]^-$

4.3 DISCUSSION

4.3.1 REACTIONS OF $[SiCo_9(CO)_{21}]^{2-}$ *(F 12)*

The reaction between $[SiCo_9(CO)_{21}]^{2-}$ and $[Ph_3PAu]^+$ was repeated and compound I was isolated as an insoluble black solid. Attempts at growing crystallographic-quality crystals of I by layering the reactants in different solvents and by varying the cation were unsuccessful.

The frequencies of the carbonyl stretching modes in the infrared spectrum of I suggest a negative charge of at least three. $[Et_4N]^+$ bands were also detected by infrared spectroscopy, however there was no evidence of Ph_3P being present. This implies that $[Ph_3PAu]^+$ is not adding onto the cluster. A previous electron probe analysis of I [33] had detected phosphorus and gold, as well as silicon and cobalt, but at

very low levels (at a ratio of approximately 1 : 1 : 3 : 39 respectively). These signals may have been due to background noise or contamination of the sample with gold-containing compounds. There was also no evidence of gold in the FABS mass spectrum of I. The mass of the parent ion suggested the following empirical relationship: $SiCo_9(CO)_{22}$. The mass spectrum shows a series of $[SiCo_8(CO)_n]^-$ peaks,which suggest a unique Co atom which is relatively easy to dislodge. Peaks which may represent $SiCo_4$ fragments were also seen. Once more it must be stressed that, because of the low solubility of I, the FABS mass spectrum which has been described may only represent a minor component of the products.

If the negative charge on this cluster is in fact three, then the $[SiCo_9(CO)_{22}]^{3-}$ cluster would contain 132 valence electrons. Possible geometries would therefore include a capped cube and an edge-bridged square antiprism.

When $[SiCo_9(CO)_{21}]^{2-}$ was reacted with (BuNC)AuCl, the $[SiCo_9(CO)_{21}]^{2-}$ carbonyl infrared bands initially appeared to shift to higher frequency. This is consistent with the addition of a $[(BuNC)Au]^+$ fragment. Reaction between BuNCAuCl and $[Co(CO)_4]^-$, from the mixed salt, also appeared to give $(BuNC)AuCo(CO)_4$. Over the next 30 h, the carbonyl spectrum shifted back to lower frequency, and this shift was accompanied by the precipitation of $Au_{(s)}$, the reformation of $[Co(CO)_4]^-$, and a significant amount of decomposition (detected by a general weakening of the carbonyl infrared spectrum). The yield of the final product, II, was low (est. 10-15%), due in part to the difficulties in isolating this species. Attempts to grow crystals of II, suitable for crystallographic analysis, were unsuccessful.

The reaction was repeated, and the initial product (**IIa**) was extracted in ether after 1.5 h. In the absence of $(BuNC)AuCo(CO)_4$, IIa still reacted to give II. The fact that $Au_{(s)}$ and $[Co(CO)_4]^-$ were not produced, appears to confirm the role played by $(BuNC)AuCo(CO)_4$ in the first reaction. A high degree of decomposition was noted, and IIa may have been reduced by other species present in the mixture.

Attempts to obtain crystallographic-quality crystals of II by varying the cation were unsuccessful.

The $[(MeCN)_4Cu][PF_6]$ complex, as well as adding $[(MeCN)Cu]^+$ on to metal clusters, also acts as a relatively strong oxidant. With $[SiCo_9(CO)_{21}]^{2-}$ the oxidation reaction appears more important, leading

to the precipitation of $Cu_{(s)}$ and the decomposition of most of the $[SiCo_9(CO)_{21}]^{2-}$. This is consistent with electrochemical investigations of $[SiCo_9(CO)_{21}]^{2-}$ (section 5.2.4.1, and reference [33]), which indicate that disruption of the $[SiCo_9(CO)_{21}]^{2-}$ cluster occurs under oxidation (the primary oxidation process is electrochemically and chemically irreversible). A small amount of an unidentified carbonyl compound was detected amongst the products of this reaction. The infrared spectrum of this species, particularly the positions of the peaks at 2078vw and 2030s cm^{-1}, could represent the product of an oxidation or a redox condensation reaction. Both of these reactions would lead to a reduction in the negative charge on the cluster by one, and a concommitant displacement of the infrared spectrum to higher frequency by approximately 28 cm^{-1} (by comparison with the shifts seen in the protonation reaction in section 4.2.1.5, and the reduction reaction in section 5.2.4.3). Unfortunately the very low yield of this compound and its apparent instability prevented further characterisation.

The attempted cobaltocene reduction of $[SiCo_9(CO)_{21}]^{2-}$ yielded a product with a carbonyl infrared spectrum very similar to that of the parent anion. This suggests that **III** is also a large cluster with a double-negative charge. Note that $CpCo(CO)_2$ has been used extensively as a source of CpCo fragments in condensation reactions, and it is possible that, in this case, Cp_2Co is acting in a similar fashion. Preliminary X-ray diffraction studies of **III** indicate a very large unit cell with a volume of 20047 $Å^3$. For the $P6_3/m$ space group, there are usually twelve formular units per unit cell, therefore for a '$[Et_4N]_2[SiCo_{10}(CO)_{21}Cp]$' species this would imply a density of *ca.* 1.52 g cm^{-3}. This value is perhaps a bit low when compared with the density of $[Et_4N]_2[CFe_5Mo(CO)_{17}]$ (1.74 g cm^{-3}) [70]. If addition of CpCo is occuring, then it is possible that the CpCo fragment is entering the vacant capping site on $[SiCo_9(CO)_{21}]^{2-}$, to complete a bicapped square antiprism.

The reaction of H_2SO_4 with $[SiCo_9(CO)_{21}]^{2-}$ in CH_2Cl_2 proceeded in a similar manner to that previously reported for H_3PO_4, producing $Co_4(CO)_{12}$ and compound **IV**. As previously discussed, the infrared spectrum of **IV** is consistent with a reduction of the negative charge on $[SiCo_9(CO)_{21}]^{2-}$ by one, which is expected with protonation. Despite further attempts, the instability of **IV** prevented full

characterisation.

Protonation of the $[Co(CO)_4]^-$ anion present in the $[Et_4N]_3[SiCo_9(CO)_{21}][Co(CO)_4]$ mixed salt probably produced $HCo(CO)_4$. Although this species was not detected at any stage, $HCo(CO)_4$ is known to decompose at temperatures greater than -26°C producing $Co_4(CO)_{12}$ [247], and this may account for the formation of the tetramer during the reaction.

When this reaction was repeated using acetonitrile as the solvent, it proceeded at a faster rate, but resulted in complete decomposition of $[SiCo_9(CO)_{21}]^{2-}$. Unlike the analagous reactions of osmium cluster dianions (see section 4.1), this did not lead to the production of a dihydride. It was hoped that a dihydride could be isolated and characterised, because this could in turn confirm the identity of IV.

The reactions of $[Et_4N]_3[SiCo_9(CO)_{21}][Co(CO)_4]$ and $[PPN]_2[SiCo_9(CO)_{21}]$ with the nitrosonium ion, NO^+, produced a new species, V. This compound exhibits a similar pattern of carbonyl stretches to the parent $[SiCo_9(CO)_{21}]^{2-}$ cluster, with an overall shift to higher frequency (average shift = 27 cm^{-1}). This displacement is more significant for the higher frequency peaks.

The peak positions for compound V are consistent with a monoanion, which suggests that an NO^+ group is binding to the cluster. The infrared spectrum of V is significantly different from that of III, which suggests that we are not just witnessing a protonation reaction (as described for $[NRu_4(CO)_{12}]^-$, section 4.1.1). No obvious NO infrared stretching mode was located, but this would tend to be much weaker than the carbonyl modes. Also, if NO occupies a bridging site, the ν_{CO} mode would occur at much lower frequency, and may be masked by other vibrations.

The unit cell dimensions for the $[Et_4N]^+$ salt of V, obtained from preliminary X-ray diffraction studies, indicate a molecular weight of approximately 4976/Z (assuming a density of 1.97 g cm^{-3}). For a crystal lattice possessing tetragonal symmetry, the most probable values for Z are 4, 8 and 16. Assigning Z equal to 4, the estimated molecular weight (M_r = 1244), is reasonably consistent with the product expected from the substitution of a CO group ($[Et_4N][SiCo_9(CO)_{20}(NO)]$, M_r = 1279). It is also possible that we are observing the addition of NO^+, accompanied by Co-Co bond cleavge (as described in section 4.1.1). This would give a $[Et_4N][SiCo_9(CO)_{21}(NO)]$ species (M_r = 1307). There

is still insufficient information to confirm the identity of compound V, and further work is required to characterise this species.

Repeating this reaction with excess NO^+ resulted in decomposition, and the formation of a small amount of V. When this is compared with the earlier protonation reactions, it seems that the addition of a second electrophile to $[SiCo_9(CO)_{21}]^{2-}$ tends to destabilise the cluster.

No reaction was observed between the $[SiCo_9(CO)_{21}]^{2-}$ cluster and $CpFe(CO)_2I$. An iron did not add onto the cluster as anticipated. Nor did $CpFe(CO)_2I$ abstract $[Co(CO)_4]^-$ from the cluster to form $CpFeCo(CO)_6$, which was also considered a possibility.

4.3.2 REACTIONS OF $[GeCo_5(CO)_{16}]^-$ *(F 7)*

No reaction was detected when $[GeCo_5(CO)_{16}]^-$ was heated with $[CpNi(CO)]_2$. The fact that a condensation reaction was not observed may be due to insufficient charge density on $[GeCo_5(CO)_{16}]^-$. In the past, Tachikawa *et al.* [236] have noted that condensation reactions involving neutral complexes occur more readily for dianionic than for monoanionic clusters (see section 4.1.1). There was also no evidence of a 'Vahrenkamp' metal-exchange reaction, nor of a reaction of the sort described for $[GeCo_5(CO)_{16}]^-$ and $Co_2(CO)_8$. This latter reaction is thought to involve the loss of the $Co_2(CO)_7$ moiety from $[GeCo_5(CO)_{16}]^-$, producing a $[(CO)_9Co_3Ge]^-$ entity which, acting as a Lewis base, substitutes for a CO on any suitable species present (Chapter 3, [32]). These reactions are likely to be concerted, and may require a (CO)Y species capable of readily losing a CO group:

$$[(CO)_9Co_3GeCo_2(CO)_7]^- + (CO)Y \rightarrow [(CO)_9Co_3GeY]^- + Co_2(CO)_8$$

In the $[GeCo_5(CO)_{16}]^-/[CpNi(CO)]_2$ reaction there may have been no suitable (CO)Y species. $[CpNi(CO)]_2$ has relatively few carbonyls and, because there are few electron-withdrawing groups, these CO groups are unlikely to be particularly labile.

The reaction between $[GeCo_5(CO)_{16}]^-$ and $CpFe(CO)_2I$ (in the presence of $TlBF_4$) caused disruption of the cluster, producing $Co_4(CO)_{12}$, $CpFeCo(CO)_6$ and $[CpFe(CO)_2]_2$. It appears that rather than adding on to the cluster, $[CpFe(CO)_2]^+$ acts by abstracting $[Co(CO)_4]^-$ from $[GeCo_5(CO)_{16}]^-$. $[GeCo_7(CO)_{20}]^-$ *(F 8)* was also produced, probably by

the reaction of $[GeCo_5(CO)_{16}]^-$ with $Co_4(CO)_{12}$ present in the mixture (in the manner described above):

$$[GeCo_5(CO)_{16}]^- + Co_4(CO)_{12} \rightarrow [GeCo_7(CO)_{20}]^- + Co_2(CO)_8$$

$[GeCo_7(CO)_{20}]^-$ was previously isolated from the preparation of $[GeCo_5(CO)_{16}]^-$, where $Co_4(CO)_{12}$ was also present [32].

4.3.3 CONCLUSIONS

Work in this chapter has been hampered by difficulties in identifying the reaction products. High nuclearity clusters tend to exhibit very simple infrared spectra. This means that, aside from providing a means of recognising compounds and an indication of the charge, infrared spectroscopy gives little structural information. Mass spectroscopy is very useful for obtaining the mass of a cluster and an empirical formula, but also has limitations when it comes to determining the structure. X-ray crystallography is really the only means of difinitively characterising these compounds. It is however, notoriously difficult to grow suitable crystals of high nuclearity ionic clusters. This problem was aggravated by the difficulties in obtaining pure sample. Where more than one product was formed, attempts at separating these on the basis of solubility, and occasionally density, often proved inadequate. The FABS mass spectra of $[SiCo_9(CO)_{21}]^{2-}$ and II showed contamination with carbido clusters. Reactions of the $[Et_4N]_3[SiCo_9(CO)_{21}][Co(CO)_4]$ mixed salt were also complicated by side reactions involving the $[Co(CO)_4]^-$ anion. This could be overcome by using the $[PPN]^+$ salt, but this compound is less stable and the size of the cation presents its own difficulties when it comes to X-ray crystallography. Some experimentation with different cations was tried, both to provide "cleaner" reactions and to find salts that would form good crystals. Perhaps this could be pursued further.

Generally, there is a lot of scope for further work of this type. Many of the products reported here remain only partially characterised. The Ph_3PAuCl reactions should perhaps be repeated in the presence of $TlBF_4$, which may facilitate the addition of $[Ph_3PAu]^+$ to $[SiCo_9(CO)_{21}]^{2-}$ and $[GeCo_5(CO)_{16}]^-$ by abstracting the halide. Also, it is probably worth reacting $[GeCo_5(CO)_{16}]^-$ directly with $Co_4(CO)_{12}$ and

$(CO)_9Co_3GeCo(CO)_4$ to confirm the proposed mechanisms for the syntheses of $[GeCo_7(CO)_{20}]^-$ and $[Ge_2Co_7(CO)_{21}]^-$ respectively. This type of reaction may provide a strategy for synthesising other high nuclearity clusters.

There remain many other complexes which have also been reported to coordinate to cluster anions, and, despite limited success to date, further investigation in this area appears promising. Surely one of these reactions will provide a product which will crystallise nicely.

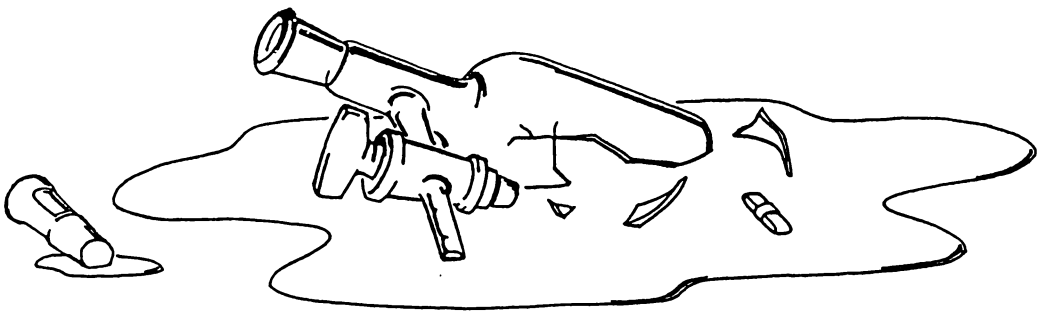

Chapter Five

Structures of compounds frequently refered to in this thesis are depicted in a fold-out section in Appendix A. The symbol *(F #)* is used in the text to refer readers to these diagrams.

CHAPTER 5 CYCLIC VOLTAMMETRY

5.1 INTRODUCTION

5.1.1 ELECTROCHEMICAL THEORY

Cyclic voltammetry [248,249,250] is a rapid and versatile electroanalytical technique for studying electrochemical reactions. Its strength lies in the interpretation of electron transfer processes, afforded by its cyclic scan programme.

The three-electrode cell commonly used for cyclic voltammetry consists of a working electrode (at which the reactive species are oxidised or reduced), a reference electrode, and a control or auxiliary electrode, all placed in a solution of the sample and an electrolyte. In a typical scan, the potential at the working electrode (WE) relative to the reference electrode (RE) is increased or decreased at a constant rate until a switching potential is reached, as shown in figure 5.1a. At this point the direction of the sweep is reversed until the next switching potential. This pattern can be repeated in a cyclic fashion. The current at the WE relative to the RE, due to sample oxidation or reduction, is recorded with respect to potential and plotted as a voltammogram (see figure 5.1b). Any variation in potential or current due to ohmic (or iR) loss through the solution is compensated for by using a control electrode (CE). The bulk of the current through the solution is passed between the WE and the CE, with the internal resistance of the instrument minimising any current involving the RE.

It is crucial in cyclic voltammetry for the migration of reacting species to or from the WE to be diffusion controlled. In this way only a small proportion of the sample in close proximity to the WE is oxidised or reduced in a given sweep; and with time the products will diffuse away to be replaced by further sample. To negate the effect of electrostatic interactions on the migration of ionic species to or from the electrodes, the electrolyte is added at 50 to 100 times the concentration of the sample.

Figure 5.1b shows a typical voltammogram for an electrochemically reversible reduction process. Starting at point s, as the potential becomes more negative, a point is reached where any sample in close proximity to the WE is rapidly reduced. This produces a current peak at A. The current then tails off to a level where further reduction is dependent upon the rate of diffusion of further sample to the WE. When

the scan direction is reversed at switching potential t, a similar process is observed whereby the products are oxidised back to the initial sample; only the current is in the opposite direction and the peak is inverted. The positions and heights of these peaks can yield information about the formal potential of the redox process, the number of electrons transferred and the reversibility of the process.

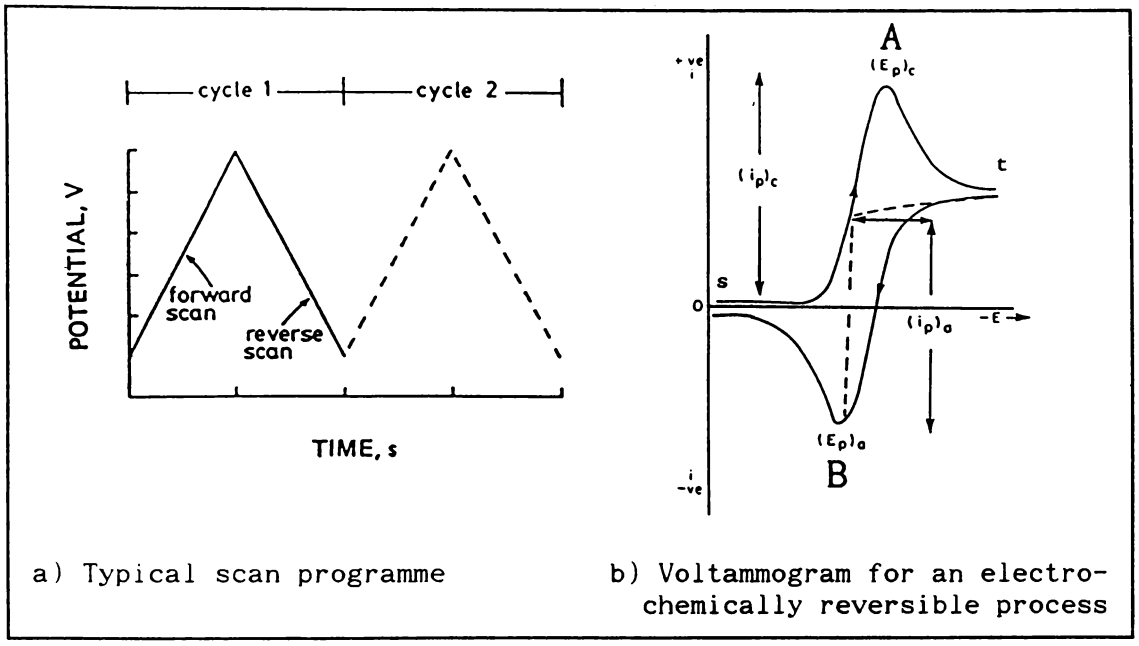

a) Typical scan programme

b) Voltammogram for an electrochemically reversible process

Figure 5.1: Cyclic Voltammetry Scan Programme and Voltammogram

An electrochemically reversible process is one in which the path connecting the two states is thermodynamically reversible and the electron transfer in both directions is sufficiently fast so that a state of equilibrium is maintained throughout. For such a system the current peak height for the cathodic process, i_p^c, is equal to the current peak height for the anodic process, i_p^a. Also, under standard conditions, the peak potentials are given by the equations:

$$E_p^c = E_{1/2} - 1.11(RT/nF) = E_{1/2} - (0.029/n) \quad \text{at 298 K} \quad (1)$$

$$E_p^a = E_{1/2} + 1.11(RT/nF) = E_{1/2} + (0.029/n) \quad \text{at 298 K} \quad (2)$$

where n is the number of electrons transferred per reactant molecule and $E_{1/2}$ is the half wave potential, which approximates the formal potential for the redox process. $E_{1/2}$ is easily obtained from the

voltammogram of a reversible process as the midpoint between E_p^c and E_p^a. Estimating formal reduction potentials becomes less reliable as the process becomes less reversible.

The following equation can be derived from (1) and (2). This provides a convenient means for determining n.

$$E_p^a - E_p^c = 0.058/n \qquad \text{at 298 K} \quad (3)$$

However this rule only holds under standard conditions. In nonaqueous solvents, clusters commonly show peak separations greater than 58 mV for apparent reversible one-electron processes.

The current peak height, which is given by equation (4), also affords a means of establishing the number of electrons involved in a given process.

$$i_p = 2.67 \times 10^5 \, n^{3/2} \, A \, D^{1/2} \, C \, v^{1/2} \qquad \text{at 298 K} \quad (4)$$

A = electrode surface area (cm^2)
D = diffusion coefficient ($cm^2 \, s^{-1}$)
C = concentration (mol cm^{-3})
v = scan rate ($V \, s^{-1}$)

The number of electrons, n, can be determined by comparison of i_p for the sample with that of an equimolar standard (eg. ferrocene) under comparable conditions (if the diffusion coefficients are known or can be estimated).

Electrochemical cell conditions can have a significant effect on peak positions. In particular, reduction potentials of metal carbonyls are exceptionally solvent dependent. Therefore, when comparing results from the literature, care must be taken that measurements were obtained under similar conditions. In general, the use of cyclic voltammetry for inferring quantitative information is limited and such measurements are best obtained by other means.

The advantages of cyclic voltammetry lie in providing qualitative information on electrode processes. The cyclic scan programme enables the fate of species generated in one scan to be probed in subsequent scans. Some common types of electrode processes and their characteristics are given in Table 5.1, taken from reference [248].

Linear sweep voltammetry (LSV) corresponds with a single cyclic voltammetric sweep in the negative direction.

	LSV			Cyclic voltammetry
Mechanism	Dependence of i_p on v	Dependence of i_p on C	Dependence of E_p on v	Dependence of $(i_p)_c$ and $(i_p)_a$ on v
(I) Reversible $A + ne \rightleftarrows B$	$i_p \propto v^{1/2}$	Linear	E_p independent of v	$(i_p)_c$ and $(i_p)_a \propto v^{1/2}$; thus $(i_p)_a/(i_p)_c = 1$ for all v
(II) Irreversible $A + ne \rightarrow B$	$i_p \propto v^{1/2}$	Linear	E_p becomes more negative with increasing v	$(i_p)_a = 0$, $(i_p)_c \propto v^{1/2}$; thus $(i_p)_a/(i_p)_c = 0$ for all v
(III) EC $A + ne \rightleftarrows B \rightarrow C$	Approaches reversible case (I) with increasing v	Generally linear; i_p/C slightly greater than reversible case	E_p more positive than reversible case; E_p becomes more negative with increasing v	$(i_p)_c > (i_p)_a$ at low scan rates; $(i_p)_a \rightarrow (i_p)_c$ and $(i_p)_a/(i_p)_a \rightarrow 1$ with increasing v
(IV) CE $Y \rightarrow A + ne \rightleftarrows B$	Plot of $i_p/v^{1/2}$ versus v decreases with increasing v	Frequently nonlinear; $i_p/C <$ reversible case	E_p becomes more positive with increasing v	$(i_p)_a/(i_p)_c$ increases with increasing v
(V) Regenerative $A + ne \rightleftarrows B \rightarrow A$	Approaches reversible case (I) with increasing v	Frequently nonlinear; $i_p/C >$ reversible case	E_p becomes more positive with increasing v	$(i_p)_a/(i_p)_c = 1$ for all v
(VI) Reactant adsorbed $A \rightleftarrows A(ads) + ne \rightleftarrows B$	i_p increases with increasing v	Nonlinear	E_p becomes more negative with increasing v	$(i_p)_a/(i_p)_c \leq 1$; approaches 1 at low scan rates
(VII) Product adsorbed $A + ne \rightleftarrows B \rightleftarrows B(ads)$	i_p decreases slightly with increasing v	Nonlinear	E_p becomes more positive with increasing v	$(i_p)_a/(i_p)_c \geq 1$; approaches 1 at low scan rates

Table 5.1: Characteristics of common electrode processes in linear sweep and cyclic voltammetry (reduction assumed)

In the EC mechanism the electron transfer step (E) is followed by a chemical reaction step (C). For the CE mechanism the order is reversed. When reduction or oxidation involves more than one electron it is generally accepted that this occurs in two steps. That is, there is no true two-electron process. Often these steps are indistinguishable, but sometimes an intervening chemical reaction or reactions can be detected. Such processes are described as ECE or ECCE processes. In cyclic voltammetry these may be detected by a reduced i_p at faster scan rates. This may be associated with the appearance of a second peak, and/or an overall increase in the base current following the peak.

5.1.2 LITERATURE REVIEW

In this chapter, cyclic voltammetry is used to investigate twelve compounds (table 5.2). Six of these clusters have structures based on the $-ECo_3$ trigonal pyramid. The other six have an M_2EM_2 skeleton consisting of two mutually perpendicular EM_2 triangles with a common apex, E. For convenience these are refered to as "spiro" clusters, which describes the arrangement about the central E atom. The electrochemistry of these two classes of compound, as presented in the literature, is reviewed below.

a) Compounds containing $-ECo_3$ trigonal pyramids	b) Compounds containing M_2EM_2 "spiro" structures
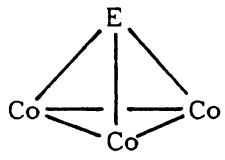	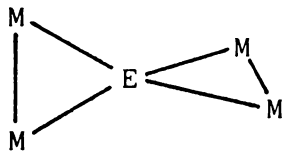
$(CO)_4CoSiCo_3(CO)_9$	$Si[Fe_2(CO)_8]_2$
$(CO)_4CoGeCo_3(CO)_9$	$Ge[Fe_2(CO)_8]_2$
$(CO)_5MnSiCo_3(CO)_9$	$Sn[Fe_2(CO)_8]_2$
$(CO)_5MnGeCo_3(CO)_9$	$SnFe_5(CO)_{19}$
$[Ge_2Co_7(CO)_{21}]^-$	$Si[Co_2(CO)_7]_2$
$[Ge_2Fe_2Co_5(CO)_{22}]^-$	$Ge[Co_2(CO)_7]_2$
(F 5,9,10)	*(F 1,2,4)*

Table 5.2: Compounds investigated in Chapter 5

5.1.2.1 Electrochemistry of Clusters Containing $-ECo_3$ Trigonal Pyramids

The electrochemistry of $ClCCo_3(CO)_9$ was first investigated in 1966 [251]. This rather brief report has been followed in the last decade by quite a comprehensive attack on clusters based on the $YCCo_3(CO)_9$ entity (where Y = halogen, alkyl, aryl, etc). The effects of substituent Y [252,253,254,255], ligand [256,257,258,259,260,254,255], capping atom [261,262] and metal substitution [262] have been

thoroughly studied.

Clusters of this type, containing 48 valence shell electrons, are not readily oxidised, but characteristically undergo an electrochemically and chemically reversible one-electron reduction to form a radical anion. This 49-electron radical anion, $[YCCo_3(CO)_9]^-$ has for a long time been thought to be quite stable, with reported half lives of up to several hours [261]. Very recently Hinkelmann *et al.* [260] have suggested that the radical anions of $MeCCo_3(CO)_9$ and its phosphine derivatives undergo a reversible CO elimination reaction. This produces an unstable 47-electron species, $[MeCCo_3(CO)_8]^-$, which decomposes to give $[Co(CO)_4]^-$. Unlike $[YECo_3(CO)_9]^-$, a $[YECo_3(CO)_8]^-$ species has never been detected by infrared or ESR spectroscopy. This has been explained by the low equilibrium concentration of the 47-electron species in all but very dilute systems.

The elimination of CO from $[YCCo_3(CO)_9]^-$ would obey first order reaction kinetics (5), while the reverse process would be second order (6):

$$v = k_1[YCCo_3(CO)_9^-] \quad (5)$$

$$v = k_{-1}[YCCo_3(CO)_8^-][CO] \quad (6)$$

This could explain why the formation of $[YCCo_3(CO)_8]^-$ is only seen at very low concentrations (less than 10^{-3} mol l^{-1}). At higher concentrations or under CO atmosphere, the reverse reaction would be more important. Note that thermodynamic effects have not been taken into account.

It must be borne in mind that the work by Hinkelmann *et al.* was performed in acetonitrile, whereas previous investigations used THF and CH_2Cl_2 as the solvent. Different processes may operate in acetonitrile, and an interaction between the radical anion and the solvent is a possibility.

Further reduction of $[YCCo_3(CO)_9]^-$ to form a dianion generally occurs at *ca.* 0.7 V negative of the initial reduction, and leads to rapid disintegration of the cluster. The complete reduction process could therefore be represented as shown in figure 5.2.

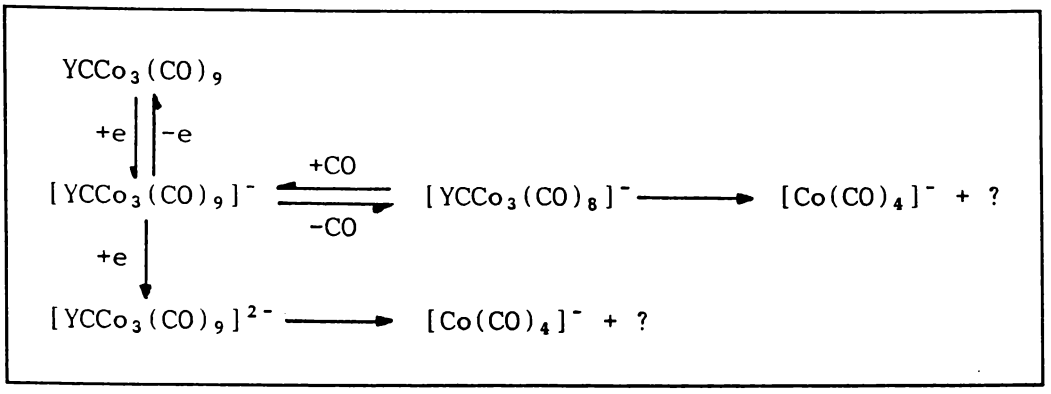

Figure 5.2: Reduction mechanism for $YCCo_3(CO)_9$ compounds.

The instability of the dianion agrees with Wade's rules where bond cleavage is associated with the addition of a pair of electrons. The monoanion should therefore show some intermediate structure where bond cleavage is not complete. Infrared and visible spectral data for $YCCo_3(CO)_9$ clusters and their radical anions suggest changes in molecular geometry and energy levels of the CCo_3 moiety are minimal [204]. The MO schemes of Hoffmann [263] and Hall [264] (figure 5.3) assign the additional electron to an antibonding orbital of a_2 symmetry strongly centred on the metal triangle. This assignment is supported by ESR evidence [204] and by a comparison of the structure of the 49-electron $\cdot SCo_3(CO)_9$ cluster with that of the 48-electron, $SFeCo_2(CO)_9$. In $\cdot SCo_3(CO)_9$ the additional electron is associated with an increase in the average M-M bond length from 2.554(3) Å to 2.627(3) Å [265]. The authors of this paper were unable to distinguish the Fe and Co atoms in $SFeCo_2(CO)_9$, but concluded that the increase in the M-M bond length was significant despite the incorporation of an Fe atom. Lindsay *et al.* [262] have suggested that the gap of *ca.* 0.7 V between the primary and secondary reduction potentials corresponds to the electronic charge repulsion energy associated with filling the a_2^* orbital.

For clusters of the form $YCCo_3(CO)_9$, the half reduction potentials ($E_{1/2}$) for the primary reduction wave generally vary over a range of *ca.* 0.15 V. Reduction is most difficult when the apical groups (Y) are electron-donating. Changes in $E_{1/2}$ for the primary reduction wave reflect changes in the LUMO a_2^* orbital energy. While the capping atom cannot directly perturb the a_2^* orbital, more electronegative substituents on the capping main group atom decrease the electron

density in the Co-Co σ-bonding orbitals (which involve the capping atom) and indirectly lower the LUMO energy.

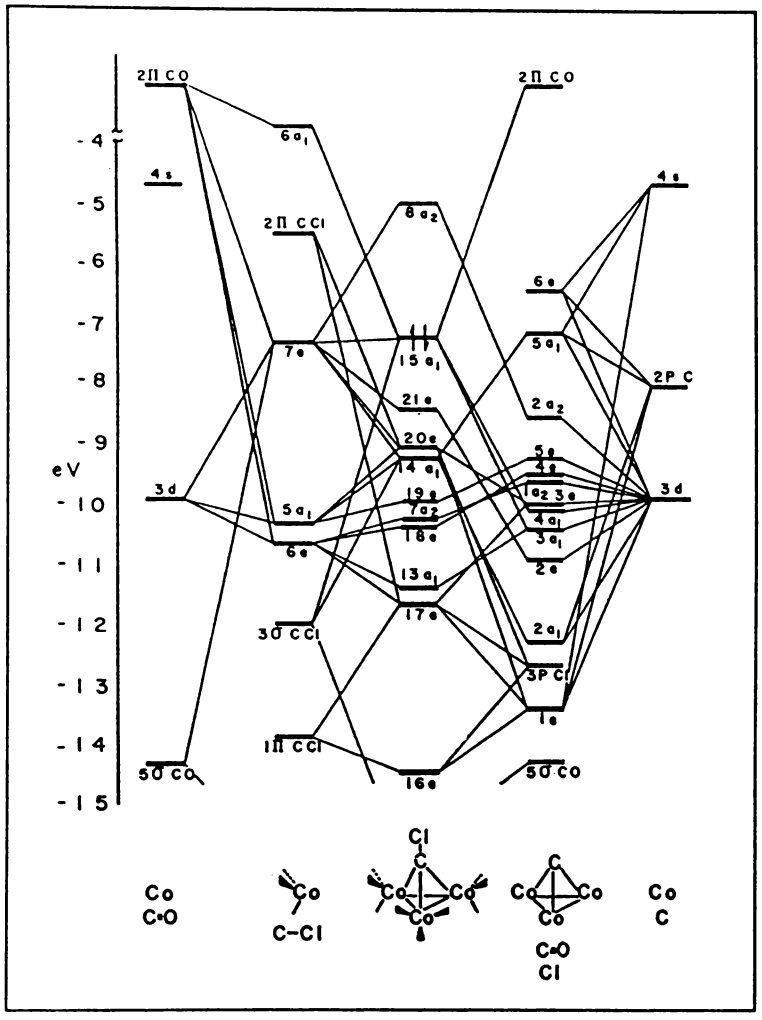

Figure 5.3: Molecular orbital bonding scheme for $ClCCo_3(CO)_9$ (taken from reference [264])

Substitution of the apical C atom affects the $E_{1/2}$ in a similar manner. Clusters containing an apical Ge atom [262] are reduced more easily, at potentials *ca.* 0.26 V more positive that their C analogues. This trend is the reverse of what is expected considering the relative electronegativities of carbon and germanium. It has been suggested that, because Ge has a larger covalent radius, the $YGeCo_3$ moiety is more strained and the orbital overlap between Ge and Co is less effective. This leads to a reduction in electron density in the cluster bonding orbitals and indirectly to a lowering of the LUMO energy.

This was confirmed by visible spectra in which the low energy band correlates with a transition between the HOMO and LUMO. A comparison of these bands for $YCCo_3$ and $YGeCo_3$ indicates that this gap is smaller for the Ge analogues. This is represented graphically in figure 5.4 taken from reference [262].

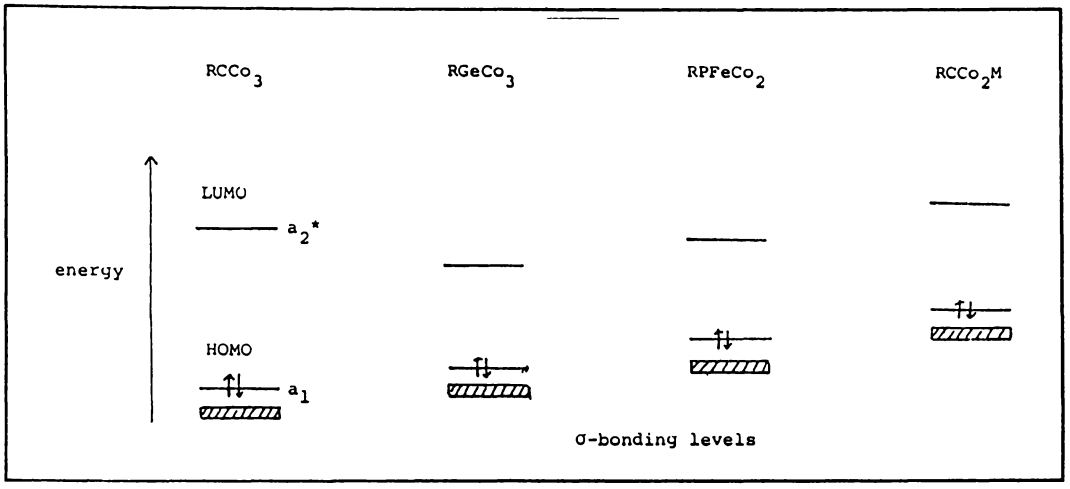

Figure 5.4: Relative energies of HOMO and LUMO orbitals for RCM_3 structures

$SCo_3(CO)_9$ and $PhPCo_3(CO)_9$ [262] already have 49 electrons and not surprisingly undergo a reversible one-electron oxidation to form the corresponding 48-electron cations. Further oxidation or reduction lead to decomposition. When a Co is replaced with Fe in each of these clusters, a 48-electron species is obtained whose redox properties are comparable with other 48-electron clusters.

The effect of incorporation of hetero-metal atoms into 48-electron CCo_3, $GeCo_3$ and PCo_2Fe trigonal pyramids was also looked at by Lindsay *et al.* [262]. By substituting $M(CO)_2Cp$ (M = Cr,Mo,W) for $Co(CO)_3$ the cluster retains the 48-electron configuration, however the kinetic stability of the radical anion decreases and the electrochemistry becomes more complicated. ESR studies indicate that the unpaired electron density is unevenly distributed with a greater proportion of spin density residing on the Co atoms.

Generally it is more difficult to reduce the heteronuclear species $RECo_2M$. Visible spectroscopy indicates that the HOMO-LUMO separation has actually decreased, so the increased energy of the LUMO is due to an overall increase in orbital energy. This is explained by extra

electronic charge being placed on the cluster by the electron rich $M(CO)_2Cp$ moiety.

$RGeCo_2Mo$ and $RPCo_2Fe$ undergo a typical reversible one-electron reduction. However the gap between the primary and secondary reduction waves is much smaller than for the corresponding $YECo_3(CO)_9$. Kinetic parameters associated with the secondary reduction wave, which was found to be an ECE (electron transfer-chemical reaction-electron transfer) process, as well as reduced charge repulsion for the heteronuclear clusters have been suggested as possible reasons.

The electrochemistry of the monosubstituted carbido clusters is much more complex with an irreversible ECE or ECCE principal reduction process, followed by an electrochemically reversible reduction. The reaction scheme shown in figure 5.5 has been suggested to account for observed behaviour.

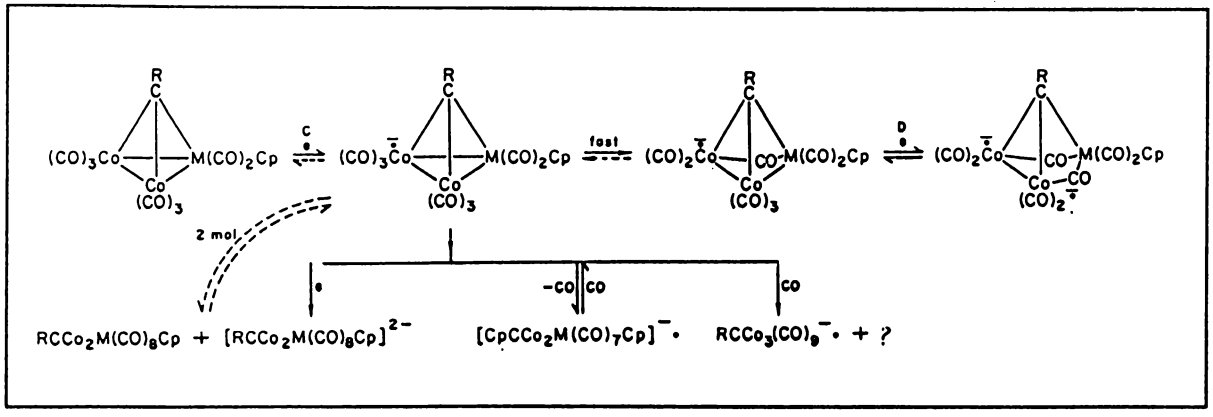

Figure 5.5: Proposed reaction scheme for the reduction of $RECo_2M$ clusters (taken from reference [262])

The presence of two hetero-metal atoms in the trigonal pyramid leads to very unstable radical anions which rapidly decompose under all conditions.

One aspect of the electrochemistry of $YCCo_3(CO)_9$ clusters which has received a lot of attention is their propensity to take part in Electron Transfer Catalysed (ETC) substitution reactions [266]. This involves the substitution of CO ligands by phosphine groups, catalysed by an initial one-electron reduction of the parent $YECo_3(CO)_9$ compound. The resulting phosphine containing radical is then able to transfer its electron to another $YECo_3(CO)_9$ molecule in a very rapid reaction

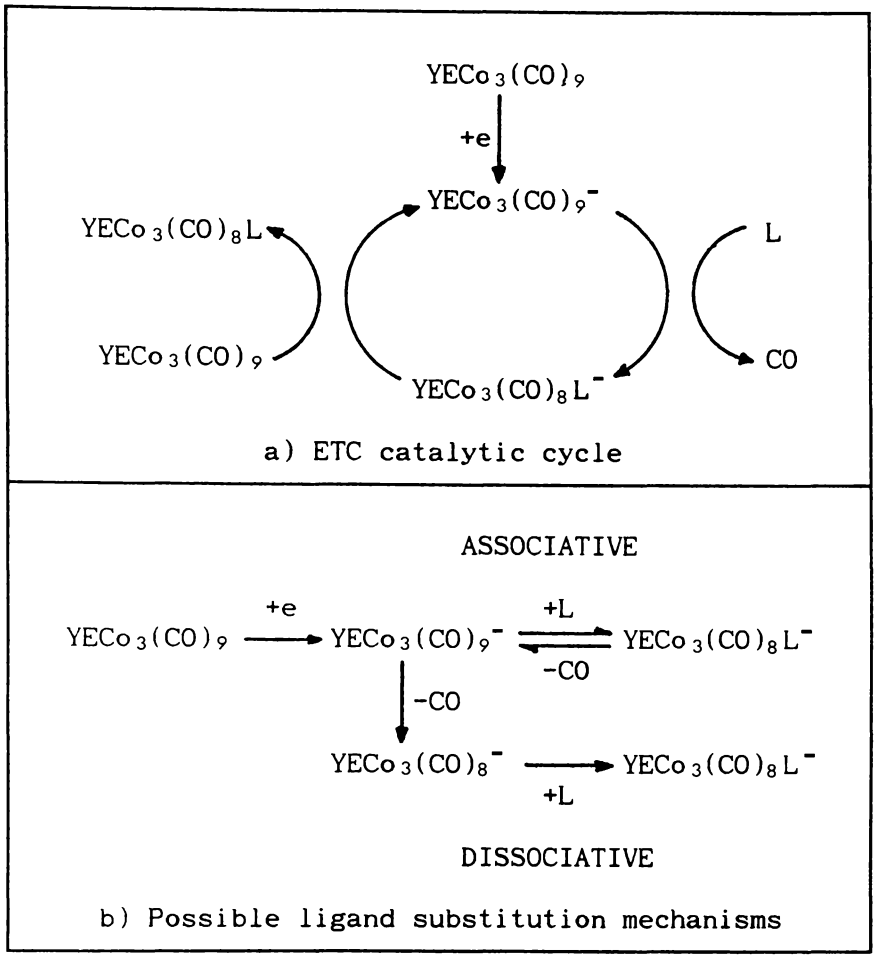

Figure 5.6: Electron Transfer Catalysis (ETC)

completing the cycle (as shown in **figure 5.6a**).There has been active debate over whether nucleophilic attack by the phosphine group involves an associative or a dissociative substitution pathway (**figure 5.6b**). The associative pathway is thought to occur via the initial stretching or cleavage of a Co-Co bond, followed by nucleophilic attack at a coordinately unsaturated metal centre (**figure 5.7**) **[267,268]**. This argument is based on the relative enthalpies of Co-Co and Co-CO bonds. Having an electron in the a_2* orbital would further weaken the Co-Co bond, and there is some indication that the presence of a negative charge on the cluster actually strengthens the Co-CO bonding **[268]**. ETC substitution has been shown to be inhibited by a high concentration of CO, but this could be explained for the associative mechanism if competition occurs between PPh_3 and CO for the vacant coordination site. Hinkelmann *et al.* have suggested such competition is improbable considering the efficiency of ETC substitution with even a small excess

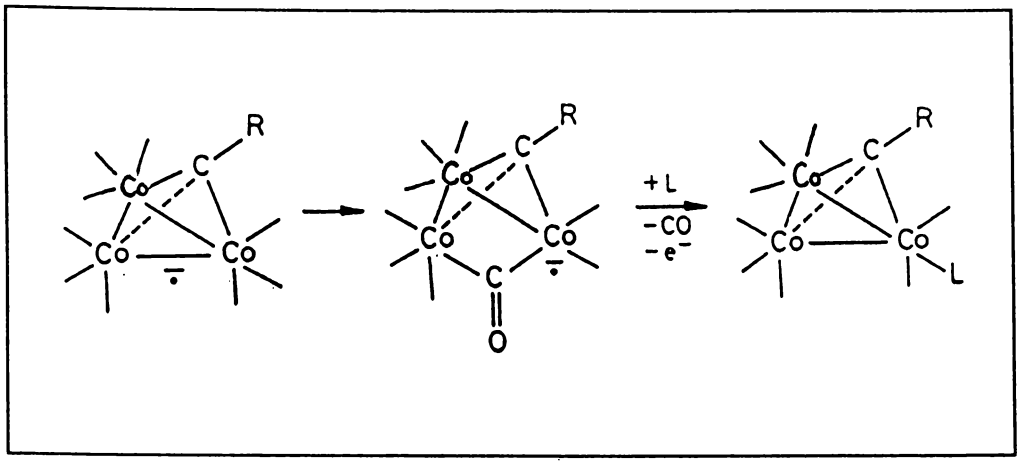

Figure 5.7: Possible associative ligand substitution mechanism for $RCCo_3(CO)_9$ clusters

of PPh_3, and have based their argument for the dissociative pathway on the detection of the decarbonylated $[YECo_3(CO)_8]^-$ species. In the meantime the electrochemistry of monodentate and bidentate phosphine substituted clusters has been thoroughly investigated [269,258,259,260].

Generally, replacement of electron withdrawing CO ligands by Lewis bases, L, leads to an overall increase in orbital energy, making reduction progressively more difficult and facilitating oxidation. Thus for clusters of the form $YCCo_3(CO)_{9-n}L_n$, when n = 2 irreversible oxidations are seen, which become reversible when n = 3.

Reduction processes are much more complicated than for their $YCCo_3(CO)_9$ congeners, as the resulting radical anions are also susceptible to PR_3 elimination reactions.

5.1.2.2 Electrochemistry of Clusters Containing *spiro*-M_2EM_2 Structures

The electrochemistry of spiro $E[Fe_2(CO)_8]_2$ (E = Ge, Sn, Pb) ***(F 3)*** has been briefly looked at by Whitmire *et al.* [31]. Cyclic voltammograms of $Pb[Fe_2(CO)_8]_2$ show a 1.8 to 2 electron electrochemically- and chemically- irreversible reduction wave. Subsequent to this reduction, an apparent 2-electron facile oxidation was observed, coinciding with the principle oxidation wave reported for $[(CO)_8Fe_2]Pb[Fe(CO)_4]_2^{2-}$. $[(CO)_8Fe_2]Pb[Fe(CO)_4]_2^{2-}$ has a similar structure to $Pb[Fe_2(CO)_8]_2$ but with one Fe-Fe bond broken ***(F 4)***.

Interconversion between $Pb[Fe_2(CO)_8]_2$ and $[(CO)_8Fe_2]Pb[Fe(CO)_4]_2^{2-}$ was also shown to be chemically possible:

$$Pb[Fe_2(CO)_8]_2 \underset{[Cu(MeCN)_4][BF_4]}{\overset{Cp_2Co}{\rightleftharpoons}} [(CO)_8Fe_2]Pb[Fe(CO)_4]_2^{2-}$$

(F 2) *(F 3)*

The tin spiro cluster, $Sn[Fe_2(CO)_8]_2$ was also produced by chemical oxidation of $[(CO)_8Fe_2]Sn[Fe(CO)_4]_2^{2-}$. Cyclic voltammetric studies of $[(CO)_8Fe_2]Sn[Fe(CO)_4]_2^{2-}$ indicated that this oxidation occurred at a more positive potential than for the Pb analogue. No open ended spiro structure was found for germanium. Instead, chemical reduction of $Ge[Fe_2(CO)_8]_2$ using cobaltocene causes the *spiro*-cluster to close down to form $[(CO)_4FeGeFe_3(CO)_{10}]^{2-}$ *(F 6)*.

5.2 EXPERIMENTAL

5.2.1 EXPERIMENTAL TECHNIQUES

The electrochemical cell used for this work consisted of a Pt disk WE embedded in soft glass, a Ag wire RE and a Pt wire CE. All samples were purified by recrystallisation. Dry distilled CH_2Cl_2 was used as the solvent and tetrabutyl ammonium perchlorate as the electrolyte; the compounds investigated are generally more stable in CH_2Cl_2 than other more commonly used solvents (eg. acetone). Unless otherwise stated concentrations of *ca.* 10^{-3} mol l^{-1} sample and *ca.* 0.1 mol l^{-1} electrolyte were used. Oxygen was excluded by performing the experiments under nitrogen atmosphere and periodically bubbling nitrogen through the solution. Ferrocene (Cp_2Fe/Cp_2Fe^+ couple $E_{1/2}$ = 0.49 V in CH_2Cl_2 [258]; diffusion coefficient D = 2 x 10^{-5} cm^2 s^{-1} [259]) and $(CO)_4CoSiCo_3(CO)_9$ ($(CO)_4CoSiCo_3(CO)_9/(CO)_4CoSiCo_3(CO)_9^-$ couple $E_{1/2}$= 0.61 V, see below) were used for calibrating the potential before each run. Ferrocene was also used to determine the number of electrons involved in each process. From equation (4), the peak current is proportional to $n^{3/2}$ $D^{1/2}$. Therefore, for equimolar amounts of sample and ferrocene:

$$\frac{ip_{(SAMPLE)}}{ip_{(FERROCENE)}} = \frac{n^{3/2}(D_{SAMPLE})^{1/2}}{(D_{FERROCENE})^{1/2}} = 0.70 \text{ (when n = 1)}$$

$$= 1.99 \text{ (when n = 2)}$$

The diffusion coefficients for the sample clusters were estimated at 9.8×10^{-6} cm^2 s^{-1} by comparison with $PhCCo_3(CO)_9$ [259].

Scans were performed using a PAR 174 A polarographic analyser equiped with a PAR 175 universal programmer. Voltammograms were recorded on an X-Y plotter.

All samples were investigated at room temperature and 210 K (dry ice) and at scan rates varying from 50 to 1000 mV s^{-1}. Unless otherwise stated, all quantitative measurements were made using a scan rate of 200 mV s^{-1}. Judicious selection of the initial scan direction and switching potentials aided interpretation of the observed processes and their interrelationships. Scans were also run under a carbon monoxide atmosphere to determine the dependence of processes on carbon monoxide elimination.

Chemical reductions were performed using cobaltocene. Cobaltocene is a one electron reductant with a redox potential of E° = -0.9 V (in DMF vs saturated calomel electrode). $[Cp_2Co]^+$ formed salts with the reduced clusters which were often only partially soluble in CH_2Cl_2. PPNCl was therefore added, sometimes in excess, to solubilise the reduced products and to make them easier to manipulate.

5.2.2 ELECTROCHEMISTRY OF CLUSTERS CONTAINING $-ECo_3$ TRIGONAL PYRAMIDS

5.2.2.1 $(CO)_4CoSiCo_3(CO)_9$ *(F 5)*

a) Electrochemistry

Cyclic voltammograms of $(CO)_4CoSiCo_3(CO)_9$ (figure 5.8) show two reduction waves. At normal sample concentrations the first of these, peak A ($E_{1/2}$ = -0.61 V), has characteristics of an electrochemically reversible electron transfer ($i_p^a/i_p^c \simeq 1$ at all scan rates from 50 to 1000 mV s^{-1}). The peak current for this wave is 70% of that observed for equimolar ferrocene, indicating a one-electron transfer.

The second reduction wave, B at *ca.* -1.52 V, is irreversible. This also appears to be a one-electron process. On the reverse scan an oxidation peak, F, occurs at E_p = 0.08 V. This peak is less intense if the scan is reversed before B, and gradually increases with the number of scans. The peak potential for F corresponds with that expected for oxidation of $[Co(CO)_4]^-$ [260]. A cyclic voltammogram of a sample of $[Co(CO)_4]^-$ under similar conditions, exhibited an irreversible oxidation wave at E_p = 0.09 V (figure 5.9). This anion is a known decomposition product for the two electron reduction of $YECo_3(CO)_9$

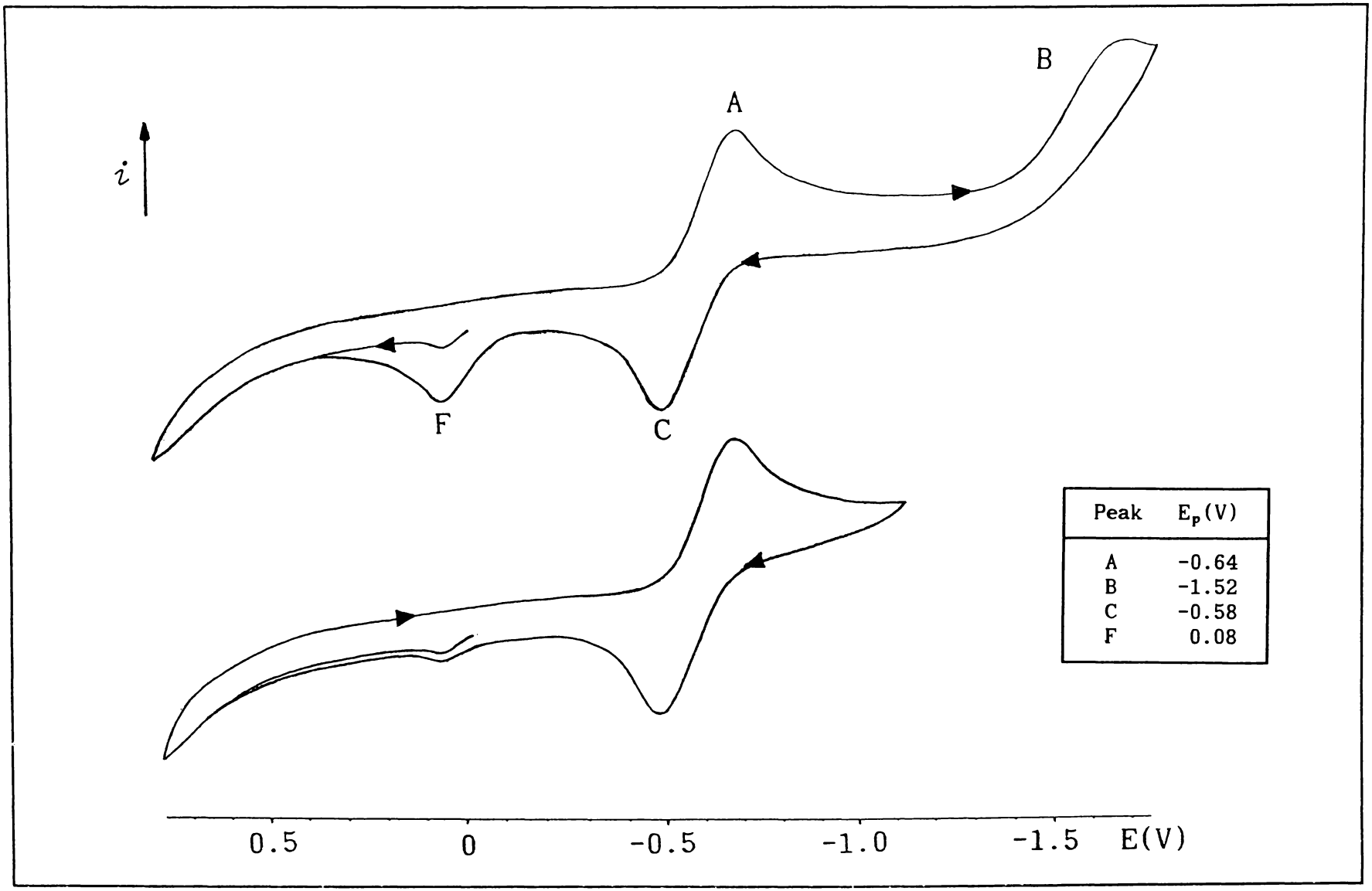

Figure 5.8: Cyclic voltammograms for $(CO)_4CoSiCo_3(CO)_9$

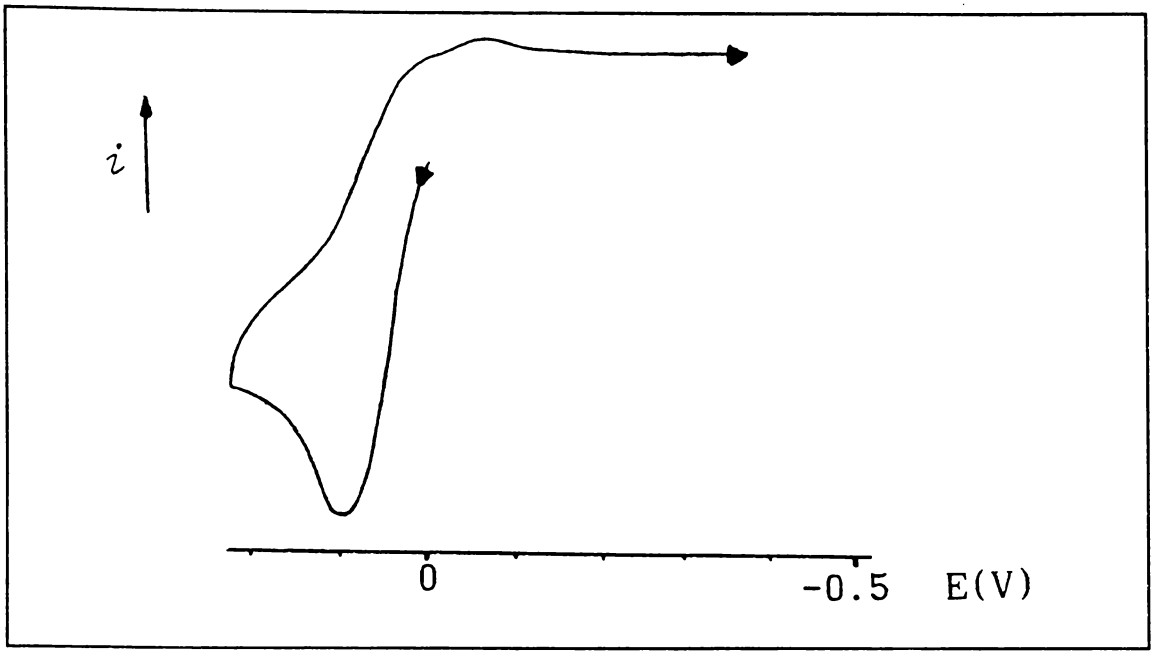

Figure 5.9: Cyclic Voltammogram of $[Co(CO)_4]^-$

clusters (see section 5.1.2). A weak F peak was found to be present for fresh sample when the scan was initiated in a positive direction. The intensity varied from sample to sample, suggesting that $[Co(CO)_4]^-$ was initially present as an impurity. However this is only a minor component of peak F compared with that due to cluster degradation at B.

No further oxidation peaks were observed within the solvent limits. Performing scans at 210 K and under CO atmosphere had negligible effect on the peak positions or heights.

ETC substitution of PPh_3 for a carbonyl ligand was used to investigate peak F. An excess of PPh_3 was added to the $(CO)_4CoSiCo_3(CO)_9$/electrolyte solution and the voltammogram was continuously cycled through the A/C couple (see **figure 5.10**). Peaks A and C gradually diminished in intensity, while a new irreversible peak, E, appeared at more negative potential (Ep = -0.98 V). This is consistent with the formation of $(CO)_4CoSiCo_3(CO)_8PPh_3$ (see section 5.1.2). Peak F remained unaffected by the substitution reaction, again suggesting that it is not directly related to the $(CO)_4CoSiCo_3(CO)_9$ cluster.

Electrochemical investigations were repeated using a lower sample concentration (*ca.* 10^{-4} mmol l^{-1}) (see **figure 5.11**). At this

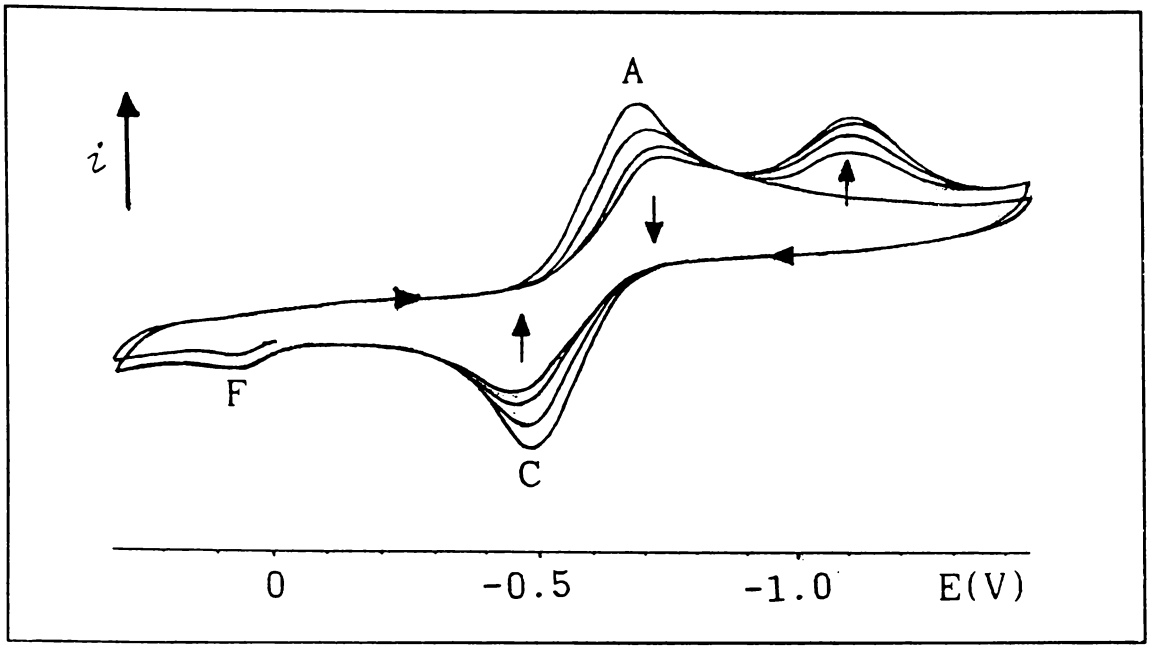

Figure 5.10: ETC substitution of PPh_3 onto $(CO)_4CoSiCo_3(CO)_9$

concentration the A/C couple, although much weaker, still appeared to be reversible ($i_p^a/i_p^c \simeq 1$). Peak F did appear to be much stronger, but was present initially for fresh sample and did not appear to increase significantly once the A/C couple was scanned through. Performing the experiment under CO atmosphere had little effect on the

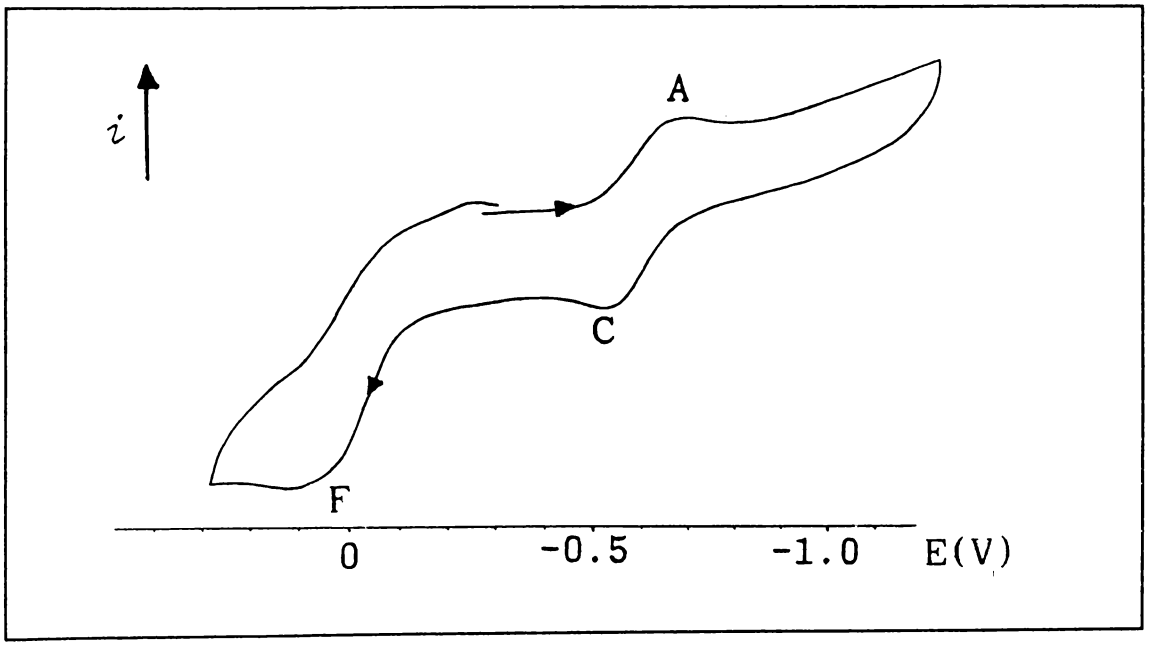

Figure 5.11: Cyclic voltammogram of $(CO)_4CoSiCo_3(CO)_9$ at *ca.* 10^{-4} mmol l^{-1} Concentration

voltammogram.

b) Chemical Studies

$(CO)_4CoSiCo_3(CO)_9$ (0.040 g, 0.06 mmol) was dissolved in 5ml of CH_2Cl_2 in a nitrogen flushed Schlenk flask. 20 ml (0.06 mmol) of a solution of cobaltocene in CH_2Cl_2 (3 mmol l^{-1}) was added dropwise to the flask, via syringe. The solution was stirred for 0.5 h, the solvent removed under vacuum, and the hexane soluble fraction was extracted. The remaining product was redissolved in CH_2Cl_2. PPNCl (0.034 g, 0.06 mmol) was added and the solution stirred for 15 min, before being filtered through a glass sinter. An infrared spectrum in the carbonyl stretching region (**figure 5.12**) showed that the product mixture contained $[Co(CO)_4]^-$ (ν_{CO} (CH_2Cl_2) 1889 cm^{-1}) and a second species. This showed a remarkably similar pattern of peaks to $(CO)_4CoSiCo_3(CO)_9$, but with an average shift of *ca.* 37 cm^{-1} to lower frequencies. The only variation in the pattern of peaks appears to be that only one weak peak is observed at 1966cm^{-1} where two very weak peaks are observed for the parent $(CO)_4CoSiCo_3(CO)_9$ cluster. The solution was placed in a freezer overnight, but decomposed to give $Co_4(CO)_{12}$ and $[Co(CO)_4]^-$.

5.2.2.2 $(CO)_4GeCo_3(CO)_9$ *(F 5)*

The i-E responses for $(CO)_4CoGeCo_3(CO)_9$ follow a similar pattern to that of the Si analogue above (**figure 5.13**). As expected, the two reduction waves, A and B, occur at more positive potentials ($E_{1/2}$ = -0.53 V and $E_p \simeq$ -1.43 V, respectively). This is the result of replacing the Si capping atom with Ge (see section 5.1.2). The reversibility of the A/C wave appeared independent of concentration, as observed for the Si analogue above. Two extra, very weak irreversible oxidation peaks, H and I, are observed at -0.69 V and -0.88 V, but only if the direction of the scan is switched after B. The intensity of these peaks increases at slower scan rates. This suggests that H and I correspond to oxidation of species formed by gradual decomposition of the immediate product of reduction B.

Peak F (E_p = -0.09 V) due to $[Co(CO)_4]^-$, is again present initially and increases if B is scanned through. Performing scans at

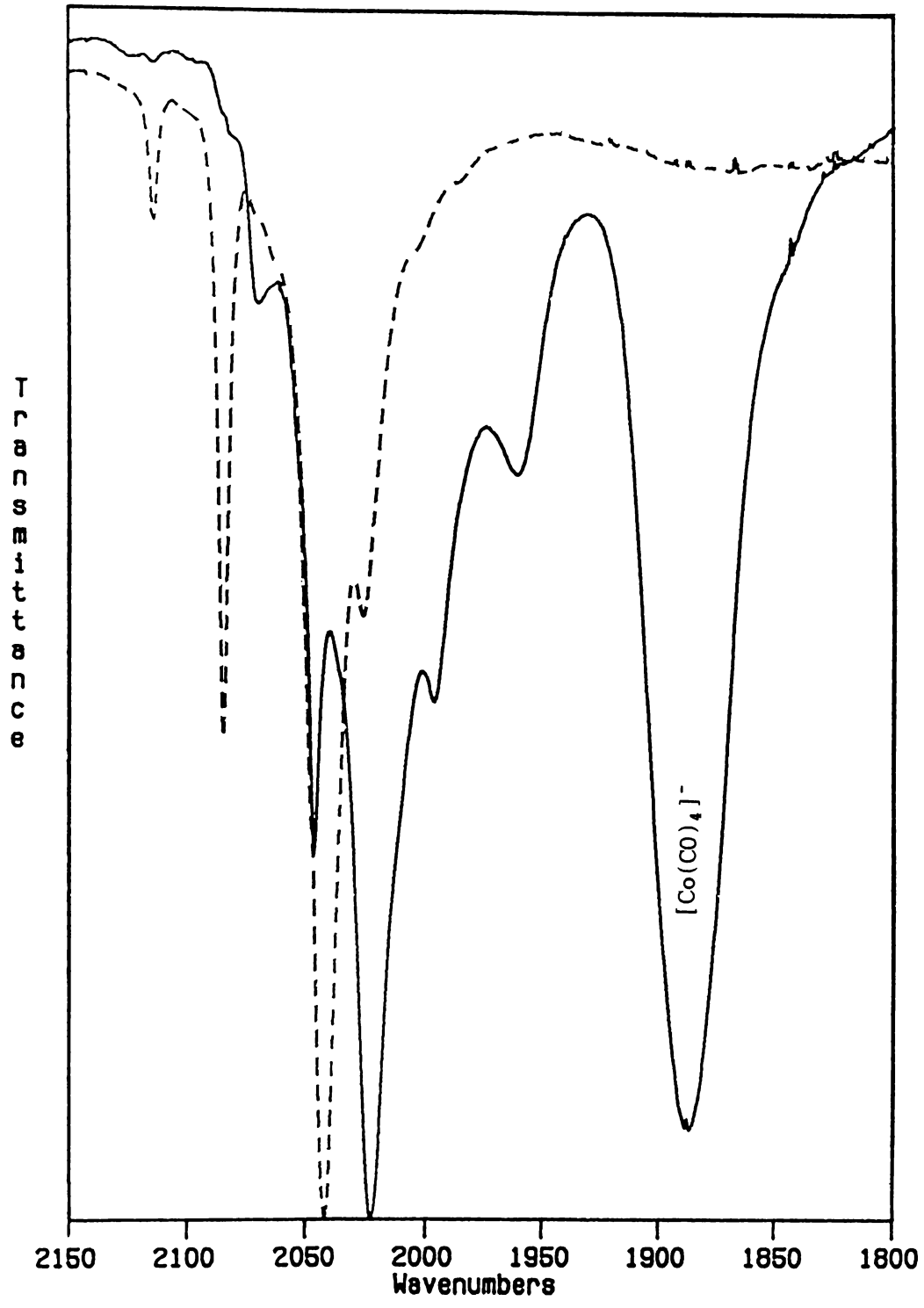

$[(CO)_4CoSiCo_3(CO)_9]^-$ (———)	$(CO)_4CoSiCo_3(CO)_9$ (— — —)
2070w	2114w
2049s	2087s
2025vs	2047vs
1998m	2031m
1966w	2011vw
	1993vw

Figure 5.12: Infrared spectrum of $[(CO)_4CoSiCo_3(CO)_9]^-$ compared with that of $(CO)_4CoSiCo_3(CO)_9$

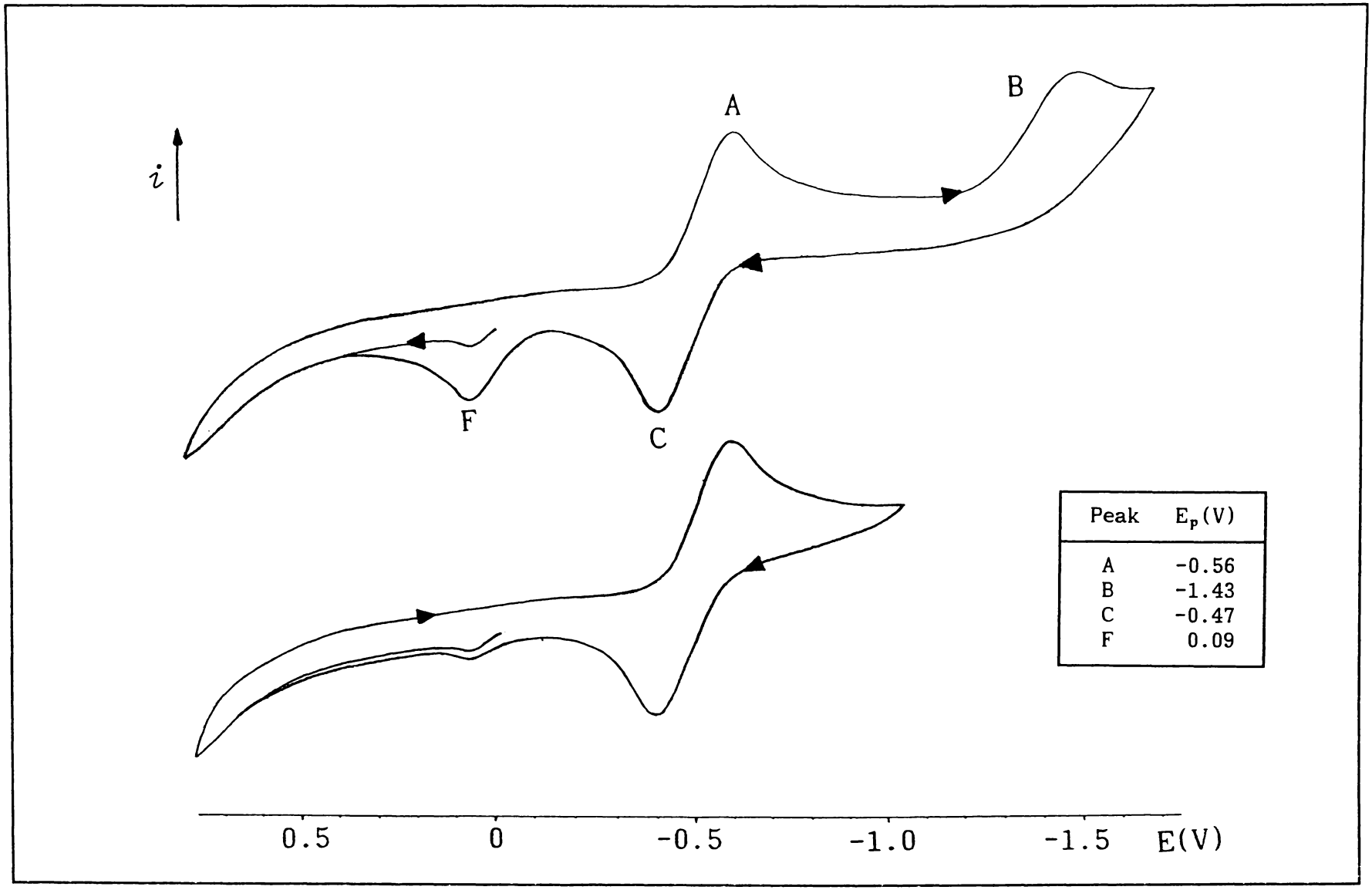

Figure 5.13: Cyclic voltammograms for $(CO)_4CoGeCo_3(CO)_9$

210 K and under carbon monoxide atmosphere had negligible effect on the peak positions and heights.

5.2.2.3 $(CO)_5MnSiCo_3(CO)_9$ and $(CO)_5MnGeCo_3(CO)_9$ *(F 5)*

Cyclic voltammograms of $(CO)_5MnSiCo_3(CO)_9$ and $(CO)_5MnGeCo_3(CO)_9$ are shown in figure 5.14. Information on peak potentials and intensities are also given in table 5.3. The i-E curves of these clusters show a remarkable similarity in the pattern, behaviour and positions of peaks, to those of their $(CO)_4CoECo_3(CO)_9$ congeners. As with the $(CO)_4CoECo_3(CO)_9$ clusters, peak F ($E_p \simeq 0.09$ V) was seen very weakly in the initial scans of fresh sample, and behaved as described above. Note that peaks H and I, reported for $(CO)_4CoGeCo_3(CO)_9$, were not detected for either of these clusters.

5.2.2.4 $[Ge_2Co_7(CO)_{21}]^-$ *(F 9)*

This anion contains two 48-electron $-ECo_3$ trigonal pyramids *(F 2)* and hence, two redox centres. It also has a negative charge which makes the cluster harder to reduce and easier to oxidise than the previous clusters. The principle reduction process, A/C occurs at $E_{1/2} = -0.87$ V (figure 5.15), compared with $E_{1/2} = -0.52$ V for $(CO)_4CoGeCo_3(CO)_9$. The peak current for this reduction process is approximately twice that observed for equimolar ferrocene for all scan rates (50-500 mV s^{-1}), which indicates a transfer of two electrons. The second reduction wave, B ($E_p \simeq 1.81$ V) also appears to be a two electron process. However this peak overlaps with the edge of the solvent reduction wave so it is not possible to accurately determine the peak position or the the number of electrons transfered.

Two irreversible oxidation peaks, F and G, are seen on the anodic scan. F ($E_p = 0.08$ V) is due to $[Co(CO)_4]^-$ and is only seen when B has been scanned through. However G ($E_p = 0.51$ V) is always present and corresponds to a two-electron oxidation of the $[Ge_2Co_7(CO)_{21}]^-$ cluster.

5.2.2.5 $[Ge_2Co_5Fe_2(CO)_{22}]^-$ *(F 10)*

$[Ge_2Co_5Fe_2(CO)_{22}]^-$ has a structure similar to that of $[Ge_2Co_7(CO)_{21}]^-$ with one of the trigonal pyramids containing two iron atoms with an additional carbonyl group bridging these *(F 2)*. The voltammogram for $[Ge_2Co_5Fe_2(CO)_{22}]^-$ (figure 5.16) displays four

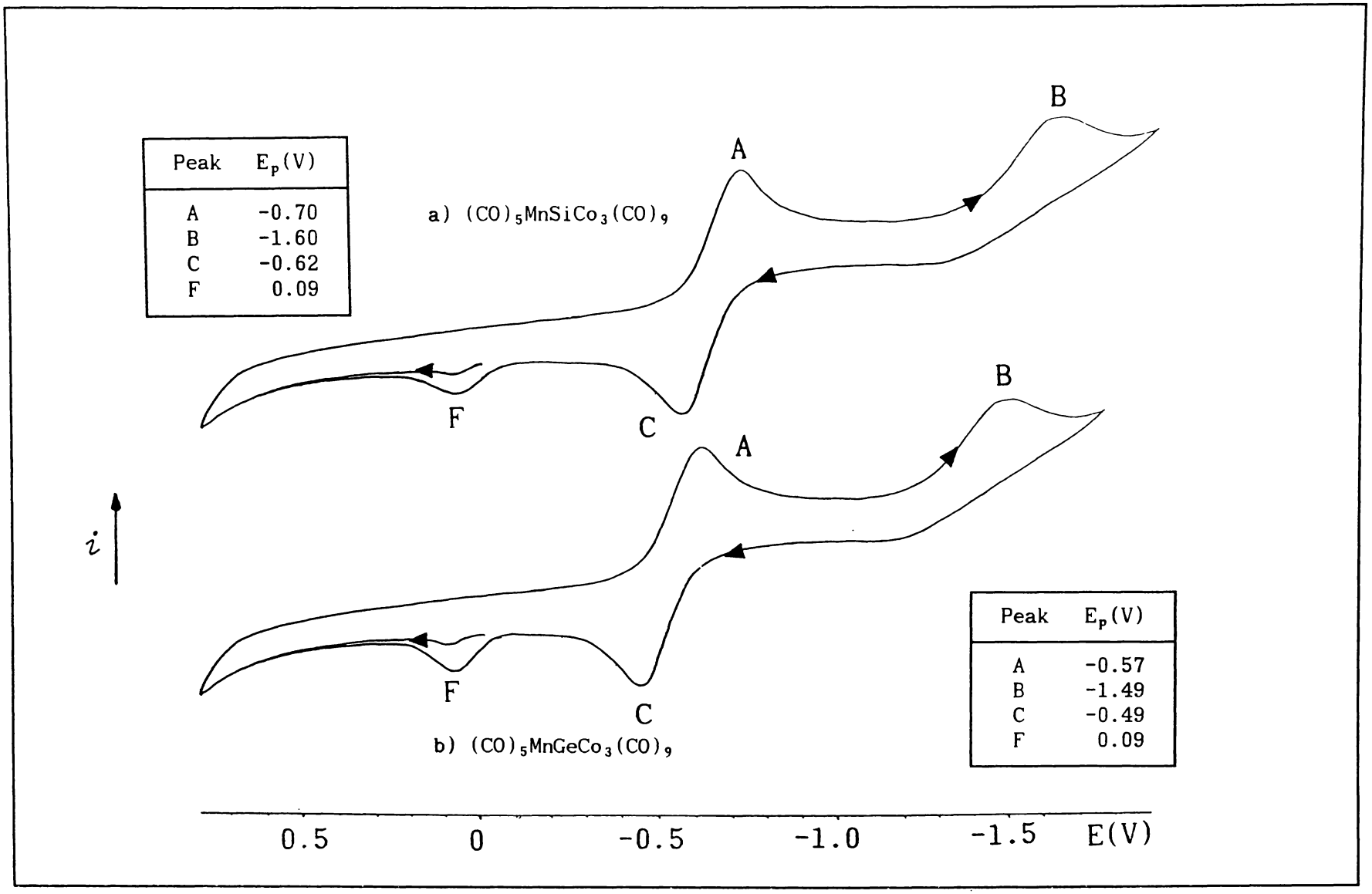

Figure 5.14: Cyclic voltammograms for a) $(CO)_5MnSiCo_3(CO)_9$ and b) $(CO)_5MnGeCo_3(CO)_9$

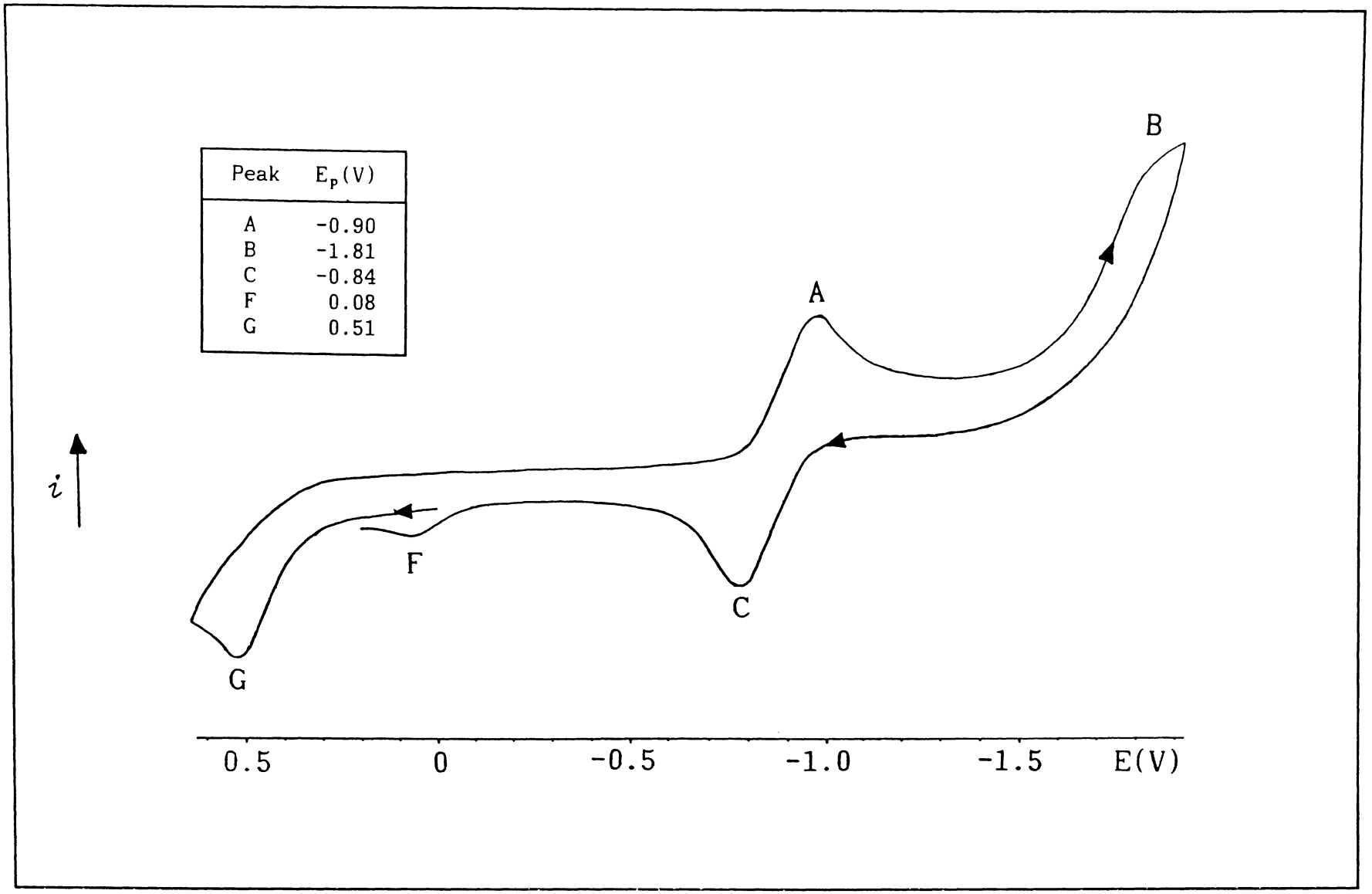

Figure 5.15: Cyclic voltammogram for $[Ge_2Co_7(CO)_{21}]^-$

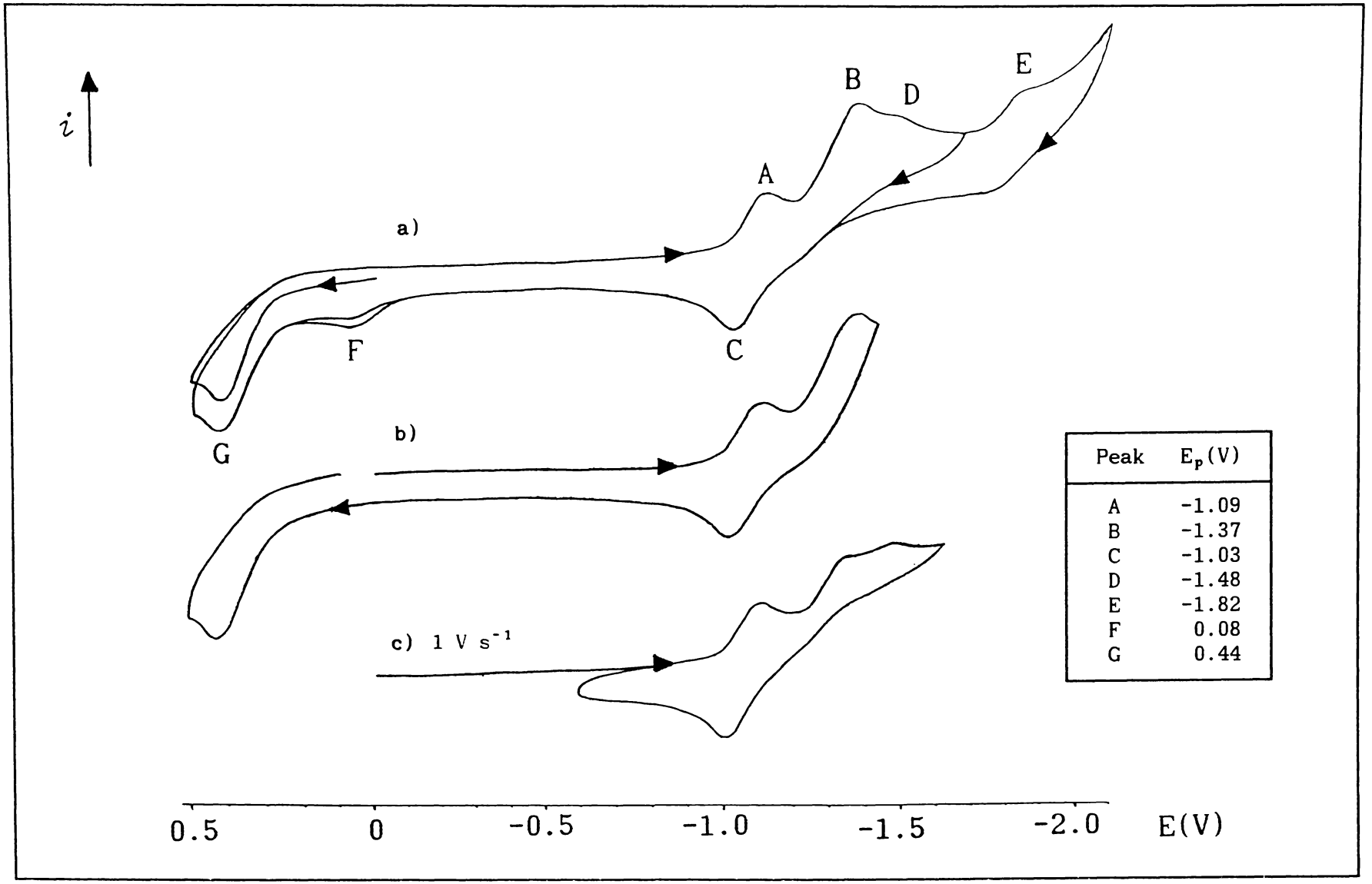

Peak	E_p(V)
A	-1.09
B	-1.37
C	-1.03
D	-1.48
E	-1.82
F	0.08
G	0.44

Figure 5.16: Cyclic voltammograms for $[Ge_2Co_5Fe_2(CO)_{22}]^-$

distinguishable reduction waves. An apparently reversible one-electron principal reduction, A and C, with E_p = -1.06 V is followed by an apparent 1.6-electron irreversible reduction, B (E_p = -1.37 V), a weak irreversible reduction D (E_p = -1.48 V), and a final irreversible reduction wave, E ($E_p \simeq$ -1.82 V) bordering on the solvent limit. The proximity of A and B hampers accurate determination of the number of electrons transferred and the reversibility of these processes. Solvent reduction causes similar problems with peak E.

Varying the scan rate influences the peak current of B. At 1 V s^{-1}, i_p approaches that expected for a one-electron process (figure 5.16$_c$). This is accompanied by a rise in the base current. Again, accurate determination of quantitative information is made difficult by the closeness of A and B. Similar effects are observed at slower scan rates when the experiment is performed under CO atmosphere. This is consistent with an ECE mechanism, where the chemical reaction step involves liberation of a carbonyl group.

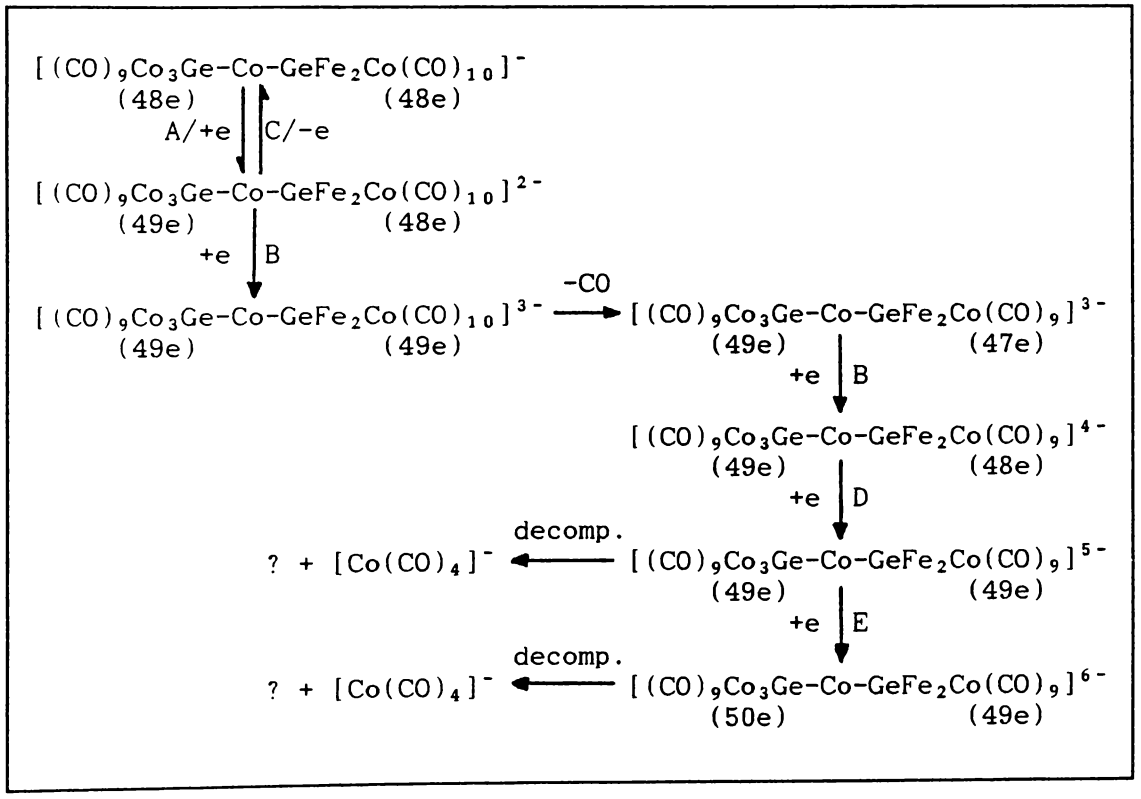

Figure 5.17: Possible mechanism for reduction of $[Ge_2Fe_2Co_5(CO)_{22}]^-$ (For simplification the carbonyl groups on the central Co atom have not been included)

It appears that peak A corresponds with peak A for $[Ge_2Co_7(CO)_{21}]^-$ and peak B is due to reduction of the $-GeFe_2Co$ trigonal pyramid (see discussion). However there is insufficient information to interpret what is happening at D and E. A possible mechanism for the reduction processes observed for $[Ge_2Fe_2Co_5(CO)_{22}]^-$ is shown in **figure 5.17.**

On the anodic scan, peak F (E_p = 0.08 V) is due to oxidation of $[Co(CO)_4]^-$. This peak is seen following reduction at D, and increases in intensity if E is also scanned through. Peak G (E_p = 0.44 V) is the principle oxidation wave for $[Ge_2Fe_2Co_5(CO)_{22}]^-$, and involves two electrons.

5.2.2.6 Discussion

The redox behaviour of the $(CO)_xMECo_3(CO)_9$ clusters investigated above appears to conform with what has already been reported for $YECo_3(CO)_9$ compounds (where Y = halogen, alkyl or aryl). $(CO)_xMECo_3(CO)_9$ clusters typically undergo an electrochemically reversible one-electron reduction. The 49-electron radical anion which is produced is relatively stable but gradually decomposes over a period of hours to eventually give $[Co(CO)_4]^-$ and $Co_4(CO)_{12}$. The radical anion can be further reduced in an electrochemically irreversible process but rapidly disintegrates, giving $[Co(CO)_4]^-$:

$$(CO)_xMECo_3(CO)_9 \underset{-e}{\overset{+e}{\rightleftharpoons}} [(CO)_xMECo_3(CO)_9]^- \xrightarrow{+e} [(CO)_xMECo_3(CO)_9]^{2-}$$

$$\downarrow \qquad\qquad\qquad\qquad \downarrow$$

$$[Co(CO)_4]^- + Co_4(CO)_{12} \qquad [Co(CO)_4]^- + ?$$

Note that a weak peak due to oxidation of $[Co(CO)_4]^-$ was found to be present initially with virtually all samples, and was probably the result of sample decomposition during handling.

Information on the reduction processes of these $(CO)_xMECo_3(CO)_9$ compounds is included in **table 5.3.** As mentioned previously, care must be taken when comparing results with those in the literature, that measurements are obtained under similar conditions. Probably the best comparison that can be made is with the work of Lindsay *et al.* [262], which employed the same solvent/electrolyte/WE/CE combination with a Ag/AgCl RE. Selected results from their investigation are incorporated into the bottom half of **table 5.3.**

Looking at this table, it can be seen that replacement of a μ_3-Si

Table 5.3: Electrochemical and Spectroscopic Data for Clusters Containing $-ECo_3$ Trigonal Pyramids

PEAKS*:	G E_p(V)	A/C $\sim E_{1/2}$(V)	B E_p(V)	D E_p(V)	E E_p(V)	E_p^c(A)-E_p^c(B) (V)	λ_{max} (nm)
$(CO)_4CoSiCo_3(CO)_9$		-0.61	-1.52			0.91	532
i_p^c/i_p^a		1	irrev.				
n		1	1				
$(CO)_5MnSiCo_3(CO)_9$		-0.66	-1.60			0.88	520
i_p^c/i_p^a		1	irrev.				
n		1	1				
$(CO)_4CoGeCo_3(CO)_9$		-0.52	-1.43			0.89	543
i_p^c/i_p^a		1	irrev.				
n		1	1				
$(CO)_5MnGeCo_3(CO)_9$		-0.53	-1.49			0.85	532
i_p^c/i_p^a		1	irrev.				
n		1	1				
$[Ge_2Co_7(CO)_{21}]^-$	0.51	-0.87	-1.81			0.89	
i_p^c/i_p^a	irrev.	1	irrev.				
n	2	2	~2				
$[Ge_2Fe_2Co_5(CO)_{22}]^-$	0.44	-1.06	-1.37	-1.48	-1.82		
i_p^c/i_p^a	irrev.	~1	irrev.	irrev.	irrev.		
n	2	~1	1-1.6	?	?		
$MeCCo_3(CO)_9$**		-0.57	-1.44			0.83	505
i_p^c/i_p^a		1	irrev.				
n		1	1				
$PhCCo_3(CO)_9$**		-0.56	-1.42			0.82	508
i_p^c/i_p^a		1	irrev.				
n		1	1				
$MeGeCo_3(CO)_9$**		-0.32	-1.18			0.82	530
i_p^c/i_p^a		1	irrev.				
n		1	1				
$PhGeCo_3(CO)_9$**		-0.32	-1.27			0.91	529
i_p^c/i_p^a		1	irrev.				
n		1	1				

* scan rate = 200 mV s^{-1}, ** Data taken from reference [262]

group with a μ_3-Ge group causes a positive shift of ~0.11 V in the half electrode potentials. A larger shift of ~0.24 V is seen when a μ_3-C group is replaced with a μ_3-Ge group [31]. This is consistent with the ECo_3 moiety becoming more strained when E is larger (section 5.1.2).

The wavelengths for the highest band in the visible spectrum (figure 5.18) of each compound are also given in table 5.3. As mentioned in section 5.1.2, the frequency of this band gives an indication of the orbital overlap or the strength of the interaction between the capping atom and the M_3 triangle. From table 5.3, the visible bands for the Ge clusters occur ~11 nm higher than for their Si analogues, and ~22 nm higher than for their C analogues. This implies the gap between the cluster HOMO and LUMO becomes less as C is replaced with Si then Ge. This complements the observed trend in the $E_{1/2}$ values.

Table 5.3 also provides an oportunity to examine the effect of having a terminal metal carbonyl group attached to the apical atom. It can be seen that $(CO)_4CoGeCo_3(CO)_9$ and $(CO)_5MnGeCo_3(CO)_9$ are more difficult to reduce than their phenyl and methyl analogues. An average positive shift of 0.20 V in the $E_{1/2}$ values is observed. This corresponds with a small increase in the wavelength of the visible band. This shift in potential is relatively large (replacement of Cl in $ClCCo_3(CO)_9$ with Ph gives a positive shift of ~0.11 V [270]). The implication is that the metal carbonyl groups are acting as better electron donors.

The reduction potentials in table 5.3 also indicate that the clusters with terminal $Mn(CO)_5$ groups are slightly more difficult to reduce than those with terminal $Co(CO)_4$ groups. A consistent shift is also seen in the λ_{max} in the visible spectra of these compounds. This is reasonable considering that the $Mn(CO)_5$ moiety is generally accepted as being more nucleophilic. It would therefore be a better electron donor than the $Co(CO)_4$ group.

When the reduction of $(CO)_4SiCo_3(CO)_9$ was repeated chemically using cobaltocene, an infrared spectrum of the $[(CO)_4CoSiCo_3(CO)_9]^-$ radical anion was obtained. This exhibits a similar pattern of carbonyl stretches to the parent cluster, with an overall red-shift of *ca.* 37 cm^{-1}. Individual peaks are shifted to varying degrees, and the two very weak low frequency peaks observed for $(CO)_4CoSiCo_3(CO)_9$

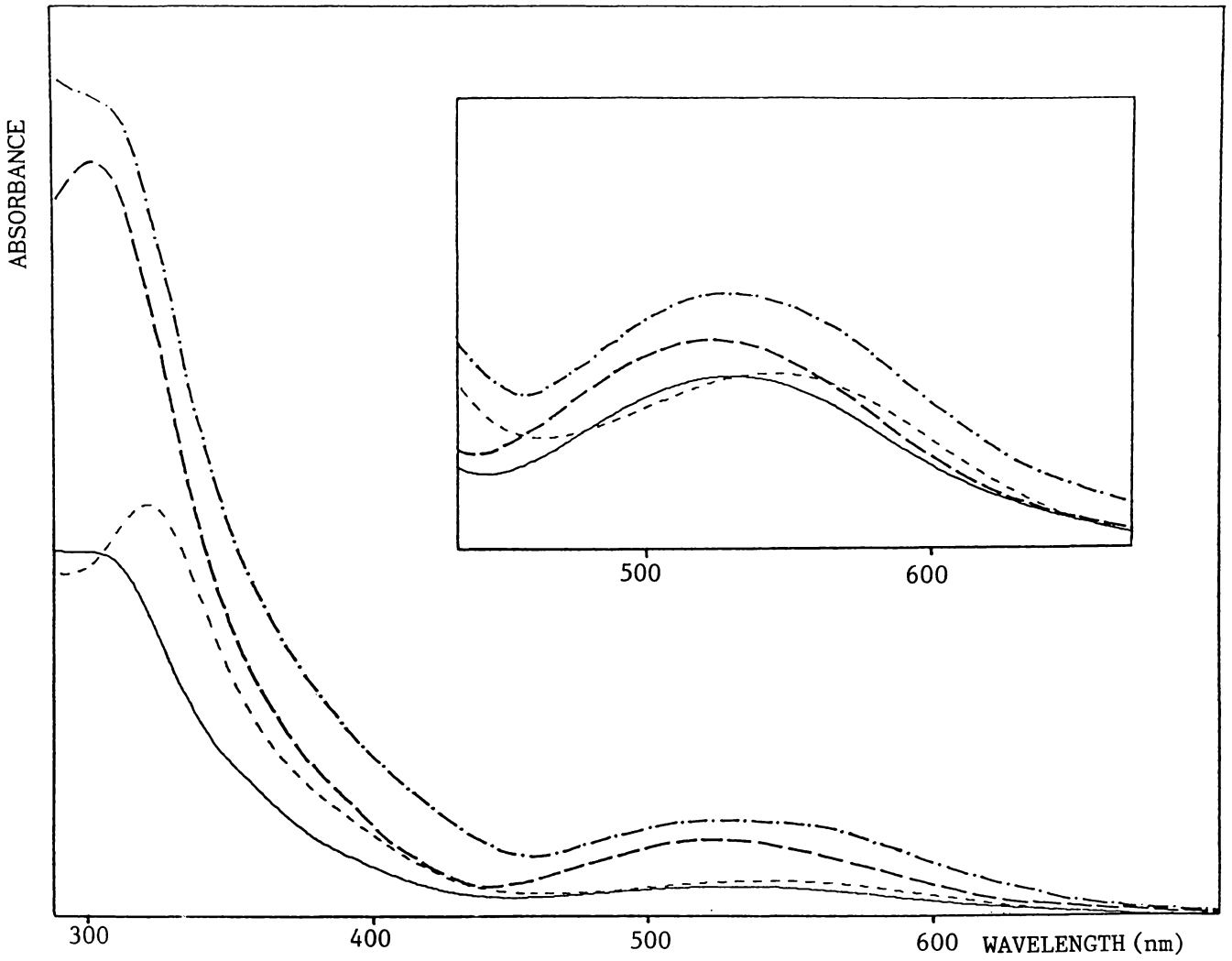

Figure 5.18: Visible spectra of $(CO)_4CoSiCo_3(CO)_9$ (———), $(CO)_4CoGeCo_3(CO)_9$ (- - - -), $(CO)_5MnSiCo_3(CO)_9$ (— — —) and $(CO)_5MnGeCo_3(CO)_9$ (—·—·—)

appear to be superimposed in the spectrum of the radical anion. But generally, the similarity of these spectra confirms that the molecular symetry does not change significantly on reduction. The magnitude of the red-shift is less than the ~60 cm^{-1} shift observed when $PhCCo_3(CO)_9$ is reduced to $[PhCCo_3(CO)_9]^-$. The $[(CO)_4CoSiCo_3(CO)_9]^-$ carbonyl infrared stretches occur between 2070 and 1970 cm^{-1} while those of $[PhCCo_3(CO)_9]^-$ lie btween 2040 and 1940 cm^{-1}. This can be explained by the distribution of the charge over a larger number of carbonyl groups on $[(CO)_4CoSiCo_3(CO)_9]^-$.

The ESR spectra of $(CO)_4CoGeCo_3(CO)_9$ and $(CO)_5MnGeCo_3(CO)_9$ in THF have been investigated by Duffy **[93]**. Both compounds exhibited 18 out of the 22 lines expected for the interaction of the unpaired electron with three equivalent Co nucleii. No coupling was observed to the apical Ge atom. This confirms that the bonding in these clusters is very similar to that of the carbon analogues, and that the low lying antibonding orbital that the unpaired electron enters is of pure Co character. Note that if a decarbonylated $[(CO)_4CoSiCo_3(CO)_8]^-$ species had been produced then one would not have expected the three Co nucleii to be equivalent. Similarly, no bridging carbonyl bands were observed in the infrared spectrum reported above.

When the redox behaviour of $(CO)_4CoSiCo_3(CO)_9$ was investigated at lower concentrations, a "Hinkelmann" decarbonylation of the radical anion to give $[(CO)_4CoSiCo_3(CO)_8]^-$, was not detected. The $[Co(CO)_4]^-$ oxidation peak was found to be much stronger at the lower concentration (*ca.* 10^{-4} mol l^{-1}), but this again is probably due to decomposition during handling; the extreme dilution of the sample would have compounded problems such as reaction with dissolved water or oxygen. Note that this work was carried out in a different solvent and under less rigorous conditions than that of Hinkelmann *et al.* **[260]**.

$[Ge_2Co_7(CO)_{21}]^-$ and $[Ge_2Fe_2Co_5(CO)_{22}]^-$ both contain two 48-electron $-EM_3$ trigonal pyramids and a negative charge. The presence of a negative charge makes these compounds more difficult to reduce. They are also able to be oxidised within the potential range allowed by the solvent. For $[Ge_2Co_7(CO)_{21}]^-$ it is interesting that each of the peaks (A to D) is a simple two-electron process. It seems that the two redox centres are acting totally independently.

For $[Ge_2Fe_2Co_5(CO)_{22}]^-$, peak A has been assigned to reduction of

the $-GeCo_3$ trigonal pyramid (by comparison with $[Ge_2Co_7(CO)_{21}]^-$), and B to the $-GeFe_2Co$ trigonal pyramid. Lindsay *et al.* have shown that the incorporation of two heterometal atoms into 48-electron $-ECo_3$ trigonal pyramids is usually associated with a loss of reversibility for the principle reduction wave (although no compounds containing $-EFe_2Co$ trigonal pyramids were investigated). This is consistent with reduction at B. It is perhaps surprising that, although the two ends of the cluster are reduced at different potentials, they both appear to be oxidised at G (0.44 V).

As mentioned in section 5.1.2, the gap between the primary and secondary reduction potentials for $YECo_3(CO)_9$ compounds is thought to correspond with the electronic charge repulsion associated with filling the a_2^* orbital. It can be seen in **table 5.3** that this gap ($E_p^c(A)$-$E_p^c(B)$) is approximately the same for all of the compounds investigated, even the $[Ge_2Co_7(CO)_{22}]^-$ anion. The values for $E_p^c(A)$-$E_p^c(B)$ are also similar to those for the compounds taken from the literature.

As stressed at the start of this chapter, cyclic voltammetry is most useful as a diagnostic tool, and precise quantitative measurements are best obtained by other methods. However this work has shown that the electrochemistry of the above clusters, containing $(CO)_xMECo_3(CO)_9$ moieties, conforms with what has previously been reported for other 48-electron $YECo_3(CO)_9$ compounds. Electrochemical studies appear to be a useful means of comparing the effects of various $M(CO)_x$ moieties and of comparing these effects with those of other Y groups. To this end, further investigation using a more quantitative electrochemical technique (eg. polarography) may be useful.

The $[(CO)_xMECo_3(CO)_9]^-$ radical anion is sufficiently long lived to be useful for further reaction. Ligand substitution can be performed within the electrochemical cell using the ETC process (section 5.2.2.1). Alternatively, cobaltocene can be used to chemically reduce $(CO)_xMECo_3(CO)_9$ clusters on any scale, and the products used for further reaction. This could provide a useful route to synthesising new species.

5.2.3 ELECTROCHEMISTRY OF CLUSTERS CONTAINING *SPIRO*-M_2EM_2 STRUCTURES

5.2.3.1 $Si[Fe_2(CO)_8]_2$ *(F 2)*

a) Electrochemistry

Figure 5.19 shows a typical voltammogram for $Si[Fe_2(CO)_8]_2$. The principle reduction wave, A, involves an irreversible two-electron transfer, occurring at E_p = -1.15 V. This is followed by a further irreversible reduction, B at E_p = -1.56 V. The peak current for B varies with scan rate, being most prominent at 50 mV s^{-1}. On the reverse, anodic scan a weak irreversible oxidation peak, C, is observed at E_p = -0.69 V. This peak is only seen subsequent to scanning through A. As the switching potential becomes more negative, the intensity of C diminishes. This appears to be mainly associated with the time lag from A to C. The intensity of C also decreases with slower scan rates, being undetectable at 50 mV s^{-1}. Peak C does not appear to be dependent upon whether reduction B has occurred, implying that a different electroactive species is involved.

At 210 K neither B nor C are seen. This implies that the immediate product of reduction A, represented as "$[Si\{Fe_2(CO)_8\}_2]^{2-*}$ ", is not the electroactive species involved in B or C (the asterisk is to indicate that some change has occurred preventing immediate reoxidation). This also shows that $[Si\{Fe_2(CO)_8\}_2]^{2-*}$ has some stability at 210 K.

Peaks G and H are only seen if the scan is switched after reduction at B, and therefore are due to oxidation of some product(s) of this reduction. The principle oxidation wave for the $Si[Fe_2(CO)_8]_2$ cluster appears to be peak D (E_p = 0.40 V). This is a one-electron irreversible transfer and is the only oxidation peak evident when the scan is initiated in a positive direction. A product of this oxidation is irreversibly reduced producing a very weak peak on the anodic scan at F (E_p = -0.50 V).

Performing the scan under carbon monoxide atmosphere had negligible effect on the peak positions and heights. This implies that none of the above electrode processes is dependent upon CO elimination

Taking these observations into account, the reaction scheme shown in figure 5.20 can be proposed.

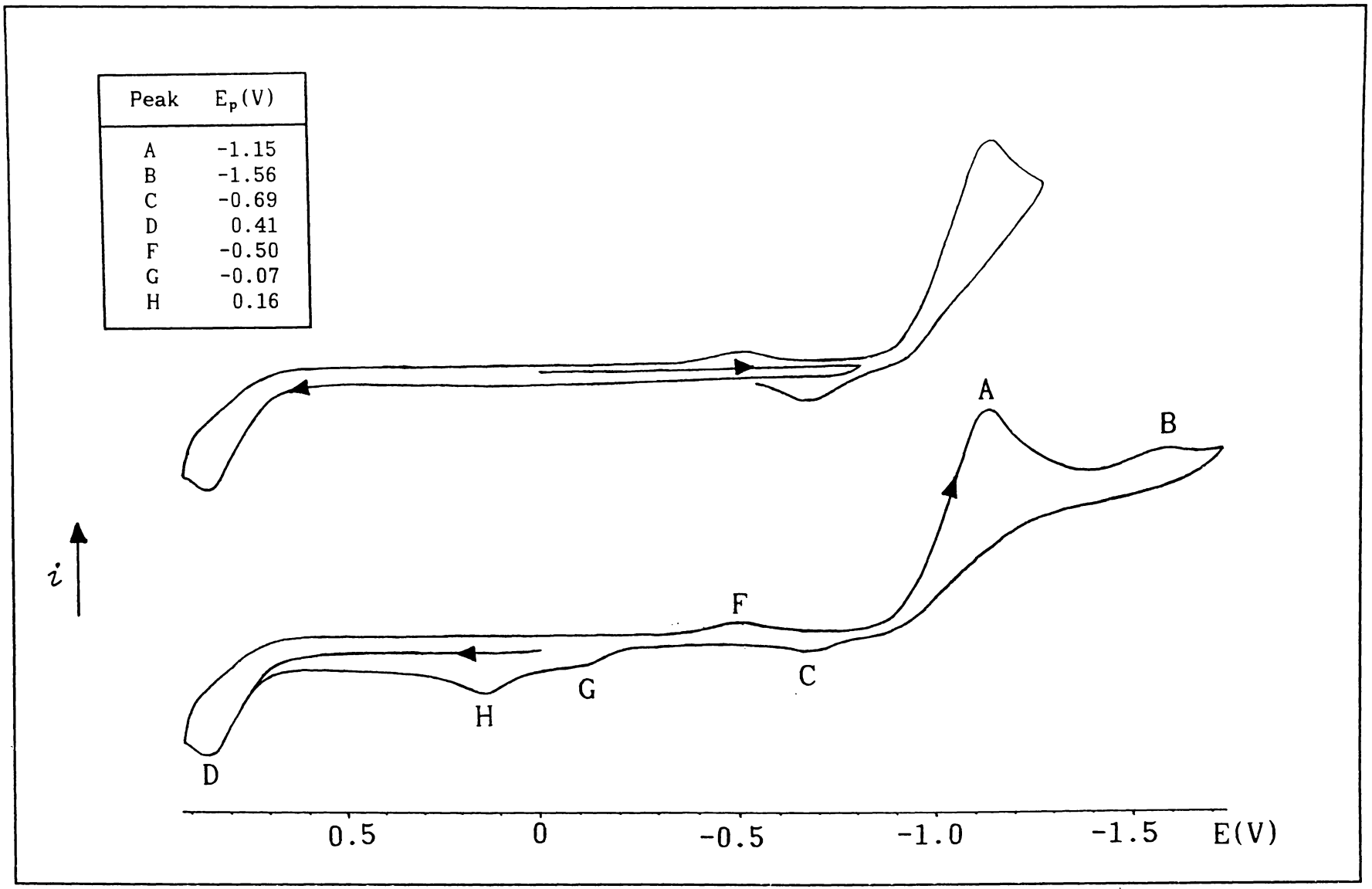

Figure 5.19: Cyclic voltammograms for $Si[Fe_2(CO)_8]_2$

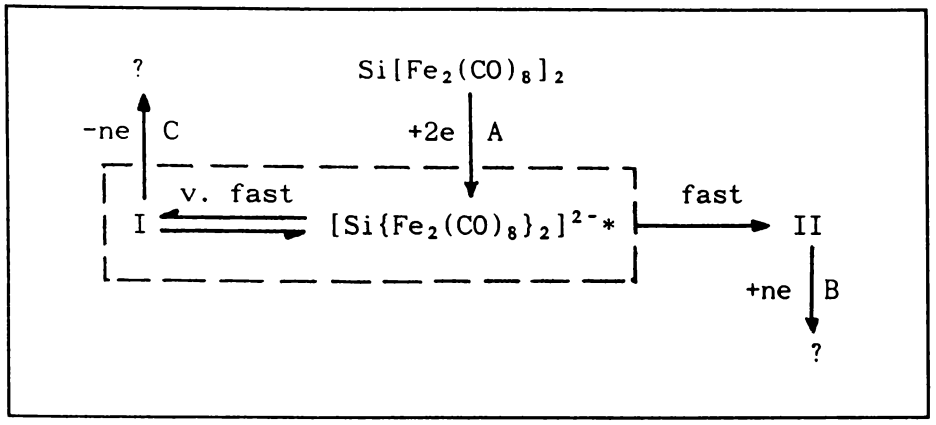

Figure 5.20: Proposed reduction mechanism for $Si[Fe_2(CO)_8]_2$

The reaction forming intermediate I is faster than that forming intermediate II. This accounts for C being strongest initially and diminishing with time as II is formed. Note that it is not clear whether $[Si\{Fe_2(CO)_8\}_2]^{2-}$* or intermediate I reacts to give intermediate II. **Table 5.4** summarises the results of electrochemical studies of $Si[Fe_2(CO)_8]_2$ and related compounds. The effects of temperature and scan rate on the intensities of B and C are represented in table 5.5.

b) Chemical Studies

(i) $Si[Fe_2(CO)_8]_2$ was chemically reduced using cobaltocene. A nitrogen flushed Schlenk flask was charged with $Si[Fe_2(CO)_8]_2$ (0.016 g, 0.023 mmol) in 15 ml CH_2Cl_2. To this a 15 ml solution of cobaltocene in CH_2Cl_2 (3 mmol l^{-1}) was added dropwise from a syringe. After stirring for 0.5 h the solvent was removed under vacuum and the hexane-soluble components were extracted. The remaining product was dissolved in a CH_2Cl_2 (20 ml) solution of PPNCl (0.029 g, 0.05 mmol). This was stirred for 15 min then filtered under nitrogen through a glass sinter. An infrared spectrum of the products in CH_2Cl_2 revealed weak peaks due to $Si[Fe_2(CO)_8]_2$ plus the following CO stretches: 2065vw 2019w 2001vs 1973s 1950w 1914w 1880s 1720w,br cm^{-1}. The observed pattern of peaks is similar to that reported for $[(CO)_4FeGeFe_3(CO)_{10}]^{2-}$ ***(F 6)*** (ν_{CO} (MeCN) 1998m 1963s 1917m 1720w,br cm^{-1}). If a $[(CO)_4FeSiFe_3(CO)_{10}]^{2-}$ species were formed, this would involve elimination of CO. Therefore $[(CO)_4FeSiFe_3(CO)_{10}]^{2-}$ does not correspond to proposed intermediates I

Typical voltammogram:

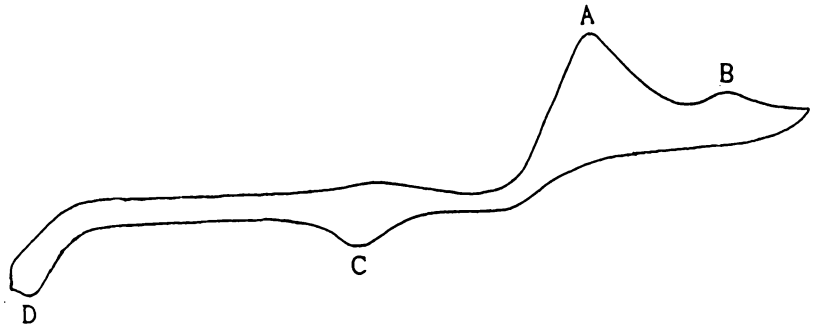

PEAKS*:	D E_p(V)	E E_p(V)	C E_p(V)	A E_p(V)	B E_p(V)
$Si[Fe_2(CO)_8]_2$ n	0.41 1		-0.69	-1.15 2	-1.56
$Ge[Fe_2(CO)_8]_2$ n	0.38 1		-0.51	-1.12 2	-1.45
$Sn[Fe_2(CO)_8]_2$ n	0.43 1	0.43	-0.04	-0.97 2	-1.36
$Sn[Fe_2(CO)_8]_2$** n		0.44*** 2			
$Pb[Fe_2(CO)_8]_2$** n		0.26 2		-0.64 1.8-2.0	

* scan rate = 200 mV s^{-1}, ** taken from reference [31]
*** reduction potential for $[(CO)_8Fe_2]Sn[Fe(CO)_4]_2^{2-}$

Table 5.4: Electrochemical data for $E[Fe_2(CO)_8]_2$ clusters

PEAKS	$Si[Fe_2(CO)_8]_2$	$Ge[Fe_2(CO)_8]_2$	$Sn[Fe_2(CO)_8]_2$
B	50-1000 mV s^{-1} not at -63°C	50-500 mV s^{-1} not at -63°C	50-200 mV s^{-1} at -63°C
C	200-1000 mV s^{-1} not at -36°C	200-1000 mV s^{-1} at -63°C	200-1000 mV s^{-1} at -63°C

Table 5.5: Occurance of peaks B and C in voltammograms of $E[Fe_2(CO)_8]_2$ clusters

or II, but could be formed by decarbonylation of II. If this were the case, some of the anomalies in the ν_{CO} infrared spectrum mentioned above could be explained by further reduction of II (as represented by peak B), giving $[HFe_3(CO)_{11}]^-$ (ν_{CO} (CH_2Cl_2) 2064w 1998vs 1972s 1940sh 1718w,br cm^{-1})). To test this, the reduction was repeated using lesser and greater amounts of cobaltocene.

(ii) $Si[Fe_2(CO)_8]_2$ (0.016 g, 0.022 mmol) was reduced using 0.022 mmol of cobaltocene by the methods described above. Once the hexane solubles were removed, a ν_{CO} infrared spectrum revealed CO stretches at: 1999m 1966s 1917m 1722w,br cm^{-1} (**figure 5.21**). This spectrum can be assigned to $[(CO)_4FeSiFe_3(CO)_{10}]^{2-}$ ***(F 6)***.

(iii) The chemical reduction was also repeated using excess cobaltocene (0.088 mmol). A ν_{CO} infrared spectrum of the products revealed $[HFe_3(CO)_{11}]^-$ to be the major product, with an additional peak at 1880 cm^{-1}.

(iv) The cobaltocene reduction was repeated at 210 K under a carbon monoxide atmosphere in an attempt to isolate $[Si\{Fe_2(CO)_8\}_2]^{2-}$* or intermediate I.

A Schlenk tube containing $Si[Fe_2(CO)_8]_2$ (0.015 g, 0.020 mmol) in 40 ml hexane was flushed with CO and cooled to 210 K using a chloroform slush bath. A solution of cobaltocene (0.040 mmol) in 20 ml hexane was added dropwise via syringe. CO was bubbled through the solution at 210 K for 40 minutes. The solution was then filtered under carbon monoxide and the solid residues dissolved in a chilled solution of excess PPNCl (0.05 g, 0.088 mmol) in 50 ml CH_2Cl_2. A ν(CO) infrared spectrum of the products was obtained using a chilled, N_2 flushed solution cell. Weak peaks due to $Si[Fe_2(CO)_8]_2$ and $[HFe_3(CO)_{11}]^-$ were observed along with peaks at 2019s 2001vs 1980vw 1950w cm^{-1}. It was not possible to obtain a pure sample but the spectrum does show a similar pattern of peaks to $Si[Fe_2(CO)_8]_2$, with a red shift of *ca.* 56 cm^{-1} and with the latter two peaks being slightly less intense. This suggests that no major structural rearrangement has yet occurred. In successive scans the intensity of the latter peaks decreased while the peaks due to $Si[Fe_2(CO)_8]_2$ became stronger.

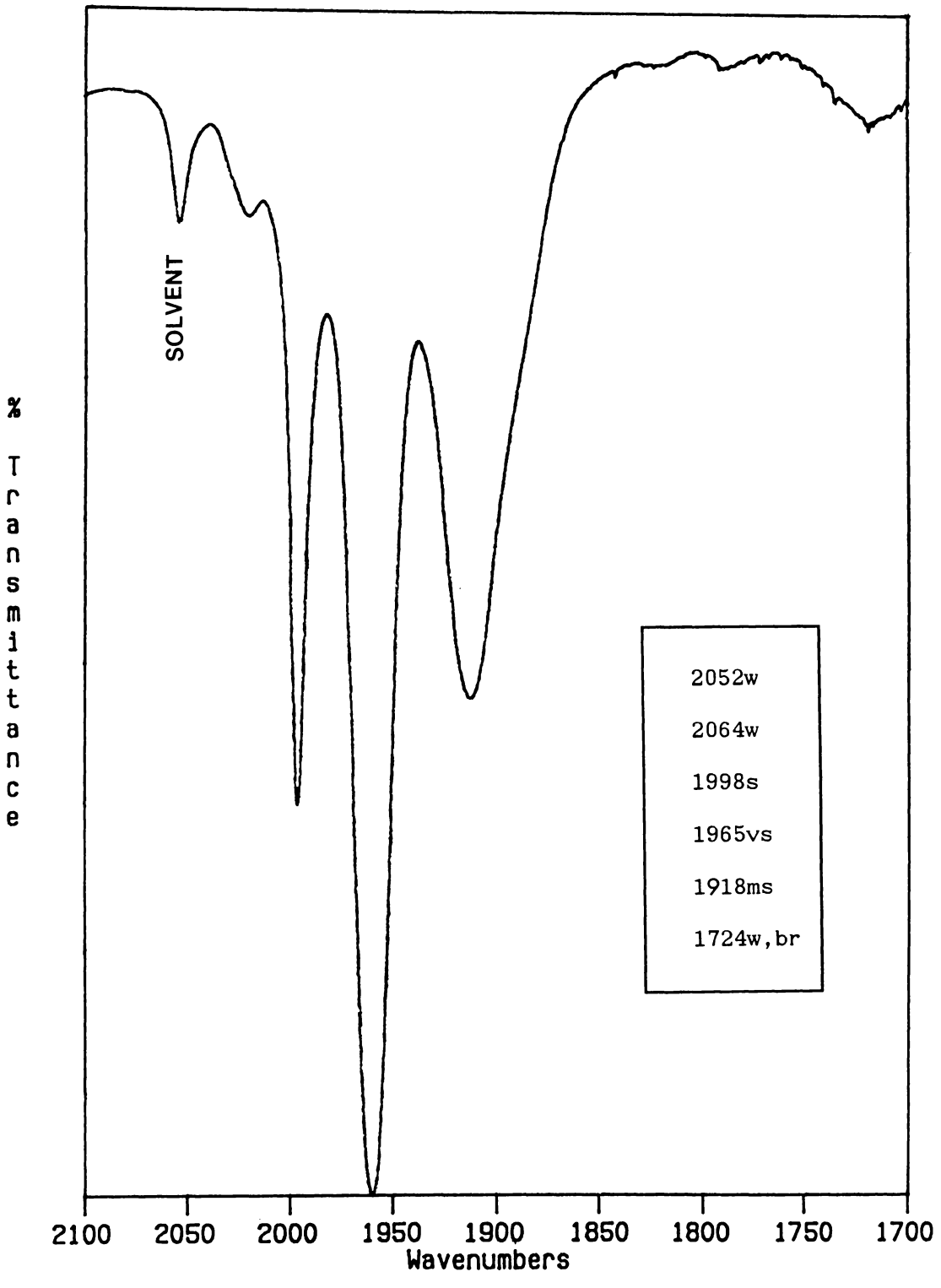

Figure 5.21: Infrared spectrum of $[(CO)_4FeSiFe_3(CO)_{10}]^{2-}$

The Schlenk flask containing the CH_2Cl_2 solution was flushed with N_2 and allowed to warm to room temperature. The reaction was monitored for 4 h using infrared spectroscopy. During this time the unidentified peaks disappeared and new peaks appeared at 1997m 1961s 1918m 1722w,br cm^{-1}. This corresponds with the formation of $[(CO)_4FeSiFe_3(CO)_{10}]^-$, as shown in figure 5.22.

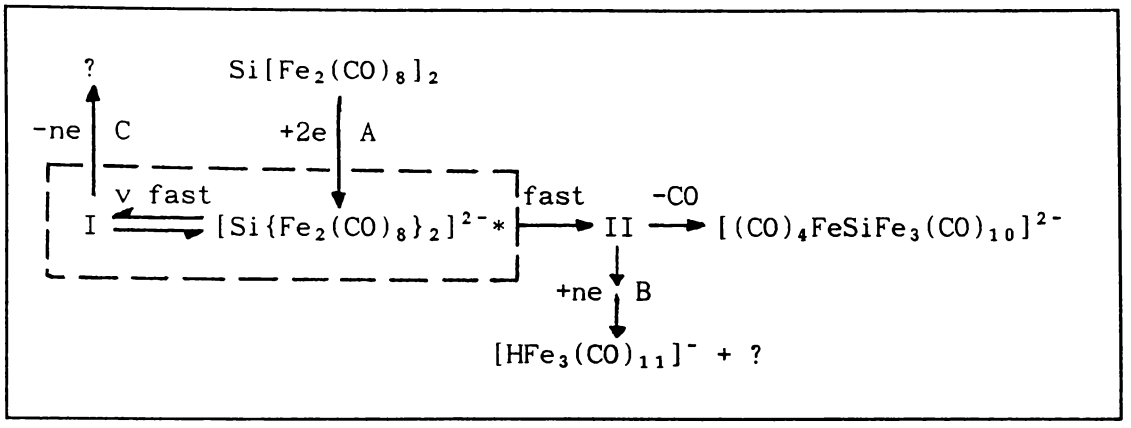

Figure 5.22: Proposed reduction mechanism for $Si[Fe_2(CO)_8]_2$

5.2.3.2 $Ge[Fe_2(CO)_8]_2$ *(F 2)*

a) Electrochemistry

A cyclic voltammogram of $Ge[Fe_2(CO)_8]_2$ is seen in figure 5.23. Peak potentials are also given in table 5.4. The i-E curves of $Ge[Fe_2(CO)_8]_2$ display a pattern of peaks similar to that of $Si[Fe_2(CO)_8]_2$, indicating that the same reaction mechanisms are operating. The only differences are that peaks G and H are not detectable for the germanium analogue, and the relative strengths of peaks B and C have altered slightly (see table 5.5). Peak B (E_p = -1.45 V) is no longer evident at scan rates of 500 to 1000 mV s^{-1}, and C (E_p = -0.51 V) is stronger and is also observed at 210 K. It appears that, for E = Ge, $[E\{Fe_2(CO)_8\}_2]^{2-}$* and intermediate II (in figure 5.22) have become slightly less stable in favour of intermediate I.

b) Chemical Studies

Whitmire *et al.* [31] reported that the chemical reduction of $Ge[Fe_2(CO)_8]_2$ using cobaltocene yielded $[(CO)_4FeGeFe_3(CO)_{10}]^{2-}$ *(F 6)*. The result from the previous section suggest that at 210 K an alternative reduction mechanism involving intermediate II is operating. This was

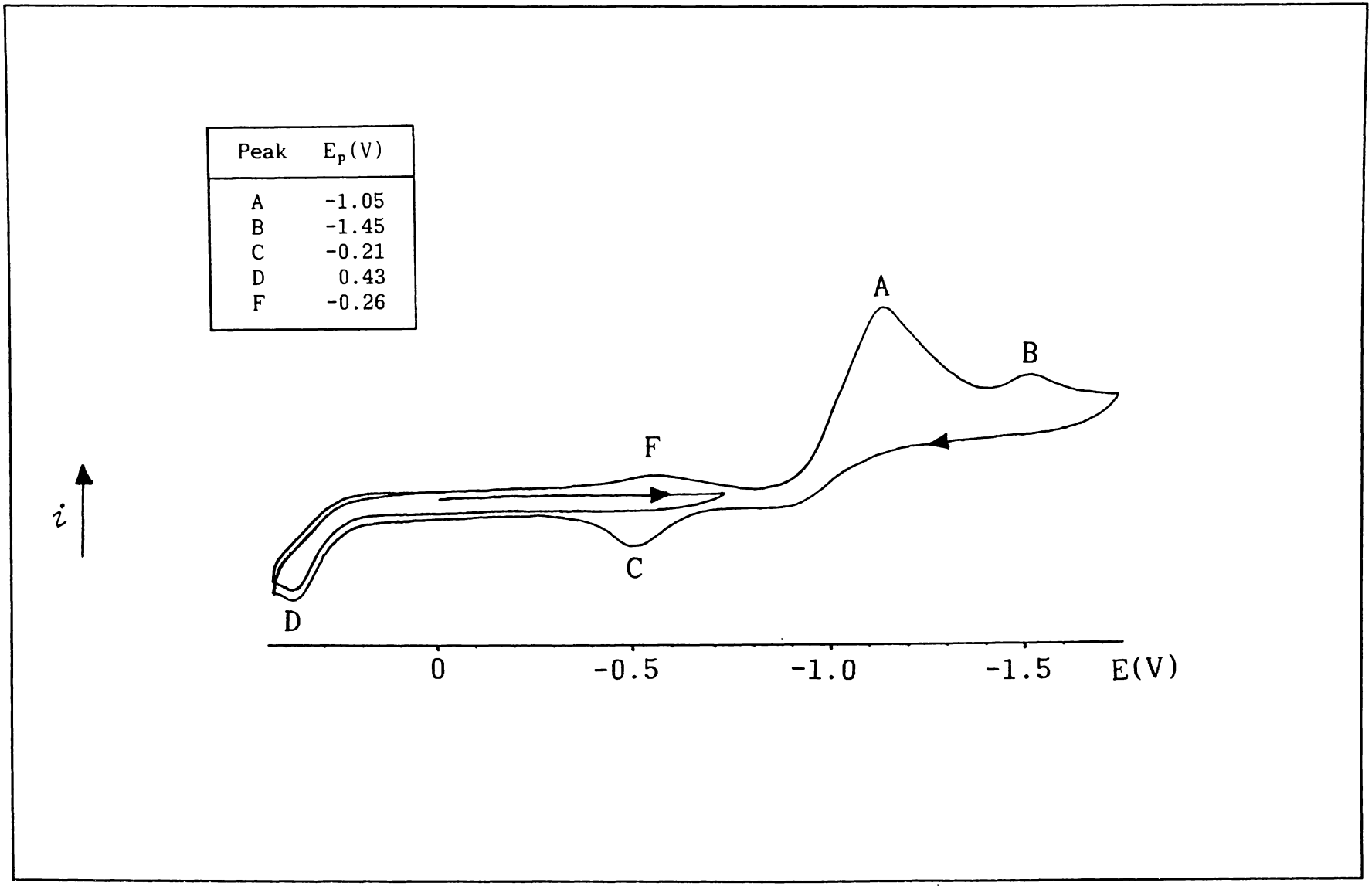

Figure 5.23: Cyclic voltammogram for $Ge[Fe_2(CO)_8]_2$

investigated by reducing $Ge[Fe_2(CO)_8]_2$ at 210 K under a carbon monoxide atmosphere. A solution of cobaltocene (0.022 mmol) in hexane (11 ml) was added dropwise to a cooled (210 K) solution of $Ge[Fe_2(CO)_8]_2$ (0.08 g, 0.011 mmol) in hexane (20 ml). Carbon monoxide was bubbled through the solution at 210 K for 40 min, before it was filtered through a glass sinter. The insoluble products were redissolved by passing a precooled solution of PPNCl (0.023 g, 0.04 mmol) in 30 ml CH_2Cl_2 back through the glass sinter. The carbonyl stretching region infrared spectrum was examined using a chilled solution cell, flushed with nitrogen. The spectrum showed weak peaks due to $Ge[Fe_2(CO)_8]_2$ and $[HFe_3(CO)_{11}]^-$ along with unidentified peaks at 2014s 1995vs and 1956w cm^{-1}. Again it was not possible to obtain a good spectrum of this intermediate, and this may explain why one of the peaks observed for the silicon analogue was not seen. With successive scans the intensity of the latter peaks diminished while those of $Ge[Fe_2(CO)_8]_2$ became stronger. The Schlenk flask containing the CH_2Cl_2 solution was flushed with nitrogen and allowed to warm to room temperature over approximately 20 min. An infrared spectrum indicated that the unidentified peaks had disappeared and new peaks appeared at 1997m 1961s 1918m 1722wbr cm^{-1}. This corresponds to the formation of $[(CO)_4FeGeFe_3(CO)_{10}]^-$ for which the following spectrum has been reported [31] : ν_{CO} (MeCN) 1998m 1963s 1917m 1720w,br cm^{-1}.

5.2.3.3 $Sn[Fe_2(CO)_8]_2$ *(F 2)*

a) Electrochemistry

The incorporation of tin into the Fe_2EFe_2 spiro cluster has a more marked effect on the cyclic voltammograms (**figure 5.24**). For $Sn[Fe_2(CO)_8]_2$ peak B is still seen at scan rates between 50 and 200 mV s^{-1}, but is very weak. On the other hand C is much stronger, corresponding to a transfer of *ca.* 0.9 electrons at 200 mV s^{-1}. Again this peak is weaker for slower scan rates and is not observed at 50 mV s^{-1}. The intensity of C appears to be associated with that of peak D/E. If the scan is initiated in a positive direction, D/E has a peak current commensurate with a one-electron process. This is due to oxidation of $Sn[Fe_2(CO)_8]_2$. On subsequent cycles (if A is being scanned through) D/E becomes more intense, with $n \simeq 1.2$. Peak D/E is most intense ($n \simeq 1.5$) at 50 mV s^{-1}, when C is no longer evident.

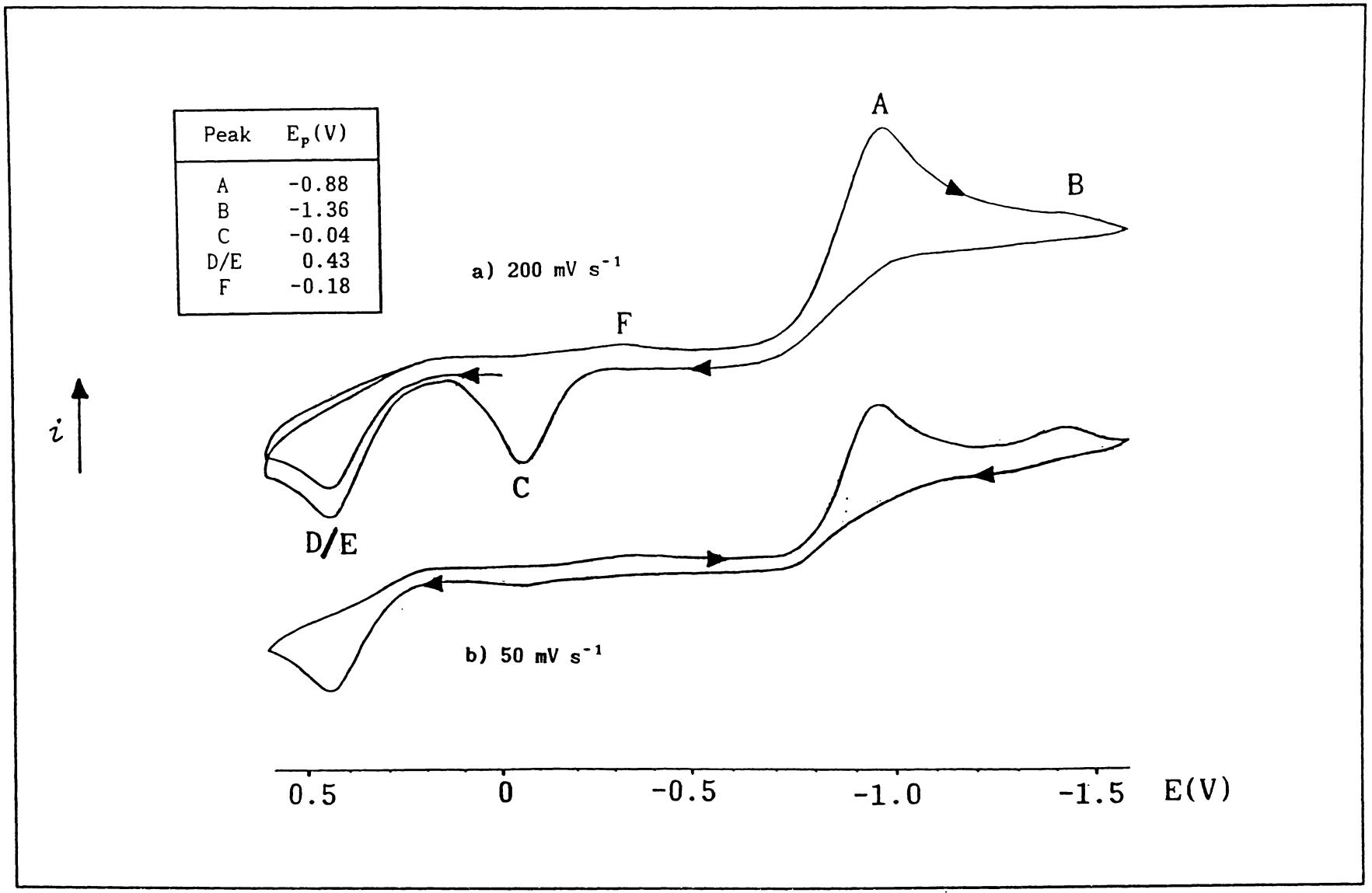

Figure 5.24: Cyclic voltammograms for $Sn[Fe_2(CO)_8]_2$

The potential of peak D (0.43 V) coincides with that reported for the oxidation of $[(CO)_8Fe_2]Sn[Fe(CO)_4]_2^{2-}$ *(F 3)* (0.44 V in CH_2Cl_2/TBAP/glassy carbon WE). It therefore appears that intermediate I (which is oxidised at C) reacts to give $[(CO)_8Fe_2]Sn[Fe(CO)_4]_2^{2-}$, and the oxidation of $[(CO)_8Fe_2]Sn[Fe(CO)_4]_2^{2-}$ (E) is superimposed upon the oxidation of the parent cluster (D). From the voltammograms, the reaction of I to give $[(CO)_8Fe_2]Sn[Fe(CO)_4]_2^{2-}$ takes somewhere between 15 and 60 s to go to completion. These results have been incorporated into the proposed mechanism in **figure 5.25**. Note that the end product of $[(CO)_8Fe_2]Sn[Fe(CO)_4]_2^{2-}$ oxidation (at E) has been shown to be $Sn[Fe_2(CO)_8]_2$. This is indicated in the proposed reaction scheme.

b) Chemical Studies

(i) A 10 ml solution containing cobaltocene (0.03 mmol) was added dropwise to a Schlenk flask containing $Sn[Fe_2(CO)_8]_2$ (0.012 g, 0.015 mmol) in 10 ml CH_2Cl_2. The solution was stirred for 0.5 h, the solvent removed under vacuum and a hexane extraction performed. The fraction insoluble in hexane was redissolved in a solution of PPNCl (0.018 g, 0.031 mmol) in CH_2Cl_2 (20 ml) and filtered. An infrared spectrum showed that $[(CO)_8Fe_2]Sn[Fe(CO)_4]_2^{2-}$ had been formed (ν(CO)(CH_2Cl_2) 2050w 2003s 1990s 1975vs 1899s 1793br cm^{-1} [31]).

(ii) The solution of $[(CO)_8Fe_2]Sn[Fe(CO)_4]_2^{2-}$ in CH_2Cl_2 was refluxed at 313 K to see whether this would induce the open-butterfly cluster to condense to form a trigonal pyramid structure *(F 6)*. Changes in the reaction mixture were monitored using infrared spectroscopy. As the reaction proceeded, the intensity of the $[(CO)_8Fe_2]Sn[Fe(CO)_4]_2^{2-}$ peaks decreased, and after 2.5 h the spectrum showed carbonyl stretches at 2048w 1988s 1903s cm^{-1}. The reaction was monitored for a further 2 h with no apparent change. The infrared spectrum of the product(s) does not correspond with that expected for a $[(CO)_4FeSnFe_3(CO)_{10}]^{2-}$ cluster. No further attempts were made to characterise this product.

5.2.3.4 $SnFe_5(CO)_{19}$ *(F 4)*

$SnFe_5(CO)_{19}$ has a structure related to that of $Sn[Fe_2(CO)_8]_2$ but with one end of the cluster bridged by a carbonyl group and an $Fe(CO)_4$ moiety. Alternatively this can be regarded as $Fe_3(CO)_{12}$ with a

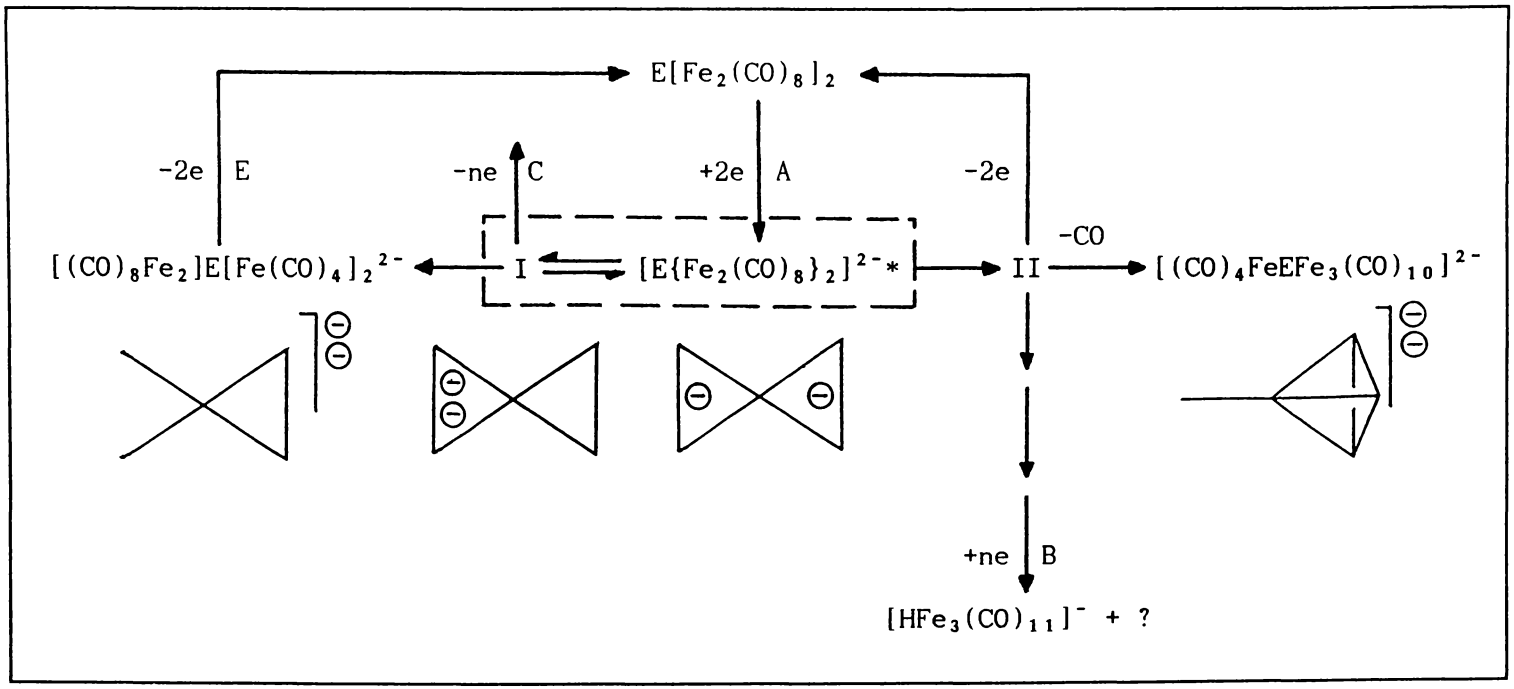

Figure 5.25: Proposed Reduction Mechanism for $E[Fe_2(CO)_8]_2$ Clusters

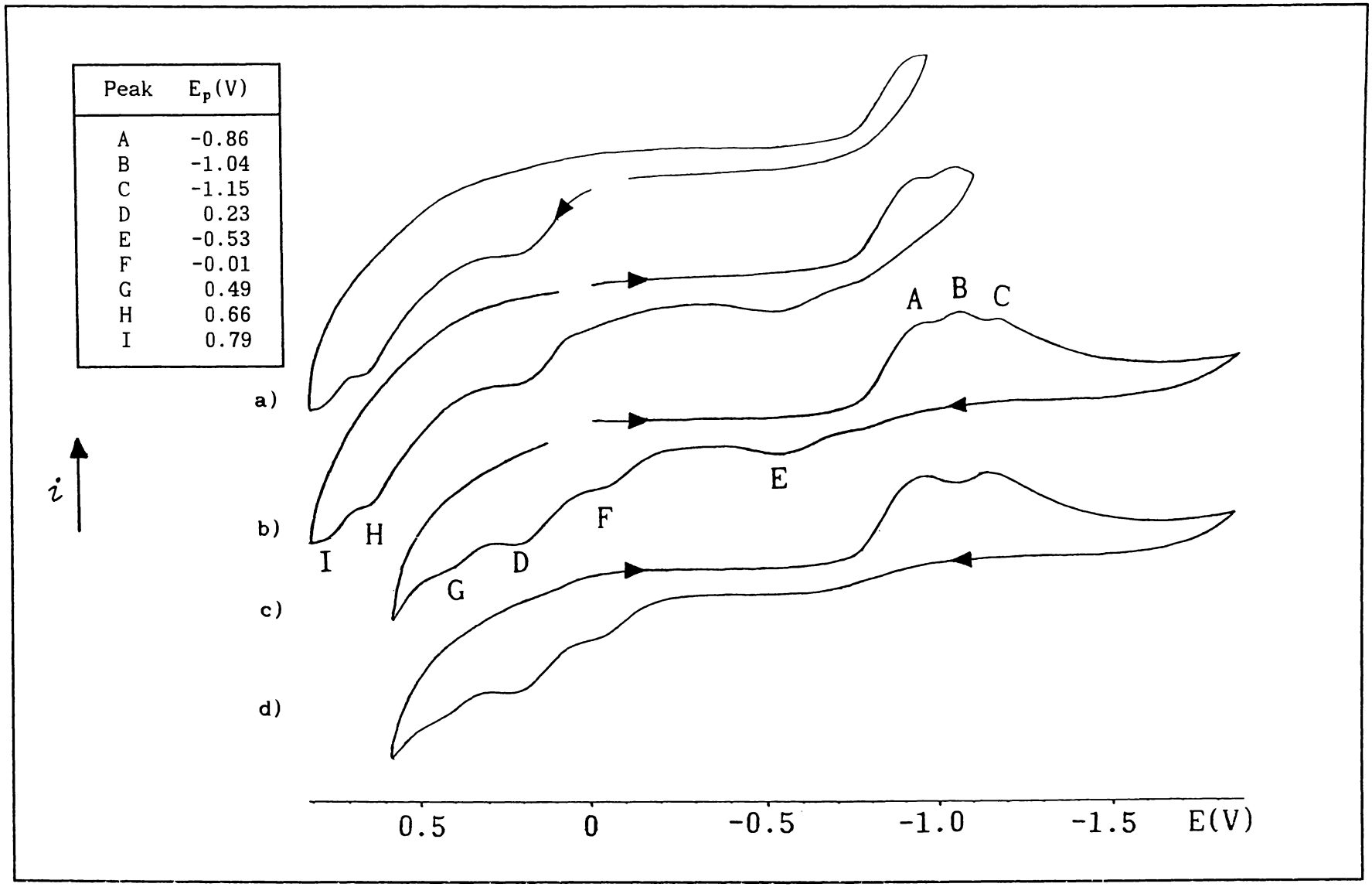

Figure 5.26: Cyclic voltammograms for $SnFe_5(CO)_{19}$ with varying scan range (a-c) and under carbon monoxide (d)

bridging $SnFe_2(CO)_8$ group. Voltammograms for this cluster are quite complicated, with three reduction and six oxidation peaks (see figure 5.26). The principle reduction and oxidation waves (A and D) are both one-electron processes. Further oxidation of the parent cluster is represented by peaks H and I (E_p = 0.66 V and 0.79 V), but these are of less interest. Reduction at A (E_p = -0.86 V) is followed by further reductions B and C at E_p = -1.04 V and -1.15 V respectively. These peaks represent two separate reduction pathways.

The intensity of peak B is dependent upon the scan rate, being maximised at 50 mV s^{-1}. This implies that reduction is preceded by a chemical reaction. B is also suppressed when the reaction is performed under carbon monoxide atmosphere (figure 5.26d), implying that this reaction involves the liberation of a CO ligand. If the scan is switched between B and C, peak E is seen on the anodic scan, along with the principle oxidation wave D. E therefore corresponds to oxidation of some product of reduction at B. If the scan is passed through C before switching, additional peaks F and G are observed. If peak B is suppressed (by performing the scan under CO atmosphere) and the voltammogram is allowed to cycle for a while, peak E is not seen, F and G become stronger, and peak A gradually diminishes. The voltammogram then starts to resemble that of $Sn[Fe_2(CO)_8]_2$, with an additional peak D at E_p = 0.23 V. Also, the solution which is initially green turns yellow, the colour of $Sn[Fe_2(CO)_8]_2$. $SnFe_5(CO)_{19}$ is therefore losing the bridging iron group. Peak D, which initially represented oxidation of the parent $SnFe_5(CO)_{19}$ cluster, must now be due to oxidation of this fragment. This is shown in the proposed reaction scheme in figure 5.27.

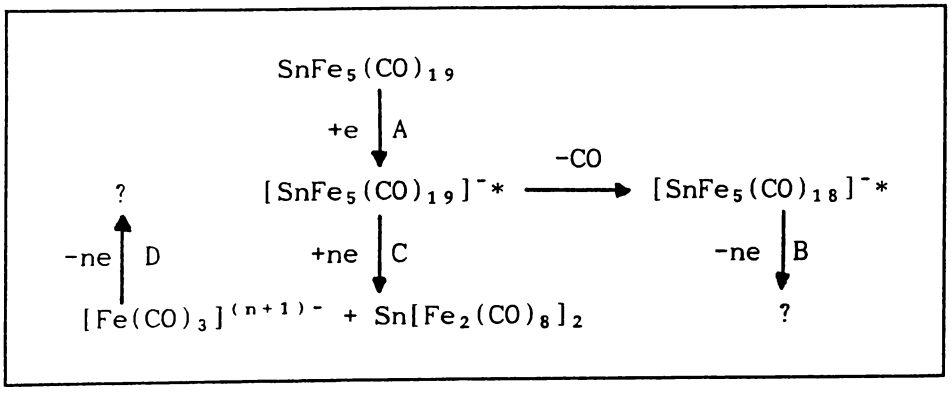

Figure 5.27: Proposed reduction mechanism for $SnFe_5(CO)_{19}$

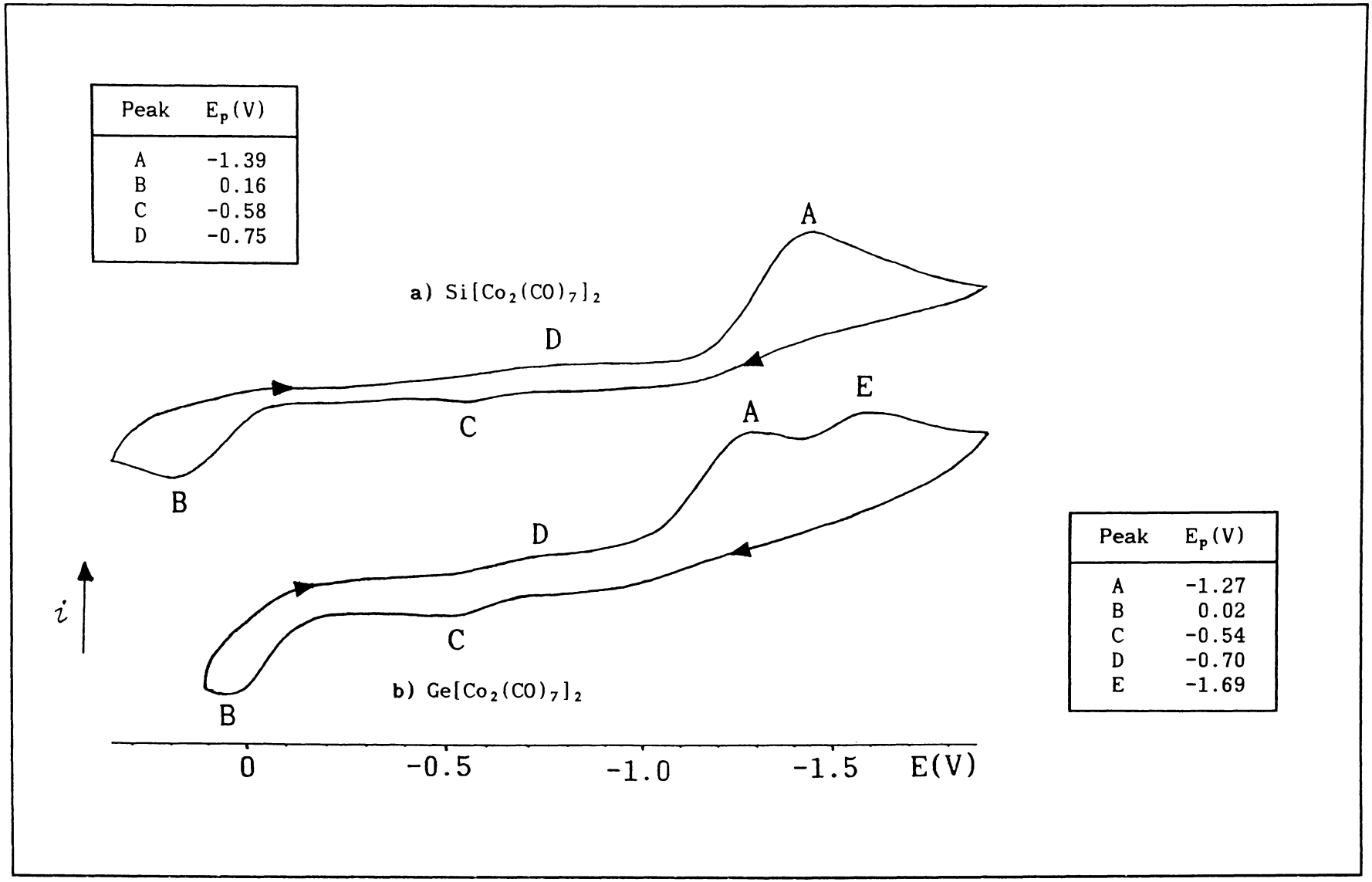

Figure 5.28: Cyclic voltammograms for a) $Si[Co_2(CO)_7]_2$ and b) $Ge[Co_2(CO)_7]_2$

5.2.3.5 $Si[Co_2(CO)_7]_2$ and $Ge[Co_2(CO)_7]_2$ *(F 1)*

These clusters also have a spiro structure, with the significant difference that each metal-metal bond is bridged by a CO group. Some fouling of the electrode occurred with $Ge[Co_2(CO)_7]_2$ so the results for this compound should be treated with caution.

Typical voltammograms for these clusters are shown in **figure 5.28**. The principle reduction wave, A, for these clusters is consistent with a one-electron irreversible transfer. Voltammograms of $Ge[Co_2(CO)_7]_2$ contain an additional reduction wave, E (E_p = -1.69 V). It is not possible to determine the number of electrons involved in this process.

If the scan is reversed at a switching potential which is more negative than peak A, a weak quasi-reversible couple, C/D, is seen on the anodic scan. From this it seems that reduction at A produces an unstable species, which can be reversibly oxidised at C to give another unstable species. The principal oxidation wave for these clusters is B. The i_p for this wave corresponds to only ~0.5 electrons. This could be due to some sort of disproportionation reaction.

A reaction scheme for $Si[Co_2(CO)_7]_2$ and $Ge[Co_2(CO)_7]_2$ is presented in figure 5.29 below:

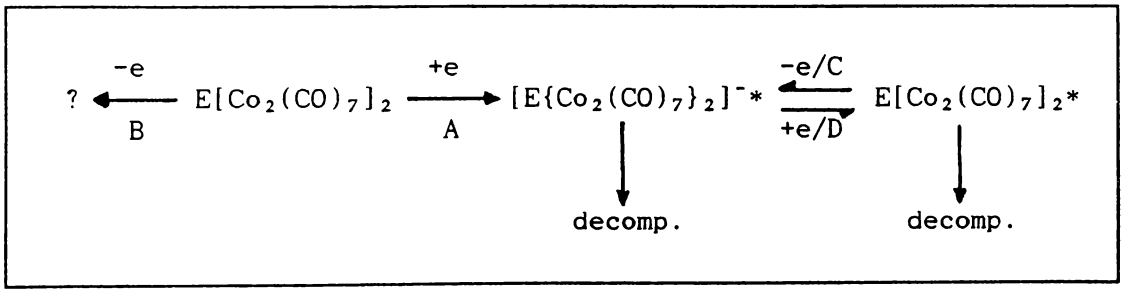

Figure 5.29: Reaction mechanism for $E[Co_2(CO)_7]_2$ (E = Si,Ge).

5.2.3.6 Discussion

The reaction scheme proposed for the reduction and oxidation of the *spiro*-$E[Fe_2(CO)_8]_2$ clusters above is shown in **figure 5.25**. The potentials for processes A to E are given in **table 5.4**. Also included are the peak potentials reported by Whitmire *et al.* from cyclic voltammograms of $Pb[Fe_2(CO)_8]_2$ and $[(CO)_8Fe_2]E[Fe(CO)_4]_2^{2-}$, obtained using a CH_2Cl_2/TBAP/glassy carbon WE electrochemical cell. The E_p reported by Whitmire for the oxidation of $[(CO)_8Fe_2]E[Fe(CO)_4]_2^{2-}$

matches well with the potential of peak E, and the principal reduction wave for $Pb[Fe_2(CO)_8]_2$ conforms with the sequence observed for peak A. Therefore it was assumed that these two sets of results are comparable. Looking down table 5.4 it can be seen that it is easier to reduce the spiro clusters when E is larger, while the oxidation peak remains relatively constant. This suggests that the HOMO has predominantly Fe character while the LUMO has E character. The visible spectra for Si, Ge and Sn clusters (figure 5.30) all show three bands. The highest of these, λ_{max} shifts from 373 to 406 to 489 nm for the Si, Ge and Sn clusters respectively. This is consistent with the Fe_2EFe_2 clusters becoming easier to reduce. Note however that the shift in λ_{max} is very large compared with that for the $(CO)_xMECo_3(CO)_9$ clusters, suggesting that other factors may be involved.

The relative importance of the various reduction pathways in figure 5.25 depends on the relative stabilities of the various species involved. $[E\{Fe_2(CO)_8\}_2]^{2-}$* is always unstable but appears to have a significant life for Si at 210 K. $[E\{Fe_2(CO)_8\}_2]^{2-}$* reacts to give intermediates I and II, which are detected by oxidation C and reduction B respectively. It can be seen from table 5.5 that the stability of II decreases from Si to Sn, and intermediate I becomes more important. It is interesting that C was not reported for the Pb analogue, but then the *spiro* structure is more strained for the lead analogue and the stability gained by opening one end of the cluster may be so great that intermediate I reacts almost as soon as it is formed. Peak D was also not reported for $Pb[Fe_2(CO)_8]_2$. A reason for this is less obvious.

It is possible to speculate that the immediate product of reduction, $[E\{Fe_2(CO)_8\}_2]^{2-}$* has one electron at either end of the cluster, while species I, which is intermediate between $[E\{Fe_2(CO)_8\}_2]^{2-}$* and the open ended $[(CO)_8Fe_2]E[Fe(CO)_4]_2^{2-}$, has both electrons at one end with the bond not yet broken. This is shown in figure 5.25. For the Si and Ge clusters, the small size of the central atom might hinder cleavage of this bond. This effect is observed for the $ECo_4(CO)_x$ system, where the Si and Ge clusters prefer the more closed *spiro* or trigonal pyramid structures as opposed to the more open $E[Co(CO)_4]_4$ structure prefered by Sn and Pb.

Infrared spectra for intermediate II were obtained for the silicon and germanium species. These spectra appeared to show a similar

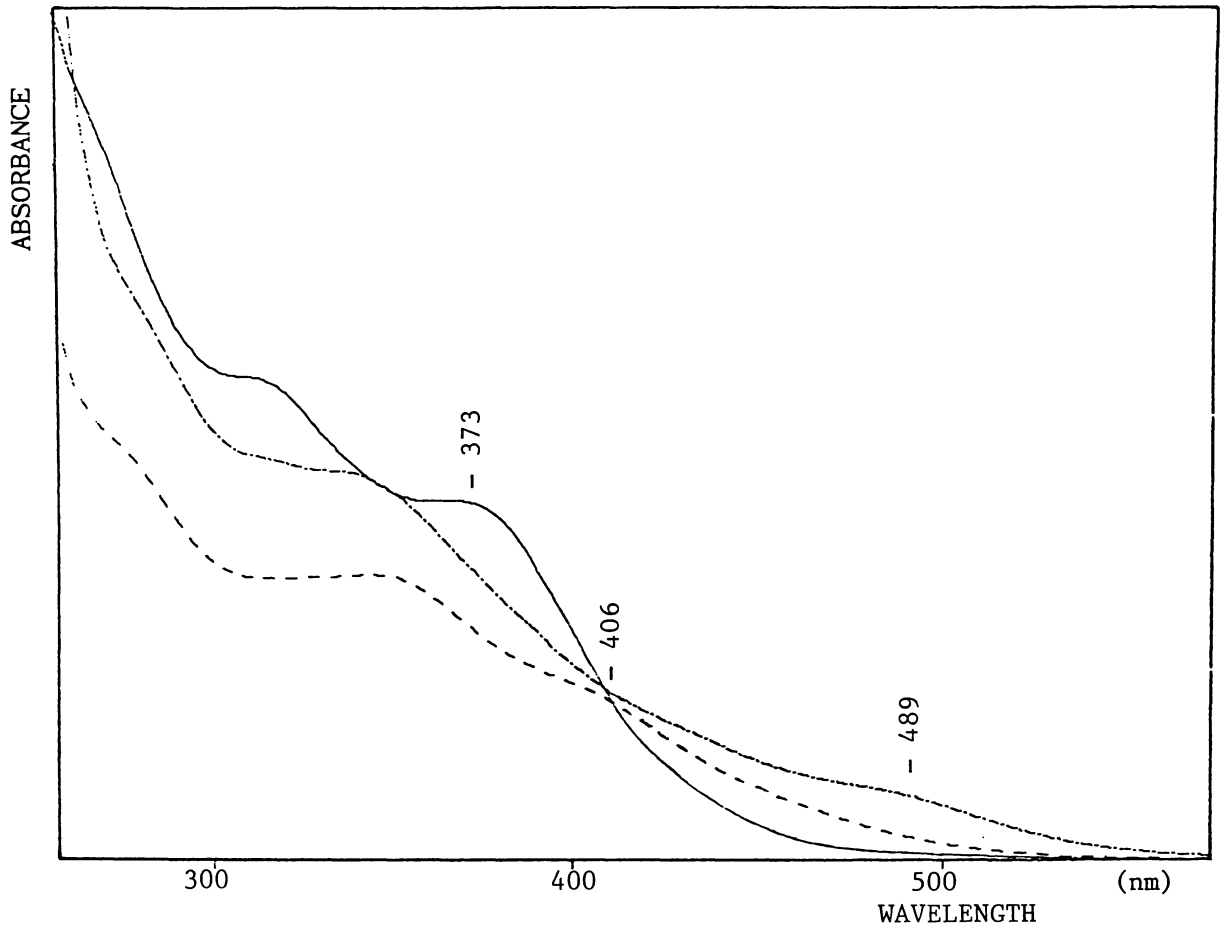

Figure 5.30: Visible spectra of $Si[Fe_2(CO)_8]_2$ (———), $Ge[Fe_2(CO)_8]_2$ (-·—·—·) and $Sn[Fe_2(CO)_8]_2$ (- - - - -)

pattern of peaks to their parent compounds, with an overall red-shift of ~56 cm^{-1}. This suggests that intermediate II has retained essentially the same structure. That is, the formation of the trigonal pyramid structure must be associated with the ensuing CO elimination reaction. It is possible that intermediate II has bridging carbonyl groups, and that these were concealed behind peaks of other species present in the infrared spectra.

When intermediate II is reduced at B, $[HFe_3(CO)_{11}]^-$ is eventually produced. There is no evidence of this compound in the voltammograms of the spiro clusters. Peaks corresponding to the products of reduction B were detected in the voltammograms of $Si[Fe_2(CO)_8]_2$, but the species responsible could not be identified. The $[HFe_3(CO)_{11}]^-$ is most likely formed by the reaction of one of these products with adventitious water present in the solvent.

As mentioned earlier, $SnFe_5(CO)_{19}$ can either be regarded as $Sn[Fe_2(CO)_8]_2$ with one end of the cluster bridged by CO and $Fe(CO)_4$ groups, or as $Fe_3(CO)_{12}$ with a bridging $SnFe_2(CO)_8$ group. In practice, $SnFe_5(CO)_{19}$ is more difficult to reduce than either $Sn[Fe_2(CO)_8]_2$ or $Fe_3(CO)_{12}$. The voltammograms indicated that two reduction pathways were in operation. In the first of these a radical monoanion, $[SnFe_5(CO)_{19}]^-$ was produced at A (E_p = -0.86 V) which underwent decarbonylation. This gave a species, probably $[SnFe_5(CO)_{18}]^-$, which was then irreversibly reduced at B (E_p = -1.04 V). The alternative pathway involves further reduction of the $[SnFe_5(CO)_{19}]^-$ anion at C (E_p = -1.15 V) at which stage the bridging iron group is lost giving $Sn[Fe_2(CO)_8]_2$. It is not clear what is happening in the first of these pathways, but in the second $SnFe_5(CO)_{19}$ definitely behaves more like a spiro cluster with a bridging iron carbonyl group.

The cyclic voltammograms of $Si[Co_2(CO)_7]_2$ and $Ge[Co_2(CO)_7]_2$ seem less promising as all the detected products of reduction appear unstable. The peak potentials for these clusters are included in table 5.6. If we look at the principal reduction (A) and oxidation (B) waves, it can be seen that both peaks shift to more positive potentials when silicon is replaced by germanium; the oxidation peak more so than the reduction peak. This suggests that the orbitals involved are different to those of the $E[Fe_2(CO)_8]_2$ clusters. This may also explain other differences in behaviour between the iron and cobalt clusters. That is, the fact that the principle reduction wave is only a

one-electron process and the principle oxidation wave involves *ca.* 0.5 electrons.

Typical Voltammogram:

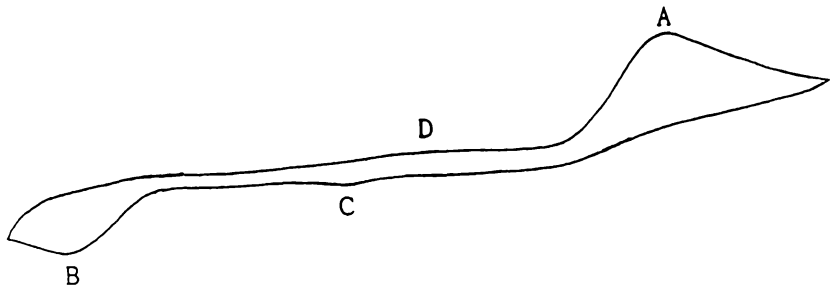

PEAKS:	B E_p(V)	C E_p(V)	D E_p(V)	A E_p(V)
$Si[Co_2(CO)_7]_2$	0.16	-0.58	-0.75	-1.39
$Ge[Co_2(CO)_7]_2$	0.02	-0.54	-0.70	-1.27

Table 5.6: Electrochemical data for $E[Co_2(CO)_7]_2$ clusters

As a route for synthesising $[(CO)_4FeGeFe_3(CO)_{10}]^-$ and $[(CO)_8Fe_2]Sn[Fe(CO)_4]_2^{2-}$, reduction of $E[Fe_2(CO)_8]_2$ using cobaltocene is probably not much more efficient than alternative routes. In their paper, Whitmire *et al.* [31] reported yields of 24% and 59% (based on Fe) respectively for the reactions of germanium(II) iodide and tin(II) acetate with $[Et_4N]_2[Fe_2(CO)_8]$. $Ge[Fe_2(CO)_8]_2$ and $Sn[Fe_2(CO)_8]_2$ have been produced in yields of 43% and 64% (chapter 2). But even assuming the cobaltocene reduction is 100% efficient, this route is more circuitous and time consuming. However because the analogous silicon(II) species do not exist, the "Whitmire" reaction could not be established using silicon. A new cluster, $[(CO)_4FeSiFe_3(CO)_{10}]^{2-}$ (the silicon analogue of $[(CO)_4FeGeFe_3(CO)_{10}]^{2-}$) was able to be produced by the reduction of $Si[Fe_2(CO)_8]_2$ using cobaltocene, and characterised by infrared spectroscopy. $[(CO)_4FeSiFe_3(CO)_{10}]^{2-}$ along with the germanium and tin dianions may in the future provide useful building blocks for further cluster synthesis.

5.2.4 ELECTROCHEMISTRY OF $[SiCo_9(CO)_{21}]^{2-}$ AND $[CCo_8(CO)_{18}]^{2-}$

The cyclic voltammetric behaviour of $[Et_4N]_3[SiCo_9(CO)_{21}][Co(CO)_4]$ has been briefly investigated in previous work [33]. This investigation has been repeated using the electrochemical cell and calibration methods described in section 5.2.1, to bring these results into line with the rest of the work presented in this chapter.

$[Et_4N]_2[CCo_8(CO)_{18}]$, isolated in section 3.2.1.2, was also investigated. Like $[SiCo_9(CO)_{21}]^{2-}$, this cluster contains a group 14 encapsulated within a square antiprism of eight Co atoms *(F 11)*. $[SiCo_9(CO)_{21}]^{2-}$, however, has an additional Co capping one square face of the antiprism *(F 12)*. It was hoped that a useful comparison could be made between these two clusters. Only later was it discovered that the electrochemistry of $[CCo_8(CO)_{18}]^{2-}$ had already been thoroughly investigated [271].

5.2.4.1 $[Et_4N]_3[SiCo_9(CO)_{21}][Co(CO)_4]$ *(F 12)*

The cyclic voltammogram in **figure 5.31a** shows two reduction processes for the $[SiCo_9(CO)_{21}]^{2-}$ cluster. The first of these, A/D ($E_{1/2}$ = -0.47 V), is an electrochemically reversible one electron process, with i_p^a/i_p^c = 1 at all scan rates from 50 to 1000 mV s^{-1}. This is followed by a two electron quasi-reversible reduction wave at B ($E_{1/2}$ = -1.62 V, i_p^a/i_p^a = 0.7 at 200 mV s^{-1}). The reversibility of this process increases with scan rate.

On the anodic scan, oxidation of the $[Co(CO)_4]^-$ anion contained in the mixed salt, occurs at E (E_p = 0.08 V). This is followed by irreversible oxidation of the $[SiCo_9(CO)_{21}]^{2-}$ cluster at F (E_p = 0.65 V). Peak F appears to represent a two-electron process, however this oxidation overlaps with the edge of the solvent oxidation wave, so it is not possible to accurately determine the peak position or the number of electrons involved.

5.2.4.2 $[Et_4N]_2[CCo_8(CO)_{18}]$ *(F 11)*

Voltammograms of $[Et_4N]_2[CCo_8(CO)_{18}]$ (**figure 5.31b**) show two reduction and two oxidation processes. Reduction peaks A ($E_{1/2}$ = -0.82 V) and B ($E_{1/2}$ = -1.39 V) both involve the electrochemically reversible transfer of one electron (i_p^a/i_p^c = 1 for all scan rates from 50 to 1000 mV s^{-1}, and E_p^c appears independent of scan rate). The E/G oxidation couple ($E_{1/2}$ = -0.01 V) is also a one-electron process, but it is only quasi-reversible becoming less reversible at slower scan

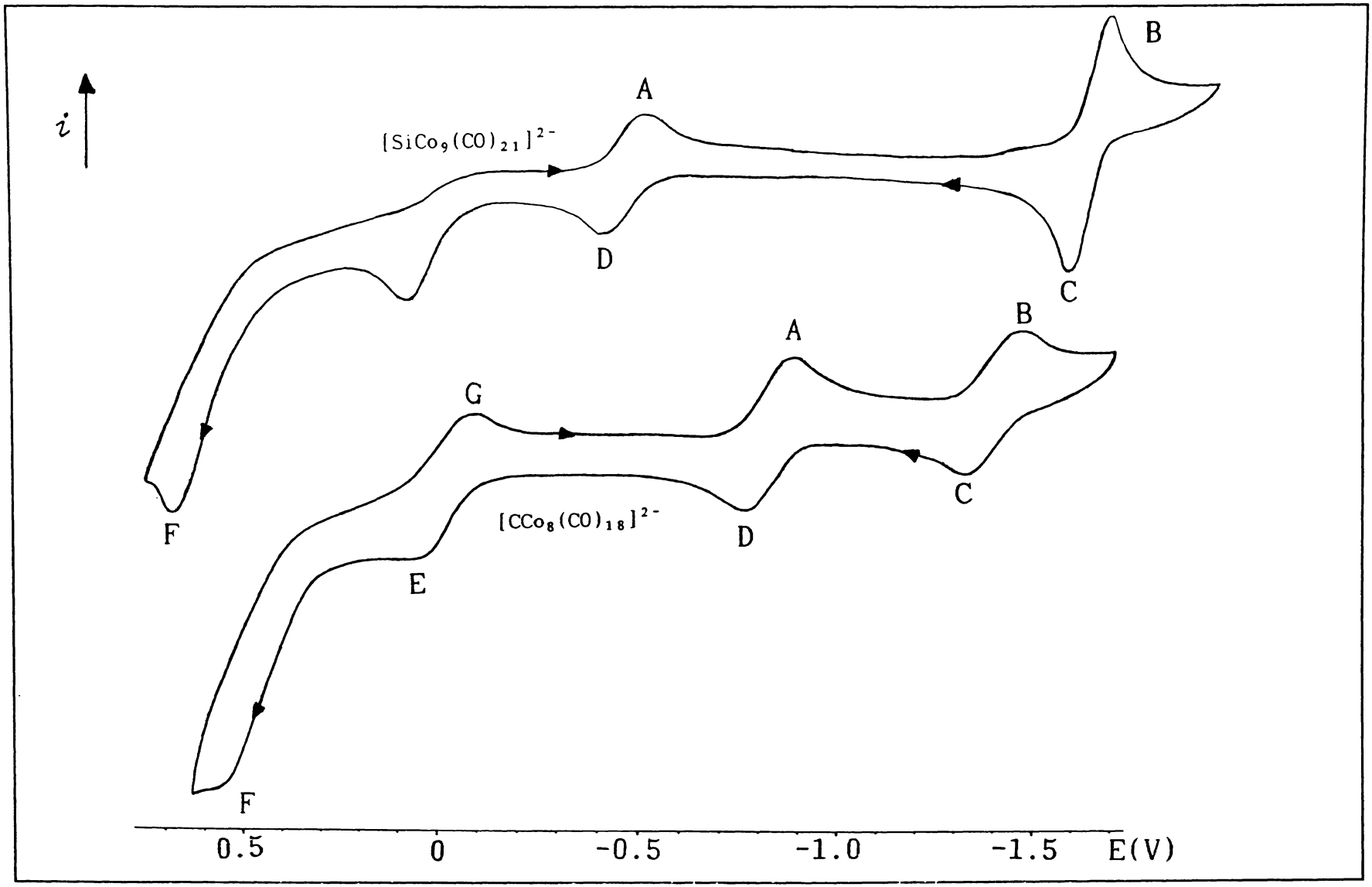

Figure 5.31: Cyclic voltammograms for $[SiCo_9(CO)_{21}]^{2-}$ and $[CCo_8(CO)_{18}]^{2-}$

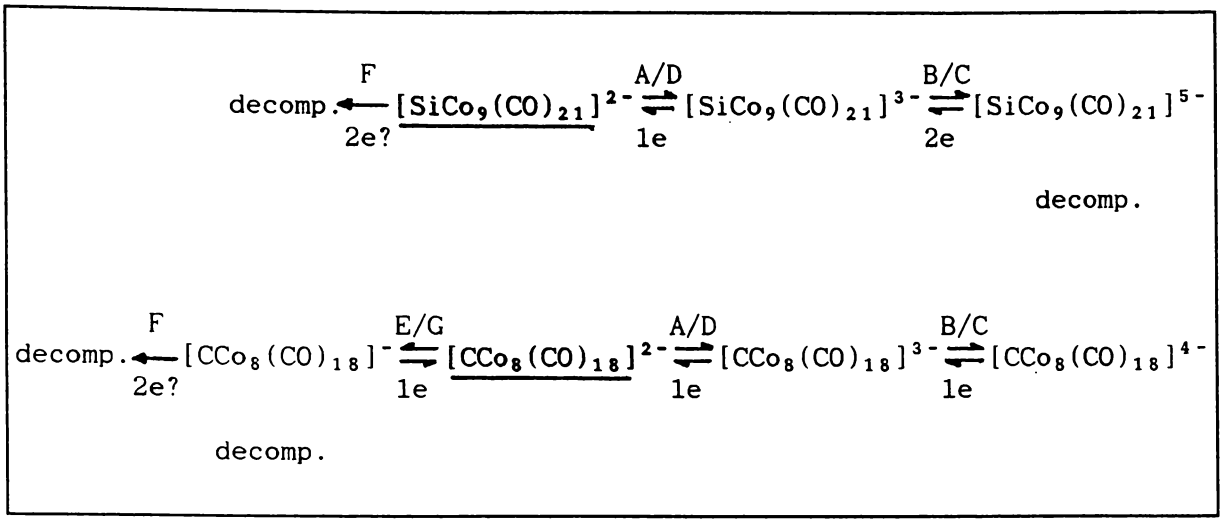

Figure 5.32: Proposed reaction schemes for the reduction and oxidation of the $[SiCo_9(CO)_{21}]^{2-}$ and $[CCo_8(CO)_{18}]^{2-}$

rates (i_p^c/i_p^a = 0.9 at 1000 mV s^{-1}, and 0.5 at 50 mV s^{-1}). Peak F (E_p = 0.54 V) appears to represent a two-electron process, but again, overlap with oxidation of the solvent prevents accurate measurement.

These results compare favourably with those reported by Rimmelin *et al.* [271] (see table 5.7). The cyclic voltammetric studies of Rimmelin *et al.* were made using a Pt WE and a saturated calomel RE, with 1,2-$C_2H_4Cl_2$ as the solvent and TBAP as the electrolyte.

		Current Results	Results from ref [271]
F	E_p(V) i_p^a/i_p^c n	0.54 irrev. ~2	$E_{1/2} \simeq$ 0.50 irrev. ~2
E/G	$E_{1/2}$(V) i_p^a/i_p^c n	-0.01 0.7 1	-0.01 0.71 1
A/D	$E_{1/2}$(V) i_p^a/i_p^c n	-0.82 1 1	-0.81 1.00 1
B/C	$E_{1/2}$(V) i_p^a/i_p^c n	-1.39 1 1	-1.35 1.00 1

Table 5.7: Electrochemical Data for $[CCo_8(CO)_{18}]^{2-}$

5.2.4.3 Discussion

The proposed reaction schemes for the reduction and oxidation of the $[SiCo_9(CO)_{21}]^{2-}$ and $[CCo_8(CO)_{18}]^{2-}$ clusters are shown in figure 5.32.

Electron counting indicates that $[SiCo_9(CO)_{21}]^{2-}$ is electron deficient. It contains 129 of the 130 valence electrons expected for a capped square antiprism. The paramagnetism of this cluster has previously been confirmed by the detection of an ESR signal (g = 2.039, no hyperfine structure, in CH_2Cl_2 at 77 K **[65,132]**). It is not surprising, therefore, that $[SiCo_9(CO)_{21}]^{2-}$ undergoes a facile one-electron reduction at A to form a stable, electron-precise trianion. Further reduction at B, or oxidation at F leads to disruption of the capped square antiprism. Both B and F appear to involve two electrons, which is consistent with the formation or cleavage of bonds.

In comparison with the compounds previously investigated, $[SiCo_9(CO)_{21}]^{2-}$ and $[CCo_8(CO)_{18}]^{2-}$ have a larger number of M-M bonding interactions. Hence the species produced under oxidation and reduction tend to be more stable, especially in the case of $[CCo_8(CO)_{18}]^{2-}$ which is able to form stable bi-, tri-, and tetraanions. The fact that fewer stable oxidation states are exhibited by $[SiCo_9(CO)_{21}]^{2-}$ may reflect the strain associated with the relatively large encapsulated Si atom. The average Co-Co distance in the $[SiCo_9(CO)_{21}]^{2-}$ square antiprism (2.76 Å) is much larger than in $[CCo_8(CO)_{18}]^{2-}$ (2.52 Å). If too many electrons are added or removed, the $[SiCo_9(CO)_{21}]^{2-}$ capped square antiprism starts to fall apart.

Chemical reduction of the $[SiCo_9(CO)_{21}]^{2-}$ cluster by stirring $[Et_4N]_3[SiCo_9(CO)_{21}][Co(CO)_4]$ with Zn powder in MeCN, has been described in the previous investigation **[33]**. This produced a compound which showed a similar pattern of ν_{CO} peaks to $[SiCo_9(CO)_{21}]^{2-}$, with an overall shift of ~28 cm^{-1} to lower frequencies. This species was assumed to be the corresponding trianion, $[SiCo_9(CO)_{21}]^{3-}$. Reduction using cobaltocene was attempted, but this reaction proved more complex, and is described elsewhere (section 4.2.1.4).

Chapter Six

Structures of compounds frequently refered to in this thesis are depicted in a fold-out section in Appendix A. The symbol *(F #)* is used in the text to refer readers to these diagrams.

CHAPTER 6 SPECTROSCOPIC STUDIES

6.1 INTRODUCTION

Infrared and Raman spectroscopy provide useful tools for investigating transition metal carbonyl clusters, particularly the more simple compounds. For more complex clusters, it is sometimes possible to assign portions of the spectra by the comparison of peak positions and intensities with those of related but more simple compounds (the spectroscopy of simple cluster subunits which are frequently encountered, are discussed in sections 6.1.1 to 6.1.3 below). In this approach, analysis is often complicated by mixing between bands. For very large clusters, vibrational spectroscopy often provides little more than a means of "fingerprinting" compounds. The heavy atom region is generally inaccessible, and carbonyl spectra of these clusters tend to be deceptively simple, exhibiting a relatively small number of broad bands.

The ν(CO) region (2200-1500 cm^{-1}) is perhaps the most useful region. Generally there is little mixing with other vibrational modes and the ν_{CO} infrared peaks tend to be very intense and well defined (see section 2.2.1). δ(M-C-O) and ν(M-C) modes occur as medium to weak bands in the 1000-300 cm^{-1} region. Vibrations of other ligands can also occur in this region, and mixing between the δ(M-C-O), ν(M-C) and ligand modes makes analysis very difficult. Although sometimes useful qualitatively, this region is largely ignored. The E-M and M-M stretching region (50-300 cm^{-1}) is less convenient for infrared spectroscopy. Experimentally this region is difficult to observe and the bands tend to be very weak. On the other hand, the high polarisability of M-M bonds gives rise to intense bands in the Raman spectrum. To date, however, the use of Raman spectroscopy in the investigation of group 14-transition metal carbonyl compounds has been very limited. Few compounds containing more than one or two transition metal atoms have been studied.

Three series of *spiro*-$E[Fe_2(CO)_8]_2$ (E = Si, Ge, Sn, Pb), *spiro*-$E[Co_2(CO)_7]_2$ (E = Si, Ge) and trigonal pyramid-based $(CO)_4CoECo_3(CO)_9$ (E = Si, Ge) clusters are now available in preparative yields and the opportunity has been taken to record and analyse the infrared and Raman spectra these compounds. The structures of all of these clusters have been determined crystallographically, yet in many cases only solution

spectra in the carbonyl infrared region are available.

Between them, these three classes of compound contain three common subunits which form the basis of many group 14-transition metal clusters: (i) $EM(CO)_4$, where E is bonded to a terminal metal atom; (ii) $EM_2(CO)_x$, where E bridges a M-M bond; and (iii) where E caps a M_3 triangle. The vibrational spectroscopy of these subunits is discussed below.

6.1.1 COMPOUNDS CONTAINING E-M(CO)$_4$ UNITS

Carbonyl Stretching Region

For simple $Y_3ECo(CO)_4$ compounds possessing C_{3v} symmetry, three carbonyl stretching modes are predicted ($2a_1(IR,R) + e(IR,R)$). Both Raman and infrared spectra for $H_3GeCo(CO)_4$ [272] and $Cl_3ECo(CO)_4$ (E = Si, Ge, Sn) [273] have been reported and assignments made (the assigned ν_{CO} spectrum of $H_3Ge(CO)_4$ is presented in **Table 6.1**). In $Y_3ECo(CO)_4$ compounds, one of the carbonyls is in an axial position, *trans* to E, and the other carbonyls are approximately co-planar with the Co atom. Structural studies show that the degree of planarity is dependent upon the size of the Y_3Ge group (E-Co-Co_{eq} angles of 81.73°, 85° and 83.8° have been reported for $H_3SiCo(CO)_4$ [274], $Cl_3SiCo(CO)_4$ [274] and $H_3GeCo(CO)_4$ [275] respectively). Force constant calculations indicate that $k(CO_{ax})$ is greater than $k(CO_{eq})$ [273,276]. This difference is most significant when E is a strong electron donor (the "π-bonding effect" [277]). This suggests that the higher energy a_1 mode ($a_1^{(1)}$) is primarily a CO_{ax} stretch, and the lower energy $a_1^{(2)}$ mode, a CO_{eq} stretch:

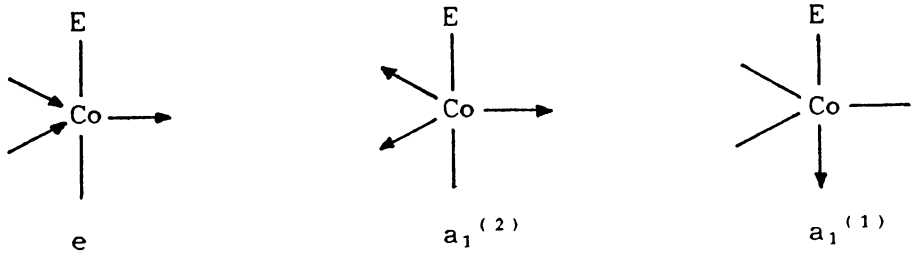

By considering the vector sum of the local dipoles for each these vibrations, the $a_1^{(1)}$ modes should give a relatively strong infrared

band, while $a_1^{(2)}$ should have low, pehaps vanishing intensity (depending on the planarity of the $Co(CO_{eq})_3$ moiety). In practice $a_1^{(1)}$ and $a_1^{(2)}$ are of almost equal intensity. This suggests strong coupling [278,273], and the two a_1 modes are probably best represented as [278]:

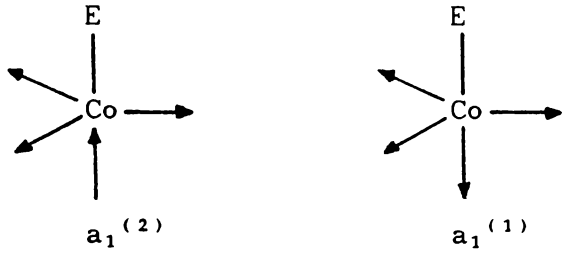

$a_1^{(1)}$ involves the simultaneous stretching of all four carbonyls, and would therefore occur at higher energy.

$H_3GeCo(CO)_4$ [272]			$MeH_2GeCo(CO)_4$ [279]	
IR(gas)	R(liq)	Assmt.	IR(gas)	Assmt.
2109 s	2110 vs(p)	a_1	2106 m	a'
2046 s	2040 sh	a_1	2046 ms	a'
2025 vvs	2010 s	e	2017 vs	a' + a"
			2012 s	
1925 w				
1982 m		^{13}C		

Table 6.1: Carbonyl region infrared spectra of some $Y_3ECo(CO)_4$ compounds

In asymmetrically substituted $Y_2Y'ECo(CO)_4$ compounds, the overall symmetry is reduced to C_s, and a splitting of the degenerate C_{3v} e band into a' + a" modes is often observed (*eg.* $MeH_2GeCo(CO)_4$ [279] Table 6.1). When E is bonded to more than one terminal $Co(CO)_4$ group, the carbonyl vibrational spectra have been interpreted by invoking coupling across the E atom [43,53,278].

Replacing E in $Y_3ECo(CO)_4$ with a heavier group 14 atom causes displacement of the ν_{CO} bands to lower frequency (by 1-2 cm^{-1}). A similar, but generally more significant, downward shift is observed when the Y substituents are replaced by less electronegative groups. Both of these substitutions allow increased electron density in the carbon π^*-orbitals, with a concomitant weakening of C-O bonding [52].

Compound	ν(E-M) (cm^{-1})	k(E-M) (N m^{-1})
$Cl_3SiCo(CO)_4$	307(soln)[a]	145[c]
$F_3GeCo(CO)_4$	222(solid)[b]	173[c]
$Cl_3GeCo(CO)_4$	241(soln)[a]	152[c]
$Br_3GeCo(CO)_4$	199(soln)[a]	130[c]
$I_3GeCo(CO)_4$	162(solid)[a]	85[c]
$H_3GeCo(CO)_4$	222(liq)[b]	130[c]
$Cl_3SnCo(CO)_4$	206(soln)[a]	130[c]
$Br_3SnCo(CO)_4$	185(soln)[a]	120[c]
$I_3SnCo(CO)_4$	158(soln)[a]	85[c]
$[Cl_3GeFe(CO)_4]^-$	249(soln)[d]	129[d]
$[Cl_3SnFe(CO)_4]^-$	207(soln)[d]	136[d]
$[Br_3SnFe(CO)_4]^-$	185(soln)[d]	108[d]

[a] ref. [280] [b] ref. [281] [c] ref. [282] [d] ref. [283]

Table 6.2: Raman ν(E-M) frequencies and force constants for simple complexes

E-M Stretching Region

Raman-active E-M vibrations have been reported for a number of $X_3ECo(CO)_4$ and $[X_3EFe(CO)_4]^-$ compounds (table 6.2). As expected, an increase in the size of E results in a downward shift in the ν(E-M) bands. Also, as X becomes more electronegative, the k(E-M) force constants increase, and this is generally accompanied by an increase in the E-M vibrational frequencies. This trend in k(E-M) values can be explained by both σ-bonding and π-back-bonding effects, and there is active debate over the relative importance of these two effects [284].

6.1.2 COMPOUNDS CONTAINING E-BRIDGED $M_2(CO)_x$ UNITS

Carbonyl Stretching Region

A generalised infrared spectrum of $(\mu_2\text{-}Y)_2M_2(CO)_6$ compounds of idealised C_{2v} symmetry has been presented by Bor [285] (figure 6.1), and in table 6.3, the infrared spectrum of $(Me_2Ge)_2Co_2(CO)_6$ has been

assigned according to the Bor model. The spectrum of $Me_2GeCo_2(CO)_6(\mu$-CO) (C_s symmetry) also shows well resolved bands consistent with the Bor model (table 6.3).

There are two carbonyl environments in $(\mu\text{-}Y)_2M_2(CO)_6$. Two CO

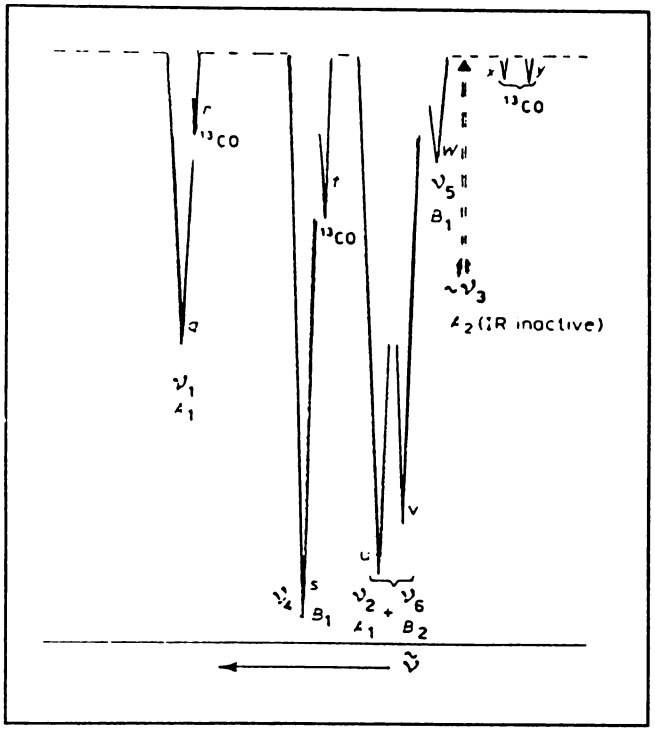

Figure 6.1: Generalised infrared spectrum of $(\mu\text{-}Y)_2M_2(CO)_6$ proposed by Bor [285]

Bor symbol	$(Me_2Ge)_2Co_2(CO)_6$ (in cyclohexane) [286]	$(Me_2Ge)Co_2(CO)_6(\mu$-CO) (in hexane) [43]
q (a_1)	2072 s	2088 s
s (b_1)	2035 vs	2048 vs
u (a_1)	2014 vs	2026 vs
v (b_2)	1994 vs	2008 vs
w (b_1)	1984 m	1998 sh,w
	1964 vw[a]	1965 sh,vw[a]
		1840 s[b]

[a] Probably ^{13}C satellite peak [b] Bridging carbonyl peak

Table 6.3: Carbonyl stretching region infrared data for dimethylgermyl substituted dicobalt carbonyl

groups can be classed as axial (approximately *trans* to the M-M bond) and four as equatorial. By comparison with $Y_3ECo(CO)_4$, the highest energy a_1 mode probably represents simultaneous stretching of all carbonyls, while the second a_1 mode represents the out-of-phase combination of the CO_{ax} and CO_{eq} stretches.

The *spiro* compounds of the type, $E[Co_2(CO)_7]_2$ (E = Si [39], Ge [42]) and $S[Fe_2(CO)_6(\mu\text{-}SR)]_2$ (R = CH_3, C_2H_5, $C_6H_5CH_2$, p-$CH_3C_6H_4$, $C_6H_5C{\equiv}C$ [287]) contain two $(\mu\text{-}E)M_2(CO)_6(\mu\text{-}Y)$ units, sharing a common E atom. These molecules approximate C_2 symmetry, which predicts 12 infrared-active ν_{CO} modes. However the observed infrared spectra (table 6.4) are a lot simpler than this, and the similarity they show to the Bor model suggests that coupling across the Ge atom is negligible. The observed modes can also be compared with those expected for a molecule of idealised D_{2d} symmetry, where all E-M bondlengths are equal and each bridging group is coplanar with the EM_2 triangle ($2a_1(R) + a_2(i.a.) + b_1(R) + 2b_2(IR,R) + 2e(IR,R)$).

$Ge[Co_2(CO)_7]_2$ (hexane) [42]	$S[Fe_2(CO)_6(SMe)]_2$ (KBr disc) [287]	$Ge[Fe_2(CO)_8]_2$ (hexane) [40]	$(CO)_8Fe_2AsFe_2(CO)_6Cl$ [288]
2079 s	2070 s	2078 m	2113 w
2061 vs	2050 vs	2050 vs	2068 s
2040 m	2020 vs	2030 w	2066 s
2032 m	1990 s	2015 s	2047 vs
2023 w	1980 s		2035 m
2005 w			2031 m
			2015 w
1848 m (μ-CO)			2005 m
			1996 w
			1981 m

Table 6.4: Carbonyl region infrared spectra of some *spiro* compounds

The infrared spectra of the related $E[Fe_2(CO)_8]_2$ (E = Si [38], Ge [40], Sn [48], Pb [31]) clusters are also remarkably simple (table 6.4). These compounds exhibit only four of the seven infrared active carbonyl stretching modes predicted for approximate D_{2d} symmetry ($3a_1(R) + a_2(i.a.) + b_1(R) + 3b_2(IR,R) + 4e(IR,R)$). An early interpretation attributed the observed bands to the vibrations of independent $Fe(CO)_4$ groups. However the intensity pattern is not similar to those of $R_2Fe(CO)_4$ compounds, and it seems unrealistic for

coupling, particularly between adjacent $Fe(CO)_4$ groups, to be negligible. Raman spectra of $E[Co_2(CO)_7]_2$ and $E[Fe_2(CO)_8]_2$ clusters should, in each case, reveal the degree of coupling across the E atom and assist in assigning bands.

The $(CO)_8Fe_2EFe_2(CO)_6Cl$ (E = P, As [288]) clusters are interesting in that they contain both a $(\mu\text{-E})M_2(CO)_6(\mu\text{-X})$ and a $(\mu\text{-E})M_2(CO)_8$ group, linked in a *spiro* fashion. The symmetry of these molecules is C_s or at best C_{2v}; nonequivalence of the two bis-metal groups invalidates any approximation to higher symmetry (*cf.* $E[Co_2(CO)_7]_2$). The low symmetry of these compounds accounts for the larger number of bands observed in the infrared spectra (**table 6.4**).

In all of these *spiro* clusters, the variation in ν_{CO} frequency as E increases in size, is very small indeed. A downward shift of only *ca.* 5 cm^{-1} is observed, going from $Si[Fe_2(CO)_8]_2$ to $Pb[Fe_2(CO)_8]_2$.

E-M and M-M Stretching Region

Of the compounds with M-M bonds so far investigated, those in which the M-M linkage is unbridged display Raman-active ν(M-M) modes at frequencies lower than 200 cm^{-1}, while M-M bonds supported by bridging ligands generally vibrate at frequencies higher than 200 cm^{-1} (**table 6.5**). This agrees with the idea that distortion of the M-Y-M bond angle (Y = bridging group) also contributes to the M-M restoring force in bridged compounds. In **table 6.5**, the ν(M-M) frequency increases by approximately 30 cm^{-1} for each bridging carbonyl.

Table 6.5 shows that, $Co_2(CO)_8$ adopts a doubly carbonyl-bridged

Compound	State	Bridge	ν(M-M) (cm^{-1})	Ref.
$[Et_4N][Fe_2(CO)_8]$	solid	-	161	[289]
$[Et_4N][HFe_2(CO)_8]$	solid	2(CO) + H	255	[284]
$Fe_2(CO)_9$	solid	3(CO)	260	[284]
$Co_2(CO)_6(P(OPh)_3)_2$	solid	-	172	[284]
$Co_2(CO)_8$	soln	-	157,185	[289]
$Co_2(CO)_8$	solid	2(CO)	229	[289]

Table 6.5: Raman-active M-M stretching modes for some bimetallic compounds

configuration in the solid phase, and displays a single Raman-active ν(M-M) mode. However in solution, three bands are observed in this region. Of these, a band at 236 cm^{-1} band has been attributed to the bridged form and the two features at 185 and 157 cm^{-1}, to different non-bridged forms.

Vibrational spectra within this region have not been reported for the *spiro*-$E[M_2(CO)_x]_2$ clusters, nor for other compounds containing EM_2 triangles.

6.1.3 COMPOUNDS CONTAINING E-CAPPED $M_3(CO)_9$ UNITS

Carbonyl Stretching Region

For $YEM_3(CO)_9$ compounds with C_{3v} symmetry, five ν_{CO} modes are predicted ($2a_1$(IR,R) + a_2(i.a.) + 3e(IR,R)). For clusters where E = C, Bor *et al.* have listed typical frequencies and relative intensities observed in the infrared spectrum (see **table 6.6**). Complete, infrared and Raman spectra have been reported for $MeCCo_3(CO)_9$ [290], and the assigned carbonyl spectra are shown in **table 6.6**, along with the infrared spectrum of the germanium analogue.

Typical $YCCo_3(CO)_9$ spectrum (Bor [291])		$MeCCo_3(CO)_9$ [290]			$MeGeCo_3(CO)_9$ [292]
IR	Int.	IR	R	Assmt.	IR
2111-2101	(0.2-1)	2103 s	2100 m	a_1	2108 m
2066-2054	(10)	2051.5 vs	2054 m	e	2055 vs
2047-2038	(4-5)	2039 vs	2029 m	a_1	2045 s
2034-2018	(0.3-0.5)	2017.5 s		e	2018 m
			2009 s	e	
			2000 s	a_2	
		1990 w	1996 m		1992 w
1987-1977	(^{13}CO)	1975.5 w		^{13}CO	

Table 6.6: Carbonyl vibrational spectra of $YECo_3(CO)_9$ compounds

In $(CO)_4CoECo_3(CO)_9$ (E = Si, Ge), the overall molecular symmetry is approximately C_{3v} and $4a_1$(IR,R) + 4e(IR,R) ν_{CO} modes are predicted. Only six of these bands have been observed in the infrared spectrum (**table 6.7**). When the spectrum of $(CO)_4CoGeCo_3(CO)_9$ is compared with those reported for $Y_3GeCo(CO)_4$ and $YGeCo_3(CO)_9$, it is obvious that there is significant mixing between the $Co(CO)_4$ and $Co_3(CO)_9$

environments, and this makes it difficult to assign bands. If Raman spectra could be obtained this would offer some assistance.

Table 6.7: Carbonyl infrared spectra of $(CO)_4CoSiCo_3(CO)_9$ and $(CO)_4CoGeCo_3(CO)_9$

$(CO)_4CoSiCo_3(CO)_9$ [179]	$(CO)_4CoGeCo_3(CO)_9$ [179]
2114 w	2112 w
2087 s	2083 s
2047 vs	2045 vs
2031 m	2029 m
2011 vw	2008 vw
1993 vw	

E-M, M-M Stretching Region

This region has not been investigated for the $(CO)_4CoECo_3(CO)_9$ compounds, but assigned spectra have been reported for several C_{3v}, $YCM_3(CO)_9$ clusters ($YCCo_3(CO)_9$, Y = H **[293]**, Me **[290]**, F, Cl, Br **[294]**; $[OCCCo_3(CO)_9]^+$ and $[OCCM_3(CO)_9]^{2-}$, M = Fe, Ru, Os **[295]**). These compounds typically display strong Raman (weak infrared) signals at 215 ± 20 cm^{-1} and 165 ± 25 cm^{-1}, representing symmetric (a_1) and antisymmetric (e) M-M stretching modes, respectively (**figure 6.2**). For $[OCCRu_3(\mu\text{-}H)(CO)_9]^-$ and $OCCRu_3(\mu\text{-}H)_2(CO)_9$ the presence of bridging hydrogen atoms leads to reduced symmetry. This is reflected by a slight splitting of the degenerate e vibration into its a' and a" components under C_s symmetry **[295]** (see **figure 6.2**).

Force constant calculations give a value of 109 N m^{-1} for the μ_3-carbyne bridged Co-Co bonds compared with values of 94 N m^{-1} for μ_2-CO bridged and 54 N m^{-1} for non-bridged Co-Co bonds **[294]**. Stretching of these Co-Co bonds also involves distortion of the bridging Co-C-Co and Co-Co-Co bond angles, and μC-Co bond stretching.

Symmetric (a_1) and antisymmetric (e) vibrations are also predicted for bonding between E and the three M atoms. For $HCCo_3(CO)_9$ the a_1 mode occurs ~300 cm^{-1} higher than the e mode, however in all other cases, this order is reversed. Assignments of these bands have been made on the basis of relative peak intensities (the a_1 mode should give rise to a significantly stronger Raman signal) supported by normal

coordinate analyses, and the reversal of the frequency order has been explained by coupling interactions with ν(C-Y) (a_1) and δ(Co-C-Y) (e) modes.

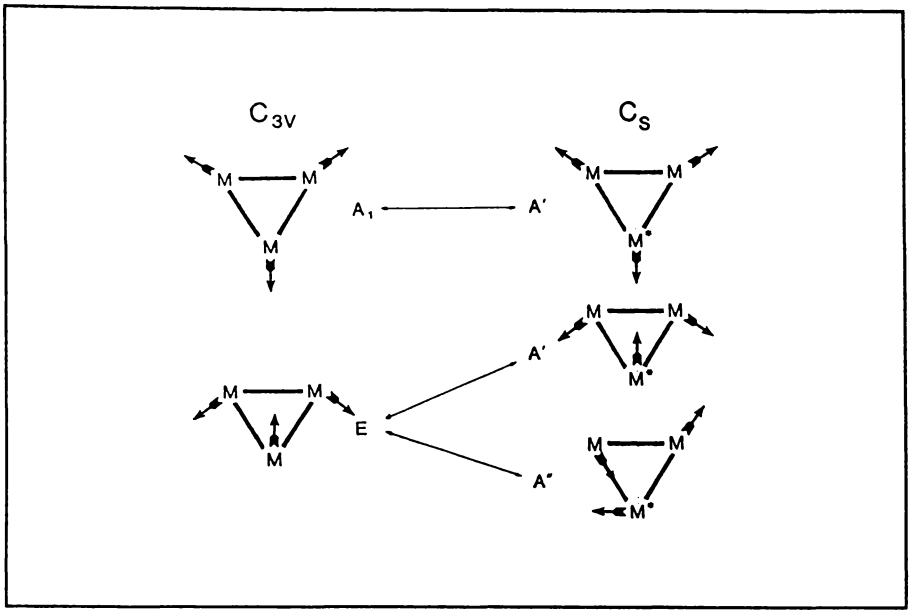

Figure 6.2: M-M stretching vibrations for C_{3v} or C_s clusters containing triply-capped M_3 triangles (from reference [295])

Table 6.8: E-Co and Co-Co stretching frequencies (cm^{-1}) for some $YCCo_3(CO)_9$ compounds

	$HCCo_3(CO)_9$ [293]		$MeCCo_3(CO)_9$ [290]		$FCCo_3(CO)_9$ [294]	
	IR	R	IR	R	IR	R
C-Co(a_1)	715 m	710 m	401 m	404 m	396 s	390 ms
C-Co(e)	417 w,sh		555 vs		637 s	638 w
Co-Co(a_1)	234 w	236 s	235 vw	234 vs	224 w	
Co-Co(e)	187 w	190 m	180 vw	178 ms	181 w	

6.2 EXPERIMENTAL

6.2.1 METHODS

Raman spectra were obtained using a SPEX 1403 0.85m Double Spectrometer linked to a SPEX DM1B computer. Samples were inserted as crystals or solutions, into a glass capilliary under a nitrogen

atmosphere, and sealed in using a flame. All of the spectra presented here were obtained using a helium/neon laser (632.8 nm wavelength). CH_2Cl_2 was employed as the solvent for all Raman solution spectra. Hexane was tried as a solvent but proved too volatile, forming bubbles when impinged by the laser beam. Solid-state KBr disc infrared spectra were obtained as described in section 2.2.1.

The Raman spectrometer has only recently been acquired by the University of Waikato, and optimum conditions for obtaining spectra of transition metal clusters are still being established. Although some improvement in the quality of the spectra may be obtained by varying the combination of laser, solvent and cell, the compounds investigated here appear to represent the limits to which the available equipment can be applied. Many of the compounds under investigation are intensely coloured, and form decomposition products which are also intensely coloured (*eg.* $Co_4(CO)_{12}$). Internal absorption by these samples results in weak Raman spectra, and the combination of intense colour and thermal sensitivity makes these compounds particularly susceptible to thermal decomposition under the laser beam. This proved more of a problem for the Co clusters, and for clusters containing larger group 14 atoms. Attempts were also made to obtain Raman spectra for the larger $[Ge_2Co_7(CO)_{21}]^-$ and $[Ge_2Co_5Fe_7(CO)_{22}]^-$ clusters, both of which form dark red crystals and "wine-red" solutions. As crystals, these compounds rapidly decomposed under the laser, and no signal was detected for either of these compounds in the solution phase.

The proximaty of the Ar laser 488 nm (blue) line to the electronic absorption bands observed for the *spiro* clusters in section 5.2.3.6, offered the possibility of resonance enhancement. However even the relatively stable $Si[Fe_2(CO)_8]_2$ cluster (in solution) rapidly decomposed under the higher energy radiation.

Raman spectra of crystalline samples can be affected by the orientation(s) of the particular crystal(s). In each case, several spectra were collected, but no significant variations were detected. Solid state Raman spectra were generally stronger than the corresponding solution spectra, except in cases where sample decomposition was a major problem (*eg.* $Pb[Fe_2(CO)_8]_2$); in solutions, diffusion of dissolved molecules in and out of the laser beam, reduces the extent of decomposition.

With solution state spectra it is also possible to measure the degree of polarisation for individual bands by inserting a polarising filter at an angle perpendicular to the polarisation of the reflected laser beam. Unfortunately the quality of the solution spectra obtained here, was not sufficient to allow the determination of accurate polarisation data. However in most cases, spectra obtained using the polariser do permit the strongly polarised bands to be identified.

Vibrational spectra obtained from solid samples tend to exhibit a larger number of bands than those obtained from solutions. In the Raman spectra presented here, this may to some extent be a function of the poorer quality of the solution spectra, but it can also represent a reduction in symmetry associated with crystal packing. In the crystal lattice, the site symmetry of molecules is in most cases less than that of the isolated molecule, intermolecular steric effects can distort the molecule, and mixing can occur between distinct molecules in the unit cell. These effects often lead to the splitting of degenerate modes, and the appearance of symmetry-forbidden and inactive modes.

6.2.2 VIBRATIONAL SPECTRA OF $E[Fe_2(CO)_8]_2$

$Si[Fe_2(CO)_8]_2$ and $Ge[Fe_2(CO)_8]_2$ form orange crystals and yellow solutions. For the heavier analogues these colours become more intense, so that $Pb[Fe_2(CO)_8]_2$ forms red-black crystals and dark red solutions.

Solid-state infrared sectra were recorded for the complete series of clusters. Solid- and solution-state Raman spectra were obtained for the Si, Ge and Sn clusters, but in the case of $Pb[Fe_2(CO)_8]_2$, crystalline samples decomposed under the He/Ne laser, and the solution spectra were so weak that only a single peak could be detected. The Raman spectra of these compounds are presented in **Appendix C, figures** C.1 to C.7. Peak positions and assignments are listed in **table 6.9** on a fold-out leaf at the end of this chapter.

6.2.3 VIBRATIONAL SPECTRA OF $E[Co_2(CO)_7]_2$

$Si[Co_2(CO)_7]_2$ and $Ge[Co_2(CO)_7]_2$ form orange-brown crystals and brown to dark brown solutions. Solid-state infrared spectra, and solid- and solution-state Raman spectra were recorded for both compounds. The difference in intensity between the solution-state spectra of $Si[Co_2(CO)_7]_2$ and $Ge[Co_2(CO)_7]_2$ appears to be a solubility

effect. The Raman spectra of these compounds are presented in Appendix C, figures C.8 to C.11. Peak positions and assignments are listed in table 6.10 on a fold-out leaf at the end of this chapter.

6.2.4 VIBRATIONAL SPECTRA OF $(CO)_4CoECo_3(CO)_9$

$(CO)_4CoSiCo_3(CO)_9$ and $(CO)_4CoGeCo_3(CO)_9$ form purple-black crystals and dark purple solutions. A solid-state infrared spectrum was recorded for $(CO)_4CoGeCo_3(CO)_9$. The Raman spectra are much weaker than for the previous compounds, presumably due to the intense colouration. For both $(CO)_4CoSiCo_3(CO)_9$ and $(CO)_4CoGeCo_3(CO)_9$, only a single Raman band was detected in the carbonyl stretching region. A solution-state spectrum was obtained for $(CO)_4CoGeCo_3(CO)_9$ in the heavy atom vibration region, and despite the very poor quality, this enabled the detection of polarisation in the strongest band at 199 cm^{-1}.

The Raman spectra of these compounds are presented in Appendix C, figures C.12 to C.14. Peak positions and assignments are listed in table 6.11 on a fold-out leaf at the end of this chapter.

6.3 DISCUSSION

6.3.1 VIBRATIONAL SPECTRA OF *SPIRO*-$E[M_2(CO)_X]_2$ COMPOUNDS

6.3.1.1 Carbonyl Stretching Region

$E[Fe_2(CO)_8]_2$

As described earlier, D_{2d} symmetry for $E[Fe_2(CO)_8]_2$ predicts $3a_1(R) + a_2(i.a.) + b_1(R) + 3b_2(IR,R) + 4e(IR,R)$ carbonyl stretching modes, seven of which are infrared-active and eleven Raman-active. The observed spectra show good agreement with this, in both the number of bands and the selection rules (table 6.9). These spectra are certainly more complex than that expected for descrete $Fe(CO)_4$ units, and there is clearly significant coupling between carbonyls on adjacent Fe atoms, and through the central E atom.

The fact that the number of bands observed in the solid state exceeds those observed for the solutions, and that symmetry forbidden bands appear in the solid state, indicates that asymmetry is being introduced by the effects of crystal packing. It is therefore useful when assigning bands to look first at the solution spectra, where the selection rules tend to be more closely adhered to.

The carbonyl region infrared and Raman spectra of the $E[Fe_2(CO)_8]_2$ clusters have been tentatively assigned in table 6.9. For

$Si[Fe_2(CO)_8]_2$ the intense Raman band at 2112 cm^{-1} is strongly polarised and is clearly an a_1 mode. Being the highest energy mode, this probably represents the simultaneous stretching of all carbonyl groups. This mode is seen very weakly in the solid state infrared spectra of $Si[Fe_2(CO)_8]_2$ and $Sn[Fe_2(CO)_8]_2$ probably due to reduced molecular symmetry in the crystal lattice. The 2036 and 2015 cm^{-1} vibrations also show strong Raman bands with no counterparts in the solution state infrared spectra, and hence these have been assigned as the two other a_1 modes. Polarisation was not detected for these compounds, but this is not surprising considering the quality of the spectra.

The e modes are likely to be strongly active in the infrared spectrum, and have been tentatively assigned to the 2076, 2050, 2030 and 2013 cm^{-1} bands, the four modes consistently seen in the solution phase infrared spectra. Turning to the solid state spectra, the remaining three infrared bands (at 2065, 1987 and 1968 cm^{-1}) have been tentatively designated as b_2 modes. The other vibrations (at 1996 and 1983 cm^{-1}) are active only in the Raman spectra. Of these, the 1996 cm^{-1} band is seen in both the solid and solution spectra and has been tentatively assigned to the b_1 mode or $\nu(^{13}C\text{-}O)$, while the 1983 cm^{-1} band is only observed in the solid state, and has been tentatively assigned to the a_2 mode (inactive under ideal D_{2d} symmetry).

The vibrational spectra of the four $E[Fe_2(CO)_8]_2$ clusters show a high degree of continuity, and the arguments used to assign the spectra of $Si[Fe_2(CO)_8]_2$, can be applied to the Ge, Sn and Pb analogues. The structures of all four of these compounds have been elucidated crystallographically, and are very similar (allowing for the increasing size of E). $Si[Fe_2(CO)_8]_2$ and $Ge[Fe_2(CO)_8]_2$ are isomorphous [38][40], crystallising in the $P2_1/c$ space group. $Sn[Fe_2(CO)_8]_2$ and $Pb[Fe_2(CO)_8]_2$ form another isomorphous pair [48][31], crystallising in the $P2_1/n$ space group. Other workers [183] have solved the structure of $Ge[Fe_2(CO)_8]_2$ in the P_c space group, however this is probably incorrect. In each case the molecules occupy assymmetric positions in the unit cell, however one might expect to see differences between the solid-state carbonyl spectra of the two isomorphous pairs. This was not found to be the case. Variations in the carbonyl spectra within this series are minimal.

E[Co$_2$(CO)$_7$]$_2$

As previously mentioned, the solution state infrared spectra reported for the E[Co$_2$(CO)$_7$]$_2$ clusters show only six of the twelve terminal carbonyl stretching modes anticipated under C_2 symmetry. This has prompted comparisons with Bor's model infrared spectrum for (μ-Y)$_2$M$_2$(CO)$_6$ compounds, and the spectrum predicted on the basis of an idealised D_{2d} symmetry (see section 6.1.2). Looking at the solution state infrared and Raman spectra of E[Co$_2$(CO)$_7$]$_2$ (**table 6.10**), it is clear that a direct comparison with the Bor spectrum is no longer valid. The highest energy infrared band at 2078 cm^{-1} is not active in the Raman spectrum and cannot be classed as a_1 (as required for the highest infrared-active band in the Bor model). Assignments, based on approximate D_{2d} symmetry seem a lot more appropriate. This implies that coupling across the group 14 atom is significant.

The Bor model, however, may still prove useful. The E[Co$_2$(CO)$_7$]$_2$ compounds can be regarded as "double-Bor" systems, and with moderate coupling across the main group atom, it may be possible to view the resulting vibrational modes as in-phase and out-of-phase combinations of the Bor modes. Derivation of a "double-Bor" (D_{2d}) model from the Bor (C_{2v}) modes is shown in **table 6.12**. Note that because the two Co$_2$(CO)$_6$ units are mutually perpendicular,the local x and y axes exchange so that in local symmetry the b_1 mode in one unit corresponds with a b_2 mode in the other. This reconciles the correlation of the b_1 + b_2 modes in C_{2v} with the e mode in D_{2d}. When this model is applied to the observed spectra, the fit is remarkably good.

Looking first at the solution-state spectra of Si[Co$_2$(CO)$_7$]$_2$, the bands at 2114 and 2051 cm^{-1} are both strong in the Raman spectra, which is consistent with the a_1 assignment. For the 2114 cm^{-1} band, this is confirmed by the detection of strong polarisation. Although symmetry forbidden, the 2051 cm^{-1} mode exhibits a moderately strong band in the infrared spectrum. The appearance of this peak is perhaps not surprising considering the approximations involved in assuming D_{2d} symmetry. Note that the 2051 cm^{-1} band is not seen in the solid-state infrared spectrum.

The double-Bor b_2 modes represent the out-of-phase combination of the Bor a_1 modes. As expected, the vibrations tentatively assigned as b_2 modes (2083 and 2035 cm^{-1}) display strong infrared bands. Of the remaining vibrations, the 2064 and 2023 cm^{-1} bands are strong in the

infrared spectrum and are also active in the Raman spectrum, and the 2005 cm^{-1} band is only seen in the infrared spectrum. The features displayed by these vibrations are not inconsistent with their assignment to e modes. The $b_1(R)$ mode remains unassigned.

Table 6.12: Correlation between $M_2(CO)_6(\mu\text{-}Y)_2$ and $(\mu_4\text{-}E)[M_2(CO)_6(\mu\text{-}CO)]_2$ carbonyl vibrations

Bor Unit Vibrations		Double-Bor Unit Vibrations	
Bor symbol	Symmetry and Activity (C_{2v})	Double-Bor Symbol	Symmetry and Activity (D_{2d})
q	a_1 (IR,R)	q'	a_1 (R)
		q"	b_2 (IR,R)
s	b_1 (IR,R)	s'	e (IR,R)
u	a_1 (IR,R)	u'	a_1 (R)
		u"	b_2 (IR,R)
v	b_2 (IR,R)	v'	e (IR,R)
w	b_1 (IR,R)	w'	e (IR,R)
z*	a_2 (R)	z'	a_2 (i.a.)
		z"	b_1 (R)

* The infrared-inactive a_2 mode was not designated by Bor [285] and the symbol z is introduced. r, t, x and y were used to denote ^{13}CO modes.

In the bridging carbonyl region, $a_1(R)$ + $b_1(IR,R)$ modes are predicted, and these are assigned to the observed Raman-active and infrared-active bands respectively.

The situation becomes more complex in the solid state. The appearance of new bands, and inconsistencies with the solution spectra makes it difficult to interpret the lower region. The four highest energy vibrations are reasonably consistent and are easily assigned. The 2035 cm^{-1} band, which has been assigned as b_2, now also exhibits a moderately strong feature in the Raman spectrum. Below this point,

assignments are extremely tentative. A drop in symmetry in the solid state may be causing splitting of the e degeneracies (*eg.* splitting of 2023(e) band may account for the strong Raman feature, observed at 2014 cm^{-1} for $Ge[Co_2(CO)_7]_2$) and the appearance of the a_2(i.a.) mode and the b_1(R) mode (which may also give an infrared signal). Also, one of the lower bands may represent a $\nu(^{13}CO)$ mode. Really there is little basis for assigning these lower bands. Considering the approximations involved, it is not surprising that this simplified 'double Bor' approach breaks down in this region. On the contrary it is interesting that it has carried this far.

Inconsistencies between the solid-state spectra of $Si[Co_2(CO)_7]_2$ and $Ge[Co_2(CO)_7]_2$, in particular the 2014 cm^{-1} vibration seen only for the Ge analogue, can be explained by differences in the crystal lattice. $Si[Co_2(CO)_7]_2$ crystallises in the monoclinic C2/c space group with the Si atom lying on a crystallographic diad, while the $Ge[Co_2(CO)_7]_2$ unit cell is of the triclinic $P\bar{1}$ space group, and contains two distinct molecules occupying assymmetric sites.

In the bridging carbonyl region, the a_1(R) mode is now observed in the infrared spectrum, and in the case of $Si[Co_2(CO)_7]_2$, this feature is relatively intense.

6.3.1.2 δ(MCO) and ν(M-C) Region

Bands in this region tend to be very weak and exhibit a high degree of mixing. This region has been identified by comparison with the vibrational spectra of $(Me_3Ge)_2Fe(CO)_4$ [296] and $H_3GeCo(CO)_4$ [272]. No attempt has been made to assign individual bands, but it should be noted that M-C-O deformations generally occur at higher energy than M-C stretches. One point of interest is whether the bands at ~280 cm^{-1} included in the heavy atom stretching region actually represents a M-C stretch. This is discussed below.

6.3.1.3 M-M, E-M Stretching Region

The metal framework of $E[Fe_2(CO)_8]_2$ and $E[Co_2(CO)_7]_2$ clusters all approximate to D_{2d} symmetry. However this approximation is less accurate for the heavier analogues and for the Co clusters. These compounds show significant asymmetry in the EM_2 triangles and distortion of the dihedral angle between the two EM_2 triangles from 90° (see table 3.1).

The D_{2d} approximation gives an irreducible representation of $2a_1 + b_1(R) + 2b_2(IR,R) + 2e(IR,R)$ for the EM_4 skeleton. The predominantly M-M stretching modes give an irreducible representation of $a_1 + b_2$, and the predominantly E-M stretching modes give $a_1 + b_2 + e$. This leaves $b_1 + e$ bending modes.

An idea of where these modes should occur can be gained by looking at related compounds. From **table 6.5**, we might expect the singly-bridged Fe-Fe bond to vibrate at *ca.* 190 cm^{-1}, and the doubly bridged Co-Co bond to vibrate at *ca.* 230 cm^{-1}. The Ge-Fe and Ge-Co bonds in $(Me_3Ge)_2Fe(CO)_4$ **[296]** and $H_3GeCo(CO)_4$ **[272]** stretch at 228 cm^{-1} and 200 cm^{-1} respectively, although considerable variation in frequency is observed for related clusters. Note that two Ge-Fe modes are expected for $(Me_3Ge)_2Fe(CO)_4$, and these appear to be superimposed; the contour of the resonance alters in polarisation studies. Two modes are seen for $(MeGeH_2)_2Fe(CO)_4$ **[296]** and $(H_3Ge)_2Fe(CO)_4$ **[297]** with separations of 15 and 13 cm^{-1}. In the *spiro* clusters, E-M stretching would require M-M stretching and/or deformation of the EM_2 bonding angles. For the *spiro* clusters we might therefore expect modes which are primarily E-M stretches to occur at even higher frequencies.

Only Raman spectra are available for the heavy atom vibration region. Up to nine modes are observed in the solid-state spectra, the additional two modes probably representing splitting of the e degeneracies. In the solution spectra, the lower bands, and bands in the 275-295 cm^{-1} region are masked by vibrations of the solvent. Hence only three or four bands are observed.

For $Si[Fe_2(CO)_8]_2$, the two polarised bands, at 196 and 149 cm^{-1}, are obviously the a_1 modes. The higher energy 196 cm^{-1} mode is likely to arise from a symmetric stretch of the entire metal framework, and it is perhaps surprising that this is not the highest energy heavy atom vibration. Because of this there is some concern over whether the band at 284 cm^{-1} is in fact a Fe-C stretch. Here it has been included as a vibration of the metal framework because of the relatively low frequencies of the other modes compared with the values predicted above. This band has tentatively been assigned as an e mode. It is weakly Raman-active (as expected for an e mode) and, in the case of $Ge[Co_2(CO)_7]_2$, it appears to split giving very weak bands at 296 and 245 cm^{-1}.

Because there is a b_2 mode predicted for both E-M and M-M stretching, we would expect at least one relatively high energy b_2 mode in the observed spectra. Hence the 174 cm^{-1} vibration, which occurs as a medium-strong to weak intensity band, has been very tentatively designated as b_2. Individual assignments for the remaining bands have not been attempted.

Assmt.	$E[Fe_2(CO)_8]_2$				$E[Co_2(CO)_7]_2$	
	Si	Ge	Sn	Pb	Si	Ge
e	284 w	288 vw	250 w		277 w	296 vw
						245 vw
a_1	196 vs	191 vs	185 vs	177	231 vs	221 vs
b_2	172 ms	163 m	157 w		218 w	205 w
a_1	148 m	144 m	133 m		153 m	148 s
b_1	118 sh	122 sh			130 w	
b_2	107 sh	108 sh			118 sh	109 sh
e	97 s	97 s	94 m		96 s	96 s
	88 sh	84 sh	68 sh		77 sh	80 sh

Table 6.13: Frequency shift for the heavy atom solid-state Raman vibration modes of *spiro*-$E[M_2(CO)_x]_2$ clusters

The heavy atom vibration regions of the solid-state Raman spectra of all six *spiro* clusters are compared in **table 6.13**. Variation between the spectra of the Fe and Co clusters is minimal, except for the higher energy a_1 and b_2 modes, which occur at *ca.* 40 cm^{-1} higher frequency for the Co analogues. This shift is much larger and in the opposite direction to that predicted from the change in the mass of M, and therefore is probably due to the presence of the bridging carbonyl in $E[Co_2(CO)_7]_2$. Hence a large component of these vibrations appears to involve M-M stretching (*ie.* the predicted a_1 + b_2 ν(M-M) modes). Note that, because the metal framework is composed of EM_2 triangles,

attributing bands to individual stretching or bending modes is probably inappropriate, and it must be recognised that each vibration would neccessarily contain both stretching and bending elements.

Within each series of compounds, an overall shift in frequency of *ca.* 6 cm^{-1} is observed as E becomes larger. As expected, the effect of E-substitution is more pronounced in this region than in the ν(CO), ν(MC) and δ(MCO) regions. It is noticeable that the frequencies of the bands at approximately 280 and 140 cm^{-1} decrease rapidly from $Ge[Fe_2(CO)_8]_2$ to $Sn[Fe_2(CO)_8]_2$ and hence appear to involve a large amount of E-M stretching ($a_1 + b_2 + e$ modes are predicted for ν(E-M)). If this shift in frequency were due solely to the difference in mass of E, then the shifts from Si to Ge and from Ge to Sn should be of similar magnitude. The fact that the latter shift is much greater, suggests that the Sn-Fe bond may be weaker than the Si-Fe and Ge-Fe bonds.

6.3.2 VIBRATIONAL SPECTRA OF $(CO)_4CoECo_3(CO)_9$ COMPOUNDS

6.3.2.1 Carbonyl Stretching Region

$(CO)_4CoSiCo_3(CO)_9$ and $(CO)_4CoGeCo_3(CO)_9$ have approximately C_{3v} molecular symmetry, and this gives irreducible representations of a_1 (axial) and $a_1 + e$ (equatorial) for the $Co(CO)_4$ group, and $3a_1 + 3e$ for $Co_3(CO)_9$ (or $a_1 + e$ for each of the upward-pointing, in-plane and downward-pointing sets). Of the total $5a_1$(IR,R) + 4e(IR,R) modes, only six have been observed in the infrared spectrum, and, because of the poor quality of the spectra, only a single Raman band has been detected (table 6.11). This Raman band occurs at approximately the same frequency as the strongest infrared band, though it is unusual for the strongest infrared-active and Raman-active modes to coincide.

On the basis of the infrared and Raman spectra of $MeCCo_3(CO)_9$, given in table 6.6, it is not possible to distinguish the a_1 and e modes from relative peak intensities. Hence, without polarisation data, no attempt has been made to assign the carbonyl spectra of $(CO)_4CoSiCo_3(CO)_9$ and $(CO)_4CoGeCo_3(CO)_9$.

6.3.2.2 δ(CoCO), ν(Co-C), ν(E-Co) and ν(Co-Co) Region

For $(CO)_4CoECo_3(CO)_9$, $a_1 + e$ cobalt-cobalt stretching modes (shown in figure 6.2) and $2a_1 + e$ E-Co stretching modes are expected under C_{3v}

symmetry. For alkylidyne $YCCo_3(CO)_9$ clusters, the ν(Co-Co) modes occur at 215 ± 20 cm^{-1} and 165 ± 25 cm^{-1} respectively (see section 6.1.3). Vibrations at ~200 and ~160 cm^{-1} correlate well with these bands, and strong polarisation for the $(CO)_4CoGeCo_3(CO)_9$ 199 cm^{-1} band confirms that this is an a_1 mode. However, all vibrations within the heavy-atom $GeCo_3$ unit would involve Ge-Co and Co-Co stretching and bond angle deformation components, and for the Si and Ge trigonal pyramids, it is probably inappropriate to separate the Co-Co and Ge-Co stretches. For the alkylidyne clusters, where the frequencies of the $\nu(\mu$-CCo) and ν(CoCo) vibrations are quite different, it is more valid to treat these vibrations separately [290,293,294,295].

In table 6.11, the transition from the δ(CoCO) and ν(CoC) vibrations to those of the $CoECo_3$ skeleton is poorly-defined. $(CO)_4CoSiCo_3(CO)_9$ and $(CO)_4CoGeCo_3(CO)_9$ are isomorphous, and crystallise in the $P\bar{1}$ space group. Hence a reasonable degree of continuity would be expected in the δ(CoCO), ν(CoC) and ν(CoCo) modes, and any variation in the spectra probably relates to E-Co stretching. Using this reasoning, the $(CO)_4CoGeCo_3(CO)_9$ bands at 326 and 224 cm^{-1}, which do not appear to correspond with bands of similar frequency in the spectra of $(CO)_4CoSiCo_3(CO)_9$, have been tentatively designated Ge-Co stretches. The latter vibration is in the region found for the Ge-Co stretch in $Y_3GeCo(CO)_4$ compounds, and has therefore been assigned to the terminal Ge-Co bond. The high energy band, 326 cm^{-1}, hence appears to be a mode of the $GeCo_3$ unit; note that a high energy vibration with significant ν(E-M) character was also observed for the EM_4 skeleton in the *spiro* clusters. Presumably this is some concerted motion of the entire heavy atom skeleton, and it is not possible to separate the Ge-Co from the Co-Co modes.

The metal framework bending region below 150 cm^{-1} shows a complex series of weak ill-defined bands. No attempt has been made to interpret this region.

Tent. Assmnt.	$Si[Fe_2(CO)_8]_2$ Solution Infrared (hexane) [38]	$Si[Fe_2(CO)_8]_2$ Solution Raman (CH_2Cl_2)	$Si[Fe_2(CO)_8]_2$ Solid Infrared (KBr disc)	$Si[Fe_2(CO)_8]_2$ Solid Raman (crystal)	$Ge[Fe_2(CO)_8]_2$ Solution Infrared (CH_2Cl_2) [40]	$Ge[Fe_2(CO)_8]_2$ Solution Raman (CH_2Cl_2)	$Ge[Fe_2(CO)_8]_2$ Solid Infrared (CsI disc)	$Ge[Fe_2(CO)_8]_2$ Solid Raman (crystal)	Tent. Assmnt.
a_1		2112p vs	2109 vw	2112 m		2111 s		2110 m	a_1
e	2076 m	2080 vw	2080 s	2079 w	2078	2075 vw	2075 m	2076 w	e
b_2			2065 w,sh				2061 sh	2061 vw	b_2
e	2050 vs		2049 vs	2051 vw	2050		2047 s	2048 w	e
e	2030 w		2028 m,sh	2035 w	2030		2030 w	2034 w	e
a_1		2036 vs		2025 vs		2024 vs		2024 vs	a_1
e	2013 s		2011 vs	2016 w	2015		2010 s	2014 w	e
a_1		2015 s		2006 m		2011 m		2006 m	a_1
b_1		2002 sh		1996 w		1998 vw		1994 w	b_1
b_2	1990 vw	1988 w	1987 s	1989 vw		1988 w	1988 s	1988 vw	b_2
a_2, ^{13}C				1983 m				1982 m	a_2, ^{13}C
b_2			1968 m				1969 m	1966 vw	b_2
δFeCO		640p? w		641 w		640 w		638 w	δFeCO
		625 vw		625 vw			625 sh	620 vvw	
			618 m				613 m		
			596 m	604 vvw			592 s		
			549 w				547 w		
								523 vw	
		489p w		488 w		486 w		484 w	
				481 vw				478 vw	
			466 vw				460 vw		
				451 vvw				453 vvw	
νFeC		435p mw		436 m		435 mw		437 m	νFeC
			425 w,br	420 vw			420 w,br		
				401 vw		400 vw			
e				284 w				288 vw	e
a_1		196p vs		196 vs		193 vs		191 vs	a_1
b_2		174 mw		172 ms		168 w		163 m	b_2
a_1		149p mw		148 m		144 mw		144 m	a_1
				118 sh				122 sh	
b_1, e				107 sh				108 sh	e, b_1
b_2				97 s				97 s	b_2
				88 sh				84 sh	

Tent. Assmnt.	$Sn[Fe_2(CO)_8]_2$ Solution Infrared (hexane) [48]	$Sn[Fe_2(CO)_8]_2$ Solution Raman (CH_2Cl_2)	$Sn[Fe_2(CO)_8]_2$ Solid Infrared (KBr disc)	$Sn[Fe_2(CO)_8]_2$ Solid Raman (crystal)	$Pb[Fe_2(CO)_8]_2$ Solution Infrared (hexane) [31]	$Pb[Fe_2(CO)_8]_2$ Solution Raman (CH_2Cl_2)	$Pb[Fe_2(CO)_8]_2$ Solid Infrared (KBr disc)	$Pb[Fe_2(CO)_8]_2$ Solid Raman (crystal)	Tent. Assmnt.
a_1		2106p vs	2106 w	2106 m			2103 vw		a_1
e	2072 s	2075 vw	2072 m		2067 m		2078 w		e
b_2			2054 w	2054 vvw			2061 sh		b_2
e	2044 vs		2044 s		2042 s		2041 s		e
e	2027 m		2027 w	2032 w	2029 w				e
a_1		2029 vs		2020 vs					a_1
e	2010 s		2009 s		2010 s		2000 m		e
a_1		2011 m		2006 s					a_1
b_1				2000 w,sh					b_1
b_2		1981 w	1983 s	1987 w			1978 m		b_2
a_2, ^{13}C				1972 mw					a_2, ^{13}C
b_2			1964 sh						b_2
δFeCO		635p? w		635 w					δFeCO
			620 sh	627 vvw			619 sh		
		614 vw	611 sh	614 vvw			610 sh		
			592 m				590 m		
			547 w				542 w		
				527 vvw					
		487p w		487 w					
				476 w					
							455 vw		
		458 vw		456 vvw					
νFeC		435p mw		438 m		434			νFeC
			427 w				426 w		
		398 vw		399 vw					
e		249 w		250 w					e
a_1		184p vs		185 vs		177			a_1
b_2		153 w		157 w					b_2
a_1		134p m		133 m					a_1
b_1, e									e, b_1
b_2				94 m					b_2
				68 w					

Table 6.9: Infrared and Raman vibrational spectra and assignments for $E[Fe_2(CO)_8]_2$ (E = Si, Ge, Sn, Pb)

Tent. Assmnt.	$Si[Co_2(CO)_7]_2$ Solution Infrared (hexane) [39]	$Si[Co_2(CO)_7]_2$ Solution Raman (CH_2Cl_2)	$Si[Co_2(CO)_7]_2$ Solid Infrared (KBr disc)	$Si[Co_2(CO)_7]_2$ Solid Raman (crystal)	$Ge[Co_2(CO)_7]_2$ Solution Infrared (hexane) [42]	$Ge[Co_2(CO)_7]_2$ Solution Raman (CH_2Cl_2)	$Ge[Co_2(CO)_7]_2$ Solid Infrared (KBr disc)	$Ge[Co_2(CO)_7]_2$ Solid Raman (crystal)	Tent. Assmnt.
a_1		2114 s		2112 ms		2111p vs		2108 s	a_1
b_2	2083 s		2074 s		2079 s		2077 s	2078 vw	b_2
e	2064 vs		2056 sh	2061 w	2061 vs	2065 sh	2051 m	2054 sh	e
a_1	2042 m	2051 s		2043 vs	2040 m	2047 vs		2043 vs	a_1
b_2	2035 ms		2034 s	2033 m	2032 ms		2028 s	2033 m	b_2
e	2023 m	2023 m		2023 m	2023 m	2021 m	2020 sh	2023 w	e
								2014 s	
e	2005 w		2015 s	2018 sh	2005 w		2006 m	2009 sh	e
b_1, b_2 ^{13}C			2003 w	2001 w			1996 m		b_1, b_2 ^{13}C
			1978 sh				1972 sh		
a_1		1847 w	1864 m	1849 w		1844 w	1843 sh	1848 w	a_1
b_1	1843 m		1832 s		1848 m		1835 m	1837 w	e
		571 vw						579 w	
			568 sh	564 w			566 sh	563 w	
δFeCO	553		555 m				547 w		δFeCO
				531 vvw		537 w	531 sh	532 vvw	
	524	518 vw	517 m				521 m		
	509		502 m				494 w		
		488 vw	484 w	478 vw		482 w		484 vw	
	453		463 w						
		444 vw	442 w	445 vw		441 vw		440 w	
				426 vw				421 w	
			405 w					395 vw	
νFeC			376 m				372 w		νFeC
		384 w		386 m		382p mw		382 w	
				360 vw				360 vw	
e				277 w				296 vw	e
						252 vw		245 vw	
a_1		230 vs		231 vs		223p vs		221 vs	a_1
b_2		213 w		218 w		202 w		205 w	b_2
a_1		169 w		153 m		148 mw		148 s	a_1
		152 w		130 w					
b_1, e				118 sh				109 sh	e, b_1
b_2				96 s				96 s	b_2
				77 sh				80 w,sh	

Table 6.10: Infrared and Raman vibrational spectra and assignments for $E[Co_2(CO)_7]_2$ (E = Si, Ge)

Tent. Assmnt.	$(CO)_4CoSiCo_3(CO)_9$ Solution Infrared (hexane) [179]	$(CO)_4CoSiCo_3(CO)_9$ Solution Raman (CH_2Cl_2)	$(CO)_4CoSiCo_3(CO)_9$ Solid Infrared (KBr disc)	$(CO)_4CoSiCo_3(CO)_9$ Solid Raman (crystal)	$(CO)_4CoGeCo_3(CO)_9$ Solution Infrared (hexane) [179]	$(CO)_4CoGeCo_3(CO)_9$ Solution Raman (CH_2Cl_2)	$(CO)_4CoGeCo_3(CO)_9$ Solid Infrared (KBr disc)	$(CO)_4CoGeCo_3(CO)_9$ Solid Raman (crystal)	Tent. Assmnt.
	2114 w				2112 w		2108 mw		
	2087 s				2083 s		2077 s		
				2052				2051	
	2047 vs				2045 vs		2055 s		
	2031 m				2029 m		2025 vs		
	2011 vw				2008 vw		2009 sh		
	1993 vw						1996 vw,sh		
	545 sh				545 sh				
	540 vs			542 vw	540 s	534 vw		535 vw	
δCoCO	518 vs				518 s	517 vw			δCoCO
	510 vs			508 vw	510 s	505 vw		512 w	
	497 w				497 w				
	482 w			488 w	482 w	485 w		482 w	
					468 w				
					450 w				
νCoC	443 m				440 m				νCoC
	423 w			427 w	423 w			427 w	
	408 w			412 w	408 w	412 w		412 w	
					330 m	326 w		325 vw	$\nu GeCo_3$
						224 w		217 w	νGeCo
$\nu SiCo_3 a_1$				210 vs		199p vs		200 s	$a_1 \nu GeCo_3$
$\nu SiCo_3$				163 m		154 m		154 m	$\nu GeCo_3$

Table 6.11: Infrared and Raman vibrational spectra and assignments for $(CO)_4CoECo_3(CO)_9$ (E = Si, Ge)

Appendix A

APPENDIX A STRUCTURES OF COMPOUNDS FREQUENTLY REFERRED TO IN THIS THESIS

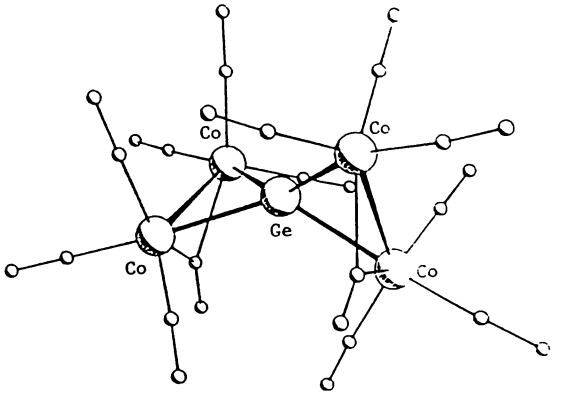

(F 1)
$E[Co_2(CO)_7]_2$
E = Si, Ge

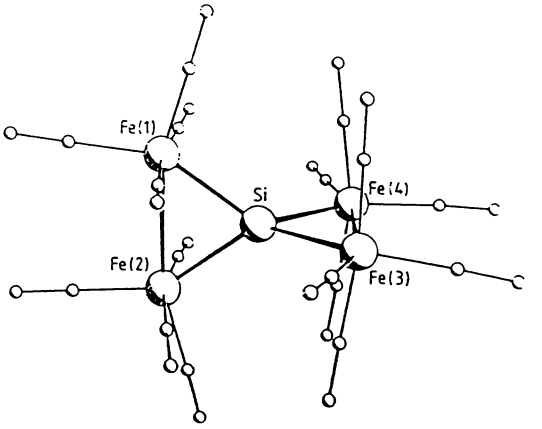

(F 2)
$E[Fe_2(CO)_8]_2$
E = Si, Ge, Sn, Pb

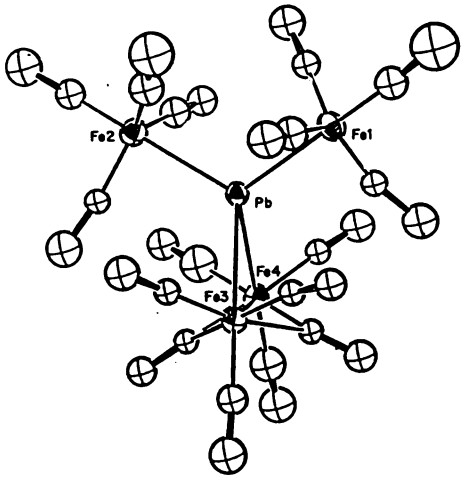

(F 3)
$[(CO)_8Fe_2]E[Fe(CO)_4]_2^{2-}$
E = Sn, Pb

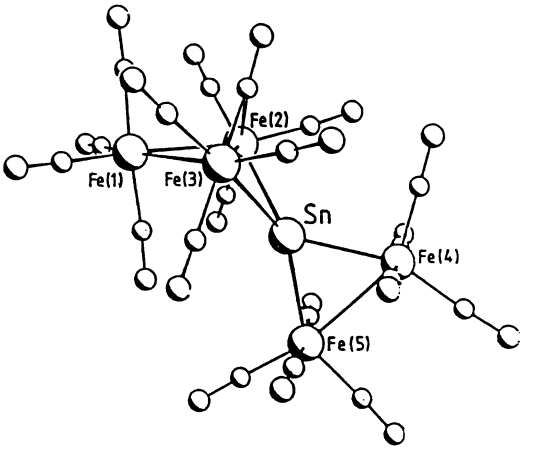

(F 4)
$SnFe_5(CO)_{19}$

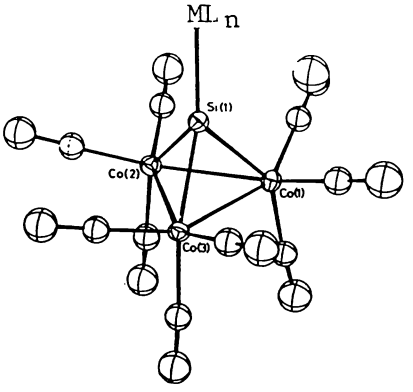

(F 5)
$(CO)_4CoECo_3(CO)_9$
E = Si, Ge
$(CO)_5MnECo_3(CO)_9$
E = Si, Ge

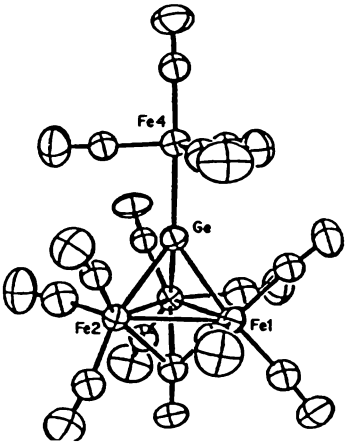

(F 6)
$[(CO)_4FeEFe_3(CO)_{10}]^-$
E = Si, Ge

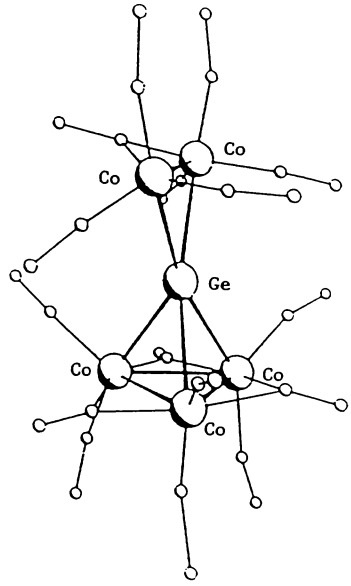

(F 7)
$[GeCo_5(CO)_{16}]^-$

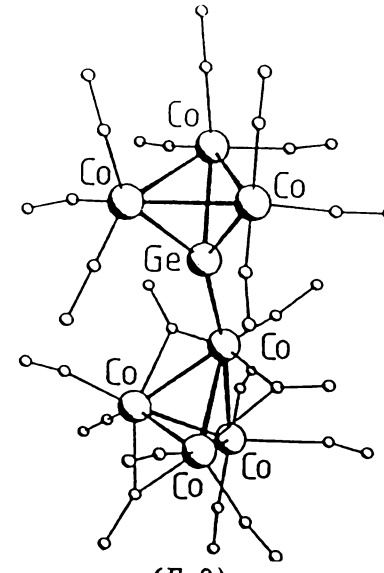

(F 8)
$[GeCo_7(CO)_{20}]^-$

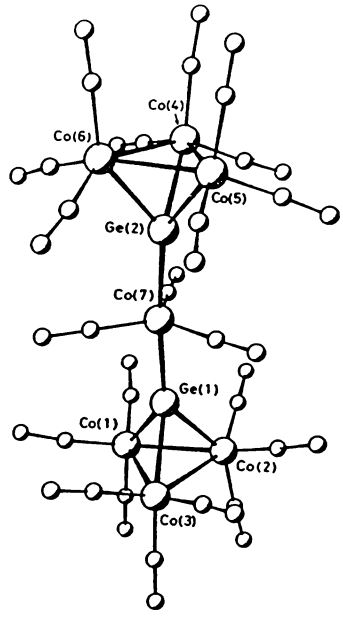

(F 9)
$[Ge_2Co_7(CO)_{21}]^-$

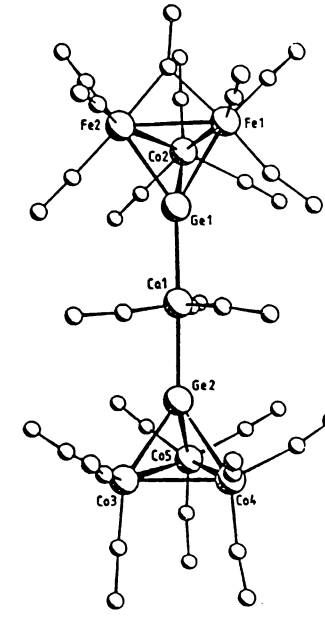

(F 10)
$[Ge_2Co_5Fe_2(CO)_{22}]^-$

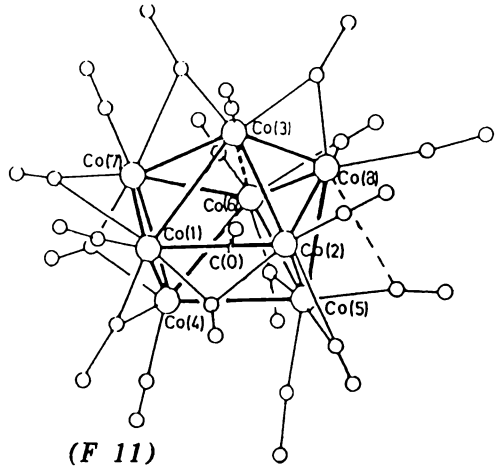

(F 11)
$[CCo_8(CO)_{18}]^{2-}$

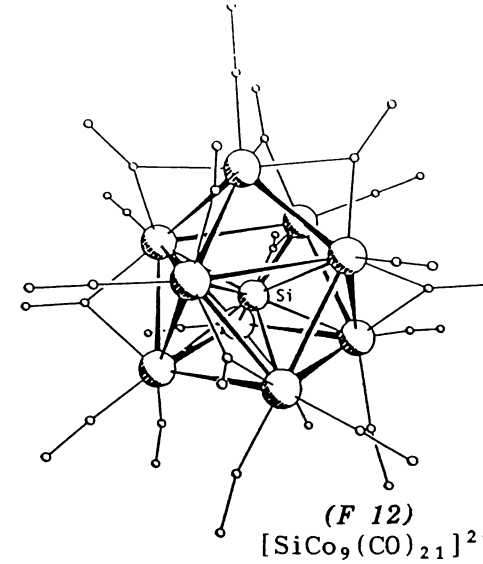

(F 12)
$[SiCo_9(CO)_{21}]^{2-}$

Appendix B

APPENDIX B TEMPERATURE FACTORS AND POSITIONAL PARAMETERS FOR $[Et_4N][Cl_2SiCo_7(CO)_{21}]$

B.1 Temperature Factors for $[Et_4N][Cl_2SiCo_7(CO)_{21}]$

ATOM	U11	U22	U33	U23	U13	U12
Co(1)	0.011(1)	0.022(1)	0.016(1)	0.000(1)	0.000(1)	-0.001(1)
Co(2)	0.017(1)	0.023(1)	0.017(2)	0.003(1)	0.002(1)	-0.002(1)
Co(3)	0.016(1)	0.023(1)	0.022(2)	-0.001(1)	0.002(1)	0.004(1)
Co(4)	0.019(1)	0.015(1)	0.016(1)	-0.001(1)	0.001(1)	0.001(1)
Co(5)	0.025(2)	0.021(1)	0.025(2)	0.003(1)	-0.001(1)	-0.005(1)
Co(6)	0.018(1)	0.020(1)	0.024(2)	0.005(1)	0.000(1)	-0.005(1)
Co(7)	0.028(1)	0.028(2)	0.019(2)	-0.001(1)	0.004(1)	-0.004(1)
Si(1)	0.015(3)	0.023(3)	0.020(3)	0.005(3)	-0.001(2)	-0.001(2)
Cl(1)	0.006(2)	0.012(2)	0.015(3)	0.003(2)	0.002(2)	-0.002(2)
Cl(2)	0.014(3)	0.013(3)	0.015(3)	-0.008(2)	-0.001(2)	0.002(2)
O(1)	0.020(3)					
O(11)	0.045(4)					
O(12)	0.031(3)					
O(13)	0.037(3)					
O(21)	0.036(3)					
O(22)	0.039(4)					
O(23)	0.037(3)					
O(31)	0.037(4)					
O(32)	0.059(4)					
O(34)	0.025(3)					
O(41)	0.037(4)					
O(43)	0.030(3)					
O(51)	0.050(4)					
O(52)	0.049(4)					
O(53)	0.044(4)					
O(61)	0.053(4)					
O(62)	0.042(4)					
O(63)	0.040(4)					
O(71)	0.057(4)					
O(72)	0.042(4)					
O(73)	0.049(4)					
C(1)	0.022(4)					
C(11)	0.022(4)					
C(12)	0.017(4)					
C(13)	0.023(4)					
C(21)	0.031(5)					
C(22)	0.030(5)					
C(23)	0.020(4)					
C(31)	0.019(4)					
C(32)	0.035(5)					
C(34)	0.020(4)					
C(41)	0.026(5)					
C(43)	0.020(4)					
C(51)	0.033(5)					
C(52)	0.023(4)					
C(53)	0.032(5)					
C(61)	0.040(6)					
C(62)	0.031(5)					
C(63)	0.030(5)					
C(71)	0.031(5)					
C(72)	0.032(5)					
C(73)	0.036(5)					
C(81)	0.025(4)					
C(82)	0.043(6)					
C(83)	0.037(5)					
C(84)	0.047(6)					
C(85)	0.034(5)					
C(86)	0.044(6)					
C(87)	0.019(4)					
C(88)	0.040(5)					
N(1)	0.022(4)					

B.2 Positional Parameters for $[Et_4N][Cl_2SiCo_7(CO)_{21}]$

ATOM	X/A	Y/B	Z/C	Ueq/U11
Co(1)	0.3406(2)	0.6032(1)	0.3949(1)	0.016
Co(2)	0.1141(2)	0.5389(1)	0.3958(1)	0.019
Co(3)	0.0856(2)	0.6470(1)	0.3786(1)	0.020
Co(4)	0.1720(2)	0.5846(1)	0.2944(1)	0.017
Co(5)	-0.1189(3)	0.7360(1)	0.0954(1)	0.024
Co(6)	-0.3149(2)	0.6593(1)	0.0925(1)	0.021
Co(7)	-0.0914(3)	0.6429(1)	0.0346(1)	0.025
Si(1)	-0.0165(5)	0.5746(2)	0.2207(2)	0.020
Cl(1)	-0.2279(4)	0.5612(2)	0.2488(2)	0.011
Cl(2)	-0.0008(5)	0.5058(2)	0.1541(2)	0.014
O(1)	-0.037(1)	0.6351(5)	0.1747(5)	0.020(3)
O(11)	0.425(1)	0.6144(6)	0.5325(7)	0.045(4)
O(12)	0.533(1)	0.5080(5)	0.3540(6)	0.031(3)
O(13)	0.481(1)	0.7106(6)	0.3507(6)	0.037(3)
O(21)	0.282(1)	0.4620(5)	0.4874(6)	0.036(3)
O(22)	-0.166(1)	0.4733(5)	0.3893(6)	0.039(4)
O(23)	0.037(1)	0.6075(6)	0.5071(6)	0.037(3)
O(31)	0.180(1)	0.7554(6)	0.4445(6)	0.037(4)
O(32)	-0.225(2)	0.6777(6)	0.3445(8)	0.059(4)
O(34)	0.200(1)	0.4545(5)	0.2990(6)	0.025(3)
O(41)	0.374(1)	0.5722(5)	0.1965(7)	0.037(4)
O(43)	0.169(1)	0.7127(5)	0.2637(6)	0.030(3)
O(51)	-0.263(2)	0.8205(6)	-0.0003(7)	0.050(4)
O(52)	-0.173(2)	0.7851(6)	0.2204(7)	0.049(4)
O(53)	0.194(2)	0.7659(6)	0.1009(7)	0.044(4)
O(61)	-0.501(2)	0.7159(6)	-0.0134(7)	0.053(4)
O(62)	-0.428(1)	0.5374(6)	0.0878(7)	0.042(4)
O(63)	-0.453(1)	0.6955(6)	0.2073(7)	0.040(4)
O(71)	-0.156(2)	0.7040(6)	-0.0903(8)	0.057(4)
O(72)	-0.172(1)	0.5208(6)	-0.0037(7)	0.042(4)
O(73)	0.227(2)	0.6238(6)	0.0572(7)	0.049(4)
C(1)	-0.113(2)	0.6540(7)	0.1232(8)	0.022(4)
C(11)	0.391(2)	0.6106(8)	0.4794(9)	0.022(4)
C(12)	0.461(2)	0.5458(7)	0.3713(8)	0.017(4)
C(13)	0.427(2)	0.6683(8)	0.3681(9)	0.023(4)
C(21)	0.219(2)	0.4934(8)	0.450(1)	0.031(5)
C(22)	-0.055(2)	0.5009(8)	0.3922(9)	0.030(5)
C(23)	0.064(2)	0.6020(7)	0.4533(9)	0.020(4)
C(31)	0.141(2)	0.7135(7)	0.4193(8)	0.019(4)
C(32)	-0.102(2)	0.6637(8)	0.361(1)	0.035(5)
C(34)	0.175(2)	0.5035(7)	0.3167(8)	0.020(4)
C(41)	0.296(2)	0.5781(8)	0.2347(9)	0.026(5)
C(43)	0.153(2)	0.6689(7)	0.2937(8)	0.020(4)
C(51)	-0.203(2)	0.7885(8)	0.039(1)	0.033(5)
C(52)	-0.150(2)	0.7683(7)	0.1699(9)	0.023(4)
C(53)	0.071(2)	0.7549(8)	0.0976(9)	0.032(5)
C(61)	-0.429(2)	0.6931(9)	0.028(1)	0.040(6)
C(62)	-0.385(2)	0.5841(8)	0.0908(9)	0.031(5)
C(63)	-0.398(2)	0.6818(8)	0.1630(9)	0.030(5)
C(71)	-0.133(2)	0.6793(8)	-0.042(1)	0.031(5)
C(72)	-0.138(2)	0.5688(8)	0.0118(9)	0.032(5)
C(73)	0.100(2)	0.6319(8)	0.046(1)	0.036(5)
C(81)	0.509(2)	0.9265(7)	0.2974(9)	0.025(4)
C(82)	0.652(2)	0.9062(9)	0.334(1)	0.043(6)
C(83)	0.365(2)	0.8471(8)	0.3494(9)	0.037(5)
C(84)	0.309(2)	0.8898(9)	0.397(1)	0.047(6)
C(85)	0.257(2)	0.9062(8)	0.2550(9)	0.034(5)
C(86)	0.127(2)	0.8661(9)	0.240(1)	0.044(6)
C(87)	0.450(2)	0.8287(7)	0.2443(8)	0.019(4)
C(88)	0.481(2)	0.8504(9)	0.1797(9)	0.040(5)
N(1)	0.395(1)	0.8769(6)	0.2857(7)	0.022(4)

Positional parameters of calculated hydrogen atoms

ATOM	X/A	Y/B	Z/C	U11
H(811)	0.462(2)	0.9620(7)	0.3236(9)	0.020
H(812)	0.535(2)	0.9429(7)	0.2515(9)	0.020
H(821)	0.695(2)	0.9510(9)	0.337(1)	0.020
H(822)	0.733(2)	0.8768(9)	0.317(1)	0.020
H(823)	0.625(2)	0.8917(9)	0.380(1)	0.020
H(831)	0.467(2)	0.8277(8)	0.3709(9)	0.020
H(832)	0.284(2)	0.8126(8)	0.3394(9)	0.020
H(841)	0.275(2)	0.8693(9)	0.439(1)	0.020
H(842)	0.213(2)	0.9040(9)	0.367(1)	0.020
H(843)	0.378(2)	0.9278(9)	0.410(1)	0.020
H(851)	0.225(2)	0.9409(8)	0.2864(9)	0.020
H(852)	0.284(2)	0.9257(8)	0.2105(9)	0.020
H(861)	0.042(2)	0.8972(9)	0.223(1)	0.020
H(862)	0.101(2)	0.8469(9)	0.285(1)	0.020
H(863)	0.134(2)	0.8313(9)	0.205(1)	0.020
H(871)	0.367(2)	0.7943(7)	0.2385(8)	0.020
H(872)	0.551(2)	0.8103(7)	0.2676(8)	0.020
H(881)	0.487(2)	0.8093(9)	0.1534(9)	0.020
H(882)	0.575(2)	0.8777(9)	0.1723(9)	0.020
H(883)	0.381(2)	0.8739(9)	0.1629(9)	0.020

Appendix C

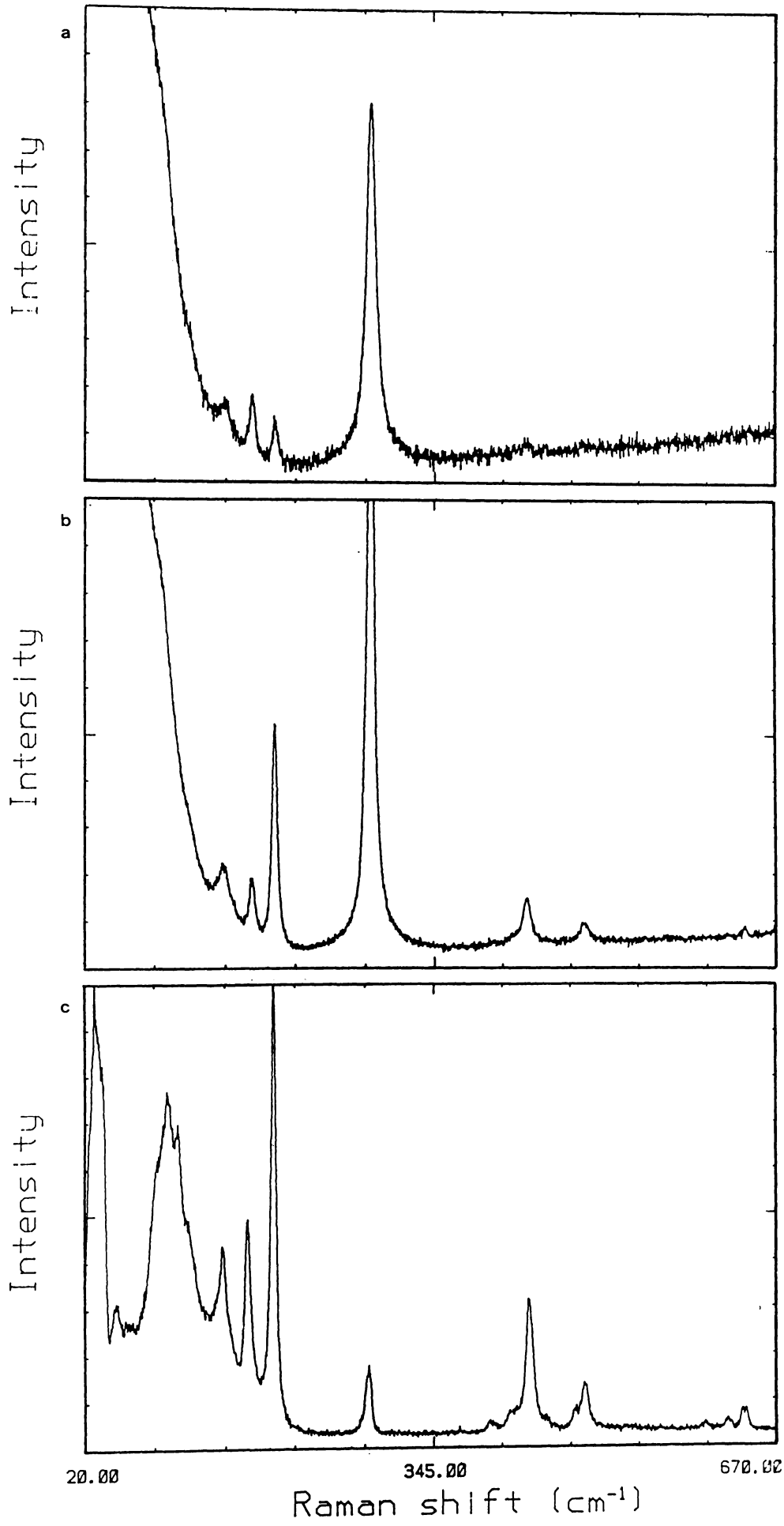

C.1 Raman vibrational spectra for $Si[Fe_2(CO)_8]_2$ in the low frequency region, a) in CH_2Cl_2 using a polarising filter, b) in CH_2Cl_2, c) as a crystalline solid

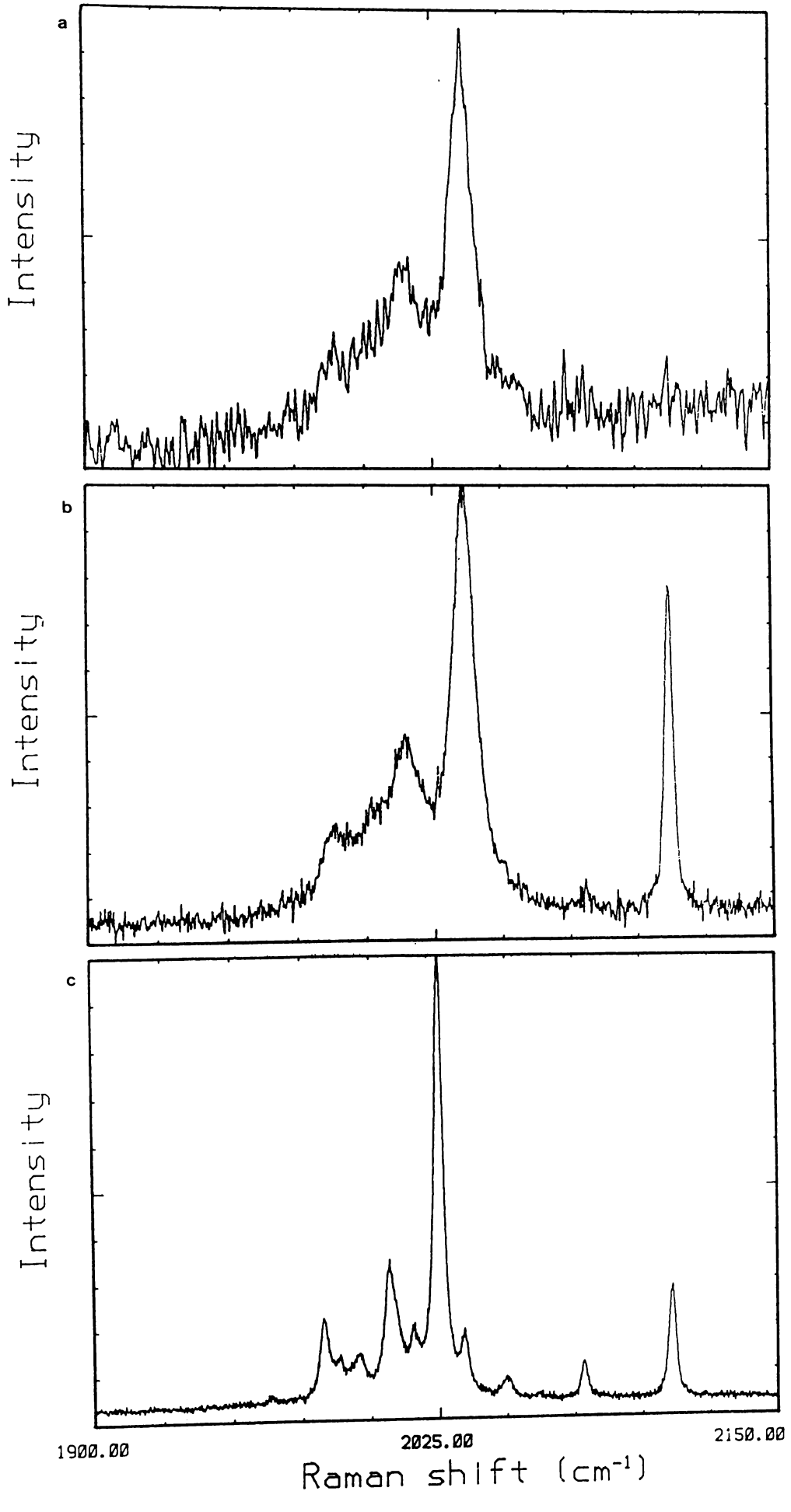

C.2 Raman vibrational spectra for $Si[Fe_2(CO)_8]_2$ in the carbonyl stretching region, **a)** in CH_2Cl_2 using a polarising filter, b) in CH_2Cl_2, c) as a crystalline solid

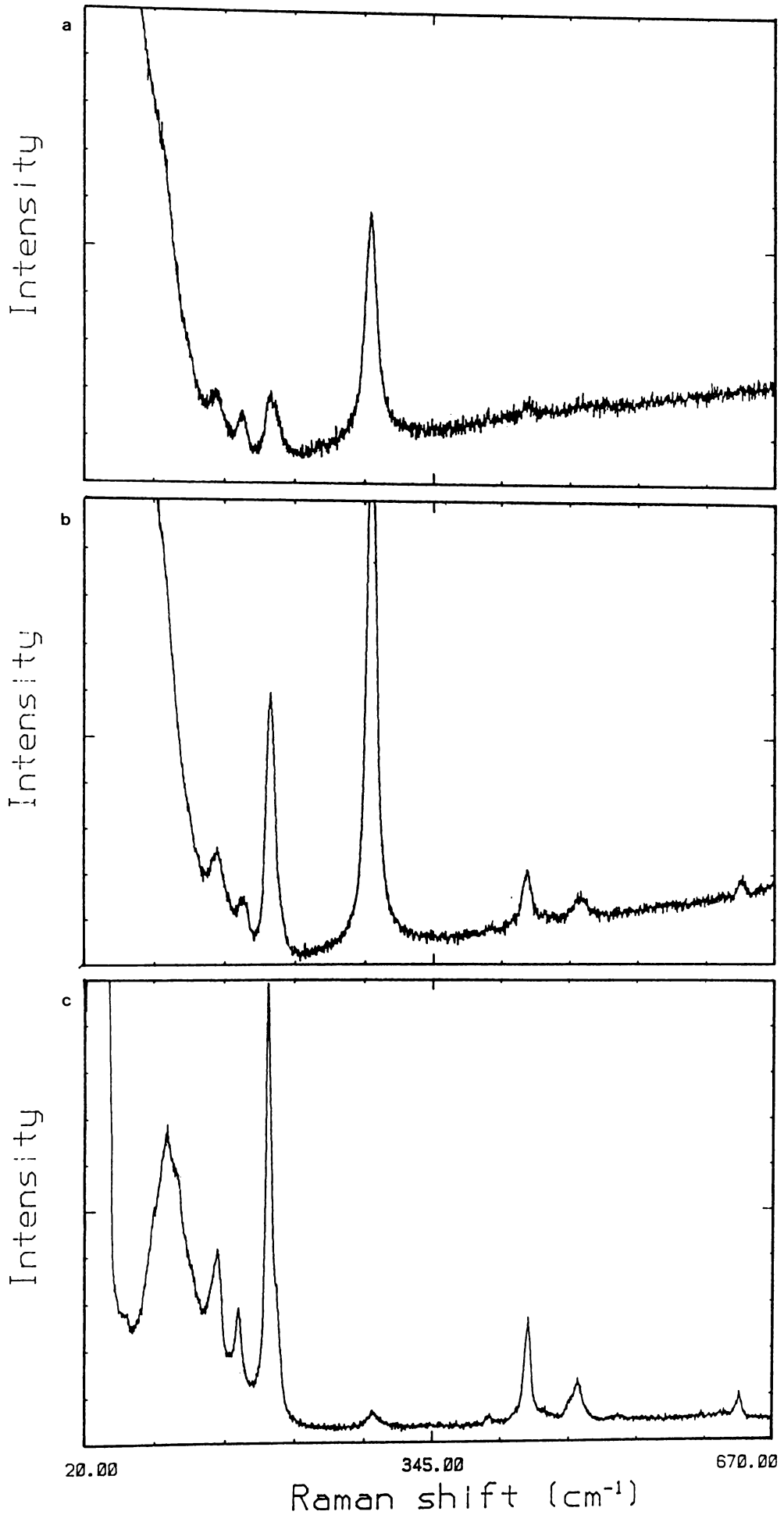

C.3 Raman vibrational spectra for $Ge[Fe_2(CO)_8]_2$ in the low frequency region, a) in CH_2Cl_2 using a polarising filter, b) in CH_2Cl_2, c) as a crystalline solid

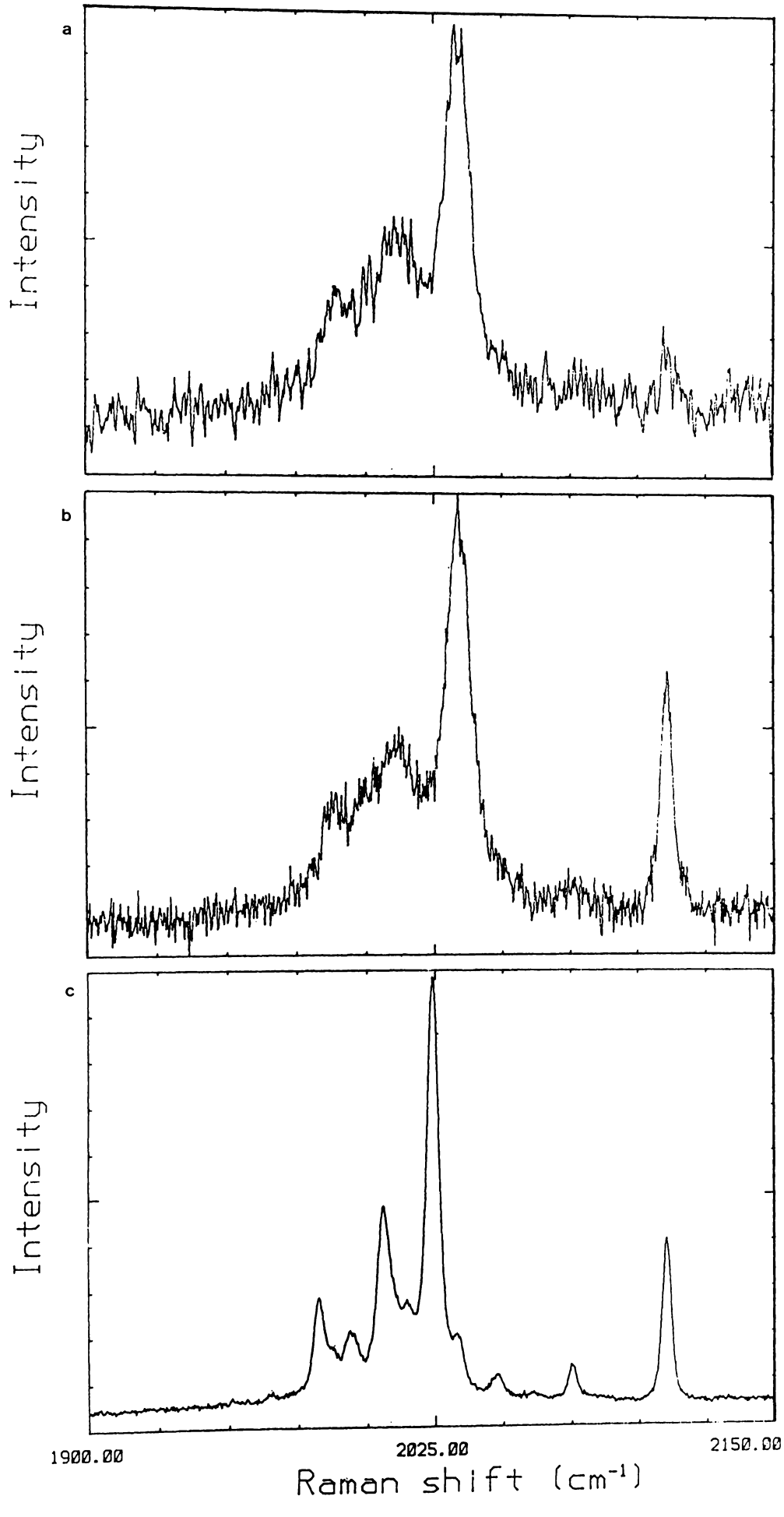

C.4 Raman vibrational spectra for $Ge[Fe_2(CO)_8]_2$ in the carbonyl stretching region, a) in CH_2Cl_2 using a polarising filter, b) in CH_2Cl_2, c) as a crystalline solid

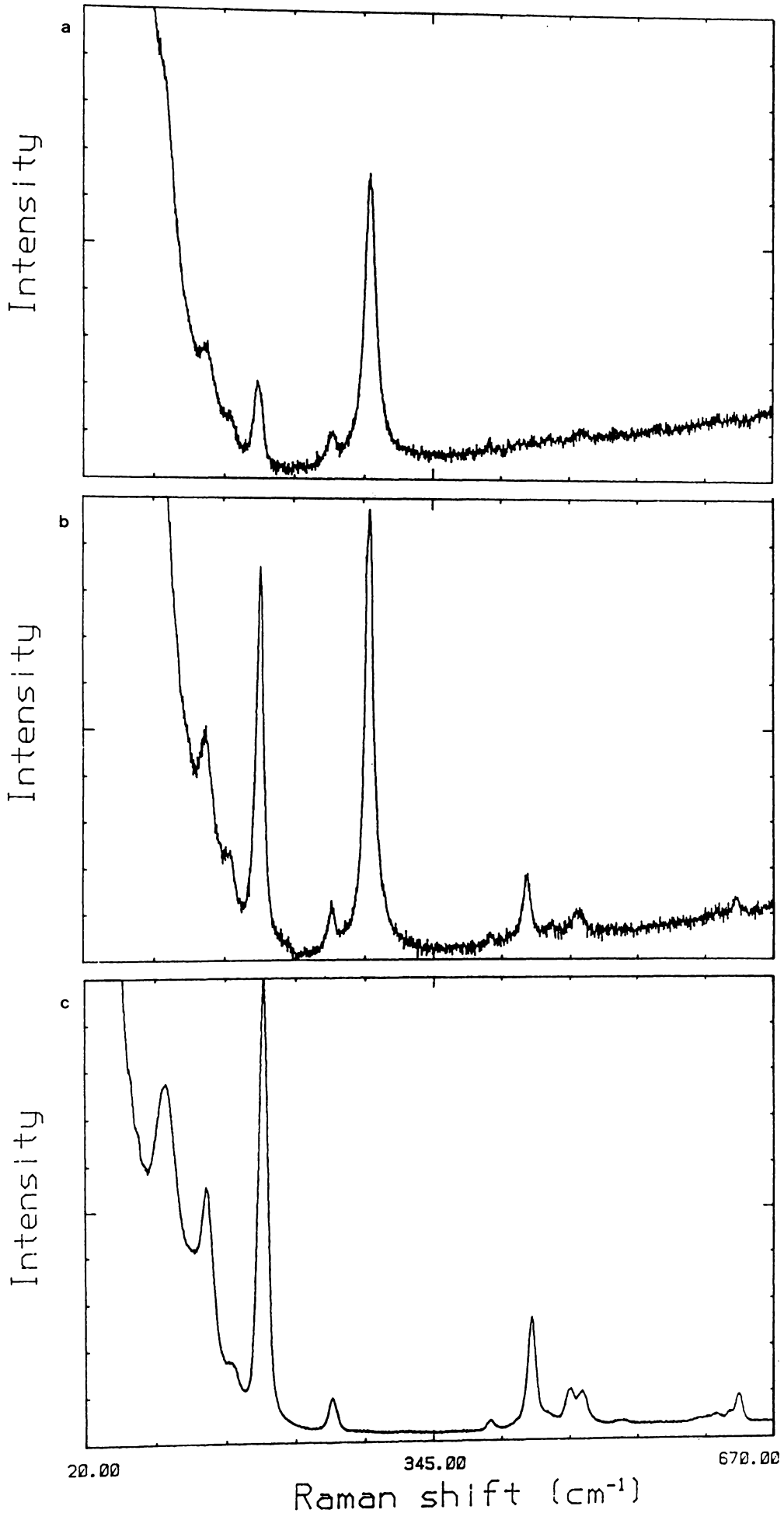

C.5 Raman vibrational spectra for $Sn[Fe_2(CO)_8]_2$ in the low frequency region, a) in CH_2Cl_2 using a polarising filter, b) in CH_2Cl_2, c) as a crystalline solid

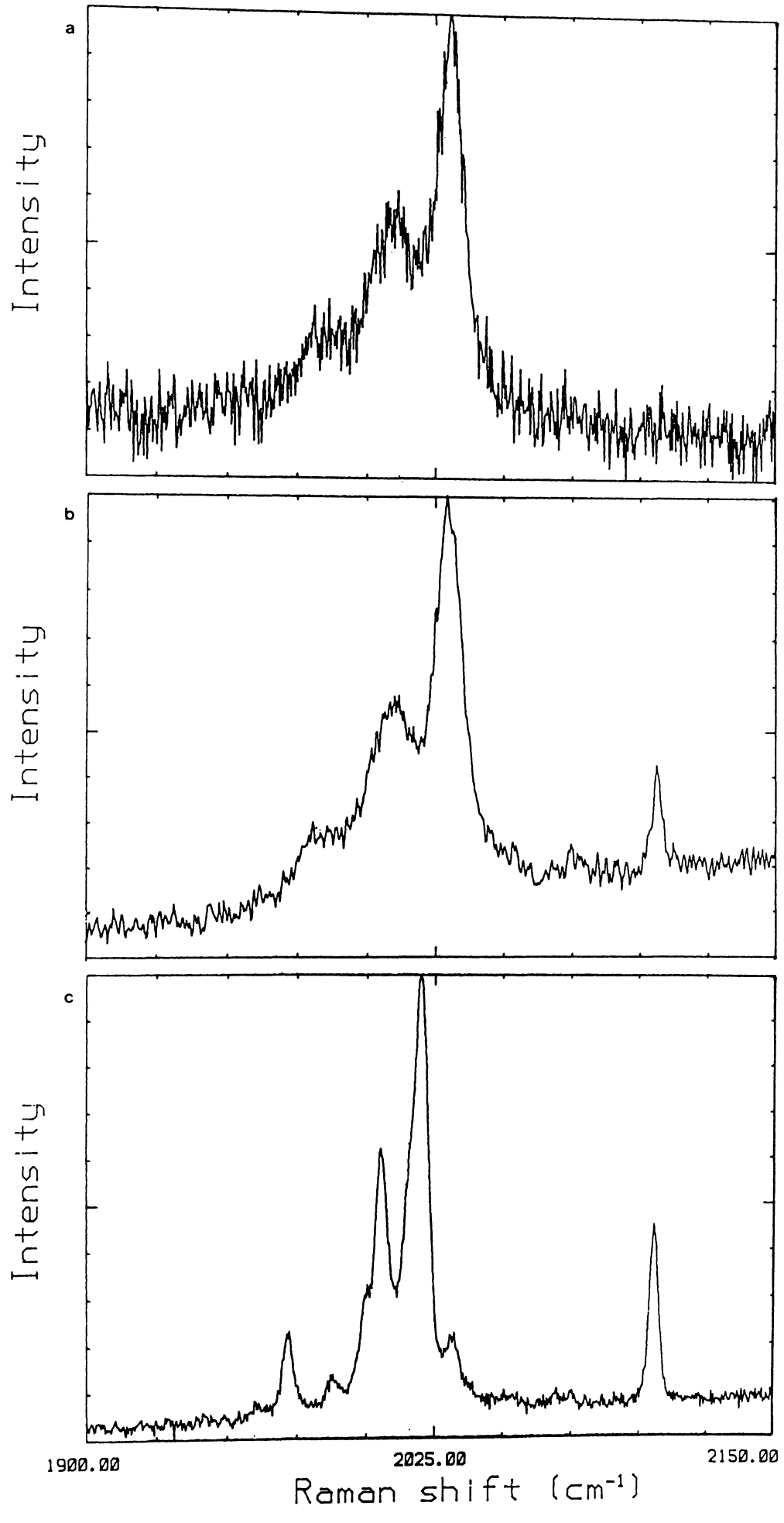

C.6 Raman vibrational spectra for $Sn[Fe_2(CO)_8]_2$ in the carbonyl stretching region, **a)** in CH_2Cl_2 using a polarising filter, **b)** in CH_2Cl_2, **c)** as a crystalline solid

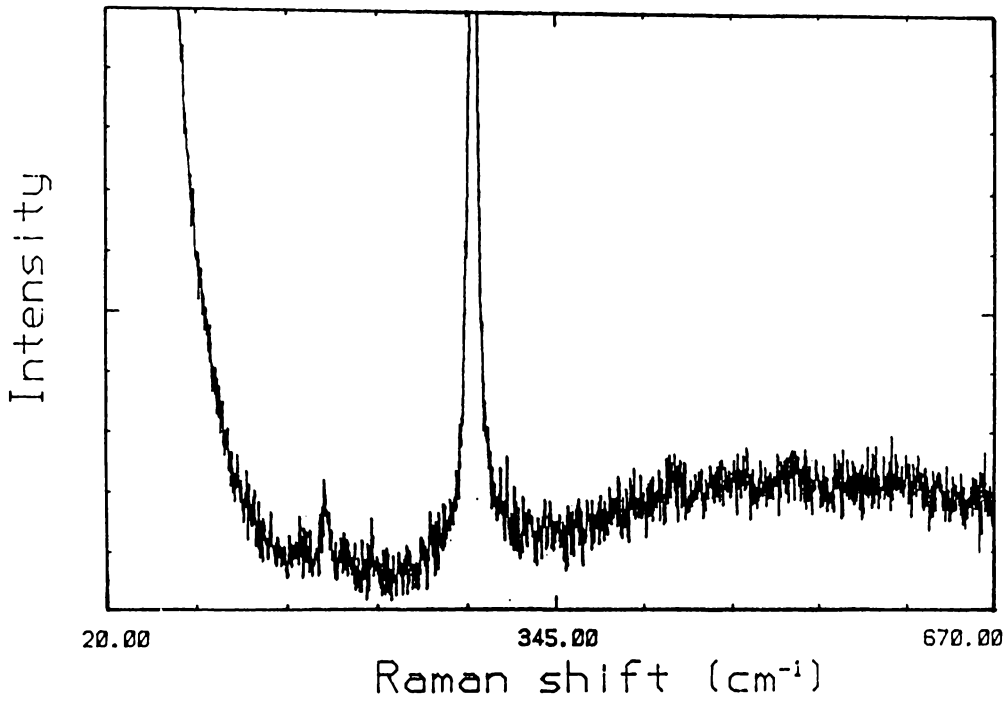

C.7 Raman vibrational spectra for $Pb[Fe_2(CO)_8]_2$ in CH_2Cl_2, in the low frequency region

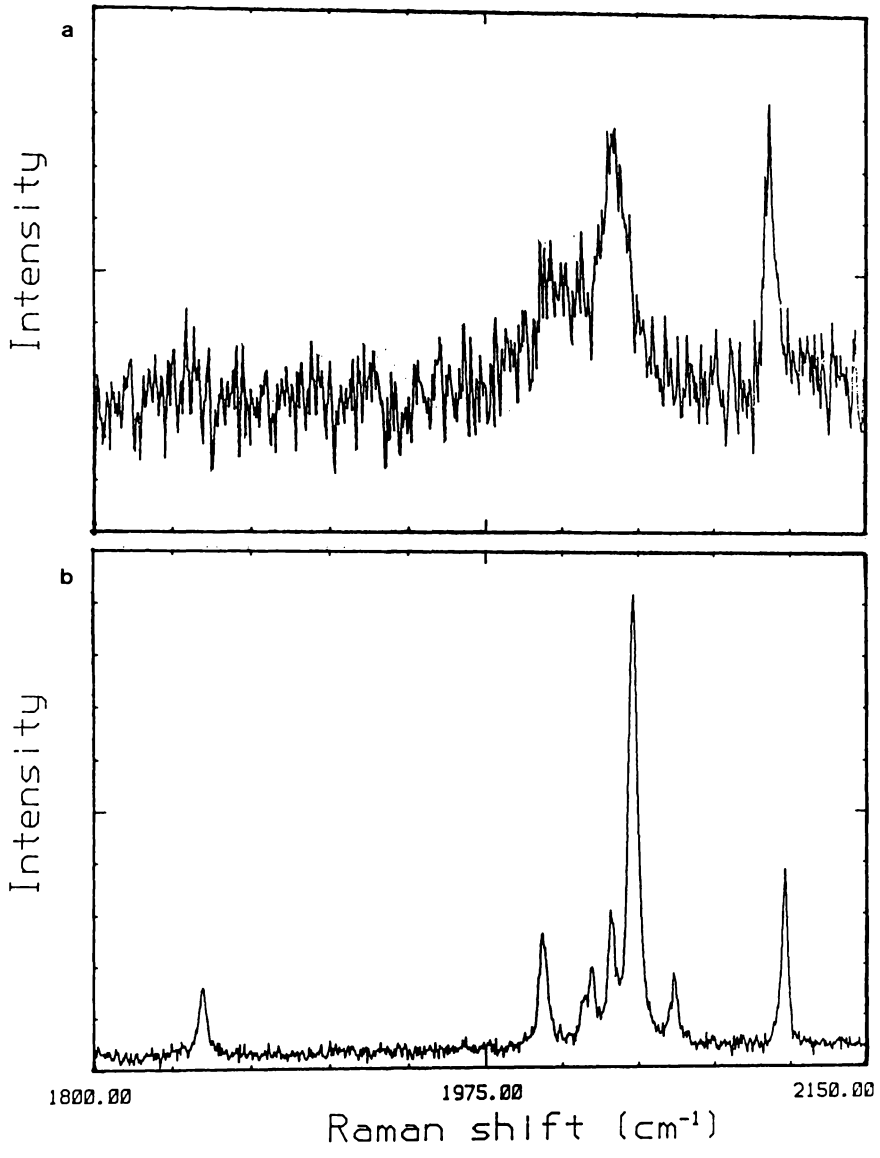

C.8 Raman vibrational spectra for $Si[Co_2(CO)_7]_2$ in the carbonyl stretching region, **a)** in CH_2Cl_2, **b)** as a crystalline solid

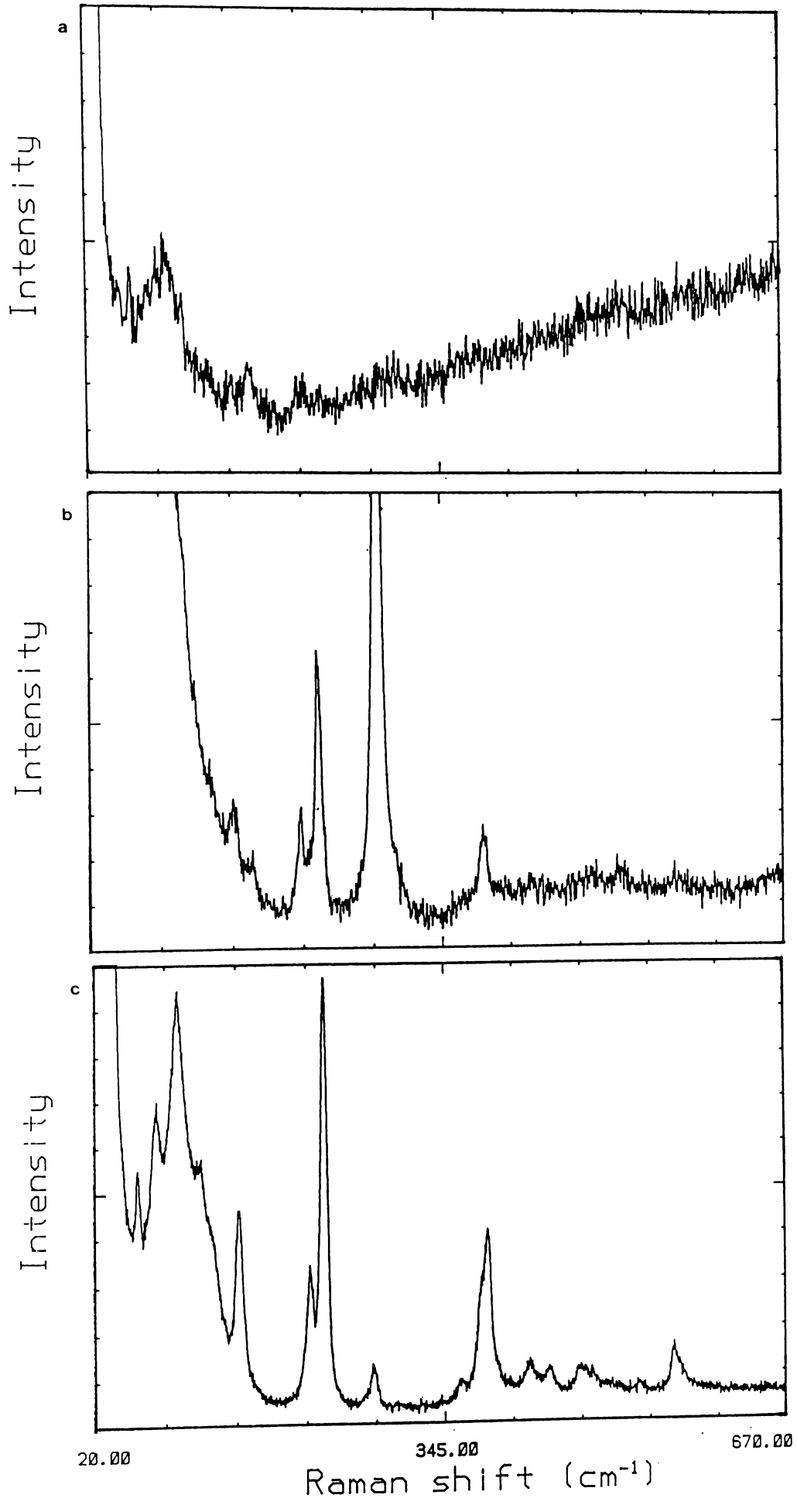

C.9 Raman vibrational spectra for $Si[Co_2(CO)_7]_2$ in the low frequency region, a) in CH_2Cl_2 using a polarising filter, b) in CH_2Cl_2, c) as a crystalline solid

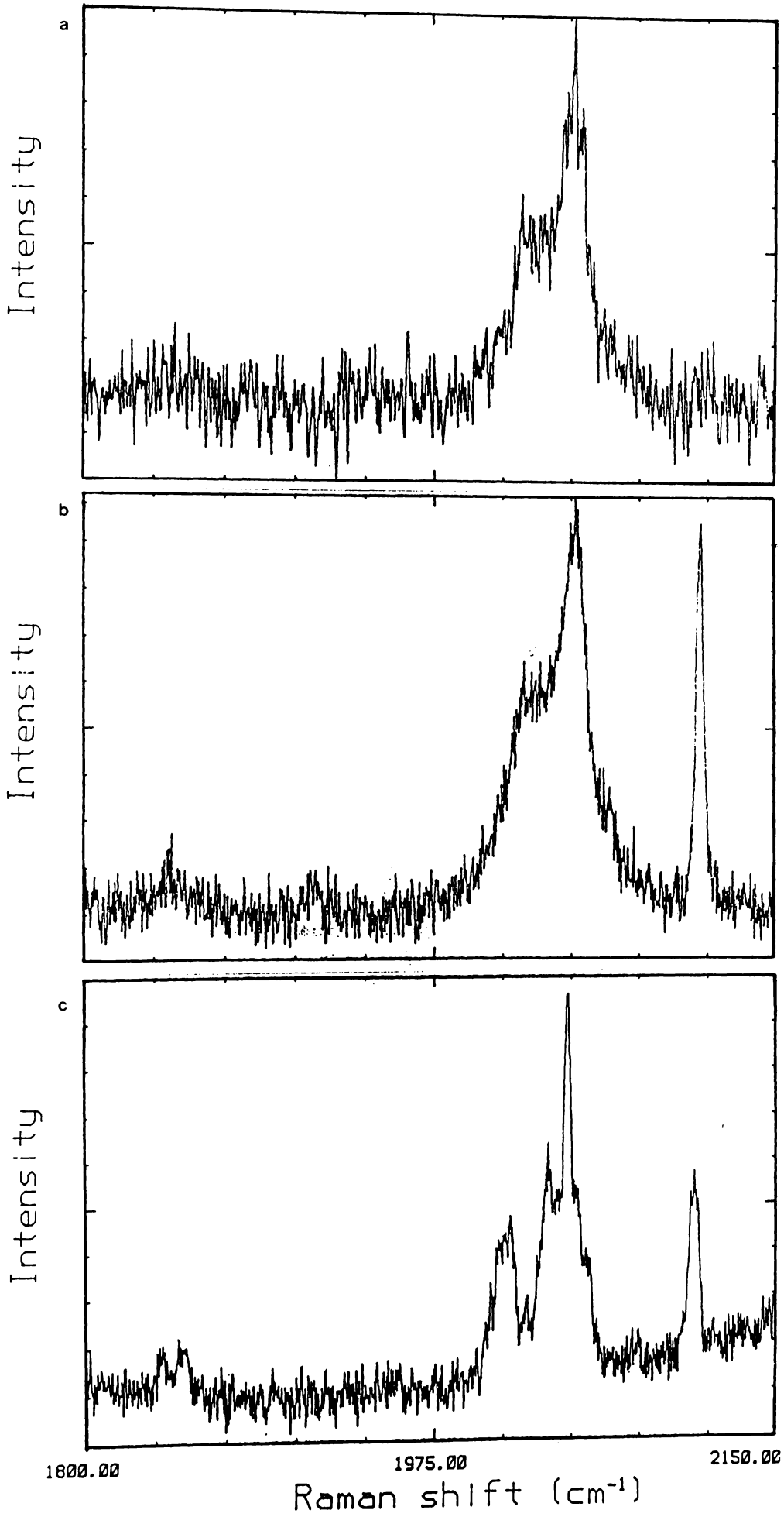

C.10 Raman vibrational spectra for $Ge[Co_2(CO)_7]_2$ in the carbonyl stretching region, **a**) in CH_2Cl_2 using a polarising filter, b) in CH_2Cl_2, c) as a crystalline solid

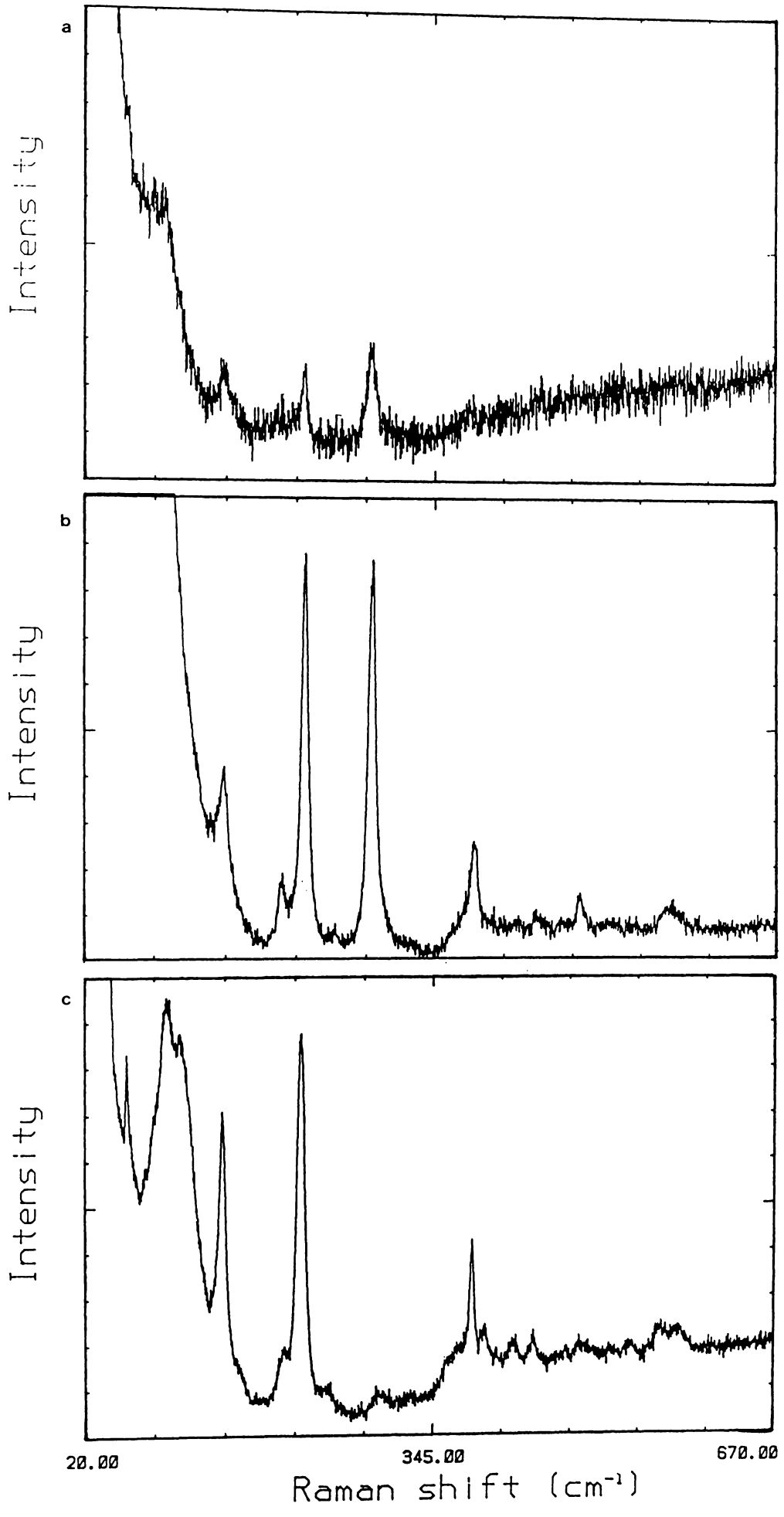

C.11 Raman vibrational spectra for $Ge[Co_2(CO)_7]_2$ in the low frequency region, **a)** in CH_2Cl_2 using a polarising filter, **b)** in CH_2Cl_2, **c)** as a crystalline solid

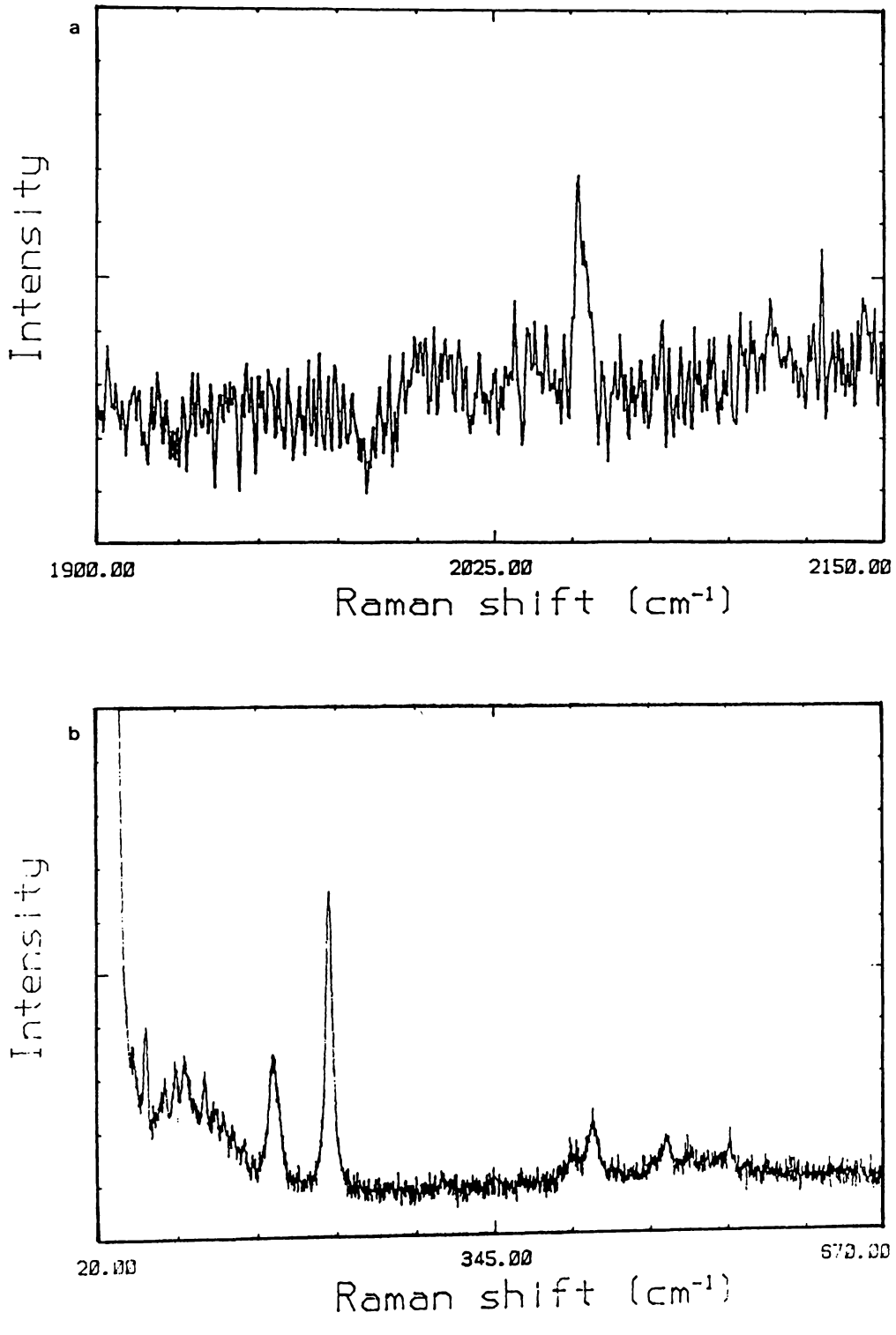

C.12 Raman vibrational spectra for $(CO)_4CoSiCo_3(CO)_9$ as a crystalline solid, a) in the carbonyl stretching region, b) in the low frequency region

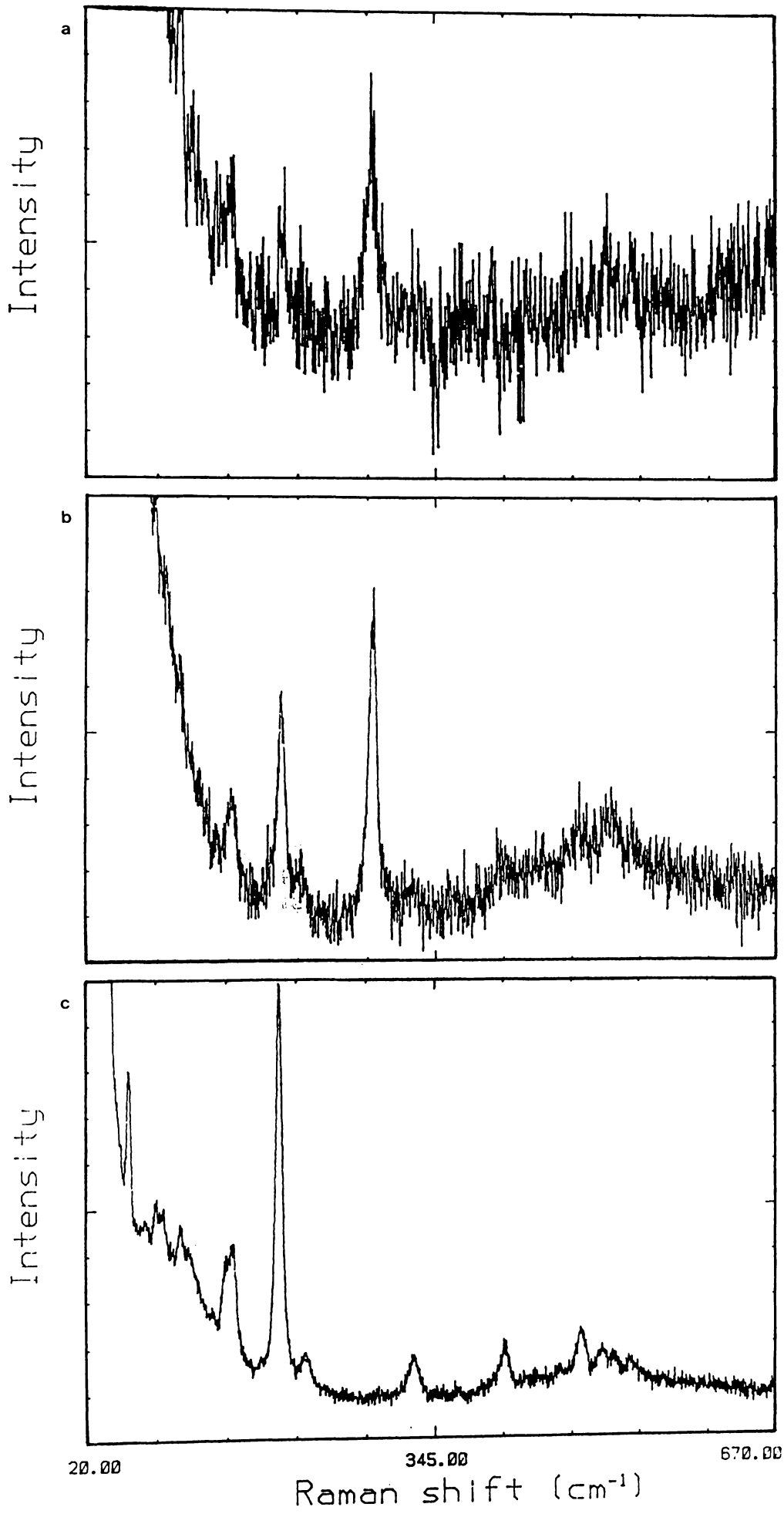

C.13 Raman vibrational spectra for $(CO)_4CoGeCo_3(CO)_9$ in the low frequency region, **a)** in CH_2Cl_2 using a polarising filter, b) in CH_2Cl_2, c) as a crystalline solid

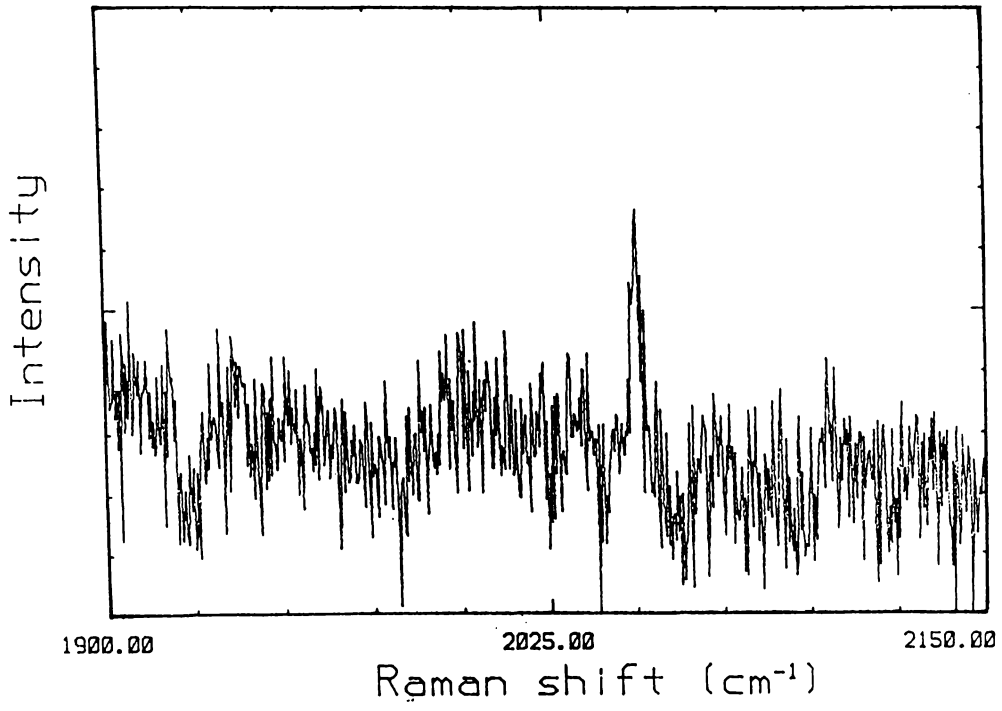

C.14 Solid-state Raman vibrational spectra for $(CO)_4CoGeCo_3(CO)_9$ in the carbonyl stretching region

References

REFERENCES

1 B.K. Nicholson, K.M. Mackay and R.F. Gerlach, Rev. of Silicon, Germanium and Tin Cpds. 5 (1981) 67.
2 'M.T.P.' Int. Rev. of Science, Inorg. Chem. Series One, Butterworths London, (1972) 6 64.
3 J.N. Nicholls, Polyhedron 3 (1984) 1307.
4 K.M. Mackay and B.K. Nicholson, Comprehensive Organometallic Chemistry 6, Ch 43, 1043.
5 H. Vahrenkamp, Adv. Organomet. Chem. 22 (1983) 169.
6 D.F. Shriver and C.B. Cooper, Adv. Infrared and Raman Spec. 6 127.
7 S.D. Wijeyesekera and R. Hoffman, Organometallics 3 (1984) 949.
8 S.D. Wijeyesekera, R. Hoffman and C.N. Wilker, Organometallics 3 (1984) 962.
9 V.G. Albano P. Chini, G. Ciani, M. Sansoni, D. Strumolo, B.T. Heaton and S. Martinengo, J. Amer. Chem. Soc. 98 (1976) 5027.
10 J.S. Bradley, Adv. Organomet. Chem. 22 (1983) 1, and references therein.
11 W.A. Herrmann, Angew. Chem., Int. Ed. Engl. 25 (1986) 56.
12 M. Tachikawa and E.L. Muetterties, Prog. Inorg. Chem. 28 (1981) 203.
13 M.D. Vargas and J.N. Nicholls, Adv. Inorg. Chem. and Radiochem. 30 (1986) 123.
14 K. Wade, Adv. Inorg. Chem. Radiochem. 18 (1976) 1.
15 D.M.P. Mingos and M.I. Forsyth, J. Chem. Soc. Dalton Trans. (1977) 610.
16 J.W. Lauher J. Amer. Chem. Soc. 100 (1978) 5305.
17 G. Schmid, Angew. Chem., Int. Ed. Engl. 17 (1978) 392.
18 K.H. Whitmire, J. Coord. Chem. 17 (1988) 95 (and references therein).
19 J.A. Hriljac, E.M. Holt and D.F. Shriver, Inorg. Chem. 26 (1987) 2943.
20 M.H. Chrisholm, K. Folting, J.C. Huffman, J. Leonelli, N.S. Marchant, C.A. Smith and L.C.E. Taylor, J. Am. Chem. Soc. 107 (1985) 3722.
21 T. Beringhelli, G. Ciani, G. D'Alfonso, A. Sironi and M. Freni, J. Chem. Soc. Chem. Comm. (1985) 979.
22 D.L. Davies, J.C. Jeffery, D. Miguel, P. Sherwood and F.G.A. Stone, J. Chem. Soc. Chem. Comm. (1987) 454.
23 G. Schmid, V. Batzel and G. Etzrodt, J. Organomet. Chem. 112 (1976) 345.
24 W. Malisch, H.U. Wekel, I. Grob, F.H. Kohler and M. Baudler, Z. Naturforsch. B. 37 (1982) 601.
25 S.D. Anema, D.Phil. Thesis, University of Waikato, 1989.
26 R. Boese and G. Schmid, J. Chem. Soc. Chem. Comm. (1979) 349.
27 P. Gusbeth and H. Vahrenkamp, Chem. Ber. 118 (1985) 1758.
28 J.A. Christie, D.N. Duffy, K.M. Mackay and B.K. Nicholson, J. Organomet. Chem. 226 (1982) 165.
29 P. Gusbeth and H. Vahrenkamp, Chem. Ber. 118 (1985) 1746.
30 P. Gusbeth and H. Vahrenkamp, Chem. Ber. 118 (1985) 1770.
31 K.H. Whitmire, C.B. Lagrone, M.R. Churchill, J.C. Fettinger and B.H. Robinson, Inorg. Chem. 26 (1987) 3491.
32 D.N. Duffy, K.M. Mackay, B.K. Nicholson and R.A. Thompson, J. Chem. Soc. Dalton Trans. (1982) 1029.
33 G.C. Barris, M.Sc. Thesis, University of Waikato, 1986.
34 S.G. Anema, K.M. Mackay, B.K. Nicholson and M. Van Tiel, Organometallics, in print.
35 H.J. Haupt and U. Florke, Acta. Cryst. C44 (1988) 472.
36 T.J. McNeese, S.S. Wrenford, D.L. Tipton and R. Bau, J. Chem. Soc. Chem. Comm. (1977) 390.
37 H.J. Haupt, U. Florke and A. Gotze, Z. Anorg. Allg. Chem. 557 (1988) 82.

38 S.G. Anema, G.C. Barris, K.M. Mackay, B.K. Nicholson, J. Organomet. Chem. 350 (1988) 207.
39 K.M. Mackay, B.K. Nicholson, A.W. Sims, C.C. Tan, Acta. Cryst. C43 (1987) 633.
40 A.S. Batsanov, L.V. Rybin, M.I. Rybinskaya and Yu.T. Struchkov, J. Organomet. Chem. 249 (1983) 319.
41 D. Melzer and E. Weiss, J. Organomet. Chem. 255 (1983) 335.
42 R.F. Gerlach, K.M. Mackay, B.K. Nicholson and W.T. Robinson, J. Chem. Soc. Dalton Trans. (1981) 80.
43 S.P. Foster, D.Phil. Thesis, University of Waikato, 1982.
44 S.K. Lee, D.Phil. Thesis, University of Waikato, 1989.
45 S.G. Anema, K.M. Mackay, L.C. McLeod, B.K. Nicholson and J.M. Whittaker, Angew. Chem., Int. Ed. Engl. 25 (1986) 759.
46 S.G. Anema, K.M. Mackay and B.K. Nicholson, Inorg. Chem. 28 (1989) 3158.
47 S.G. Anema, J.A. Audett, K.M. Mackay and B.K. Nicholson, J. Chem. Soc. Dalton Trans. (1988) 2629.
48 P.F. Lindley and P. Woodward, J. Chem. Soc. (A) (1967) 382.
49 C.B. Lagrone, K.H. Whitmire, M.R. Churchill and J.C. Fettinger, Inorg. Chem. 25 (1986) 2080.
50 T.J. McNeese and S.S. Wrenford, J. Chem. Soc. Chem. Comm. (1977) 390.
51 B.J. Aylett and M.T. Taghipour, J. Organomet. Chem. 249 (1983) 55.
52 R.F. Gerlach, D.Phil. Thesis, University of Waikato, 1978.
53 D.J. Patmore and W.A.G. Graham, Inorg. Chem. 7 (1968) 771.
54 R.M. Sweet, C.J. Fritchie and R.A. Schunn, Inorg. Chem. 6 (1967) 749.
55 G. Schmid and G. Etzrodt, J. Organomet. Chem. 131 (1977) 477.
56 B.R. Penfolds and B.H. Robinson, Acc. Chem. Res. 6 (1973) 73.
57 P.Gusbeth and H. Vahrenkamp, Chem. Ber. 118 (1985) 1746.
58 P.Gusbeth and H. Vahrenkamp, Chem. Ber. 118 (1985) 1758.
59 P.Gusbeth and H. Vahrenkamp, Chem. Ber. 118 (1985) 1770.
60 H. Vahrenkamp, Adv. Organomet. Chem. 22 (1983) 169.
61 D.N. Duffy, K.M. Mackay, B.K. Nicholson and W.T. Robinson, J. Chem. Soc. Dalton Trans. (1981) 381.
62 R.H. Summerville and R. Hoffmann, J. Am. Chem. Soc. 101 (1979) 3821.
63 C.C. Ngo, M.Sc. Thesis, University of Waikato, 1982.
64 A.W. Sims, M.Sc. Thesis, University of Waikato, 1984.
65 J.M. Whittaker, M.Sc. Thesis, University of Waikato, 1986.
66 A. Gourdon and Y. Jeanin, J. Organomet. Chem. 209 (1985) 199
67 C.G. Cooke and M.J. Mays, J. Organomet. Chem. 88 (1975) 231.
68 P.L. Bagdon, M. Sabat, S.A. Sunshine, C. Woodcock and D.F. Shriver, Inorg. Chem. 27 (1988) 1904.
69 V.E. Lopatin, S.P.Gubin, N.M. Mikova, M.Ts. Tsybenov, Yu.L. Slovokhotov and Yu.T. Struchkov, J. Organomet. Chem. 292 (1985) 275.
70 M. Tachikawa, A.C. Sievert, E.L. Muetteries, M.R. Thompson, C.S. Day and V.W. Day, J. Amer. Chem. Soc. 102 (1980) 1725.
71 D.H. Farrar, P.F. Jackson, B.F.G. Johnson, J. Lewis, J.N. Nicholls and M. McPartlin, J. Chem. Soc. Chem. Comm. (1981) 415.
72 B.F.G. Johnson, J. Lewis, W.J.H. Nelson, J.N. Nicholls, J. Puga, P.R. Raithby, M.J. Rosales, M. Schroder and M.D. Vargas, J. Chem. Soc. Dalton Trans. (1983) 2447.
73 B.F.G. Johnson, J. Lewis, J.N. Nicholls, J. Puga, P.R. Raithby, M.J. Rosales, M. McPartlin and W. Clegg, J. Chem. Soc. Dalton Trans. (1983) 277.
74 K. Henrick, B.F.G. Johnson, J. Lewis, J. Mace, M. McPartlin and J. Morris, J. Chem. Soc. Chem. Comm. (1985) 1617.
75 S.L. Cook, J. Evans, L.R. Gray and M. Webster, J. Chem. Soc. Dalton Trans. (1986) 2149.

76 J. Evans, B.P. Gracey, L.R. Gray and M. Webster, J. Organomet. Chem. 240 (1982) C61.

77 A.G. Cowie, B.F.G. Johnson, J. Lewis, J.N. Nicholls, P.R. Raithby and M.J. Rosales, J. Chem. Soc. Dalton Trans.(1983) 2311.

78 M.I. Bruce, B.W. Skelton, A.H. White and M.L. Williams, J. Chem. Soc. Chem. Comm. (1985) 744.

79 P.F. Jackson, B.F.G. Johnson, J. Lewis, J.N. Nicholls, M. McPartlin and W.J.H. Nelson, J. Chem. Soc. Chem. Comm. (1980) 546.

80 C.R. Eady, J.M. Fernandez, B.F.G. Johnson, J. Lewis, P.R. Raithby and G.M. Sheldrick, J. Chem. Soc. Chem. Comm. (1978) 421.

81 J.S. Bradley, E.W. Hill, G.B. Ansell and M.A. Modrick, Organometallics 1 (1982) 1634.

82 B.F.G. Johnson, D.A. Kaner, J. Lewis and P.R. Raithby J. Organomet. Chem. 231 (1982) C59.

83 B.F.G. Johnson, J. Lewis, J.N. Nicholls, J. Puga and K.H. Whitmire, J. Chem. Soc. Dalton Trans. (1983) 787.

84 A.G. Cowie, B.F.G. Johnson, J. Lewis, P.R. Raithby and A.G. Swanson, J. Chem. Soc. Chem. Comm. (1984) 637.

85 A.G. Cowie, B.F.G. Johnson, J. Lewis and P.R. Raithby, J. Chem. Soc. Chem. Comm. (1984) 1711.

86 B.F.G. Johnson, J. Lewis, P.R. Raithby, M.J. Rosales and D.A. Welch, J. Chem. Soc. Dalton Trans. (1986) 453.

87 D. Braga, B.F.G. Johnson, J. Lewis, M. McPartlin, W.J.H. Nelson, J.N. Nicholls and M.D. Vargas, J. Chem. Soc. Chem. Comm. (1982) 966.

88 P.F. Jackson, B.F.G. Johnson, J. Lewis, W.J.H. Nelson and M. McPartlin, J. Chem. Soc. Dalton Trans. (1982) 2099.

89 J.M. Fernandez, B.F.G. Johnson, J. Lewis and P.R. Raithby, J. Chem. Soc. Dalton Trans. (1981) 2250.

90 M. Van Tiel, K.M. Mackay and B.K. Nicholson, J. Organomet. Chem. 326 (1987) C101.

91 S.P. Foster, K.M. Mackay and B.K. Nicholson, Inorg. Chem. 24 (1985) 909.

92 R.A. Croft, D.N. Duffy and B.K. Nicholson, J. Chem. Soc. Dalton Trans. (1982) 1023.

93 D.N. Duffy, D.Phil. Thesis, University of Waikato, 1981.

94 G. Ciani, G. D'Alfonso, P. Romiti, A. Sironi and M. Freni, J. Organomet. Chem. 224 (1983) C27.

95 T. Beringhelli, G. D'Alfonso and M. De Angelis J. Organomet. Chem. 322 (1987) C21.

96 T. Beringhelli, G. D'Alfonso, G. Ciani, A. Sironi and H. Molinari, J. Chem. Soc. Dalton Trans. (1988) 1281.

97 T.J. Henly, J.R. Shapley and A.L. Rheingold, J. Organomet. Chem. 310 (1986) 55.

98 T.J. Henly, J.R. Shapley, A.L. Rheingold and S.J. Geib, Organometallics 7 (1988) 441.

99 G. Ciani, G. D'Alfonso, M. Freni, P. Romiti and A. Sironi, J. Chem. Soc. Chem. Comm. (1982) 705.

100 M.R. Churchill and J. Wormald, J. Chem. Soc. Dalton Trans. (1974) 2410.

101 A. Gourdon and Y. Jeannin, J. Organomet. Chem. 282 (1985) C39.

102 R.D. Adams, P. Mathur and B.E. Segmuller, Organometallics 2 (1983) 1048.

103 B.F.G. Johnson, D.A. Kaner, J. Lewis and M.J. Rosales, J. Organomet. Chem. 238 (1982) C73.

104 B.F.G. Johnson, D.A. Kaner, J. Lewis and M. Rosales, J. Organomet. Chem. 238 (1982) C73.

105 S.R. Bunkhall, H.D. Holden, B.F.G. Johnson, J. Lewis, G.N. Pain, P.R. Raithby and M.J. Taylor, J. Chem. Soc. Chem. Comm. (1984) 25.

106 Yu.L. Slovokhotov, Yu.T. Struchkov, V.E. Lapatin and S.P. Gubin, J. Organomet. Chem. 266 (1984) 139.
107 B.F.G. Johnson J. Lewis, W.J.H. Nelson, J. Puga, P.R. Raithby, D. Braga, M. McPartlin and W. Clegg, J. Organomet. Chem. 243 (1983) C13.
108 B.F.G. Johnson, J. Lewis, W.J.H. Nelson, J. Puga, M. McPartlin and A. Sironi, J. Organomet. Chem. 253 (1983) C5.
109 S.C. Brown, J. Evans and M. Webster, J. Chem. Soc. Dalton Trans. (1981) 2263.
110 M.P. Gomez-Sal, B.F.G. Johnson, J. Lewis, P.R. Raithby and A.H. Wright, J. Chem. Soc. Chem. Comm. (1985) 1682.
111 B.F.G. Johnson, J. Lewis, S.W. Sanky, K. Won, M. McPartlin and W.J.H. Nelson, J. Organomet. Chem. 191 (1980) C3.
112 P.F. Jackson, B.F.G. Johnson, J. Lewis, M. McPartlin and W.J.H. Nelson, J. Chem. Soc. Chem. Comm. (1980) 224.
113 P.F. Jackson, B.F.G. Johnson, J. Lewis, M. McPartlin and W.J.H. Nelson, J. Chem. Soc. Chem. Comm. (1982) 49.
114 B.F.G. Johnson, J. Lewis, W.J.H. Nelson and J. Puga, J. Organomet. Chem. 266 (1984) 173.
115 S.R. Drake, K. Henrick, B.F.G. Johnson, J. Lewis, M. McPartlin and J. Morris, J. Chem. Soc. Chem. Comm. (1986) 928.
116 B.F.G. Johnson, J. Lewis, W.J.H. Nelson, M.D. Vargas, D. Braga and M. McPartlin, J. Organomet. Chem. 246 (1983) C69.
117 V. Dearing, S.R. Drake, B.F.G. Johnson, J. Lewis, M. McPartlin and H.R. Powell, J. Chem. Soc. Chem. Comm. (1988) 1331.
118 V.G. Albano, D. Braga and S. Martinengo, J. Chem. Soc. Dalton Trans. (1986) 981.
119 S. Bordoni, B.T. Heaton, C. Seregni, L. Strona, R.J. Goodfellow, M.B.Hursthouse, M. Thornton-Pett and S. Martinengo, J. Chem. Soc. Dalton Trans. (1988) 249.
120 A. Fumagalli, S. Martinengo, V.G. Albano, D. Braga, F. Grepioni, J. Chem. Soc. Dalton Trans. (1989) 2343.
121 V.G. Albano, D. Braga, F. Grepioni, R.D. Pergola, L. Garlaschelli and A. Fumagalli, J. Chem. Soc. Dalton Trans. (1989) 879.
122 S. Martinengo, D. Strumolo, P. Chini, V.G. Albano and D. Braga, J. Chem. Soc. Chem. Comm. (1985) 35.
123 G. Ciani, G. D'Alfonso, M.Freni, P. Romiti and A. Sironi, J. Chem. Soc. Chem. Comm. (1982) 705.
124 A. Fumagalli, S. Martinengo, V.G. Albano and D. Braga, J. Chem. Soc. Dalton Trans. (1988) 1273.
125 V.G. Albano, D. Braga, S. Martinengo, P. Chini, M. Sansoni and D. Strumolo, J. Chem. Soc. Dalton Trans. (1980) 52.
126 D. Braga, K. Henrick, B.F.G. Johnson, J. Lewis, M. McPartlin, W.J.H. Nelson, A. Sironi and M.D. Vargas, J. Chem. Soc. Chem. Comm. 20 (1983) 1131.
127 G. Ciani and A. Sironi, J. Organomet. Chem. 241 (1983) 385.
128 V.G. Albano, M. Sansoni, P. Chini, S. Martinengo and D. Strumolo, J. Chem. Soc. Dalton Trans. (1976) 970.
129 A. Ceriotti, G. Longoni, M. Manassero, N. Masciocchi, L. Resconi and M. Sansoni, J. Chem. Soc. Chem. Comm. (1985) 181.
130 A. Ceriotti, G. Longoni, M. Manassero, M. Perego and M. Sansoni, Inorg. Chem. 24 (1985) 117.
131 A. Ceriotti, R.D. Pergola, G. Longoni, M. Manassero and M. Sansoni, J. Chem. Soc. Dalton Trans. (1984) 1181.
132 K.M. Mackay, B.K. Nicholson and A.W. Sims, J. Chem. Soc. Chem. Comm. (1984) 1276.
133 A. Ceriotti, F. Demartin, B.T. Heaton, P. Ingallina, G. Longoni, M. Manassero, M. Marchionna and N. Masciocchi, J. Chem. Soc. Chem. Comm. (1989) 787.

134 D.M.P. Mingos and L. Zheniang, J. Organomet. Chem. 341 (1988) 523.
135 J.L. Vidal and J.M. Troup, J. Organomet. Chem. 213 (1981) 351.
136 A. Fumagalli, S. Martinengo and G. Ciani, J. Chem. Soc. Chem. Comm. (1983) 1381.
137 J.A.K. Howard, J.L. Spencer and D.G. Turner, J. Chem. Soc. Dalton Trans. (1987) 259.
138 M.Y. Darensbourg, Prog. Inorg. Chem. 33 (1985) 221 (and references therein)
139 C.P. Horwitz and D.F. Shriver, Adv. Organomet. Chem. 23 (1984) 219.
140 G. Fachinetti, C. Floriani, P. Francesco-Zanazzi and A.R. Zanzari, Inorg. Chem. 17 (1978) 3002.
141 W.F. Edgell and J. Lyford, J. Am. Chem. Soc. 93 (1971) 6407.
142 D.P. Schussler, W.R. Robinson and W.F. Edgell, Inorg. Chem. 13 (1974) 153.
143 J.M. Burtlich, J. Am. Chem. Soc. 91 (1969) 4562.
144 R.E. Dessy, R.L. Pohl and R.B. King, J. Am. Chem. Soc. 88 (1966) 5121.
145 D.F. Shriver, J. Organomet. Chem. 94 (1975) 259.
146 M.Y. Darensbourg, D.J. Darensbourg and H.L.C. Barros, Inorg. Chem. 17 (1978) 297.
147 CRC. Handbook of Chemistry and Physics, 64th Ed.
148 W.F. Edgell, J. Lyford, A. Barbetta and C.I. Jose, J. Am. Chem. Soc. 93 (1971) 6403.
149 A. Alvanipour, H. Zhang and J.L. Atwood, J. Organomet. Chem. 358 (1988) 295.
150 M.Y. Darensbourg and J.M. Hankel, Organometallics 1 (1982) 82.
151 R.A. Thomson, M.Sc. Thesis, University of Waikato, 1981.
152 T. Beringhelli, G. D'Alfonso, M. Freni, G. Ciani and A. Sironi, J. Organomet. Chem. 295 C7 (1985)
153 M.Y. Darensbourg, Prog. Inorg. Chem. 33 (1985) 221.
154 J.F. Halet, R. Hoffman and J.Y. Saillard, Inorg. Chem. 24 (1985) 1695.
155 J.D. Smith and J.D. Corbett, J. Am. Chem. Soc. 108 (1986) 1927.
156 M.I. Bruce and M.J. Lidell, App. Organomet. Chem. 1 (1987) 191.
157 W.L. Jolly and J.E. Drake, Inorg. Syn. 7 (1963) 34.
158 J.K. Ruff and W.J. Schlientz, Inorg. Syn. 15 (1974) 84.
159 W.F. Edgell, Adv. Organomet. Chem. 2 (1964) 157.
160 P.S. Braterman and A.E. Leslie, J. Organomet. Chem. 238 (1982) 307.
161 J.M. Burtlich, R.B. Petersen, H.L. Condor and W.R. Robinson, J. Am. Chem. Soc. 92 (1970) 1783.
162 J.E. Ellis and E. Flom, J. Organomet. Chem. 99 (1975) 263.
163 R.G. Finke and T.N. Sorrell, Org. Syn. 59 102 (1979).
164 K. Famery, M. Kilner, R. Greatrex and N.N. Greenwood, J. Organomet. Chem. 206 (1981) C17.
165 H. Strong, P.J. Krusic and J. San Filippo, Inorg. Syn. 45 157.
166 R.B. King Organomet. Syn. 1 165 (1965).
167 D.N. Duffy, M.Sc. Thesis, University of Waikato, 1978.
168 G.J. Kubas, Inorg. Syn. 19 90 (1979).
169 A.N. Nesmeyanov, E.G. Perevalova, Yu.T. Struchkov, M.Yu. Antipin, K.I. Grandberg and V.P. Dyadchenko, J. Organomet. Chem. 201 (1980) 343.
170 R.S. Dickson, B.J. Dobney and F.W. Eastwood, J. Chem. Ed. 64 (1987) 898.
171 R.B. King, Organomet. Syn. 1 (1965) 70.
172 E.C. Johnson, T.J. Meyer and N. Winterton, Inorg. Chem. 10 (1971) 1673.
173 J.R. Wilkinson and L.J. Todd, J. Organomet. Chem. 118 (1976) 199.
174 J.D. Cotton, S.A.R. Knox, I. Paul and F.G.A. Stone, J. Chem. Soc. (A) (1967) 265.
175 S. Alvarez, M. Ferrer, R. Reina, O. Rossell and M. Seco, J. Organomet. Chem. 377 (1989) 291.

176 P.A. Dawson, B.M. Peake, B.H. Robinson and J. Simpson, J. Am. Chem. Soc. 19 (1980) 465.
177 J.D. Cotton, S.A.R. Knox, I. Paul and F.G.A. Stone, J. Chem. Soc. (A) (1967) 264.
178 W. Beck, J. Organomet. Chem. 10 (1967) 307.
179 G. Schmid and G. Etzrodt, J. Organomet. Chem. 137 (1977) 367.
180 V.G. Albano, D. Braga, P. Chini, G. Ciani and S. Martinengo, J. Chem. Soc. Dalton Trans. (1982) 645.
181 G. Schmid and G. Etzrodt, J. Organomet. Chem. 131 (1977) 477.
182 J.D. Cotton and R.M. Peachey, Inorg. Nucl. Chem. Lett. 6 (1970) 727.
183 D. Melzer and E. Weiss, J. Organomet. Chem. 255 (1983) 335.
184 O.V. Kuz'm, A.L. Bykoivets and V.M. Vdovin, Izv. Akad. Nauk. SSSR Ser. Khim. (1980) 1448.
185 G. Schmid and G. Etzrodt, J. Organomet. Chem. 112 (1976) 348.
186 G. Ciani, G. D'Alfonso, M. Freni, P. Romiti and A. Sironi, J. Chem. Soc. Chem. Comm. (1982) 339.
187 R.F. Gerlach, B.W.L. Graham and K.M. Mackay, J. Organomet. Chem. 118 (1976) C23.
188 A.N. Nesmeyanov, K.N. Anisimov, N.E. Kolabova and N.V. Khandozhoko, Invest. (Khim.) 2 (1971) 462.
189 A.N. Nesmeyanov, K.N. Anisimov, N.E. Kolabova and N.V. Khandozhoko, Zhur. Obshchei. Khim. 44 (1974) 313.
190 D.E. Fjare and W.L. Gladfelter, J. Am. Chem. Soc. 103 (1981) 1572.
191 A. Gourdon and Y. Jeannin, Organometallics 5 (1986) 2406.
192 P. Chini and V.G. Albano, J. Organomet. Chem. 15 (1968) 433.
193 G. Longoni, P. Chini, L.D. Lower and L.F.Dahl, J. Am. Chem. Soc. 97 (1975) 5034.
194 D.J. Darensbourg and M.J. Incorvia, Inorg. Chem. 20 (1981) 1911.
195 K. Bartl, R. Boese and G. Schmid, J. Organomet. Chem. 206 (1981) 331.
196 M.J. Went, C.P. Brock and D.F. Shriver, Organometallics 5 (1986) 755.
197 C.P. Horwitz and D.F. Shriver, Adv. Organomet. Chem 23 (1984) 219.
198 V.G. Albano, D. Braga, G. Longoni, S. Campanella, A. Ceriotti and P. Chini, J. Chem. Soc. Dalton Trans. (1980) 1820.
199 F. Klanberg, W.B. Askew and L.J. Guggenberger, Inorg. Chem. 7 (1968) 2265.
200 V. Batzel, U. Muller and R. Allmann, J. Organomet. Chem. 102 (1975) 109.
201 G. Schmid, V. Batzel and B. Stutte, J. Organomet. Chem. 113 (1976) 67.
202 M. Van Tiel, personal communication.
203 K. Famery, M. Kilner, R. Greatrex and N.N. Greenwood, J. Chem. Soc. (A) (1969) 2339.
204 B.M. Peake, B.H. Robinson, J. Simpson and D.J. Watson, Inorg. Chem. 16 (1977) 405.
205 D.A. Roberts and G.L. Geoffray, Comp. Organomet. Chem. 6 (1982) 40.
206 S. Martinengo, G. Ciani, A. Sironi, B.T. Heaton and J. Mason, J. Am. Chem. Soc. 101 (1979) 7095.
207 R.S. Dickson and P.J. Fraser, Adv. Organomet. Chem 12 (1974) 323.
208 P. McArdle and A.R. Manning, J. Chem. Soc. (A) (1971) 717.
209 T. Madach and H. Vahrenkamp, Chem. Ber. 113 (1980) 2675.
210 R. P. Stewart, U. Anders and W.A.G. Graham, J. Organomet. Chem. 32 (1971) C49.
211 B.K. Nicholson and J. Simpson J. Organomet. Chem. 155 (1978) 237.
212 W.M. Ingle, G. Preti and A.G. MacDiarmid, J. Chem. Soc. Chem. Comm. (1973) 497.
213 M.J. Bennett, W.A.G. Graham, R.A. Smith and R.P. Stewart, J. Am. Chem. Soc. 95 (1973) 1684.
214 W.L. Gladfelter, Adv. Organomet. Chem. 24 (1985) 41.
215 R.F. Gerlach, B.W.L. Graham and K.M. Mackay, J. Organomet. Chem. 118 (1976) C23.

216 J.E. Ellis and E.A. Flom, J. Organomet. Chem. 99 (1975) 263.
217 J.K. Ruff, Inorg. Chem. 7 (1968) 1818.
218 C.R. Eady, J.J. Guy, B.F.G. Johnson, J. Lewis, M.C. Malatesta and G.M. Sheldrick, J.Chem. Soc. Chem. Comm. (1976) 807.
219 C.R. Eady, B.F.G. Johnson and J. Lewis, J.Chem. Soc. Chem. Comm. (1976) 302.
220 M.R. Churchill and J. Wormald, J. Am. Chem. Soc. 93 (1971) 5670.
221 B.F.G. Johnson, R. Khattar, J. Lewis, G.L. Powell and M. McPartlin, J.Chem. Soc. Chem. Comm. (1986) 50.
222 B.T. Heaton, L. Strona, S. Martinengo, D. Strumolo, R.J. Goodfellow and I.H. Sadler, J. Chem. Soc. Dalton Trans. (1982) 1499.
223 A. Ceriotti, P. Chini, R. Della Pergola and G. Longoni, Inorg. Chem. 22 (1983) 1595.
224 D.E. Fjare and W.L. Gladfelter, Inorg. Chem. 20 (1981) 3533
225 D. Braga, K. Henrick, B.F.G. Johnson, M. McPartlin, W.J.H. Nelson and J. Puga, J.Chem. Soc. Chem. Comm. (1982) 1083.
226 P. Braunstein, J. Rose, A. Tiripicchio and M. Tiripicchio Carmellini, Angew. Chem. Int. Ed. Engl. 24 (1985) 767.
227 M. Fajardo, H.D. Holden, B.F.G. Johnson, J. Lewis and P.R. Raithby, J.Chem. Soc. Chem. Comm. (1981) 753.
228 S.R. Drake, B.F.G. Johnson, J. Lewis, M. McPartlin, K. Henrick and J. Morris, J.Chem. Soc. Chem. Comm. (1986) 928.
229 B.F.G. Johnson, J. Lewis, P.R. Raithby and M.D. Vargas, J.Chem. Soc. Chem. Comm. (1983) 608.
230 D.G. Evans and D.M.P. Mingos, J. Organomet. Chem. 232 (1982) 171.
231 J.W. Lauher and K. Wald, J. Am. Chem. Soc. 103 (1981) 7648.
232 M.I. Bruce and B.K. Nicholson, Organometallics 3 (1984) 101.
233 D.M.P. Mingos, Polyhedron 3 (1984) 1289.
234 R.A. Brice, S.C. Pearse, I.D. Salter and K. Henrick, J. Chem. Soc. Dalton Trans. (1986) 2181.
235 B.F.G. Johnson, J. Lewis, P.R. Raithby, S.N.A.B. Syed-Mustaffa, M.J. Taylor, K.H. Whitmire and W. Clegg, J. Chem. Soc. Dalton Trans. (1984) 2111.
236 M. Tachikawa, R.L. Geerts and E.L. Muetterties, J. Organomet. Chem. 213 (1981) 11.
237 L.J. Vidal, W.E. Walker and R.C. Shoering, Inorg. Chem. 20 (1981) 238.
238 G. Ciani, L. Gorlaschelli and A. Sironi, J. Chem. Soc. Chem. Comm. (1981) 563.
239 L.M. Bower and M.B.H. Stiddard, J. Chem. Soc. (A) (1968) 706.
240 E.O. Fischer and E. Moser, Inorg. Syn. 12 35 (1970).
241 W.P. Giering and M. Rosenblum, J. Chem. Soc. Chem. Comm. (1971) 441.
242 D.L. Reger, C.J. Coleman and P.J. M^{c}Elligott, J. Organomet. Chem. 171 (1979) 73.
243 E. Sappa, M. Lanfranchi, A. Tiripicchio and M. Tiripicchio Camellini, J. Chem. Soc. Chem. Comm. (1981) 995.
244 D. Osella, E. Sappa, A. Tiripicchio and M. Tiripicchio Camellini, Inorg. Chim. Acta. 34 (1979) L289.
245 A.R. Manning, J. Chem. Soc. (A) (1971) 2321.
246 A.R. Manning, J. Chem. Soc. (1968) 1319.
247 H.W. Sterberg, I. Wender, R.A. Friedel and M. Orchin, J. Am. Chem. Soc. 75 (1953) 2717.
248 A.M. Bond, Modern Polarographic Methods in Analytical Chemistry, Marcel Dekker Inc. (N. Y.) (1980).
249 G.A. Mabbott, J. Chem. Ed. 60 (1983) 697.
250 P.T. Kissinger, W.R. Heineman, J. Chem. Ed. 60 (1983) 702.
251 R.E. Dessy, R.B. King, M.Waldrop, J. Amer. Chem. Soc. 88 (1966) 5112.
252 J.C. Katz, J.V. Petersen, R.C. Reed, J. Organomet. Chem. 120 (1976) 433.

253 A.M. Bond, B.M. Peake, B.H. Robinson, J. Simpson, D. J. Watson, Inorg. Chem. 16 (1977) 410.
254 S B. Colbran, B.H. Robinson, J. Simpson, Organometallics 2 (1983) 943.
255 S.B. Colbran, B.H. Robinson, J. Simpson, Organometallics 2 (1983) 952.
256 P.A. Dawson, Ph.D. Thesis, University of Otago, (1978).
257 A.M. Bond, P.A. Dawson, B.M. Peake, P.H. Reiger, B.H. Robinson, J. Simpson, Inorg. Chem. 18 (1979) 1413.
258 A.J. Downard, B.H. Robinson, J. Simpson, J. Amer. Chem. Soc. 5 (1986) 1132.
259 A.J. Downard, B.H. Robinson, J. Simpson, J. Amer. Chem. Soc. 5 (1986) 1140.
260 K.Hinkelmann, J. Heinze, H.-J. Schacht, J.S. Field, H. Vahrenkamp, J. Amer. Chem. Soc. 111 (1989) 5078.
261 B.M. Peake, P.H. Reiger, B.H. Robinson, J. Simpson, Inorg. Chem. 20 (1981) 2540.
262 P.N. Lindsay, B.M. Peake, B.H. Robinson, J. Simpson, U. Honrath, H. Vahrenkamp, Organometallics 3 (1984) 413.
263 B.E.R. Schilling, R. Hoffmann, J. Amer. Chem. Soc. 101 (1979) 3456.
264 P.T. Chesky, M.B. Hall, Inorg. Chem. 20 (1981) 4419.
265 D.L. Stevenson, C.H. Wei, L.F. Dahl, J. Amer. Chem. Soc. 93 (1971) 6032.
266 D. Astruc, Angew. Chem. Int. Ed. Engl. 27 (1988) 643.
267 G.J. Bezems, P.H. Rieger and S. Visco, J. Chem. Soc. Chem. Comm. (1981) 264.
268 M. Arewgoda, B.H. Robinson and J. Simpson, J. Am. Chem. Soc. 105 (1983) 1893.
269 A.J. Downard, B.H. Robinson, J. Simpson, Organometallics 5 (1986) 1122.
270 J.C. Kotz, J.V. Petersen and R.C. Reed, J. Organomet. Chem. 120 (1976) 433.
271 J. Rimmelin, P. Lemoine, M. Gross, R. Mathieu and D. De Montauzon, J. Organomet. Chem. 309 (1986) 355.
272 R.D. George, K.M. Mackay and S.R. Stobart, J. Chem. Soc. Dalton Trans. (1972) 974.
273 K.L. Walters, J.N. Britain and W.M. Risen, Inorg. Chem. 8 (1969) 1347.
274 A.G. Robiette, G.M. Sheldrick, R.N.F. Simpson, B.J. Aylett and J.A. Campbell, J. Organomet. Chem. 14 (1968) 283.
275 D.W. Rankin and A. Robertson, J. Organomet. Chem. 104 (1976) 179.
276 K.L. Walters. W.M. Butler and W.M. Risen, Inorg. Chem. 9 (1971) 1970.
277 W.A.G. Graham, Inorg. Chem. 7 (1968) 315.
278 D.J. Patmore and W.A.G. Graham, Inorg. Chem. 6 (1967) 981.
279 R.F. Gerlach, B.W. Graham and K.M. Mackay, J. Organomet. Chem. 182 (1979) 285.
280 G.C. van der Berg, A. Oskam and K. Vrieze, J. Organomet. Chem. 57 (1973) 329.
281 G.C. van der Berg, A. Oskam and K. Vrieze, J. Organomet. Chem. 69 (1974) 169.
282 G.C. van der Berg and A. Oskam, J. Organomet. Chem. 78 (1974) 357.
283 W.M. Butler, W.A. McAllister and W.M. Risen, Inorg. Chem. 13 (1974) 1702.
284 D.F. Shriver and C.B. Cooper, Adv. Infrared Raman Spec. 6 127(1980)
285 G. Bor, J. Organomet. Chem. 94 (1975) 181.
286 R.D. Adams, F.A. Cotton, W.R. Cullen, D.L. Hunter and L. Mihichuk, Inorg. Chem. 14 (1975) 1395.
287 L-C. Song, M. Kadiata, J-T. Wang, R-J. Wang and H-G. Wang, J. Organomet. Chem. 340 (1988) 239.
288 G. Huttner, G. Mohr, B. Pritzlaff, J. von Seyerl and L. Zsolnai, Chem. Ber. 115 (1982) 2044.

289 S. Onaka and D.F. Shriver, Inorg. Chem. 15 (1976)915.
290 P. Skinner, M.W. Howard, I.A. Oxton, S.F.A. Kettle, D.B. Powell and N. Sheppard, J. Chem. Soc. Faraday Trans. 2 77 (1981) 1203.
291 G. Bor, L. Marko and B. Marko, Chem. Ber. 95 (1962) 333.
292 G. Etzrodt and G. Schmidt, J. Organomet. Chem. 169 (1979) 259.
293 M.W. Howard, S.F.A. Kettle, I.A. Oxton, D.B. Powell, N. Sheppard and P. Skinner, J. Chem. Soc. Faraday Trans. 2 77 (1981) 397.
294 M.W. Howard, I.A. Oxton, D.B. Powell and P. Skinner, Spectrochimica Acta. 37A (1981) 473.
295 M.J. Sailor, M.J. Went and D.F. Shriver, Inorg. Chem. 27 (1988) 2666.
296 A. Bonny and K.M. Mackay, J. Organomet. Chem. 144 (1978) 389.
297 S.R. Stobart, J. Chem. Soc. Dalton Trans. (1972) 2442.